DOCTOR OF PHILOSOPHY

Direct numerical simulations of non-premixed MILD flames

Nagarajan, Raguram

Award date:
2022

Awarding institution:
Coventry University

Direct numerical simulations of non-premixed MILD flames

Raguram Nagarajan

Faculty of Engineering, Environment and Computing

Coventry University

This dissertation is submitted for the degree of

Doctor of Philosophy

March 2022

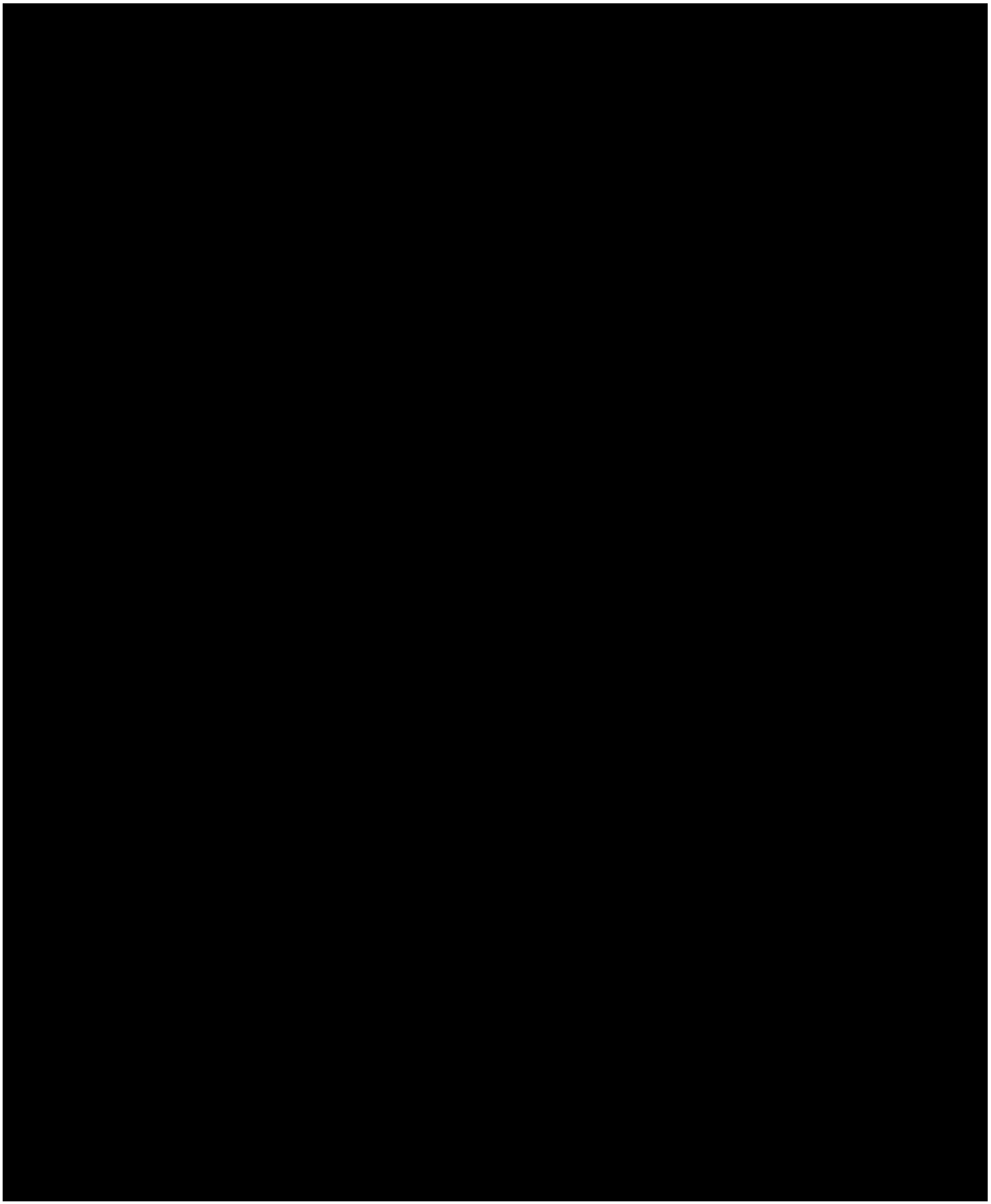

Certificate of Ethical Approval

Applicant:	Raguram Nagarajan
Project Title:	Direct Numerical Simulations of non-premixed MILD flames

This is to certify that the above named applicant has completed the Coventry University Ethical Approval process and their project has been confirmed and approved as Low Risk

Date of approval:	21 Dec 2020
Project Reference Number:	P116347

Acknowledgements

I would like to take this opportunity to express my gratitude to those who have offered me immense support throughout my PhD journey.

First of all, I would like to thank Dr Ebrahim Abtahizadeh, Dr Mansour Qubeissi, and Dr Nwabueze Emekwuru for giving me this great opportunity and guiding me throughout this strenuous journey. I would like to express my sincere gratitude to them for providing me with extraordinary technical and mental support during my PhD journey, and invaluable moral support during this ongoing pandemic. Moreover, without their input, constructive feedback and those numerous discussions with them, I would not have succeeded in constructing and shaping my thesis into an acceptable academic outcome.

I want to thank Dr Lorna Everall, the doctoral college team and Dr Alex Pedcenko for giving me administration support and IT support which helped me avoid many inconveniences, and carry out my research without unnecessary delays. I definitely cannot miss mentioning Mike, Lawrence, Ikram, Meryem, Emily, Reza, Alisson, Max and others who have given me fun filled memorable moments which made my PhD journey complete. It was very reassuring to have all those chats (both meaningful and meaningless) with other colleagues, who were sailing in the same boat and shared the same frustrations. I am amazed by the patience of Mike, Ikram, Meryem, and Emily, who never complained about my constant grizzling and instead showered me with confidence.

I would like to acknowledge Dr Jeroen Van Oijen and their group for giving me the guest researcher opportunity. Due to unexpected events, I had to take a new direction to complete my thesis during the middle of my PhD journey. Dr Jeroen helped me identify a new direction in which I was able to progress forward. He also offered me with exceptional technical guidance and helped me get required IT resources to run my simulations without which my PhD would have been impossible. I cannot thank him enough, I am feeling extremely grateful to find an opportunity to collaborate with h im. I would also like to thank Dr Ugur Goktolga for guiding me through the simulation setups and post-processing.

As you all are aware, PhD is a long journey during which I met numerous people on countless occasions who have helped me in their own ways in completing my journey, so I extend my sincere apologies to those whom I might have missed to acknowledge and also express my gratitude.

Abstract

Moderate or Intense Low-oxygen Dilution (MILD) combustion is an emerging combustion technology which can simultaneously improve the efficiency and reduce the emission levels of the combustion systems. In this study, Direct Numerical Simulation (DNS) is used to study the role of gaseous additives on combustion characteristics and reaction pathways of MILD combustion. The heat loss effects on the ignition behaviour of MILD flames and the effects of exhaust gas addition on the combustion characteristics of syngas enriched methane flames are also investigated. Syngas and carbon monoxide are used as the gaseous additives, and methane is used as the base fuel.

Syngas addition affects the ignition delay, flame structure, NO formation and reaction pathways of MILD methane flames. Syngas addition reduces the CH_4 content of MILD methane flames which decreases their NO mass fraction levels (prompt NO) at least by an order of 10^{-1}. The preferential diffusion effects become important in MILD methane flames with syngas addition. Furthermore, in case of MILD methane flames, the ignition characteristics are controlled by the exhaust gas content of the oxidiser stream. Upon the addition of syngas, both exhaust gas content of the oxidiser stream and hydrogen content of the fuel control the ignition characteristics of MILD methane flames. For instance, syngas addition to MILD methane flames shortens their ignition delay by up to 10^{-2} s. The syngas addition also increases the flux rate between the major intermediate species formed during the combustion process, and affects the major intermediate species formed during the ignition stage. Exhaust gas addition to syngas enriched methane flames reduces their flame temperature, flame structure, NO formation, and ignition delay. The changes observed in these parameters and properties depend on the amount of exhaust added to the flames.

The carbon monoxide addition to adiabatic MILD methane flames shortens its ignition delay up to 1.28 ms (at oxidiser temperature 1400 K). This shortened ignition delay is found to be significant especially at oxidiser temperatures lower than 1600 K. Additionally, the carbon monoxide addition affects the concentration of the major intermediate species, increases the scalar dissipation rate, and makes preferential diffusion effects important especially in the flame development stage post the ignition stage.

The heat loss effects lengthen the ignition delay of MILD methane flames by 1.11 ms (from 1.01 ms to 2.12 ms) and the ignition delay of carbon monoxide enriched MILD methane flames by 1.01 ms (from 0.91 ms to 1.92 ms) at oxidiser temperature 1700 K. In case of adiabatic MILD methane flames, the ignition characteristics are governed by the molecular diffusion process. However, in MILD flames with the inclusion of heat loss effects, both molecular diffusion and turbulence govern the ignition characteristics. The investigation of carbon monoxide addition to turbulent MILD methane flames with the inclusion of heat loss reveals that such trends agree well with those observed in the adiabatic turbulent MILD methane flames.

The reaction pathway analysis shows that the carbon monoxide addition to MILD methane flames increases the flux rate between the intermediate species. In addition, in MILD methane flames, only the ethane to vinyl pathway seems to be important in the methane to carbon dioxide oxidation pathway. In carbon monoxide enriched MILD methane flames both ethane to vinyl and formaldehyde pathways become important in the methane to carbon dioxide oxidation pathway. However, in both the flames, the top intermediate species involved in methane to water vapour oxidation pathways are identical, and their oxidation pathways are similar.

Table of contents

List of figures

List of tables

Nomenclature

Abbreviations

SFR	*Species Flux Rate*
0D	Zero-Dimensional
1D	One-Diemnsional
2D	Two-Dimensional
3D	Three-Dimensional
CFDF	CounterFlow Diffusion Flame
DME	Dimethyl Ether
DNS	Direct Numerical Simulations
EGR	Exhaust Gas Recirculation
EINO	NO emission indicies
FGM	Flamelet Generated Manifold
HitAC	High Temperature Air Combustion
IML	Igniting Mixing Layers
JHC	Jet-in-Hot Coflow
LES	Large Eddy Simulations
LMI	Linear Mixing Ignition
LPG	Liquefied Petroleum Gas
MILD	Moderate or Intense Low-oxygen Dilution
PFR	Plug Flow Reactor

QRPD	Quantitative Reaction Path Diagram
RANS	Reynolds Averaged Navier-Stokes

Atoms

Symbol	Definition
C	Carbon atom
H	Hydrogen atom
N	Nitrogen atom
O	Oxygen atom

Chemical species

Formula	Definition
C_2H_2	Acetylene
C_2H_3	Ethylenyl
C_2H_5	Ethyl radical
C_2H_6	Ethane
CH_2O	Formaldehyde
CH_3	Methyl radical
CH_4	Methane
CO	Carbon monoxide
CO_2	Carbon dioxide
H_2	Hydrogen
H_2O	Water vapour
HCN	Hydrogen cyanide

HCO	Formyl radical
N_2	Nitrogen
N_2O	Nitrous oxide
NCN	Cyanonitrene
NO	Nitric oxide
O_2	Oxygen
OH	Hydroxyl radical

Greek symbols

Symbol	Definition	Units
χ	Scalar dissipation rate	s^{-1}
$\dot{\omega}_\alpha$	Source term of species α	$kg\,m^{-3}\,s^{-1}$
$\dot{\omega}_T$	Source term of temperature,	$J\,m^{-3}\,s^{-1}$
ε	Turbulence dissipation rate	$m^2\,s^{-3}$
λ	Thermal conductivity	$J\,m^{-1}\,s^{-1}\,K^{-1}$
μ	Dynamic viscosity	$kg\,m^{-1}\,s^{-1}$
ν	Kinematic viscosity	$m^2\,s^{-1}$
ν''_α	Reaction stoichiometric coefficient of the product species α	–
ν'_α	Reaction stoichiometric coefficient of the reactant species α	–
Φ	Equivalence ratio	–
ρ	Mixture density	$kg\,m^{-3}$
τ_{ign}	Ignition delay	s
β	Temperature exponent (Arrhenius equation)	–

Mathematical symbols

Symbol	Definition
$*$	Multiplication
$+$	Addition
$-$	Subtraction
$/$	Division
$<$	Less than
$<=>$	Reversible reaction
$=$	Equal to
$>$	Greater than
[]	Brackets
%	Percentage
$\cdot$	Dot product
∂	Partial derivative
$\prod$	Parentheses
$\sum$	Summation
()	Parentheses

Roman symbols

Symbol	Definition	Units
ΔT	Temperature difference	K
ΔU	Relative velocity between fuel and oxidiser stream	$\mathrm{m\,s^{-1}}$
$\dot{m}^{egr}$	Mass flow rate of EGR	$\mathrm{kg\,s^{-1}}$
$\dot{m}^{egr}_{ox}$	Mass flow rate of the EGR and oxidiser mixture	$\mathrm{kg\,s^{-1}}$

$\dot{m}_{fu}$	Mass flow rate of fuel	$\mathrm{kg\,s^{-1}}$
$\dot{m}_{ox}$	Mass flow rate of fresh oxidiser	$\mathrm{kg\,s^{-1}}$
a	Applied strain rate	$\mathrm{s^{-1}}$
$c_{p\alpha}$	Specific heat capacity at constant pressure of species α	$\mathrm{J\,kg^{-1}\,K^{-1}}$
c_p	Specific heat capacity at constant pressure	$\mathrm{J\,kg^{-1}\,K^{-1}}$
D	Diffusivity of scalar	$\mathrm{m^2\,s^{-1}}$
$D_{\alpha k}$	Multicomponent diffusion coefficient of species α	$\mathrm{m^2\,s^{-1}}$
D_α	Diffusivity coefficient of species α	$\mathrm{m^2\,s^{-1}}$
D_α^T	Thermal diffusion coefficient of species α	$\mathrm{m^2\,s^{-1}}$
E_a	Activation energy (Arrhenius equation)	J
h	Total enthalpy of the mixture	$\mathrm{J\,kg^{-1}}$
h_α	Total enthalpy of species α	$\mathrm{J\,kg^{-1}}$
h_s	Sensible enthalpy	$\mathrm{J\,kg^{-1}}$
J	Pressure curvature	
$jetRe$	Jet Reynolds number	–
K	Stretch rate	$\mathrm{s^{-1}}$
k	Wave number	$\mathrm{m^{-1}}$
k_c	Cut-off wave number	$\mathrm{m^{-1}}$
k_{eq}	Equilibrium constant	–
k_f	Reaction rate coefficient of forward reaction	–
k_r	Reaction rate coefficients of backward reaction	–
L	Characteristic length	m
l_λ	Taylor microscale	m

l_o	Integral length scale	m
L_x, L_y, L_z	Computational domain lengths used in DNS	m
Le	Lewis number	–
Le_α	Lewis number of species α	–
M_α	Molecular weight of species α	$\mathrm{kg\,mol^{-1}}$
N_x, N_y, N_z	Number of grid points in computational domain	–
p	Pressure	atm
Pr	Prandlt number	–
r_f	Reaction rate of forward reaction	$\mathrm{mol\,m^{-3}\,s^{-1}}$
r_r	Reaction rate of backward reaction	$\mathrm{mol\,m^{-3}\,s^{-1}}$
Re	Reynolds number	–
T	Temperature	K
T_b	Burnt gas or product temperature	K
T_{ign}	Autoignition temperature	K
T_{in}	Inlet temperature	K
T_{max}	Maximum combustion temperature	K
T_{si}	Self-ignition temperature	K
Th	Sets lower limit for QRPD arrow thickness	–
Th	Sets upper limit for QRPD arrow thickness	–
$u^{'}$	Root-mean-square of turbulent velocity fluctuation	$\mathrm{m\,s^{-1}}$
V_α	Diffusion velocity of species α	$\mathrm{m\,s^{-1}}$
X_{NO}	Molar fraction of NO	–
Y_α	Mass fraction of species α	–

Y_{egr}	Exhaust gas mass fraction in the EGR and oxidiser mixture	–
Z	Elmental mixture fraction	–
z	Elemental mass fraction	–
Z_{mr}	Most reactive mixture fraction	–
Z_{st}	Stoichiometric mixture fraction	–
$\bar{M}$	Mean molecular weight	$\mathrm{kg\,mol^{-1}}$
$\bar{\bar{I}}$	Unit vector	–
$\boldsymbol{u}$	Velocity vector	$\mathrm{m\,s^{-1}}$
A	Pre-exponential factor (Arrhenius equation)	–
M	Molecular weight	$\mathrm{kg\,mol^{-1}}$
R	Universal gas constant	$\mathrm{J\,mol^{-1}\,K^{-1}}$

Subscripts and superscripts

Symbol	Definition
ar	Arrow
b	Burnt gas
c	Cut-off
egr	Exhaust gas recirculation
eq	Equilibrium
f	Forward
fu	Fuel
ign	Ignition
in	Inlet
$initial$	Initial

ll	Lower limit
max	Maximum
min	Minimum
ox	oxidiser
r	Reverse
si	Self-ignition
ul	Upper limit
a	Activation

Chapter 1. Introduction

1.1 Background

Energy has become a basic necessity in the day-to-day life of modern humans. It plays an important role in the socio-economic development of countries across the globe. Energy consumption of the world has significantly increased in the past two centuries. As shown in Figure 1.1, the forecast by the United States Energy Information Administration (EIA 2019) shows that the energy consumption of the world will continue to increase in the next few decades. The figure shows that a significant share of the energy demand was and still is by the consumption of fossil fuels, and fossil fuels would remain a key player in the energy sector for the foreseeable future.

These fossil fuels are hydrocarbon compounds trapped deep inside the crust of the earth through the accumulation of atmospheric carbon dioxide over millions of years through plants and animals. Carbon dioxide is released back into the atmosphere when these fossil fuels are combusted to produce energy. Since carbon dioxide is a greenhouse gas, it traps heat in the atmosphere which results in global warming (Cook 2012). However, it is hard to give a single number, the lifetime of carbon dioxide in the atmosphere can be as long as 200 years (Archer et al. 2009). The carbon dioxide emission trends by source between the years 1751 and 2017 are presented in Figure 1.2. It is apparent in the figure that the carbon dioxide concentration in the atmosphere increases exponentially after the year 1850, the beginning of the second industrial revolution. It should be noted that the contribution of fossil fuels alone in carbon dioxide emission is more than eighty-six percent during the year 2017. This increase in carbon dioxide concentration in the atmosphere due to human activities has warmed up the earth by 0.95° C (as per 2019) compared to that of the pre-industrial era

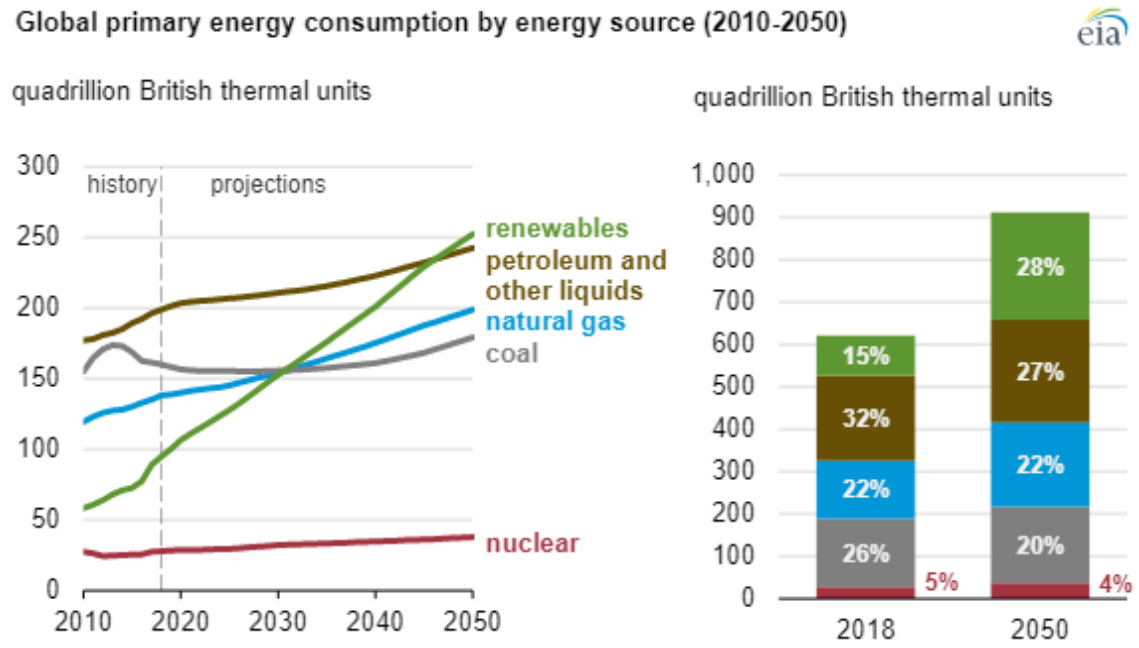

Fig. 1.1 Global energy consumption by fuel type between years 2010 and 2050 plotted in quadrillion British Thermal Units (BTU). The figure shows that fossil fuels would remain as a key player in the energy sector for the foreseeable future. Source: International energy outlook 2019, U.S. Environment Information Administration (EIA 2019).

(NC Environmental Information 2020). If this trend continues, by the end of the twenty-first century, the mean global temperature rise compared to that of the pre-industrial era might be more than 3° C (UNEP & Partnership 2020). Such an increase in global mean temperature might push millions of species to extinction (Boktin 2013).

In addition to carbon dioxide, emission of harmful pollutants such as nitrogen oxides (NO_x) and carbon monoxide (CO) are released during the combustion process of hydrocarbon -based fossil fuels. A significant quantity of NO is formed in a few seconds at temperatures close to 1873 K, or in a few milliseconds for temperature greater than 2273 K (Wünning & Wünning 1997). Carbon monoxide is formed as a result of the decomposition of carbon dioxide which is unstable at temperatures greater than 1900 K, please refer to Figure 1.3.

Even though these gases do not contribute to global warming, they have adverse effects on the environment and health. The inhalation of a high concentration of NO_x can aggravate respiratory diseases, can lead to the development of asthma, and can cause irritation in the

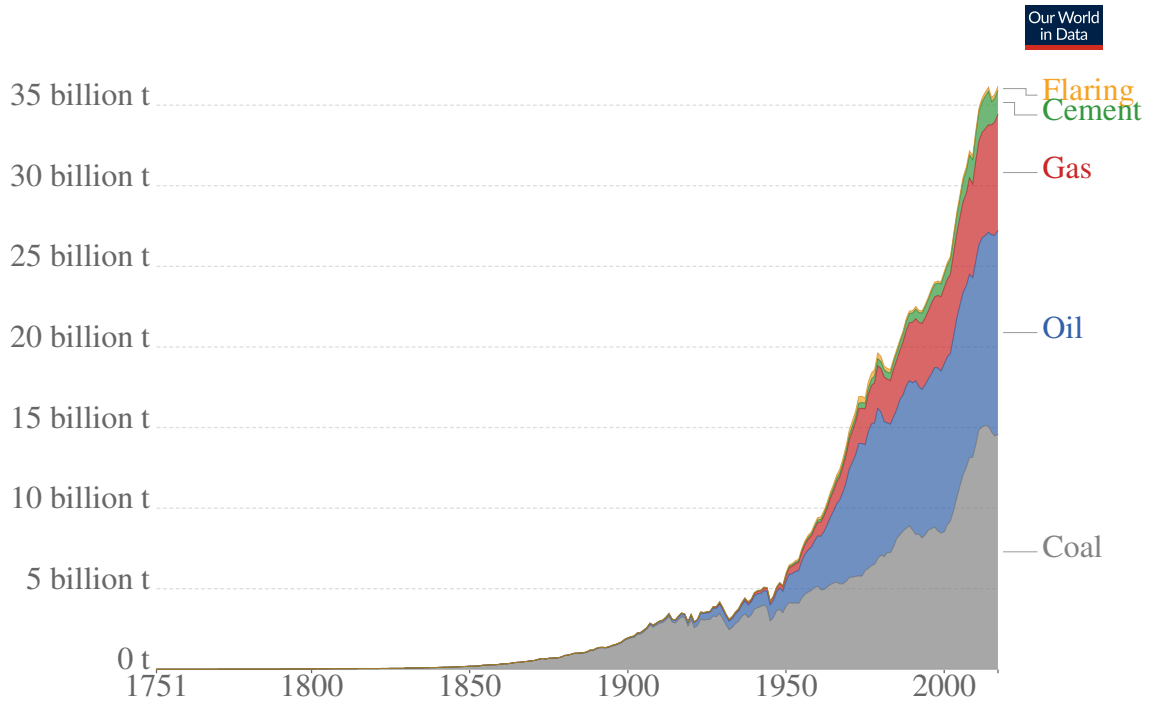

Fig. 1.2 Global carbon dioxide emission trends by source. The emission data is given for years between 1751 and 2017. Source: Global Carbon Project, CDIAC (Boden, Andres & Marland 2017).

airways of the human respiratory system (Centre for Environmental Assessment RTP division 2016). In the environment, NO_x can cause acid rain (Singh & Agrawal 2007). The inhalation of carbon monoxide can cause confusion, coma, clumsiness, impaired judgment, myocardial ischemia, and even death (Abelsohn et al. 2002). Carbon monoxide and NO_x can cause ozone formation at ground level which is very harmful to the human respiratory system (Beck et al. 1998). Therefore, stringent emission standards are introduced by governments across the globe to regulate emission levels of these pollutants.

As is evident above, it is necessary to develop new combustion technologies for the combustion of fossil fuels which could help us to achieve low emission levels. Such technologies should also allow us to make a smooth transition towards renewable energy that has zero carbon foot-prints to mitigate carbon dioxide emission and to delay or reverse global warming. Thus, new combustion technologies such as lean-premixed combustion

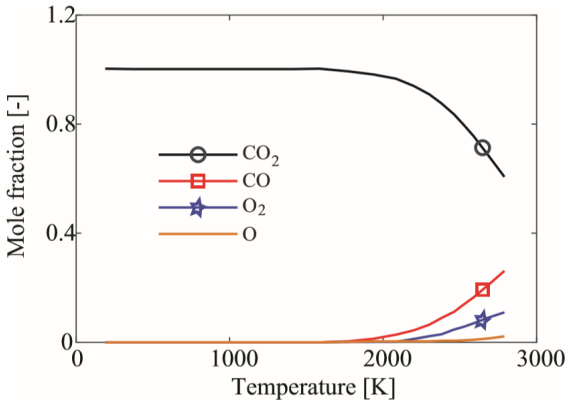

Fig. 1.3 Equilibrium composition of carbon dioxide (CO_2) plotted as a function of temperature. As it can be seen, CO_2 is stable until 1900 K. Above 1900 K, CO_2 becomes unstable and starts to dissociate into carbon monoxide (CO), oxygen molecule (O_2) and oxygen atom (O). The equilibrium calculations are performed using CHEMKIN (*ANSYS Chemkin Theory Manual 17.0 (15151)* 2015).

and Moderate or Intense Low-oxygen Dilution (MILD) combustion are being developed by researchers across the world. The fuel-lean combustion or lean-premixed combustion are prone to flashback which could damage the combustion systems and can lead to severe accidents. In case of gas turbines, the lean-premixed combustion are vulnerable to thermoacoustic instabilities which can lead to flame blow-off. The number of instances of the development of thermoacoustic instabilities can be significantly reduced by preheating the inlet reactants through heat recovery from the exhaust gas. However, preheating the inlet reactants temperature in premixed combustion would increase the peak flame which would rise the thermal NO emission levels. These drawbacks impede us from the consideration of this technology for practical combustion application.

MILD combustion, also know as flameless combustion, can be a more promising alternative for the conventional combustion technologies which would help us to achieve low pollutants formation in the exhaust gas produced from the combustion of fossil fuels and to make a smooth transition towards renewable energy with zero-carbon footprints to mitigate carbon dioxide emission levels.

As the name suggests, Moderate or Intense Low-oxygen Dilution or MILD combustion is achieved by a high degree of dilution and a high degree of preheating of oxidser stream with burnt combustion products. Because of high dilution levels of oxidiser and low initial oxygen molar fraction, MILD combustion is characterised by relatively low-temperature rise and slow reaction rates with very low or no emission of visible radiation (Cavaliere & de Joannon 2004). Since MILD combustion is characterised by a very low or no emission of visible radiation, it is also known as flameless combustion. Due to the low-temperature rise in MILD combustion, the peak combustion temperature of MILD combustion is generally lower than 1900 K (Wünning & Wünning 1997, Cavaliere & de Joannon 2004); this is much less than the adiabatic temperature of the hydrocarbon fuels which is usually much greater than 2000 K (Glassman et al. 2014). As a result, NO and CO formation in MILD combustion is completely avoided or significantly reduced (Wünning & Wünning 1997, Katsuki & Hasegawa 1998, Cavaliere & de Joannon 2004). Figure 1.4 shows the images of conventional and MILD combustion of heavy oil fuel burnt in a prototype swirl burner (Milani & Saponaro 2001). As is evident in the figure, MILD combustion is flameless and no visible radiation is observed compared to that of conventional combustion in which the flame is distinctly visible.

Fig. & Saponaro (2001). As is evident in the figure, MILD combustion is flameless and no visible radiation is observed compared to that of conventional combustion.

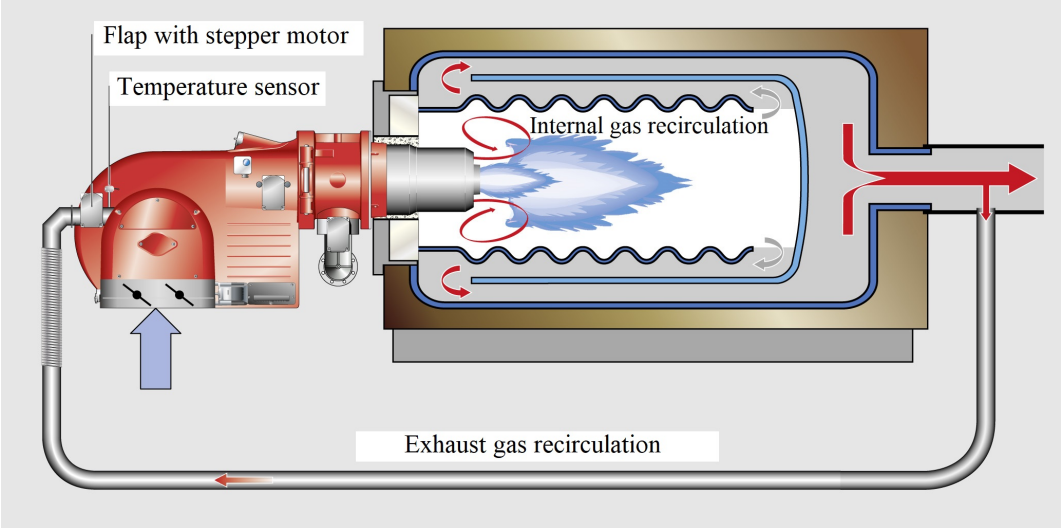

Fig. 1.5 MILD combustion is achieved through internal and external recirculation zone. Source: *Typical setup of flue gas recirculation system with WM burner* (n.d.).

The high degree of preheating and dilution of oxidiser in MILD combustion is achieved by mixing the oxidiser stream with burnt combustion products or flue gases. The burnt gases can be supplied using two methods: internal and/or external recirculation of burnt gases, and burnt combustion products from a different or secondary burner. Figure 1.5 shows the internal and external recirculation of burnt gases in a MILD burner. Figure 1.6 shows that the flue gas of Burner B is supplied to Burner A to achieve MILD combustion. Since waste heat is recovered from the burnt combustion products in MILD combustion, the combustion efficiency is enhanced in the combustors operating in MILD regime (Wünning & Wünning 1997, Katsuki & Hasegawa 1998, Cavaliere & de Joannon 2004).

According to Cavaliere & de Joannon (2004), MILD combustion is defined as the combustion mode in which the fuel and/or oxidiser are preheated to a temperature, so that the initial temperature of the reactants (fuel and oxidiser) mixtures T_{in} is greater than the autoignition temperature T_{ign} of the reactants mixture, and the maximum temperature rise ($\Delta T = T_b - T_{in}$) inside the combustor is smaller than T_{ign}, i.e. $\Delta T < T_{ign}$, where T_b is the maximum temperature attained by the burnt gases or products of combustion. Even though MILD combustion is characterised by low oxygen level, low-temperature rise and slow

Fig. 1.6 MILD combustion is achieved in Burner A using the burnt combustion products or flue gas from Burner B. Source: Li et al. (2011).

reaction rate, the high temperature of the reactants helps to maintain the combustion process. Figure 1.7 shows the combustion type diagram to distinguish MILD combustion mode from pilot assisted, high temperature air (HiTAC), and conventional premixed combustion modes achievable for a $CH_4/O_2/N_2$ mixture in a well-stirred reactor (Cavaliere & de Joannon 2004). The calculations of well-stirred reactor are performed for a mixture of $CH_4/O_2/N_2$ with $10\%/5\%/85\%$ molar fraction percentages for residence time 1 s at one atmosphere. As is seen, the diagram is classified into three regimes by the interception of two lines (the self-ignition temperature T_{si}) on both axes. The figure clearly shows that MILD combustion is only sustainable when the inlet reactants temperature is greater than that of T_{si}, and the temperature rise (ΔT) during the MILD combustion process is lower than that of T_{si}.

As is evident above, the major advantages of MILD combustion are: high efficiency and low emission levels. The high degree of preheating of inlet reactants in MILD combustion (achieved through external recirculation) allows the combustor to be operated at high-velocity jet fields, and the necessity for internal recirculation of burnt combustion products in the

Fig. 1.7 Combustion type diagram to distinguish MILD combustion mode from other combsution modes achievable for a methane/oxygen/nitrogen mixture in a well stirred reactor, source: Cavaliere & de Joannon (2004). The figure shows that MILD regime is only possible when initial temperature of the reactants is greater than the self-ignition temperature and the overall temperature rise is less than T_{si} of the reactants.

combustor can be avoided (Medwell 2007). Consequently, the MILD combustor design is no more constrained by the requirements of flame holders or internal recirculation zones to achieve continuous stable combustion. The elimination of these design constraints in MILD combustion makes this combustion technology attractive for high-speed combustion applications.

The results of the experiment performed by Tang et al. (2010) showed that high efficiency can be achieved on the pulverised coal gasifier during the coal gasification process when the gasifier is operated at MILD combustion mode. The results of the experiments performed by Medwell & Dally (2012*a*) revealed that the MILD combustion of different types of hydrocarbon fuels mixed with hydrogen (natural gas/hydrogen, ethylene/hydrogen, and LPG/hydrogen) resulted in similar reaction zone structures even though the combustion properties of each pure hydrocarbon fuels significantly differ from each other. Similarly, Ye et al. (2018), in their experiments, observed that the evolution of intermediate species (such as

Fig. 1.8 Potential applications of MILD combustion technology in several industries. Source: Li et al. (2011).

OH and CH_2O) and their overall spatial distribution and combustion temperature were very similar for DME and ethanol flames under MILD conditions. Steel and metallurgy industries have been utilising MILD combustion in their industrial burners since the 1990s (Li et al. 2011). Figure 1.8 shows the potential applications of MILD combustion technology in various industries in high-intensity applications, heat utilisations, coal and chemical processing plants, and low calorific fuel to energy applications (Li et al. 2011). The above discussions clearly show that MILD combustion has high efficiency and low emission levels. In addition, its insensitivity towards different types of hydrocarbon fuels is a potential advantage for the implementation and application of MILD combustion in practical combustion systems.

Flame stabilisation is an important requirement of a combustion system to ensure a continuous operation, to achieve high efficiency and low emission levels. In general, the

stabilisation of flame is achieved by the attachment of flame to the burner of the combustion system. Failure to achieve flame stabilisation results in flame blow-off and flashback. Flame blow-off leads to flame extinction, incomplete combustion, low combustion efficiency, and increased emission levels which are not desirable during the operation of a combustion system (Lieuwen 2012). Flashback, which exclusively occurs in lean-premixed combustors could damage the combustion system (Benim & Syed 2014). Therefore, the achievement of flame stabilisation is of utmost importance in the design and operation stages of the combustion systems.

The flame stabilisation of a combustion system depends on the ignition behaviour and flame characteristics of the combustion process that takes place within it. For instance, flame propagation plays a key role in the flame stabilisation of conventional flames (Jansohn 2013). The flame stabilisation mechanism in MILD combustion is different from that of the conventional combustion process; previous experimental investigation (Oldenhof et al. 2010) and DNS results (Göktolga et al. 2015, Yoo et al. 2009) reveal that autoignition plays an important role in flame stabilisation rather than flame propagation. Moreover, as MILD combustion is characterised by slow reaction rate and low-temperature rise, comprehension of its flame stabilisation mechanism has been a central topic of investigation in many research works (Göktolga et al. 2015, Yoo et al. 2009, Oldenhof et al. 2010, Van Oijen 2013, Oldenhof et al. 2011, Zhou et al. 2020, Jung et al. 2018, Doan & Swaminathan 2019, Arteaga Mendez et al. 2015, Medwell et al. 2014, Choi & Chung 2010, Al-Noman et al. 2018, Dally et al. 2002, Cabra et al. 2002).

In previous studies, efforts have been made to understand the role of hydrogen addition on the MILD flames. Sabia et al. (2007) performed numerical simulations of well-stirred-reactors to understand the effects of hydrogen addition on MILD methane flames. Their results reveal that the addition of even a small fraction of hydrogen in MILD methane flames enhances the mixture reactivity of the methane flames and also significantly alters its

oxidation kinetics. Medwell et al. (2008) investigated the effects of hydrogen addition on MILD ethylene flames using experimental techniques. Their results reveal that the addition of hydrogen on MILD ethylene flames increases the OH formation levels and peak mean temperature compared to that of pure ethylene flames. The numerical studies performed by Christo & Dally (2005) and Mardani et al. (2010) consistently predicted the experimental measurements of Dally et al. (2002), and they showed that the preferential diffusion effects of hydrogen are of significant importance in MILD flames. Numerical investigation of Mardani & Tabejamaat (2010) showed that the increment of hydrogen molar fraction in the fuel increases the diffusive mixing of fuel and oxidiser streams of MILD flames. Arteaga Mendez et al. (2015) studied the effects of hydrogen addition on the MILD methane flames using experimental techniques. Their results reveal that hydrogen is a very good flame stabiliser even at hydrogen molar fraction in the fuel as low as 5%. They also observed that hydrogen addition significantly changed the flame structure, reduced the lift-off height, increased the turbulence intensity, and the diffusive mixing of fuel and oxidiser. As is evident above, hydrogen addition in MILD flames clearly enhances its flame stabilisation by increasing the mixture reactivity, turbulence intensity levels, OH formation levels, diffusive mixing, and mean peak temperature.

Although the advantages of hydrogen addition in MILD flames are extensively analysed and well established, the economic and other practical aspects of production, storage and distribution of renewable hydrogen on large-scales for practical applications are still far from feasible (Abbasi & Abbasi 2011, Kurtz et al. 2019, Al Qubeissi & El-Kharouf 2020).

Hydrogen-rich gases such as syngas obtained from biomass gasification, reformate gases, organic waste and coke oven gas have a huge economic potential and are environmentally friendly (Gökalp & Lebas 2004). Processing waste to produce biofuels (such as syngas) can also help us reduce their cost and appears as a sustainable choice to address the issues associated with increasing energy demand (Al Qubeissi 2019). Therefore, these hydrogen-

rich gases can be used as gaseous additives in MILD combustion instead of using pure hydrogen, yet, the advantages of hydrogen addition can be accomplished. Although the specific composition of these gases varies based on production methods and raw materials, these gases are primarily a mixture of hydrogen and carbon monoxide.

Even though the effects of syngas addition to MILD flames have not yet been investigated, the addition of syngas in hydrocarbon flames is found to be advantageous in previous studies. Catalytic combustion of CH_4/CO/H_2 mixtures for pressures until ten bar is investigated using experimental techniques by Barbato et al. (2013). Outcomes of their study revealed that the syngas addition to methane flames improves their ignition characteristics and ignition range i.e. at lower pressures by enhancing the reactivity of the mixture. The effects of methane, carbon monoxide, and hydrogen on NO and CO emissions from non-premixed CH_4/CO/H_2 and air flames in porous burner configuration was investigated experimentally by Alavandi & Agrawal (2008). He and his co-workers observed that, for a fixed adiabatic temperature, increasing syngas proportion in the fuel mixtures lowered CO and NO emission levels. Furthermore, they observed that the addition of syngas to the fuel mixtures reduce the temperatures of lean blowout limits. Effects of composition and N_2 dilution levels on nitric oxide emissions of syngas in one-dimensional counterflow diffusion flame configuration is investigated using numerical tools by Park & Kim (2017). Results of their study show that, for dilution levels greater than 80%, increasing the concentration of H_2/CO in the fuel mixture decreases the NO formation levels. Dai et al. (2012) investigated the effects of the addition of syngas on the performance of a gasoline engine at fuel lean conditions. They observed that syngas addition increased the peak cylinder pressure, indicated cylinder efficiency, and reduces the flame development and propagation duration.

As is discussed above, the addition of syngas to hydrocarbon flames is found to be advantageous. The isolated effects of hydrogen, one of the two major components of syngas, on MILD flames are extensively investigated. However, the isolated effects of carbon

monoxide, the other major component of syngas, are only investigated on conventional hydrocarbon flames and its effects on MILD flames are yet to be understood.

The isolated effects of carbon monoxide addition to conventional flames are discussed as follows. Konnov et al. (2008) investigated the addition of carbon monoxide on premixed unstretched flames using experimental and numerical methods. The molar fraction of CO in the fuel is increased up to 15%. The results show that the CO addition increases adiabatic burning velocity, flame temperature, and thermal NO formation levels (due to the rise in flame temperature). Wu et al. (2009) investigated the effects of carbon monoxide addition on premixed opposed jet flames using experimental and numerical techniques. The molar fractions of carbon monoxide in the fuel are increased up to 80%. The results reveal that the carbon monoxide addition increases the laminar burning velocity and affects the oxidation mechanism. Wu et al. (2012) investigated the effects of carbon monoxide addition on a laminar triple-flame. The results of their study reveal that the addition of carbon monoxide increases propagation velocity (due to reaction chemistry) and affects heat release volume. They observed that in methane flames with a small amount of added carbon monoxide, the global propagation of triple flame is proportional to the density ratio of the reactants and the products. On the other hand, with a large amount of added carbon monoxide, the global propagation of triple flame is not exactly proportional to the density ratio between reactants and products. Amin et al. (2015) in their work investigated the effects of carbon monoxide addition on counterflow diffusion flames. The results show that the addition of carbon monoxide on oxidiser streams increases the extinction strain rate. On the other hand, carbon monoxide addition on the fuel stream does not have any effect on the extinction strain rate. Oh et al. (2013) investigated the effects of addition of CO on non-premixed oxy-methane flames jet in a lab-scale furnace. The results of their studies show that the addition of CO in the fuel jet increased the attached flame region and lifted flame region, and it reduced the flame length, flame slope, and light emission intensity.

The above discussions and the findings of the literature survey show that the addition of gaseous additives such as syngas and carbon monoxide in methane flames has a definite effect on its flame characteristics and enhances its flame stabilisation properties. This shows that the addition of these renewable additives on MILD flames could be advantageous, nevertheless, these have to be investigated. The findings of these investigations would encourage the usage of syngas, carbon monoxide, and the application of MILD combustion to combustion systems which have several environmental and economical advantages. Investigation of these topics would also shed light on the role of CO on syngas enriched methane flames. As mentioned already, comprehension of the underlying physics of syngas enriched combustion is important as it would help us to accomplish the advantages of hydrogen addition on MILD combustion which would further encourage its application and overcome the challenges that are associated with hydrogen production, transportation, and storage.

Heat loss can occur in flames through several mechanisms such as heat loss through the combustion chamber wall (Lammel et al. 2012), heat loss due to radiation (Dally et al. 1998), heat losses prior to reactants entering the combustion chamber (Dally et al. 2002, Arteaga Mendez et al. 2015), etc. As it will be discussed in Chapter 2 and Section 4.2, the flame configuration considered for performing the 2D and 3D numerical simulations in the present study represents Jet-in-Hot Coflow (JHC) flames. In a previous experimental study of JHC flames (Dally et al. 2002), a large variation in oxidiser temperature was observed when the oxidiser entered the combustion chamber. This is due to the presence of a cooling jacket that envelopes the fuel pipe. Hence, the heat loss mechanism in JHC flames resembles the heat losses prior to reactants entering the combustion chamber. Göktolga et al. (2015) investigated the heat loss effects on ignition delay and flame structure of MILD CH_4/H_2 JHC flames. They considered a varying temperature profile to model this heat loss mechanism. They found that the consideration of heat loss significantly increased the ignition delay of CH_4/H_2 flames. It also significantly altered the flame characteristics and ignition mechanism

of MILD JHC flames. The results of their study clearly shows that heat loss has a significant effect on the combustion characteristics of MILD flames.

The combustion process can be investigated in two ways: using experimental methods or using numerical methods. Although the experimental investigation has some advantages, they are not comprehensive. An experimental setup built for the investigation of a particular combustion problem may not be suitable for another problem. Building a new set up would be very expensive and time-consuming. Since MILD combustion is characterised by very low or no visible emission of visible radiation, investigation of MILD combustion using existing experimental techniques such as laser diagnostics is extremely challenging. The consideration of various gaseous additives in MILD combustion further complicates the experimental procedure. On the other hand, the investigation of various combustion problems using numerical methods can be accomplished by just changing the boundary conditions, initial conditions, and combustor geometry. Investigation of new combustion problems using numerical methods requires no or relatively less investment compared to that of experimental methods. Some powerful numerical software like OpenFOAM is even available as freeware. Hence, in the present thesis, numerical methods are considered for the investigation of the MILD combustion process.

1.2 Aim and objectives

This thesis describes a numerical investigation into the MILD combustion of renewable and fossil fuel mixtures. It is aimed to account for the simulation accuracy, and the underlying physics of ignition and combustion of non-premixed MILD methane flames enriched with renewable gases. Numerical techniques will be used to carry out the study conducted in this thesis. The following objectives have been reached to deliver the thesis:

1. Identify the numerical modelling techniques that are suitable for the examination of combustion characteristics and reaction pathways of non-premixed MILD flames (please refer to Chapter 2). Identify the numerical codes, chemical mechanisms, geometry, and simulation parameters that are appropriate for the investigation of the combustion characteristics of non-premixed MILD flames. For syngas enriched MILD methane flames, this objective is addressed in Chapter 3 and for carbon monoxide enriched MILD methane flames, this objective is addressed in Chapter 4 and Chapter 5.

2. Perform numerical simulations of adiabatic MILD methane flames and adiabatic MILD methane flames enriched with syngas (please refer to Chapter 3) and carbon monoxide (please refer to Chapter 4).

3. Compare and analyse the adiabatic numerical simulation results to understand the effects of syngas and carbon monoxide addition on the combustion characteristics of adiabatic MILD methane flames. Additionally, analyse the effects of exhaust gas addition to syngas enriched methane flames. The comparison and analysis of results address this objective relevant to syngas addition are presented in Chapter 3 and relevant to carbon monoxide addition are given in Chapter 4.

4. Perform numerical simulations of non-adiabatic MILD methane flames and non-adiabatic MILD methane flames enriched with carbon monoxide. This objective is addressed in Chapter 5.

5. Analyse the non-adiabatic results to understand the effects of heat loss on the ignition characteristics of MILD flames. Additionally, investigate the effects of carbon monoxide addition on the combustion characteristics of non-adiabatic MILD methane flames. The analysis, investigation, and discussions that address this objective are presented in Chapter 5.

6. Generate Quantitative Reaction Path Diagrams (QRPDs) of MILD flames, and investigate the effects of syngas addition (please refer to Section 3.3.3) and carbon monoxide addition (please refer to Section 5.3.5) on the reaction pathways of MILD methane flames.

7. Evaluate the possibility of the development of Igniting Mixing Layers (IML) based Flamelet Generated Manifold (FGM) model for the prediction of ignition behaviour and flame characteristics of adiabatic (please refer to Section 4.3.1) and non-adiabatic MILD flames (please refer to Section 5.3.1).

1.3 Thesis outline

In Chapter 2, a theoretical overview of various concepts that are relevant to the numerical modelling of combustion is explained in this chapter. In addition, the governing equations that describe the reacting flows are presented. In Chapter 3, the effects of exhaust gas content on the combustion characteristics, NO_x emissions and oxidation pathways of methane flames enriched with syngas (including the MILD regimes) are examined using 1D and 0D direct numerical simulations. Additionally, the effects of syngas addition to MILD methane flames are discussed by comparing the results obtained in this study with the results of MILD methane flames simulations performed by Abtahizadeh et al. (2012). In Chapter 4, the effects of carbon monoxide addition on the ignition behaviour, flame characteristics, and preferential diffusion characteristic of adiabatic MILD methane flames are investigated using direct numerical simulations. In addition, the possibilities and challenges involved in the development of Igniting Mixing Layer (IML) based Flamelet Generated Manifold (FGM) model for the prediction of adiabatic MILD flames are discussed. Chapter 5 is devoted to all the aspects of investigations related to non-adiabatic MILD flames. In this chapter, the effects of heat loss on MILD flames are investigated. Then, the effects of carbon monoxide addition

on the combustion characteristics of non-adiabatic MILD methane flames are investigated. Finally, the effects of carbon monoxide addition on the oxidation pathways of MILD methane flames are analysed using reaction pathway diagrams. In Chapter 6, the major findings of the study conducted in this thesis are summarised. Finally, suggestions and recommendations for future studies and numerical model development to further our knowledge on MILD flames are discussed.

1.4 Overall contribution to knowledge and importance of this research work

Fossil fuels are going to be a major player in the energy sector in the near future. However, the combustion of fossil fuels results in carbon dioxide, nitric oxide, and carbon monoxide emission. Carbon dioxide is a greenhouse gas and causes global warming, one of the biggest challenges of the twenty-first century. Nitric oxide and carbon monoxide cause adverse effects on health and the environment. So, it is necessary to develop advanced combustion technologies that can help us reduce emission levels of these gases. Also, they should help us achieve a smooth transformation towards biofuels. MILD combustion is an unconventional combustion technology that could help us achieve all the above-mentioned objectives. However, the diffusion of MILD combustion technology in industrial applications is slow due to the lack of sufficient data in the existing literature and numerical models specific to this combustion. Also, MILD combustion has a slow reaction rate and slow temperature rise compared to conventional combustion technologies. These could make it less interesting for some industrial applications. The data in the existing literature shows that the addition of hydrogen in MILD combustion increases the reactivity of the mixture. However, hydrogen production and transportation are still challenging tasks, and large scale implementation of hydrogen projects is not feasible.

In the present thesis, state-of-the-art direct numerical simulations of MILD combustion are performed to generate high-quality data that can help us get a better insight into the physics and chemistry of MILD combustion. Also, the generated data can help the researchers to validate the numerical models that are developed specifically for MILD combustion. In addition, direct numerical simulations are performed to understand the MILD combustion enriched with syngas and carbon monoxide. These data can help us see if we can replace hydrogen with syngas to increase the reactivity of the MILD combustion. Above all, the findings obtained from the investigation of carbon monoxide addition to MILD methane flames question the earlier findings available and our understanding of carbon monoxide addition to hydrocarbon flames in literature. All these above-mentioned generated data in this thesis and findings of this thesis will be a valuable addition to the existing literature. Also, they can accelerate the diffusion of this technology in industrial applications. It can help us reduce emission levels and accelerate our shift towards renewable energy. Also, it can change our view on how carbon monoxide addition affects the combustion process of hydrocarbon flames.

Chapter 2. Basics of numerical combustion

2.1 Overview

Numerical modelling of combustion requires the knowledge of fluid mechanics, chemical kinetics, thermodynamics and numerical techniques. In this chapter, a brief overview of concepts is provided from these disciplines that are relevant for this thesis.

2.2 Combustion

Combustion is an exothermic chemical reaction in which the fuel and oxidiser react to form products and release heat. The combustion process is demonstrated in Figure 2.1. For the occurrence of combustion, the fuel, and oxidiser molecules must interact in the molecular level in the presence of heat to initiate the process. The fuel and oxidiser can be a solid, liquid or gas. The amount of heat required to initiate a combustion process depends on the type of reactants involved in the combustion process. Once the combustion reactions begin, the heat released during the process is in general sufficient enough for the reactions to be self-sustaining. However, in many practical applications, the interaction of chemical kinetics and fluid dynamics dictates whether or not the combustion process will be self-sustaining. A self-sustaining combustion process occurs at a location where the required criteria are fulfilled, and that location is known as the flame front or reaction zone. For instance, if the net energy increase in the reaction zone is less than the activation energy of the reactants due to convective, conductive, and radiative heat losses from the reaction zone, the combustion process cannot self-sustain.

Fig. 2.1 Illustration of combustion process. Source: *Combustion* (1999).

2.3 Types of flames

Flames can be grouped into two categories based on how the oxidiser and fuel are introduced into the reaction zone: premixed flames and non-premixed flames. In premixed flames, the oxidiser and fuel are thoroughly mixed prior to combustion. In non-premixed flames, the oxidiser and fuel are introduced inside the reaction zone separately. For the combustion reactions to occur, the reactants (fuel and oxidiser) must diffuse into each other. Therefore, these non-premixed flames are also referred to as diffusion flames. The difference between premixed and non-premixed flames is illustrated in Figure 2 .2. The premixed flames and non-premixed flames can also be classified based on the quantity mixture fr -action. The definition of mixture fraction is given in Subsection 2.4.7. In perfectly premixed flames, the mixture fraction takes a constant value throughout the reaction zone. On the other hand, in non-premixed flames, the mixture fraction is a variable, and the mixture fraction value 1 refers to pure fuel and 0 refers to the pure oxidiser. However, it should be noted that the categorisation of flames into premixed flames or non-premixed flames is not a binary relationship. Under certain circumstances, it might be possible for a flame to possess the attributes of both premixed and non-premixed flames, and such a flame is called partially premixed flames.

Illustration of premixed and non-premixed flames. Source: Peters (1992).

In general, premixed flames are susceptible to flashback which could damage the combustion systems, and they have several limitations (narrow operating range, flammability limits). On the other hand, non-premixed flames are inherently safer than premixed flames as flashback is not possible in non-premixed flames. They can occur at a wider range of operating conditions and fuel/oxidiser flow rates. For these reasons, the practical combustion applications are generally designed to be operated in non-premixed flame regimes. In this thesis, investigations are limited to non-premixed flames.

Non-premixed flames are further classified into coflow and counterflow diffusion flames based on how the oxidiser and fuel jets are positioned inside the combustion chamber. Figure 2.3 illustrates the difference between counterflow diffusion flames and coflow diffusion flames. As is seen in the figure, in counterflow diffusion flames, the oxidiser and fuel jets are positioned opposite to each other. Hence, counterflow diffusion flames are also called opposed jet flames. In this configuration, the fuel and oxidiser are injected into each other through opposing jets. The degree of mixing of fuel and oxidiser depends on the velocity at which the

fuel and oxidiser are injected. The flame is stabilised using a stagnation flame that is formed at the intersection of fuel and oxidiser jets. The counterflow diffusion flame configuration is the widely used non-premixed flame configuration for the investigation of flame temperature, flame structure, pollution formation, ignition delay, reaction pathway analysis, diffusion analysis, and evolution of flames. Another advantage of this flame configuration is, it can be represented as a 1D non-premixed flame problem which allows us to perform these investigations using detailed chemical mechanisms at a reduced computational cost. Yet, the results of 1D counterflow flame simulations can be used to understand and can be related to 2D or 3D non-premixed flames. The investigations in Chapter 3 of this thesis are performed using the 1D CounterFlow Diffusion Flame (CFDF) configuration.

As is seen in Figure 2.3 (b), in coflow diffusion flame configuration, the fuel and oxidiser streams are introduced in the combustion zone using coannular jets in which the fuel jet is usually placed at the centre and is enclosed by the oxidiser jet. Coflow flame configuration is the most popular flame configuration that is used in the experimental investigations of MILD combustion. MILD combustion is achieved in coflow flame configuration by the dilution of oxidiser or air stream with burnt gases from a secondary burner (Dally et al. 2002) or in some cases, the air in the oxidiser stream is simply replaced by the exhaust gas of a pilot premixed flame (Cabra et al. 2005). Such a coflow configuration in which the cold fuel is issued into the hot and diluted oxidiser to achieve MILD combustion is popularly called as Jet-in-Hot-Coflow (JHC) flames (Perpignan et al. 2018). In this configuration, flame stabilisation is achieved without the need for exhaust gas recirculation. Hence, this eliminates the necessity to include exhaust gas recirculation in flame geometry design which simplifies the burner geometry. The elimination of the recirculation zone offers several advantages. Exhaust gas recirculation leads to the formation of complex recirculation patterns within the combustion zone. Exhaust gas recirculation also leads to the mixing of burnt gas from the downstream with burnt gases of flame at the combustion zone, and this makes it impossible

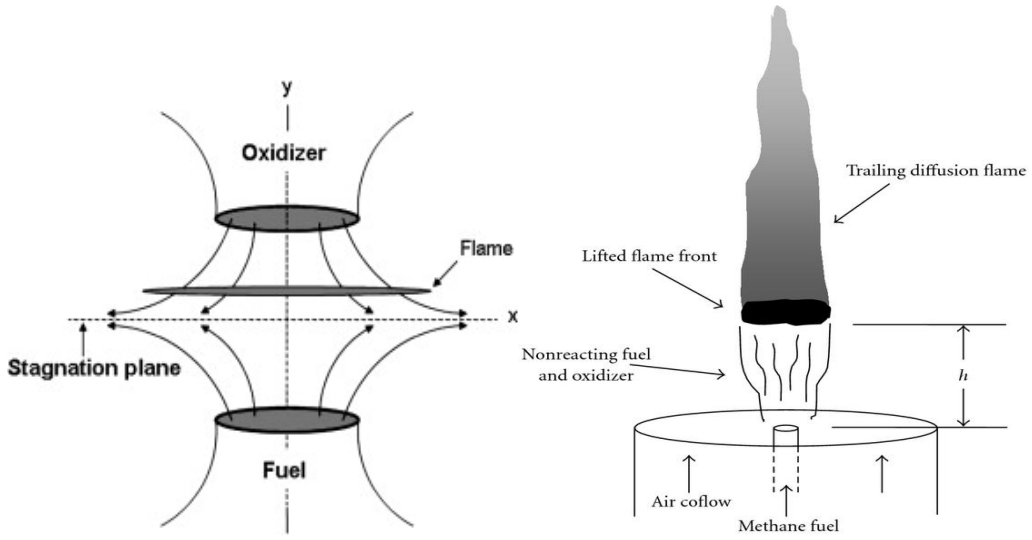

(a) (b)

Fig. 2.3 Illustration of (a) counterflow diffusion flames (to the left). Source: Shih (2009). and (b) coflow diffusion flames (to the right). Source: Moore et al. (2008).

to differentiate from each other. These make the examination of flames unfeasible. Thus, it is not possible to gain fundamental insights into the flame that is being investigated. Hence, the coflow flame configuration provides deeper insights on flames that are being investigated compared to that of flames with a recirculation zone by simplifying their configuration. The investigation in Chapter 4 and Chapter 5 are performed using a geometry that replicates JHC flame configuration. The simulations of Chapter 4 are performed without the inclusion of heat loss. So, only 1D and 2D flame simulations are performed for investigating these flames, and 3D flame simulations are not considered for these cases due to the limitation on the availability of computational resources. Also, discussions are presented to show that 1D and 2D flame simulations are sufficient to get a deeper insight into the combustion characteristics of JHC flames without the inclusion of heat loss. In chapter 5, 1D, 2D, and 3D flame simulations are performed to understand the combustion characteristics of JHC flames with the inclusion of heat loss effects.

Igniting Mixing Layers (IML) otherwise called as Linear Mixing Ignition (LMI) is a type of 1D non-premixed numerical flame configuration. The difference between 1D CFDF and

1D IML flame configuration arises from the modelling of mixing of fuel and oxidiser. In the case of 1D CFDF, mixing is modelled using both convection (by specifying strain rate) and molecular diffusion. However, mixing of fuel and oxidiser in IML flames is modelled only using molecular diffusion. The IML flames are demonstrated using the temperature profiles

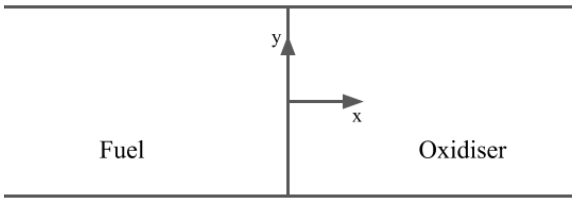

(a) Initial unmixed state of fuel and oxidiser (t = 0 ms) in IML flames

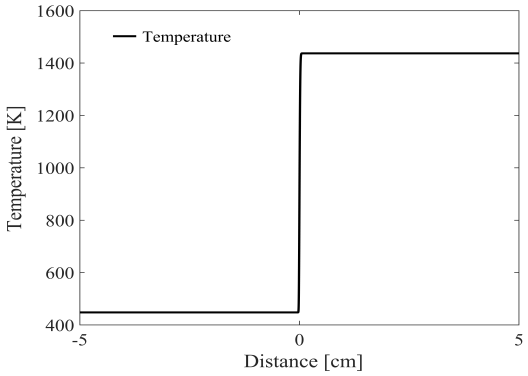

(b) Initial temperature profile (t = 0 ms) of IML flames

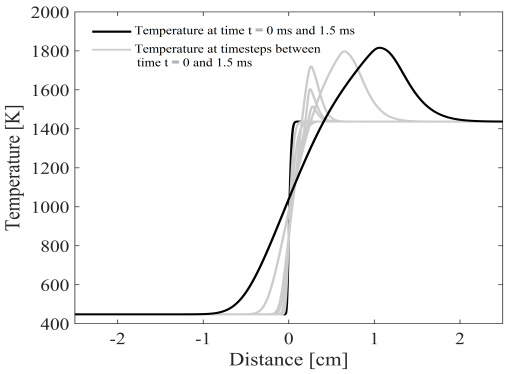

(c) Evolution of temperature profile on IML flames

Fig. 2.4 (a) Initial unmixed state of oxidiser and fuel pockets placed adjacent to each other in IML flame model. Demonstration of Igniting Mixing Layers (IML) or Linear Mixing Ignition (LMI) flames using temperature profiles at (b) t = 0 ms (to the left) and (c) t $>$ 0 (to the right) using a sample case. In (c), the darker black lines correspond to the initial and final states of temperature, and the grey lines correspond to the time-dependent solutions of 1D IML flames.

at time t=0 ms and t $>$ 0 in Figure 2.4. As is seen in Figure 2.4 (a) and (b), to model IML flames, initial profiles of species and temperature profiles of fuel and oxidiser are modelled as a Heaviside function. Due to the difference between the density and temperature of fuel and oxidiser, at time t = 0 ms, theoretically the scalar dissipation rate between the fuel and oxidiser stream is infinity. However, in reality, infinite scalar dissipation rate is not possible,

hence, the initial Heaviside function is modelled to have a very high scalar dissipation rate, usually in the order of 10^4. At time t $>$ 0, due to the high scalar dissipation rate, the fuel and oxidiser mix at the molecular level and the combustion reaction takes place. Finally, the reacting mixture reaches equilibrium when the scalar dissipation rate reduces to zero at time t $>>$ 0. This is clearly demonstrated in Figure 2.4 (b). Previous studies show that IML flamelets are the best representation of JHC flames and the tabulated model or the Flamelet Generated Manifold (FGM) model developed using IML flamelets capture the ignition and combustion physics of JHC flames with a closer accuracy compared to that of other flamelet solutions such as CFDF and homogeneous reactor (Abtahizadeh et al. 2017, Knikkerr et al. 2003).

2.4 Governing equations

The combustion process that takes place in practical applications can be classified as compressible reacting flow. The governing equations of the compressible reacting flow is a set of partial differential equations called as Navier-Stokes equations. The Navier-Stokes equations refer to the mass, momentum and energy conservation equations. In a Three-Dimensional flow problem, the N-S equations consist of a set of five equations: mass conservation equation, energy conservation equation and three momentum equations for each component of the velocity. The dependant variables or unknown variables of the equations are density (ρ), pressure (p), three components of the velocity vector ($\boldsymbol{u}$), and total enthalpy (h). The dependent variables considered are continuous functions in both space and time. The number of equations is five, and the number of unknown variables is six. In order to have a closed set of equations, it is necessary to augment the list of equations with another equation. In most reacting flow problems, the gas mixture and its component are considered to behave as perfect gases, therefore, ideal gas law is used to augment the list of equations.

2.4.1 Mass conservation equation

The mass conservation equation otherwise called as continuity equation is the governing equation for mass is derived based on the definition, "*mass is neither created nor destroyed, it is conserved*". The mass conservation equation without the source and/or sink term(s) is given in Equation 2.1. The equation can be interpreted as the rate of change of mass per unit volume (density) is equal and opposite to the divergence of the mass flux.

$$\frac{\partial \rho}{\partial t} + \nabla \cdot (\rho \boldsymbol{u}) = 0, \tag{2.1}$$

where, ρ is the mixture density, $\boldsymbol{u}$ is the velocity vector, and t is time.

2.4.2 Momentum conservation equation

The momentum conservation equation is derived based on the principle of Newton's second law of motion. The law states, "*for a fluid element with volume V_0 and surface area S_0, the rate of change of momentum of the fluid element is equal to the sum of all the forces exerted on the mass of the fluid element*". The widely used general form of momentum conservation equation is given in Equation 2.2.

$$\frac{\partial (\rho \boldsymbol{u})}{\partial t} + \nabla \cdot (\rho \boldsymbol{u}\boldsymbol{u}) = -\nabla p + \nabla \cdot \left(\mu \left[\nabla \boldsymbol{u} + (\nabla \boldsymbol{u})^T - \frac{2}{3} (\nabla \cdot \boldsymbol{u}) \bar{\bar{I}} \right] \right), \tag{2.2}$$

where, p is pressure, μ is dynamic viscosity, $\bar{\bar{I}}$ is unit vector.

2.4.3 Energy Conservation equation

The energy conservation equation is derived based on the first law of thermodynamics, which states, "*energy can neither be created nor be destroyed, it is conserved*". Therefore, for a fluid element with V_0 and S_0, the rate of change of energy equals the work and heat exchanged per

unit volume. The widely used general form of energy conservation equation is the enthalpy transport equation given in Equation 2.3.

$$\frac{\partial(\rho h)}{\partial t}+\nabla\cdot(\rho \boldsymbol{u} h)=\nabla\cdot\left(\frac{\lambda}{c_p}\right)\nabla h+\sum_i \nabla\cdot\left[h_\alpha\left(\rho D_\alpha-\frac{\lambda}{c_p}\right)\nabla Y_\alpha\right], \tag{2.3}$$

where, Y_α is the mass fraction of species α, h_α is the total enthalpy of species α, h is the total enthalpy of the mixture ($h=\sum_\alpha Y_\alpha h_\alpha$), λ is the thermal conductivity of the fluid, and D_α is the mass diffusivity coefficient of species α.

2.4.4 Ideal gas law

The ideal gas law is the equation of state which is given as follow,

$$P=\rho RT\sum_{\alpha=1}^{N_s}\frac{Y_\alpha}{M_\alpha}, \tag{2.4}$$

where, T is the temperature, R is the universal gas constant and M_α is the molecular weight of species α.

2.4.5 Species transport eqauation

Since combustion process involves consumption of reactants, and formation and destruction of intermediate species and products, transport equations for species involved in the combustion process are required to be solved along with Navier-Stokes equations to resolve the combustion process. Since the species are formed or consumed during the course of the combustion process, unlike Navier-Stokes equations, the species transport equations are not conserved. The species transport equation is given in Equation 2.5.

$$\frac{\partial(\rho Y_\alpha)}{\partial t}+\nabla\cdot(\rho \boldsymbol{u} Y_\alpha)=\nabla\cdot(\rho D_\alpha\nabla Y_\alpha)+\dot{\omega}_\alpha, \tag{2.5}$$

where, $\dot{\omega}_\alpha$ refers to the source term of the species α.

It should be noted that the governing equations given above are presented based on their widely used forms. However, the terms considered in the governing equations may differ from problem to problem-based on the numerical assumptions and the physics of the problem.

2.4.6 Lewis number

Equation 2.3 can be rewritten as follow,

$$\frac{\partial(\rho h)}{\partial t} + \nabla \cdot (\rho \boldsymbol{u} h) = \nabla \cdot \left(\frac{\lambda}{c_p}\right) \nabla h + \nabla \cdot \left(\frac{\lambda}{c_p} \sum_{\alpha=1}^{N_s} \left(\frac{1}{Le_\alpha} - 1\right) h_\alpha \nabla Y_\alpha \right) \tag{2.6}$$

In Equation 2.6, Le_α is the Lewis number which is a dimensionless number defined as the ratio of thermal diffusivity to mass diffusivity. The Lewis number (Le_α) is given as,

$$Le_\alpha = \frac{\lambda}{\rho c_p D_\alpha} \tag{2.7}$$

When $Le_\alpha = 1$ is assumed for all the species, the enthalpy transport equation in Equation 2.6 reduces to a much simpler form as in Equation 2.8. As is seen, the unity Lewis number assumption significantly simplifies the enthalpy transport equation. This simplified model, still valid for many combustion problems, significantly reduces the computational cost of numerical simulations.

$$\frac{\partial(\rho h)}{\partial t} + \nabla \cdot (\rho \boldsymbol{u} h) = \nabla \cdot (\frac{\lambda}{c_p} \nabla h) \tag{2.8}$$

2.4.7 Mixture fraction

As mentioned in Section 2.3, most of the practical combustion systems operate under non-premixed conditions. In non-premixed combustion systems, fuel and oxidiser are separately

introduced into the combustion chamber. The mixing process brings fuel and oxidiser into the reaction zone for the combustion process to start and progress. Therefore, accurate modelling of the mixing process in numerical modelling of combustion is utmost important. The parameter mixture fraction (Z) is used for modelling the mixing process. The parameter Z helps to calculate the local fuel/oxidiser ratio in the mixture at any given location. In this thesis, Bilger's definition (Bilger, Stårner & Kee 1990) of elemental mixture fraction is used to define mixture fraction which is given as follow,

$$Z = \frac{\frac{1}{2}W_H^{-1}[z_H - z_{H,2}] + 2W_C^{-1}[z_C - z_{C,2}] - W_O^{-1}[z_O - z_{O,2}]}{\frac{1}{2}W_H^{-1}[z_{H,1} - z_{H,2}] + 2W_C^{-1}[z_{C,1} - z_{C,2}] - W_O^{-1}[z_{O,1} - z_{O,2}]}, \tag{2.9}$$

where, subscripts H, C and O denote elemental hydrogen, carbon and oxygen, respectively. The variables W and z correspond to the elemental atomic weight and elemental mass fraction, respectively.

2.5 Overview of combustion chemistry

2.5.1 Reaction kinetics

For the numerical modelling of reacting flow, apart from the flow dynamics, the chemistry of the flow is also required to be resolved. In Section 2.4, the governing equations for the reacting flows are presented. However, the source terms ($\dot{\omega}_\alpha$) appeared in the species transport equation is still need to be specified which is required to resolve the chemistry of the reacting flow. In this section, an introduction for combustion chemistry, basics of chemical kinetics and the expression for source term calculations are presented.

On the global scale, the fuel and oxidisers react to form the product and give off heat. For example, the global reaction of methane and air combustion is given in Equation 2.10. On the other hand, in reality, the interaction of fuel and oxidiser molecules in molecular level

followed by a sequence of numerous elementary reactions and the formation and destruction of numerous intermediate species before the formation of products. The sequence of intermediate reactions that take place is otherwise called as chain reaction. The intermediate species that are formed and destroyed during the combustion process are otherwise called as chain carriers which are responsible for the initiation, propagation and termination of the chain reaction.

$$CH_4 + 2(O_2 + 3.76N_2) \rightarrow CO_2 + 2H_2O + 7.52N_2 \tag{2.10}$$

The simplistic global calculation may yield sufficient information required for certain applications. However, modelling of many practical applications requires the inclusion of intermediate reactions that take place and intermediate species that form during the combustion process in the numerical calculations. In addition, the investigation of intermediate reactions and intermediate species formation provides a deep insight on pollution formation which is a primary objective in many calculations.

For example, in the following chemical reaction,

$$R1 + R2 \rightarrow P1 + P2, \tag{2.11}$$

the reactants $R1$ and $R2$ react and form the product $P1$ and $P2$. The forward reaction rate r_f is proportional to the concentration of reactants:

$$r_f = k_f[R1][R2], \tag{2.12}$$

where the square brackets denote the concentration of the reactants R1 ($\rho Y_{R1}/M_{R1}$) and R2 ($\rho Y_{R2}/M_{R2}$), and k_f is the reaction rate coefficient with subscript f denoting the forward reaction. In general, reaction rate coefficient is expressed in a modified Arrhenius form (Warnatz et al. 1996),

$$k_f = AT^{\beta} exp(-E_a/RT), \tag{2.13}$$

where, A and β are the reaction constants, and E_a refers to the activation energy (J/mol). In a homogenous system, the species concentration of the various species involved in the chemical reaction will change due to the progress of the reaction as per relation given in Equation 2.14.

$$\frac{d[R1]}{dt} = \frac{d[R2]}{dt} = -\frac{d[P1]}{dt} = -\frac{d[P2]}{dt} = r_f \tag{2.14}$$

In general, the reaction given in Equation 2.11 may also progress in reverse direction,

$$R1 + R2 \leftarrow P1 + P2, \tag{2.15}$$

The reaction rate of the backward reaction in Equation 2.15 is given as r_r. The net reaction rate of the forward reaction and backward reaction in Equation 2.11 and Equation 2.15 is given as follow,

$$r = r_f - r_r = k_f[R1][R2] - k_r[P1][P2] \tag{2.16}$$

The reaction rate coefficient (k_r) of the backward reaction can be calculated using the equilibrium constant (k_{eq}) using the following relation,

$$k_{eq}(p,T) = \frac{k_f}{k_r}, \tag{2.17}$$

The equilibrium constant k_{eq} in Equation 2.17 can be clearly described using the thermodynamic properties of the species involved in the chemical reaction (Rossini et al. 1971). Moreover, the calculation of k_r from k_{eq} and k_f using the relation in Equation 2.17 yields a much more accurate result compared to the calculation of k_r based on the relation given in Equation 2.13.

The chemical reaction j can generally be expressed as,

$$\sum_{\alpha=1}^{N_s} \nu'_{\alpha j} \chi_\alpha \Leftrightarrow \sum_{\alpha=1}^{N_s} \nu''_{\alpha j} \chi_\alpha \tag{2.18}$$

where, χ_α represents species α, $\nu_{\alpha j} = \nu''_{\alpha j} - \nu'_{\alpha j}$ is the stoichiometric coefficients that indicate the number of molecules of species α participate in reaction j.

The most general relation for the reaction rate of reaction 2.18 is given as,

$$r_j = k_{fj} \prod_{\alpha=1}^{N_s} [\chi_\alpha]^{\nu'_{\alpha j}} - k_{rj} \prod_{\alpha=1}^{N_s} [\chi_\alpha]^{\nu''_{\alpha j}} \tag{2.19}$$

All the reactions contribute to the source term of the species transport equation (Equation 2.5). The expression for the calculation of source term of the species transport equation is given as,

$$\dot{\omega}_\alpha = \chi_\alpha \sum_{\alpha=1}^{N_r} \nu_{\alpha j} r_j, \tag{2.20}$$

where N_r refers to the total number of chemical reactions.

The reaction mechanisms otherwise called as reaction schemes consist of the reactions and their rate constants (A, β) and activation energy (E_a). Comprehensive and extensively validated reaction mechanisms that can accurately resolve the natural gas/syngas mixtures are produced by various research groups, e.g. Burke et al. (2015), Wang et al. (2007), and Smith et al. (1999).

2.5.2 Reaction pathway analysis

In this section, an overview of the reaction path diagram is presented. The reaction path diagrams provide an overview of the path followed by the reactants towards the formation of a product. The reaction path diagram shows the atomic transfer rate from one species to another species that are involved in the combustion process. The direction of arrows between the species show the direction of atomic transfer, and the thickness of the arrow is proportional to the atomic transfer rate between the species. Therefore, the reaction path

diagram provides both quantitative and qualitative information. As mentioned, the thickness of the arrows provide information about the transfer rate otherwise called as reaction flux which is defined as the amount of substance transformed per unit volume and time and then integrated over space (Grcar et al. 2006). An example of reaction path diagram showing the pathways of CH_4 decomposition and CO_2 formation of a MILD flame is illustrated in Figure 2.5.

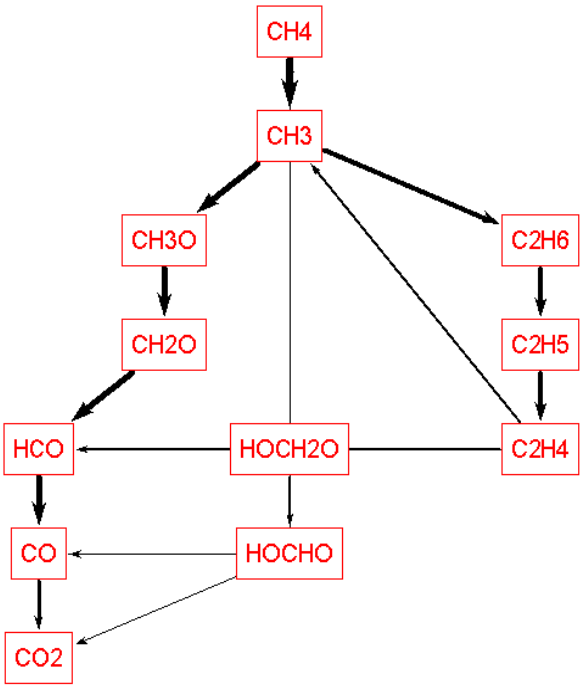

Fig. 2.5 Illustration of an example reaction pathways diagram showing the pathways of CH_4 decomposition and CO_2 formation of a MILD flame.

2.6 Overview of turbulence

Most of the practical combustion applications operate under turbulent flow conditions which involve a strong coupling between turbulence and chemistry. The majority of the simulations in the thesis are performed under turbulent flow conditions. In this section, explanations are provided to the fundamental aspects of turbulence that are relevant to the current study.

Laminar flows can be described as steady flow in which the flow velocity does not vary at a given point in space over time. In addition, any flow perturbation that occurs in the flow field is damped by the viscosity of the fluid. On the other hand, turbulent flow can be described as an unsteady flow, and the flow velocity considerably varies in space and time. In general, turbulent flows are random, irregular and chaotic (Pope 2000). In turbulent flow, unlike laminar flow, the flow disturbances are amplified and are not damped by the viscosity of the fluid (Williams 1985). Figure 2.6 illustrates the difference between laminar flow and turbulent flow in a pipe.

Lamianr flow

Turbulent flow

Fig. 2.6 Illustration of the difference between laminar and turbulent flow inside a pipe. This figure is obtained from the web article written by Popovich (2016).

As mentioned earlier, turbulence is caused by the flow instabilities when they are not sufficiently damped by the viscosity of the fluid. Therefore, for turbulence to occur, there must be some form of flow disturbances or perturbations occur in the flow field. Even though how careful a device is designed or operated, there will be always some small imperfections in the initial conditions, boundary conditions, material surface, etc. which could cause

perturbations in the flow field. At low velocities, these perturbations are damped out by the surrounding fluid elements, therefore, these perturbation do not have the opportunity to grow into flow instabilities. On the other hand, at higher velocities, the flow field does not have sufficient time to respond to the flow disturbances or perturbations, therefore, they spread into the entire flow field which results in flow turbulence.

It is possible to predict whether or not a flow perturbation will damp out or develop into flow instabilities that result in flow turbulence based on Reynolds number *Re*. The Reynolds number is a dimensionless number defined as the ratio of inertial forces to the viscous forces, given as;

$$Re = \frac{\mathbf{u}L\rho}{\mu} = \frac{\mathbf{u}L}{\nu}, \tag{2.21}$$

where, u is the flow velocity, L is the characteristic length, μ is the dynamic viscosity and ν $(= \mu/\rho)$ is the kinematic viscosity. For a flow inside a pipe, in general, the flow is laminar for $Re < 2300$, and turbulent for $Re > 4000$. However, it should be noted that laminar flow is possible even at higher Reynolds numbers. For Reynold's number between 2300 and 4000, the flow does not exhibit either laminar behaviour or turbulence behaviour.

The irregular motions of the turbulent flow field are described as eddies. Turbulent flows are comprised of a cluster of eddies of varying sizes, structures, orientation, and strengths, embedded into one another (Chigier 1981). The distinctive features of each eddy are: it moves inside the flow field as a single unit, and it also engulfs the surrounding fluid during its motion. Therefore, eddies transfer heat, matter, and momentum as it moves in the flow field. Since eddies are embedded into one another, the eddies also transfer matter, momentum and energy between each other. As a result, eddies accelerate the mixing process.

2.6.1 Turbulent length scales

The eddy sizes are characterised by length scales, and the frequently used length scales are presented as follow in the decreasing order of magnitude.

- **Macroscale (L)** The macroscale is the largest length scale of the turbulent flow called as the characteristic length. The macroscale of the turbulent flow is dictated by the dimensions of the system which indicates the upper limit of the eddy size.

- **Integral length scale (l_o)** The integral length scale is the average size of the large eddies in the flow field. The integral length scale is smaller than the macroscale L, however, their magnitude is similar to that of L.

- **Taylor microscale (l_λ)** Taylor microscale is associated with the mean strain rate. This quantity is smaller than that of integral length scale, however, larger than that of Kolmogorov's length scales.

- **Kolmogorov's microscale** The Kolmogorov's microscale is the smallest of the turbulent length scales, and it is related to the ratio of the fluid's viscosity to the rate of dissipation of turbulent kinetic energy (Turns 2000).

2.7 Numerical approaches for turbulent reacting flow

As mentioned earlier, MILD combustion problem is investigated using numerical simulations. The common numerical approaches for modelling turbulent combustion are briefly discussed in this section. Numerical simulation of turbulent reacting flow can be classified into three different strategies such as Reynolds Averaged Navier-Stokes (RANS) equations, Large Eddy Simulation (LES), and Direct Numerical Simulations (DNS), based on up to what level the spatial and temporal scales are computed during the simulation of turbulent flow.

2.7.1 Reynolds Averaged Navier-Stokes equations

The RANS equations are the widely used simulation technique as it requires the least computational resources compared to the other two simulation techniques. The RANS

Fig. 2.7 Turbulent energy spectrum plotted as a function of wave numbers. RANS, LES, and DNS are summarised in terms of spatial frequency range. Here, k_c refers to the cut-off wave number used in categorising eddies in LES. Source: Poinsot & Veynante (2005).

Fig. 2.8 Illustration of evolutions of local temperature calculated using RANS, LES, and DNS or experiment in turbulent flow. Source: Staffelbach et al. (2008).

equations or Favre Averaged Navier-Stokes equations (if the equations are density-weighted) are derived by averaging the governing equations or the instantaneous balance equations that are shown in Section 2.4. As a result of this averaging process, additional terms appear in equations: turbulent flux terms, Reynolds stress terms and mean reaction rate. Therefore, closure models and transport equations are required to close the averaged balance equations. As shown in Figure 2.7, the entire wavenumber range is modelled. As a result, as shown in Figure 2.8, the accuracy achieved by the RANS model is the lowest of all the three simulation techniques.

2.7.2 Large Eddy Simulation

In LES approach, the large scale eddies of the turbulent flow fields are explicitly solved, while the subgrid closure models are used to solve the small scale eddies (Poinsot & Veynante 2005). The balance equations for LES are deduced by applying spatial filtering operation to the instantaneous Navier-Stokes equations. The spatial filter classifies the turbulent eddies into small scale eddies and large scale eddies. As shown in Figure 2.7, the eddies are categorised using the cut-off wavenumber k_c. The wavenumber k of an eddy of spatial dimension L is given by, $k = (2\phi)$Ł. Eddies with wave number smaller than k_c are classified as large scale eddies, while the other eddies are classified as small scale eddies. Since the large scale eddies are computed, the large scale motion of the turbulent flow field, which contains most of the turbulent kinetic energy, is resolved. Therefore, the accuracy of the LES results are higher than that of RANS, however, since the small scale eddies are modelled, its accuracy is lower than that of DNS, please refer to Figure 2.8.

2.7.3 Direct Numerical Simulation

In DNS approach, the instantaneous fully-compressible Navier-Stokes equations are numerically solved without any model for turbulence and combustion. Therefore, all the spatial

scales [from the smallest dissipative scales or Kolmogorov's scales up to the integral scales] and temporal scales of the turbulence flow fields and their effect on chemistry are fully resolved, please refer to Figure 2.7. Since the flow field is fully resolved without using any model, the accuracy of DNS is higher than that of the other two approaches. Moreover, the parameters estimated using DNS could exactly agree with the experimental measurements, please refer to Figure 2.8. However, since even the smallest of the smallest turbulent scales (Kolmogorov's scales) are fully computed in DNS, it requires a very fine mesh which makes DNS computationally very intensive.

Since the thesis involves the fundamental investigation of MILD flames, due to its accuracy, DNS is the suitable approach for the investigations performed in this thesis. Therefore, DNS is chosen for all the investigations performed in this study. Since DNS is computationally intensive, DNS investigations are restricted to simpler flow geometries with a smaller domain size compared to that of the domain sizes considered for other numerical approaches. Further details about the flow geometry and the DNS code employed for performing the numerical simulations are explained in the later chapters.

Chapter 3. DNS of syngas enriched MILD CH_4 flames

3.1 Overview

In this chapter, a fundamental investigation is performed to understand the effects of Exhaust Gas Recirculation or EGR on the combustion characteristics and reaction pathways of the syngas enriched methane flames using 1D laminar counterflow diffusion flames and 0D origin flame simulations. Firstly, the numerical methods and simulations set-up are explained. Then, the steady-state results are presented to discuss the effects of exhaust gas addition on flame temperature, flame structure and NO_x emissions of syngas enriched methane flames. Next, the unsteady results are presented to analyse the effects of exhaust gas addition on ignition behaviour and flame development of syngas enriched methane flames. In addition, the effect of strain rate, the choice of chemical mechanisms and transport models on the evolution of the temperature of these flames with exhaust gas addition are analysed. Then, the effect of exhaust gas addition on the reaction pathways of syngas enriched methane flames and the effect of syngas addition on the reaction pathways of MILD methane flames are analysed using the Quantitative Reaction Path Diagrams (QRPDs). Afterwards, the results of the syngas enriched MILD methane flames (or the results of this chapter that correspond to the initial oxygen mole fraction in the oxidiser stream less than or equal to 9%) are compared with the results of MILD methane flames calculated by Abtahizadeh et al. (2012) to understand the effects of syngas addition on MILD methane flames. Finally, the major findings and conclusions derived based on the observations made in this chapter are summarised.

3.2 Numerical methods and simulations set-up

The numerical set-up used to solve 1D counterflow diffusion flames with EGR is shown in Figure 3.1. To justify the comparison of syngas enriched MILD methane flames results obtained in this chapter with the results of MILD methane flames presented in Abtahizadeh et al. (2012), a similar numerical set-up is used in this study compared to that of the one used by Abtahizadeh et al. (2012).

The numerical set-up consists of a network of an equilibrium solver, a plug flow reactor and a counterflow diffusion flame-solver. Initially, a fresh stream of CH_4/CO/H_2 or syngas enriched methane [1] and air mixture is fed to the equilibrium solver at 300 K, 1 atm and equivalence ratio (Φ) =1. The equilibrium solver is used to simulate the burnt gas. The burnt gas from the equilibrium solver is cooled down to 1400 K to take in account the heat loss. The cooled burnt gas is then mixed with oxidiser stream.

Fig. 3.1 Numerical set-up used in the simulations of 1D counterflow diffusion flame with EGR. PFR and CFDF stand for Plug Flow Reactor and Counterflow Diffusion Flame, respectively. This numerical set-up is similar to the numerical set-up used by Abtahizadeh et al. (2012).

In Figure 3.1, $\dot{m}^{egr}$ refers to the mass flow rate of the burnt gas or exhaust gas directed into the oxidiser stream, $\dot{m}_{ox}$ refers to the mass flow rate of pure oxidiser, and $\dot{m}_{ox}^{egr}$ refers to the mass flow rate of exhaust gas in the oxidiser and exhaust gas mixture in the oxidiser

[1] It should be noted that, both syngas enriched methane (flames) and CH_4/CO/H_2 (flames) refer to the same context. In this chapter, both contexts are used frequently depending on the topic that is being discussed. However, the readers are requested not to be bewildered due to this. Moreover, if required, additional explanation is provided in the discussions.

stream. In the present work, the exhaust gas content in the oxidiser stream is indicated in terms of mass fraction. The relation used for the calculation of EGR mass fraction (Y_{egr}) in the oxidiser stream is given in Equation 3.1. The MATLAB program used for the addition of exhaust gas in the fresh oxidiser stream is given in Appendix Appendix A.

$$Y_{egr} = \frac{\dot{m}_{ox}^{egr}}{\dot{m}_{ox} + \dot{m}_{ox}^{egr}} \tag{3.1}$$

As shown in Figure 3.1, the temperature of the fresh inlet reactants is kept at 300 K. A small amount of active radicals (O, OH, H, etc.) present in the burnt gas instantaneously reacts when they come in contact with the fresh reactants. In the plug flow reactor, chemical decomposition of active radicals in the burned gas would take place without significantly affecting the composition of reactants. A short residence time of $5e-4$ s (approx) is given between the burnt gases and the fresh reactants for the decomposition of any active radicals present. Otherwise, without the plug flow reactors, the diluted reactants start to react at the computational boundaries of the counterflow diffusion flame which could result in unwanted species gradients and fluxes.

In the present work, NO formation analysis is only focused towards thermal, prompt, N_2O intermediate and NNH routes. Therefore, nitrogen containing species in the recirculated exhaust gas are neglected as it could contribute to NO formation via re-burn mechanism.

Since this is a fundamental investigation and a first attempt to understand these flames in MILD regimes, a simple flame configuration is considered for this study. Therefore, the flames considered in the present study are flat flames, and heat loss through radiation is neglected. Since most of the practical applications operate under non-premixed conditions, the investigations in this chapter is performed using 1D non-premixed flame configuration except in Section 3.3.2, where the 0D (origin reactor) flame configuration is used to investigate the effect of exhaust gas addition on the evolution of temperature of syngas enriched methane

flames without diffusional effects. Additionally, all the simulations in this chapter are performed in laminar flow regime. The popular 1D reaction flow solvers that are widely used for research works are CHEMKIN (*ANSYS Chemkin Theory Manual 17.0 (15151)* 2015), CANTERA (Goodwin 2019), STAR-CCM+ (Siemens Digital Industries Software 2016), and CHEM1D (Somers 1994). However, the reaction flow solver CHEM1D (Somers 1994), developed at the Eindhoven University of Technology is employed to solve the set of transport equations governing the 1D counterflow diffusion flame (CFDF) problems considered in the present study instead of other solvers. The reason is, in the present study, the effects of syngas addition on the MILD methane CFDF flames are analysed in both steady and unsteady conditions. Among the above-listed solvers, only the CHEM1D has the feature to perform 1D unsteady CFDF simulations. The other solvers do not have the feature to perform unsteady 1D CFDF simulations. Hence, the CHEM1D solver is considered for the 1D reacting flow calculations performed in this study. CHEMKIN reaction path analyser (*ANSYS Chemkin Theory Manual 17.0 (15151)* 2015) is used to generate Quantitative Reaction Path Diagrams (QRPDs) or simply the reaction pathway diagrams because that feature is not available in CHEM1D. Both CHEM1D and CHEMKIN reaction flow solvers are rigorously used and extensively validated. Moreover, in the latter part of this section, CHEM1D solver is validated using experimentally measured flame speeds of a premixed flame. The CHEM1D reaction flow solver utilizes an exponential finite-volume discretisation scheme for spatial discretisation and a fully implicit modified Newton technique to solve the resulting system of equations (Somers 1994). The solver uses adaptive gridding to increase the grid resolution at the reaction zone and the flame front. The governing equations solved by CHEM1D for 1D counterflow diffusion flame problems in planar co-ordinates is given below.

$$\frac{\partial \rho}{\partial t} + \nabla \cdot (\rho \boldsymbol{u}) = -\rho K, \tag{3.2}$$

$$\frac{\partial(\rho Y_\alpha)}{\partial t} + \nabla\cdot(\rho \boldsymbol{u} Y_\alpha) - \nabla\cdot(\rho V_\alpha Y_\alpha) - \dot{\omega}_\alpha = -\rho K Y_\alpha, (\alpha = 1, ..., N-1), \tag{3.3}$$

$$\frac{\partial(\rho h)}{\partial t} + \nabla\cdot(\rho \mathbf{u} h) - \nabla\cdot\left(\frac{\lambda}{c_p}\nabla h\right) = \nabla\cdot \quad \sum_{\alpha=1}^{N_s} h_\alpha(\rho V_\alpha Y_\alpha - \frac{\lambda}{c_p}\nabla Y_\alpha)\Bigg) - \rho K h, \tag{3.4}$$

where, ρ, u and Y_α correspond to the mixture density, velocity, and mass fraction of the species α, respectively. The variable $\dot{\omega}_\alpha$ refers to the molecular production rate of the species α. The variables V_α, μ,and λ denote diffusion velocity, dynamic viscosity and thermal conductivity, respectively. The variables h and c_p denote the total enthalpy and specific heat capacity of the mixture, respectively. The variables N_s and t refer to the total number of species in the chemical scheme considered, and time, respectively. The variable K is the stretch rate, computed by solving an additional transport equation for K (refer to Equation 3.5) which is modelled after Dixon-Lewis (1968).

$$\frac{\partial \rho K}{\partial t} + \nabla\cdot(\rho \mathbf{u} K) - \nabla\cdot(\mu \nabla K) = J - 2\rho K^2, J = \rho a^2, \tag{3.5}$$

where, a denotes applied strain rate, and $J(=\rho a^2)$ refers to the pressure curvature and it is constant across the domain (Oijen 2002). Since, Equation 3.2 - Equation 3.5 consist of 10 unknown variables, additional data and equations are required for satisfying the degree of freedom. The variables μ and λ refer to the dynamic viscosity and thermal conductivity, respectively. The variables u, Y_α, h and K are solved using the transport equations. The remaining unknown variables such as ρ, $\dot{\omega}_\alpha$, c_p and V_α are solved, respectively, using the following relations

$$\rho = \frac{p\bar{M}}{RT}, \tag{3.6}$$

where, R, p and T refer to universal gas constant, pressure and temperature, respectively. The variable $\bar{M}$ is the mean molar mass of the mixture and it is determined using $\left(\sum_{\alpha=1}^{N_s} \frac{Y_\alpha}{M_\alpha}\right)^{-1}$, where, M_α is the molar mass of the species α.

$$\dot{\omega}_\alpha = M_\alpha \sum_{j=1}^{N_r} \left(\nu''_{\alpha j} - \nu'_{\alpha j}\right) r_j, \tag{3.7}$$

where, $\nu'_{\alpha j}$ and $\nu''_{\alpha j}$, respectively, correspond to the number of molecules of type α that are consumed and produced with elementary reaction j. The variables N_r and r_j refer to the number of reactions and reaction rate of elementary reaction j, respectively.

$$c_p = \sum_{\alpha=1}^{N_s} Y_\alpha c_{p\alpha}, \tag{3.8}$$

where, $c_{p\alpha}$ refers to the specific heat capacity of the species α. The variable $c_{p\alpha}$ is calculated using the coefficients of fits to thermodynamic data and these are user input quantities.

$$V_\alpha = -\sum_{k=1}^{N_s} D_{\alpha k} d_\alpha - D_\alpha^T \frac{\nabla T}{T}, \tag{3.9}$$

where, $D_{\alpha k}$, D_α^T and d_α correspond to the multi-component diffusion coefficients, thermal diffusion coefficients and effects of various gradients and external forces, respectively. The temperature T of the mixture is still an unknown quantity. It is integrated from the following relation:

$$h = h^{ref} + \int_{T_{ref}}^{T} c_{p\alpha}(T) dT, \qquad where, \qquad h = \sum_{\alpha=1}^{N_s} Y_\alpha h_\alpha. \tag{3.10}$$

The boundary conditions for the above mentioned governing equations (Equation 3.2 - Equation 3.5) for counterflow diffusion flames are:

$$Y_\alpha(x \to -\infty) = Y_{\alpha,1}$$

$$h(x \to -\infty) = h_1$$

$$Y_\alpha(x \to +\infty) = Y_{\alpha,2}$$

$$h(x \to +\infty) = h_2$$

$$K(x \to +\infty) = a$$

$$\frac{\partial K}{\partial x}(x \to -\infty) = 0,$$

where, the subscripts 1 and 2, in the above equations correspond to fuel and oxidiser stream, respectively. For time dependent simulations, the steady state solution of the above equations with frozen chemistry ($\dot{\omega}_\alpha$=0) is used as an initial condition.

Bilger's definition (Bilger, Stårner & Kee 1990) for mixture fraction is used to quantify the mixing of fuel and oxidiser streams, refer to Equation 2.9. As mentioned in Chapter 2, the mixture fraction (Z) is a passive scalar normalized between $Z = 0$ and $Z = 1$ in the oxidiser and fuel boundaries, respectively. Since hydrogen rich fuel mixture is investigated in this study, complex transport model including Soret and Dufour effects (Dixon-Lewis 1968) is used in a majority of the calculations to model the preferential diffusion effects accurately. The molar fractions of CH_4/CO/H_2 are fixed to $70\%/15\%/15\%$. This fuel composition ($70\%/15\%/15\%$) is adapted from Sequera & Agrawal (2007).

As mentioned above, governing equations (3.2-3.4) along with Equations 3.6-3.9 are solved numerically to resolve 1D reacting flow problem. However, reaction data are required to calculate the source terms of Equation 3.7. GRI 3.0 (53 species and 325 reactions) (Smith et al. 1999), USC Mech II (111 species and 784 reactions) (Wangbetbal. 2007) and Curran (113 species and 710 reactions) (Burke et al. 2015) reaction mechanisms are evaluated for resolving the flow chemistry and to calculate species source terms.

Flame speeds are calculated for a premixed CH_4/CO/H_2 ($10\%/32\%/58\%$) and air flame using CHEM1D with all the three mechanisms. The results of the flame calculations

are shown in Figure 3.2. The numerically predicted flame speeds are validated using the experimental measurements reported by Park et al. (2009). The experimental measurements are plotted with a $\pm 3\%$ uncertainty (errorbars). Similar to the experiments, inlet temperatures of the reactant streams are fixed at 300 K in the numerical calculations. Figure 3.2 shows that, the numerical flame speeds calculated using all the chemical mechanisms fall within the accepted experimental measurement uncertainties (errorbars). Therefore, the numerical results show a good agreement with experimental measurements. However, USC Mech II and Curran mechanisms do not include nitrogen oxidation mechanisms. Furthermore, the number of species and reactions in GRI 3.0 mechanism is 60% less than that of USC Mech II and Curran mechanisms which would significantly reduce the computation time. Therefore, GRI 3.0 reaction mechanism is used for all the calculations performed in this paper unless otherwise specified. Transport properties and thermodynamic data of the species are also obtained from GRI 3.0. Apart from these, it can be seen that, the flame speed results obtained

Fig. 3.2 Flame speeds are calculated using CHEM1D with GRI 3.0, USC Mech II and Curran. Numerical results are validated using experimental measurements reported by Park et al. (2009). It can be seen that the flames speed calculated by all the chemical mechanisms fall well within the accepted experimental measurement uncertainties (errorbars) and therefore, show a good agreement with the experimental measurements.

Table 3.1 Boundary conditions, operating conditions and other simulation parameters of non-premixed flames.

Fuel composition (molar fraction)	$CH_4/CO/H_2$ $(70\%/15\%/15\%)$
Oxidiser composition (molar fraction)	air/EGR $(100\% - 0\%/0\% - 100\%)$
Fuel temperature	300 K
Oxidiser temperature	Varies depends on Y_{egr}
Pressure	1 atm
Domain size (L_x)	20 cm
Number of grid points (N_x)	500
Heatloss	None (adiabatic flame)
Chemical mechanisms	GRI 3.0
Transport model	Complex or multicomponent diffusion model

using CHEM1D agree well with the experimental measurements. Thus, the CHEM1D solver is validated. The operating conditions, boundary conditions and other simulations parameters that are used to run the 1D non-premixed simulations of this chapter are summarised in Table 3.1.

3.3 Results

3.3.1 Steady state flames

I. Effect of exhaust gas addition on flame characteristics

Steady state results of $CH_4/CO/H_2$ and air counterflow diffusion flames are presented and discussed in this section. Steady state solutions are important to obtain a knowledge on the maximum domain temperature T_{max}, flame structure and emission levels for the given fuel and operating conditions. In this section, the effects of exhaust gas addition on flame

temperature and flame structure are analysed. The CH_4/CO/H_2 and air counterflow diffusion flame with exhaust gas addition is simulated under atmospheric pressure condition. A strain rate of 125 s^{-1} which is considered to be dominant in jet diffusion flames is used for the simulations performed in this chapter (except for the strain rate analyses). This choice of strain rate is similar to the choices made in previous studies performed by Park & Kim (2017), Abtahizadeh et al. (2012), Guo & Neill (2009), and Som et al. (2008) to simulate laminar counterflow diffusion flames.

The results of the simulations performed to analyse the effects of EGR mass fraction (Y_{egr}) on T_{max} is shown in Figure 3.3. The figure shows that T_{max} decreases monotonically with increasing Y_{egr}. The reason is obvious; exhaust gas addition dilutes the reactants and reduces the oxygen concentration which leads to a lower combustion temperature. Apart from this, significant amount of sensible enthalpy is lost in heating the product gases such as N_2, H_2O and CO_2.

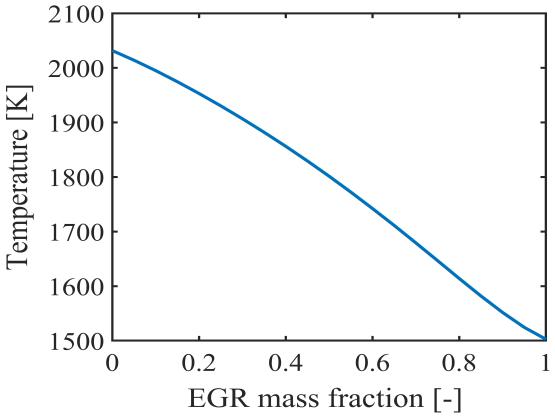

Fig. 3.3 Effects of Y_{egr} on maximum domain temperature T_{max}. The plot shows that the addition of exhaust gas in the oxidiser stream of CH_4/CO/H_2 flames reduces its maximum domain temperature T_{max}.

The simulations to analyse the effects of exhaust gas addition in flame distribution and heat release rates are performed. Temperature and heat release rate are plotted as a function of Z for Y_{egr} cases 0.20, 0.50, and 0.80. The plots are shown in Figure 3.4. The circle marks in the plots correspond to the stoichiometric mixture fraction Z_{st}. It can be seen that, T_{max}

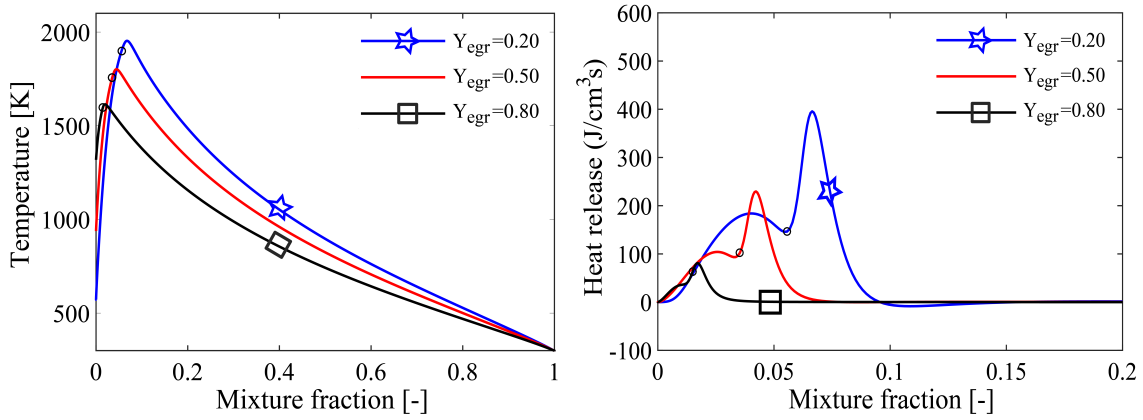

Fig. 3.4 (a) Temperature profile (left) and (b) heat release rate (right) plotted as a function of mixture fraction for various values of Y_{egr}. The circle marks in the plots correspond to the location of stoichiometric mixture fraction. The figures show that the temperature and heat release rate decreases with increase in Y_{egr}. Additionally, the location of maximum temperature and maximum heat release rate moves closer towards oxidiser inlet ($Z = 0$) as Y_{egr} increases.

does not occur at Z_{st} but at a mixture fraction close to it. Similar to the T_{max} plot (refer to Figure 3.3), both temperature and heat release rate decrease with increasing Y_{egr} for all cases. In the heat release rate plots, a negative heat release region is observed. In this region, the energy consumed by the pyrolytic reactions is greater than the energy released by the oxidation reactions. Similar combustion regimes were observed by Abtahizadeh et al. (2012) and De Joannon et al. (2009, 2007) while investigating pre-heated and diluted combustion.

Furthermore, a distinctive behaviour can be observed from the temperature and heat release rate plots. As Y_{egr} increases, Z_{st} moves toward the oxidiser boundaries on which the exhaust gas is entrained. Figure 3.5 and Figure 3.6 show, respectively, the effect of strain rate and inlet temperature on the flame distribution of CH_4/CO/H_2 and air counterflow diffusion flames without exhaust gas addition. These figures clearly show that, Z_{st} is almost same for all the cases and Z_{st} does not change significantly when strain and inlet temperature of the reactants are increased. This proves that, the location of Z_{st} mainly depends on the amount of burnt gas in the reactants, and it is not significantly affected by strain rate and inlet

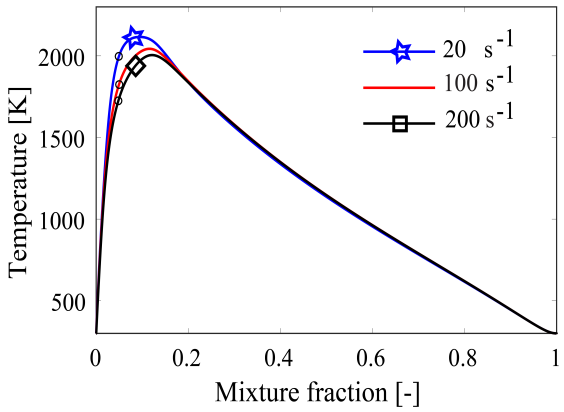

Fig. 3.5 Effect of strain rate on the temperature profile plotted as a function of mixture fraction. The circle marks in the plot correspond to the location of stoichiometric mixture fraction. The figure show that the effects of the choice of strain rate on stoichiometric mixture fraction is negligible.

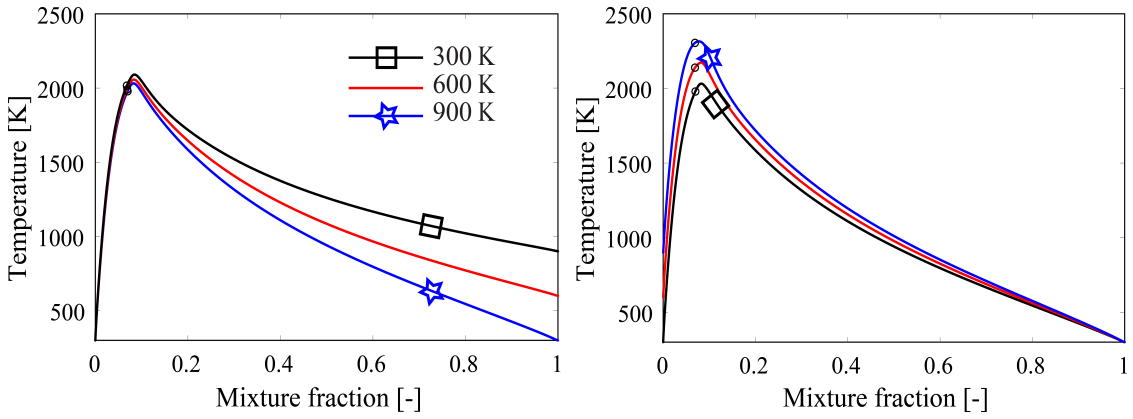

Fig. 3.6 Effect of inlet temperature of (a) fuel and (b) oxidiser on temperature profile plotted as a function of mixture fraction. The circle marks in the plots correspond to the location of stoichiometric mixture fraction. The figures show that the effect of the choice of the inlet streams temperature on stoichiometric mixture fraction is negligible.

temperature. The reason is, that in general, Z_{st} occurs at a location where adequate amount of oxygen molecules is available per fuel molecule necessary for complete combustion. The dilution of oxidiser stream reduces the oxygen concentration in the reactant stream. As a consequence, fuel molecules diffuse deep into the oxidiser stream to find sufficient oxygen molecules to achieve stoichiometry. Therefore, Z_{st} moves closer to $Z = 0$ when Y_{egr} is increased in oxidiser stream.

II. Effect of exhaust gas addition on pollution formation

In this section, the effect of exhaust gas addition on NO formation is investigated. Figure 3.7 (a) shows the effect of exhaust gas addition on maximum NO mass fraction in the domain $(Y_{NO,max})$. The plot shows that $Y_{NO,max}$ profile follow a similar trend compared to T_{max} profile. In addition to that, $Y_{NO,max}$ is almost negligible for Y_{egr} greater than 0.80. Figure 3.7 (b) shows the effect of exhaust gas addition on NO emission indices (EINO). The figure shows that EINO decreases with increasing Y_{egr}. In the present work, EINO is defined as the ratio of total mass of NO integrated along the flame to the total heat release integrated along the flame. The equation used for calculating EINO is adapted from (Sahu & Ravikrishna 2016) and it is given as,

$$EINO = \frac{M_{NO}.\int_0^L (X_{NO}p/RT)_x dx}{\int_0^L (h_s)_x dx}$$

where, MW_{NO} and X_{NO} represent the molecular weight and mole fraction of NO, respectively. The variable h_s denotes the local sensible enthalpy released during the combustion reaction.

In the present work, the important nitrogen reaction pathways that lead to NO formation are also investigated. In hydrocarbon flames, prompt, thermal, NNH and N_2O intermediate pathways are the main routes for NO formation (Miller & Bowman 1989, Guo et al. 2005). The formation of NO via thermal routes relies on two factors: temperature and residence time. At very high temperatures, particularly $>$ 1800 K, diatomic nitrogen molecules present in air

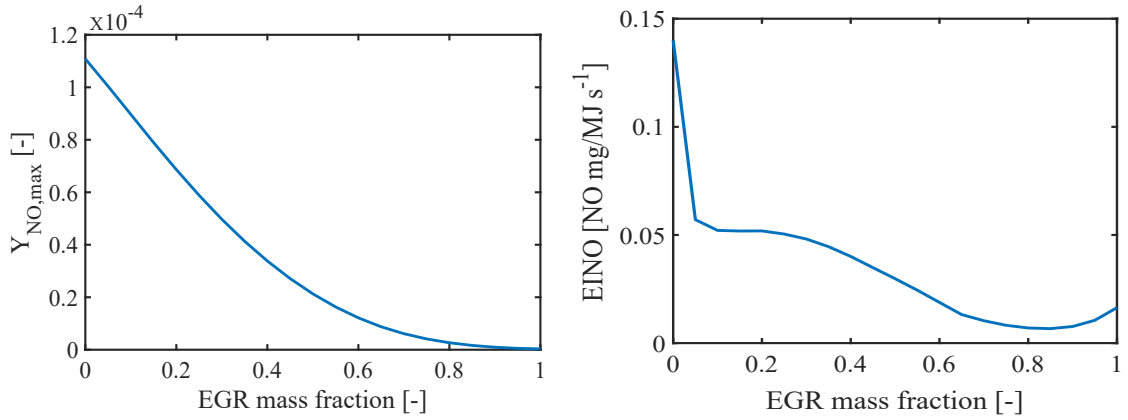

Fig. 3.7 (a) Maximum NO mass fraction $Y_{NO,max}$ in the domain plotted as a function of Y_{egr}. (b) NO emission indices (EINO) plotted as a function of Y_{egr}. The plots show that the addition of EGR in the oxidiser stream of CH_4/CO/H_2 flames reduces the NO formation and EINO indices.

combines with oxygen radical to form nitrous oxide. NO production through the oxidation of nitrogen molecules increases with increasing residence time. The set of highly temperature dependent reactions R178 (N+NO <=> N_2+O); R179 (N+O_2 <=> NO+O); and R180 (N+OH <=> NO+H); referred as the extended Zeldovich mechanisms (Bakali et al. 2006), are responsible for thermal NO formation. In RXXX, *R* stands for *reaction* and *XXX* refers to the *reaction number* in GRI 3.0 mechanism list. NO formation through N_2O intermediate and NNH routes are calculated using the reaction list mentioned in Guo et al. (2005).

The prompt mechanism, represents the NO formation path via NCN pathway. Earlier studies believed that prompt NO is formed through HCN pathway. HCN molecules are produced as the result of the interaction of hydrocarbon molecules (CH) with nitrogen molecules. However, study performed by Moskaleva & Lin (2000) disproved that concept and showed that NCN route is the major route for prompt NO formation. They also proposed that the reaction CH+N_2<=>NCN+H is responsible for prompt NO and they also calculated the rate constants for that reaction. The prompt NO route in the actual GRI 3.0 is based on HCN pathway. To implement NCN pathway, the original NO sub-mechanism of GRI

3.0 mechanism is modified. Therefore, the reaction CH+N_2<=>HCN+N is replaced with the reaction CH+N_2<=>NCN+H. In addition, fours reactions to complete the NCN NO formation pathway are added: i) NCN+O<=>CN+NO, ii) NCN+H<=>HCN+N, iii) NCN+OH<=>HCN+NO, and iv) NCN+O_2<=>NCO+NO. The rate constants for these reactions were obtained from (Moskaleva & Lin 2000, Zhu & Lin 2005, 2007, Zhu et al. 2009). The implementation of these reactions in GRI 3.0 is based on the guidelines proposed in Sepman et al. (2013). The modified GRI 3.0 mechanism with the inclusion of NCN pathway that is used in the prompt NO calculations of this chapter is given in Appendix Appendix B. In the present work, prompt NO is calculated by subtracting the thermal, NNH and N_2O mass fractions from the total NO mass fraction which is calculated with the consideration of reactions responsible for NCN pathways.

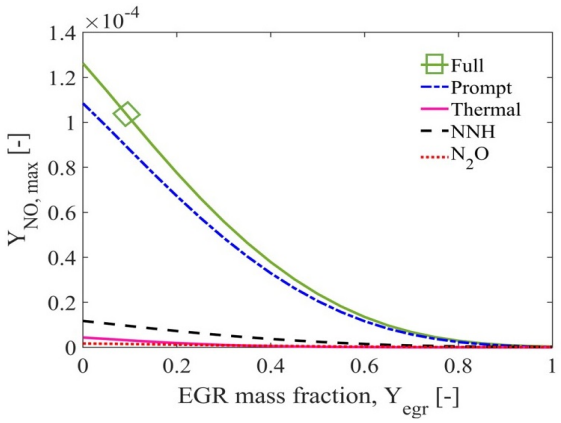

Fig. 3.8 Effect of EGR on $Y_{NO,max}$ via thermal, prompt, NNH and N_2O routes. The plots show that prompt route is the major contributor to total NO formation compared to other routes.

The effect of exhaust gas addition on the NO formation via individual NO routes is calculated using counterflow diffusion flame configuration. The results are shown in Figure 3.8. It can be seen that NO formation via the prompt route is the major contributor to the total NO formation. And all the other routes such as thermal, NNH and N_2O intermediate seem to be negligible. In addition, NO formation via thermal route is much lower compared to prompt route even in case of $Y_{egr} = 0$ i.e. pure CH_4 and air counterflow diffusion flame. Similar

behaviour was observed in CH_4 and air counterflow diffusion flames under MILD condition by Abtahizadeh et al. (2012). This behaviour of NO formation in counterflow diffusion flame is contrary to premixed flame. This could be attributed to the following factors,

- Unlike premixed flames, counterflow diffusion flames consist of a thicker reaction zone and a broad spectrum of fuel rich regions, where CH molecules responsible for triggering the prompt mechanism are available in a high concentration.
- Due to a short residence time of the reactants, T_{max} of the counterflow diffusion flames would be usually lower than that of premixed flames. Moreover, in premixed flames T_{max} is usually close to equilibrium temperature.

The above discussion shows that, in general, in low temperature counterflow diffusion flames, the prompt route is the major contributor to the total NO formation, and NO formation via prompt route decreases with increasing Y_{egr}.

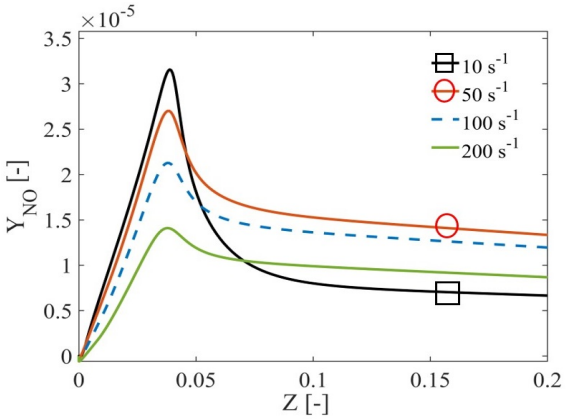

Fig. 3.9 Effects of strain rate on NO formation via prompt route with Y_{egr}=0.50. The plots show that increasing strain rate reduces the formation of prompt NO.

The effect of strain rate on NO formation has also been investigated. Since, NO formation via thermal, NNH and N_2O intermediate routes are negligible, only the effect of strain rate on prompt NO is investigated. For this purpose, the strain rate of the simulations is increased from 10 s^{-1} to 200 s^{-1} by keeping all the other parameters constant. The effect of strain rate

on prompt NO formation is performed only for the case Y_{egr}=0.50. Because, perfoming this calculation for any one Y_{egr} value is sufficient enough to predict the trend and the choice of Y_{egr} would not affect the observed trend. Y_{NO} of prompt NO route versus distance for various strain rates with $Y_{egr} = 0.5$ are shown in Figure 3.9. The figure shows that strain rate has a significant influence on prompt NO (refer to Figure 3.9). A 50% (approx.) drop in prompt $Y_{NO,max}$ is observed when the strain rate is increased from 10 s^{-1} to 200 s^{-1}. The reason is, when strain rate is increased, the residence time of the reactants decreases consequently decreasing the prompt NO formation.

The above discussions show that hydrocarbon (CH) and oxygen concentrations, and strain rate have a significant impact on prompt NO.

3.3.2 Unsteady flames

I. Effect of exhaust gas addition on ignition delay and the evolution of temperature

An origin flame configuration is used to analyse the effect of exhaust gas alone on ignition delay by excluding the effects of molecular diffusion and scalar dissipation. The origin flame simulations are calculated using a simplified form of Equations 3.2-3.4 with unity Lewis number assumption Peters (2000), and the equation is given as follow:

$$\rho \frac{\partial T}{\partial t} = \dot{\omega}_T + \frac{1}{2}\rho\chi\frac{\partial^2 T}{\partial Z^2}, \tag{3.11}$$

where $\dot{\omega}_T$ is the source term for temperature from chemical reactions, and χ is the scalar dissipation rate. As is seen in Equation 3.11, the second term in the RHS is the mixing part and χ determines the mixing rate that characterises the diffusion effects. In the present calculations, the species composition and temperature of the initial profile are uniform across the domain. Therefore, the term $\frac{\partial^2 T}{\partial Z^2}$ in the RHS becomes zero. As a result, the mixing term or the second term in the RHS of Equation 3.11 vanishes, and the problem reduces to

origin calculations. The initial conditions of the origin flame configuration are obtained by simulating frozen counter-flow diffusion cases. Ignition is possible only when the mixture temperature is above the self-ignition temperature of the reactants present in the mixture. The mixture temperature rises above self-ignition temperature of the reactants for Y_{egr} values greater than approximately 0.50 in the oxidiser stream.

In Figure 3.10 (a), the effect of exhaust gas addition on ignition delay is plotted for Y_{egr} values from 0.60 to 0.90. Ignition delay τ_{ign} values plotted in the figure correspond to the most reactive mixture fraction Z_{mr} and Z_{st}. In non-premixed flames, ignition starts at Z_{mr} which is different from Z_{st} (Mastorakos 2009). As a result, τ_{ign} of Z_{mr} is lower than that of Z_{st} which is apparent in Figure 3.10 (a). In the present work, ignition delay is considered as the time taken for a 50 K temperature rise (ΔT) in the reacting mixture, where ΔT is defined as $\Delta T(t) = T_{max}(Z,t) - T_{max}(Z,0)$. This method, based on temperature rise for the determination of ignition delay is similar to the definition used by Abtahizadeh et al. (2012) and Sabia et al. (2013). The reason for the choice of ΔT =50 K is, as seen in Figure 3.10 (b), the evolution of temperature or combustion takes place in two stages. The evolution of ΔT plotted in the figure corresponds to Z_{st} of various Y_{egr} cases. In all the cases, initially ΔT increases up to 50 K, and then the inception of thermal runaway can be observed. The reason for this two stage ignition is due to the presence of unstable reactive species in the initial state that results from frozen mixing solution. Moreover, Figure 3.10 (c) shows the evolution of ΔT for two different initial temperatures which are similar to that of Y_{egr} =0.80 and 0.90, however, Y_{egr} =0 is assumed for reactant composition. The figure shows that the evolution of ΔT takes place in a single stage and the two stage ignition observed in Y_{egr} >0 cases is not observed. This clearly shows that the two stage ignition is due to the reactive species present in the initial state.

Figure 3.10 (a) shows that the addition of exhaust gas has a significant effect on ignition delay. The ignition delay decreases from the order of 10^{-3} s at Y_{egr} =0.60 to 10^{-5} s at

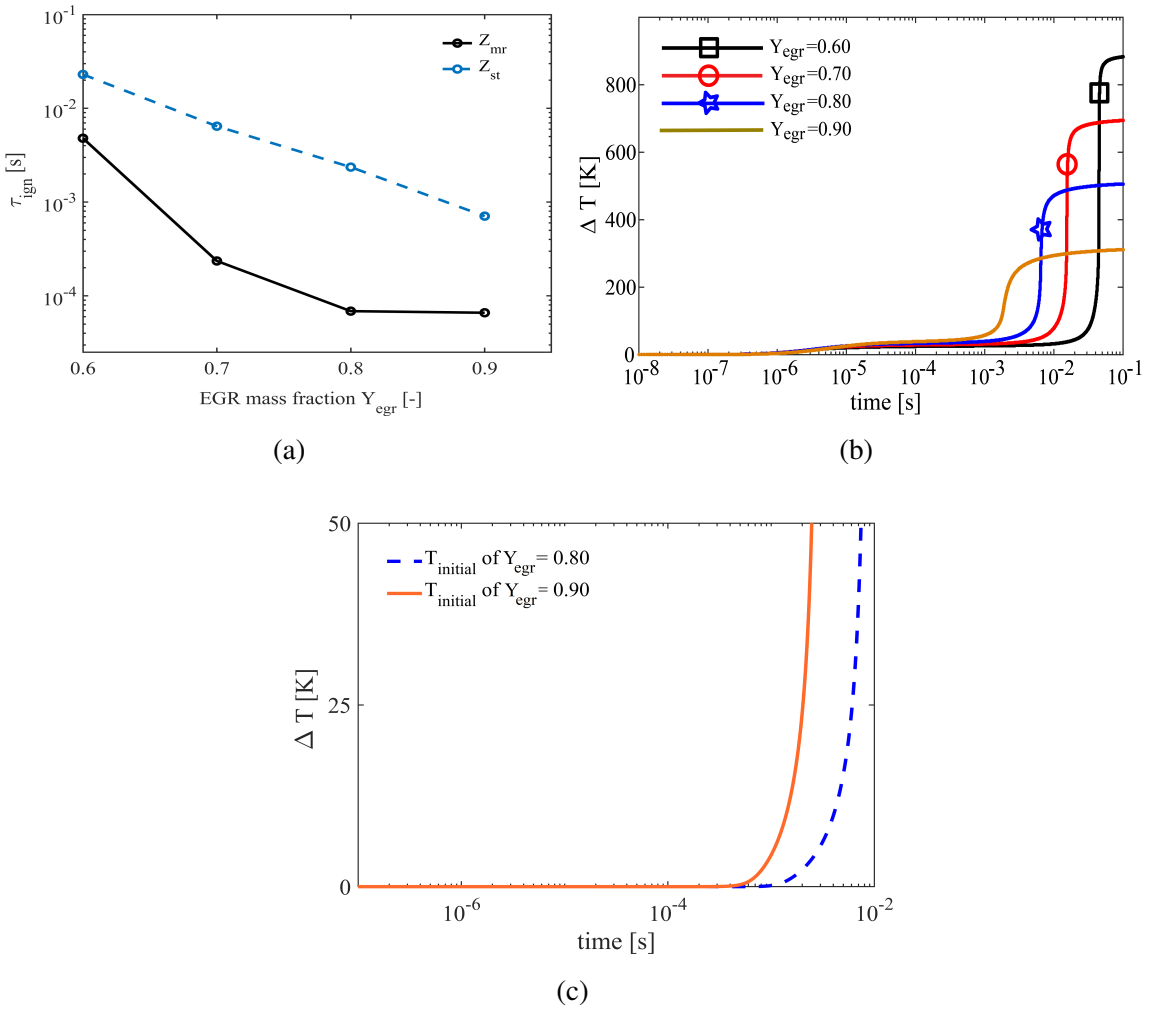

Fig. 3.10 (a) Effect of EGR on ignition delay (τ_{ign}) plotted as a function of EGR mass fraction (Y_{egr}). As is seen, τ_{ign} of Z_{mr} are shorter than that of Z_{st}. (b) Effect of EGR on the evolution of ΔT plotted as a function of time for Y_{egr} values from 0.60 to 0.90. The evolution of ΔT plots correspond to Z_{st}. (c) Evolution of ΔT up to 50 K for pure cases $Y_{egr} = 0$. The initial temperature ($T_{initial}$) of origin simulations is set similar to $Y_{egr} = 0.80$ and 0.90 cases. The comparison of figures (b) and (c) show that the two stage ignition observed in (b) is due to the presence of active radicals in the reactants. All the plots are generated using origin flame results.

Y_{egr} =0.90. In methane combustion with EGR, τ_{ign} observed by Abtahizadeh et al. (2012) were in the magnitude of 10^{-1} s to 10^{-3} s with increasing Y_{egr}. Comparison of τ_{ign} behaviour of CH_4 cases and CH_4/CO/H_2 cases shows that, in both flames, increase in Y_{egr} in the oxidiser stream reduces the magnitude of τ_{ign} by the order of 10^{-2}. However, τ_{ign} of CH_4/CO/H_2 and air flames with EGR is much lower than that of CH_4 and air flames with EGR. The reason for such low values of τ_{ign} is clearly due to the presence of hydrogen in the fuel. Apart from this, Figure 3.10 (b) clearly shows that exhaust gas addition significantly affects the evolution of temperature. The time required to reach the maximum temperature decreases significantly with increase in Y_{egr}. The reason is, the addition of exhaust gas significantly increases the reactants temperature. The increase in reactants temperature accelerates the combustion process and it reduces the time taken for the evolution of temperature. In addition, the maximum temperature of the flame itself reduces with increase in Y_{egr}. The reason is, the addition of exhaust gas in the oxidiser stream reduces the reactants concentration. As a result, the maximum flame temperature decreases with increase in Y_{egr} in the oxidiser stream (please refer to Figure 3.3).

The effects of exhaust gas addition on the evolution of counterflow diffusion flames are shown by plotting the evolution of temperature profile as a function of mixture fraction for Y_{egr} values 0.65, 0.75 and 0.85, respectively, in Figure 3.11 (a), (b) and (c). The plots show that, for all the values of Y_{egr}, the ignition starts at a mixture fraction close to oxidiser stream at Z_{mr} and it evolves toward Z_{st}. Apart from this, it can be observed that, as expected, Z_{st} occurs close to the oxidiser stream (Z=0) with increasing Y_{egr}. In addition, the evolution of ΔT for the above mentioned cases of the counterflow diffusion flames are presented in Figure 3.11 (d). The figure shows that, the effect of exhaust gas addition on the evolution of ΔT of counterflow diffusion flames is similar to that of origin flame configuration, i.e. the time required to reach the maximum combustion temperature decreases with increasing

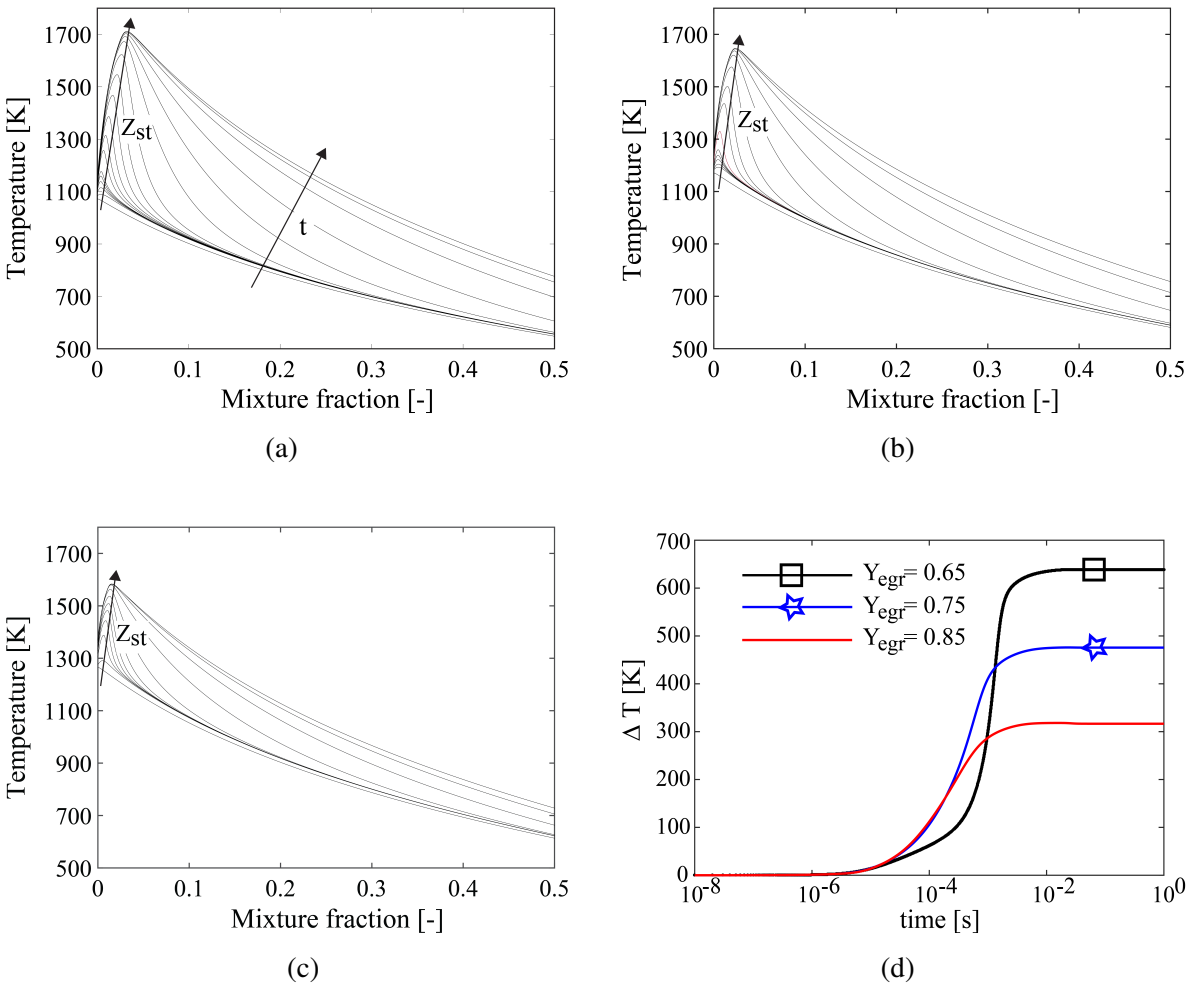

Fig. 3.11 Effect of EGR on the evolution of temperature profile plotted as a function of mixture fraction for various values of Y_{egr} such as (a) 0.65, (b) 0.75 and (c) 0.85. (d) The evolution of ΔT for the above mentioned cases of the counterflow diffusion flames. All the other parameters including strain rate$(= 125)$ s^{-1} are kept constant.

Y_{egr}. The effects of diffusion on autoignition behaviour in the presence of exhaust gas is investigated in detail and discussed in Section 3.3.2.

Overall, both the presence of hydrogen and the addition of exhaust gas to CH_4/CO/H_2 mixture considerably affect τ_{ign}. In addition, exhaust gas addition has a significant influence on the evolution of ΔT.

II. Effect of strain rate on ignition delay and the evolution of temperature

Strain rate has a significant influence on diffusive transport of reactants and in their mixing process. In a counterflow diffusion flame, increasing the strain rate accelerates the mixing process and increases the influx of reactants into the flame. On the other hand, increasing the strain rate also reduces the contact time of the reactants and accelerates the heat loss through diffusion. Consequently, T_{max} of the flame reduces with increasing strain rate. At higher values of strain rate, due to the swift transport of cool reactants toward the flame and also due to the accelerated diffusive heat loss, the flame may extinguish. Therefore, strain rate plays a major role in the structure and evolution of counterflow diffusion flame. In the present section, effect of strain rate on τ_{ign} and the evolution of ΔT in counterflow diffusion flames is discussed.

The effect of strain rate on τ_{ign} is analysed by increasing the strain rate from 10 s^{-1} to 900 s^{-1} while keeping all the other parameters constant. The value of Y_{egr} is kept at 0.85 for all the simulations in this section. τ_{ign} for the above mentioned strain rate range are shown in Figure 3.12. The figure shows increasing the strain rate has only a negligible effect on the ignition delay. The reasons are; (i) the presence of hydrogen in the reactants, and (ii) the high temperature of the reactants due to exhaust gas addition. Therefore, the chemistry is such fast so that the time required for a temperature rise of 50 K is not considerably affected by strain rate. Moreover, the time-dependent simulations are initiated using frozen cases in which the reactants are already in contact. However, the small increase in the ignition delay with increase in strain rate is due to the diffusion effects.

The effect of strain rate on the evolution of ΔT for various values of strain rate between 10 s^{-1} and 900 s^{-1} is shown in Figure 3.13. From the figure, it is apparent that T_{max} achieved by the counterflow diffusion flame decreases with increasing strain rate. As already discussed, the reason is, enhanced heat loss and a drop in residence time due to increasing strain rate. Apart from this, it can be noticed that, the evolution of temperature is less sensitive to strain

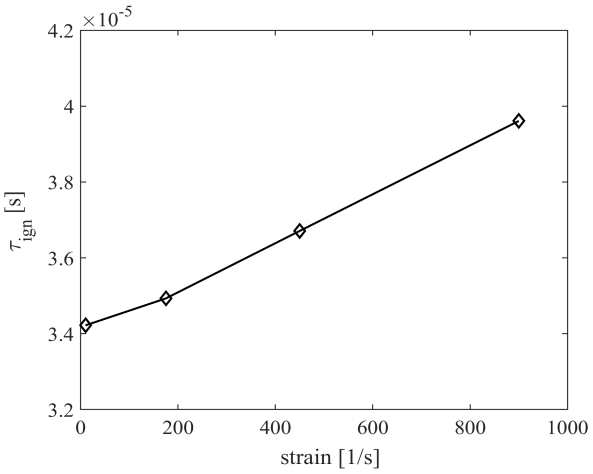

Fig. 3.12 Effect of strain rate on ignition delay is plotted by increasing the strain rate from 10 s^{-1} to 900 s^{-1}. All the other parameters including $Y_{egr}(= 0.85)$ are kept constant. The plot shows that increasing strain rate has only a negligible effect on the τ_{ign}.

rate. A similar behaviour was observed in the evolution of temperature when exhaust gas is entrained in both streams which was investigated by Abtahizadeh et al. (2012) in CH_4 and air counterflow diffusion flame with EGR. This could be attributed to the high temperature of the reactants due to exhaust gas addition.

To have a further insight, the effect of strain rate on the evolution of counterflow diffusion flames has also been analysed. For this purpose, the evolution of temperature profiles are plotted as a function of Z for strain rates 10 s^{-1}, 175 s^{-1} and 450 s^{-1} with $Y_{egr} = 0.85$. The plots are shown in Figure 3.14. The figure shows that, increasing the strain rate has a significant effect on the evolution of temperature profiles. At a lower strain rate (i.e. at 10 s^{-1}), the diffusive transport of reactants and their mixing process would be slow. Therefore, at lower strain rates, chemical time scales would be dominant. As a consequence, after autoignition at Z_{MR}, deflagration takes place in the mixture fractions close to Z_{st}. As seen, initially, a sharp increase in temperature is observed in the region close to Z_{st} followed by a very even increase in the temperature profile across the entire mixture fraction space, refer to Figure 3.14 (a). At higher strain rates (refer to Figure 3.14 (b) and (c)), however, the diffusive transport of the reactants and heat loss due to convection is much faster compared

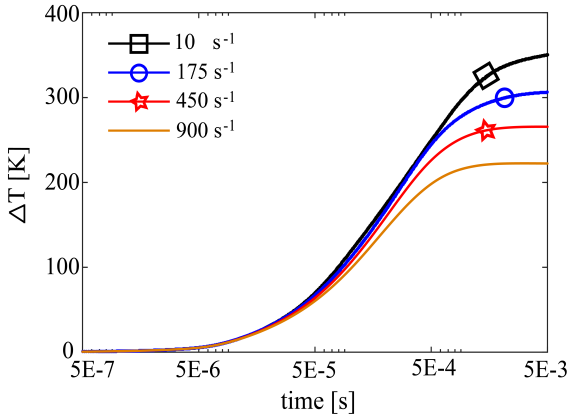

Fig. 3.13 Effect of strain rate on the evolution of ΔT for various values of strain rates between 10 s^{-1} and 900 s^{-1}. All the other parameters including $Y_{egr}(= 0.85)$ are kept constant. The plots show that T_{max} decreases with increasing strain rate.

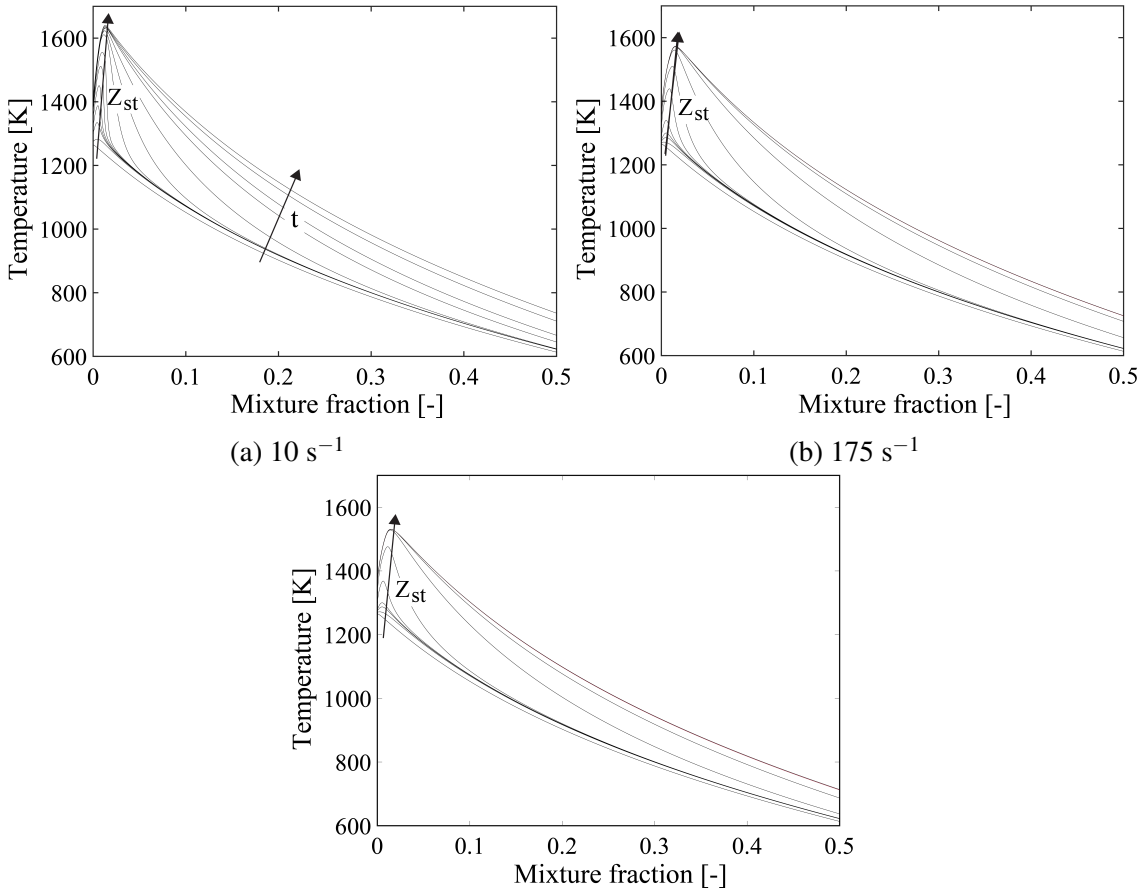

Fig. 3.14 Effect of strain rate on the evolution of temperature plotted for various values of strain rates such as 10 s^{-1}, 175 s^{-1} and 450 s^{-1}. All the other parameters including $Y_{egr}(= 0.85)$ are kept constant.

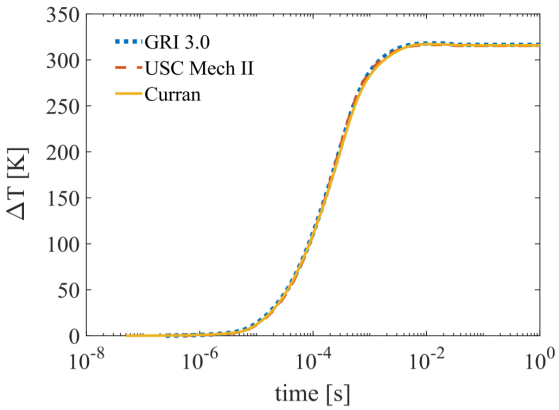

Fig. 3.15 Effect of chemical mechanisms on the evolution of ΔT. As is evident in the figure, the evolution of temperature predicted by all the three chemical mechanisms show a good agreement.

to lower strain rates. Therefore, the temperature profile increases more evenly across the mixture fraction space with increasing time. The above discussion shows that the diffusion and mixing process dominates the combustion process at higher strain rates, while chemistry dominates the combustion process at lower strain rates.

III. Effect of chemical mechanisms on the evolution of temperature

The effect of chemical mechanisms on the evolution of ΔT is evaluated in this section using counterflow diffusion flames. For this purpose, $Y_{egr} = 0.85$ is considered with a strain rate of 125 s^{-1}. GRI 3.0, USC Mech II and Curran mechanisms are used to simulate the time dependent simulations. Since, USC Mech II and Curran Mech do not include nitrogen oxidation mechanisms, the time dependent simulation of GRI 3.0 is also performed by omitting the nitrogen oxidation mechanisms. The evolution of ΔT predicted by all these three chemical mechanisms are shown in Figure 3.15. The figure shows that the temperature evolution predicted by all these three mechanisms shows an excellent agreement with each other.

IV. Effect of transport models on the evolution of temperature

In this section, the effect of transport models on ignition is analysed by comparing the evolution of ΔT predicted by various transport models. Similar to the previous sections, the simulations are performed for $Y_{egr} = 0.85$ with a strain rate 125 s^{-1}. Four transport models are considered for this study: mixture-averaged, complex, constant Lewis number assumption and unity Lewis number assumption. The results are shown in Figure 3.16(a). The plot shows that the evolution of ΔT predicted by complex, mixture-averaged and constant Lewis number assumption transport models are approximately same. On the other hand, the evolution of ΔT predicted using unity Lewis number assumption is much slower than the other models considered in this study. This is due to the preferential diffusion effects caused by the presence of hydrogen are not modelled in unity Lewis number assumption calculations. This shows that, even though the unity Lewis number assumption transport model reduces the computational time, it is not appropriate for modelling syngas enriched methane flames with EGR.

A parameter study is performed by changing the Y_{egr} for complex transport and unity Lewis number steady state cases to further understand the preferential diffusion effects on the mixture due to the presence of exhaust gas. Figure 3.16 (b) shows that the difference in T_{max} predicted by complex transport and unity Lewis number increases with increasing Y_{egr}. In Figure 3.16 (b), $\Delta T = T_{max,C} - T_{max,L}$, where, $T_{max,C}$ and $T_{max,L}$ correspond to the maximum combustion temperature calculated using complex and unity Lewis transport model, respectively. The figure shows that ΔT increases with increase in EGR mass fraction in the mixture until Y_{egr} =0.85. Furthermore, at Y_{egr} =0.90, only a small drop in ΔT is observed. Nevertheless, the figure reveals that, apart from the preferential diffusion effects of hydrogen, the preferential diffusion effects of various species present in the exhaust gas also become realisable when exhaust gas content is increased in the reactants mixture.

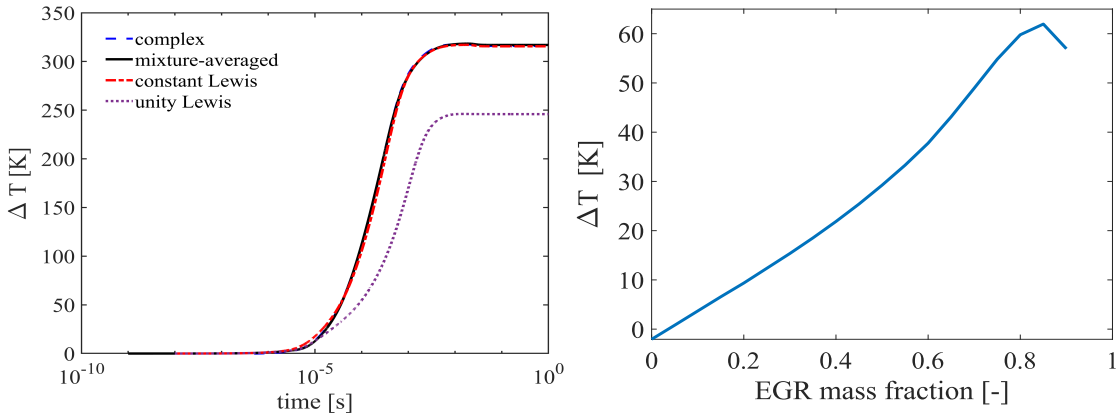

(a) (b)

Fig. 3.16 (a) Unsteady state results: effect of transport model on the evolution of ΔT. (b) Steady state results: effect of Y_{egr} on T_{max} predicted using complex transport model and unity Lewis number model. Figure (a) shows that, because of the presence of hydrogen in CH_4/CO/H_2 mixture, the unity Lewis number results differ significantly from complex, mixture-averaged and constant Lewis number assumption transport models due to preferential diffusional effects. Also, figure (b) shows that when exhaust gas content is increased in the oxidiser stream, preferential diffusional effects become realisable

3.3.3 Reaction pathway analysis

As mentioned in the previous sections, exhaust gas addition has a significant effect on the combustion characteristics of CH_4/CO/H_2 or the syngas enriched methane flames. In this section, QRPDs are presented to discuss the effect of exhaust gas addition on the reaction pathways of fuel decomposition and product formation. The intermediate species formed in the respective oxidation paths are also reported. For this purpose, QRPDs are generated for syngas enriched methane flames without EGR (*Pure case or Case A*) where $Y_{egr} = 0$ and syngas enriched methane flames with EGR where Y_{egr} = 0.50 (*Case B*). The fuel decomposition and product formation pathways of these two cases are presented in Figure 3.17 (a) & (b) and discussed. The EGR mass fraction in the oxidiser stream (Y_{egr}) is set to 0.50, because at this mass fraction, the oxygen mole fraction in the oxidiser stream is approximately 9% for the all the cases considered in this section. This oxygen mole fraction in oxidiser stream correspond to MILD combustion regime. Moreover, a similar oxygen

mole fraction in the oxidiser stream was used by Dally et al. (2002) and Medwell (2007) in non-premixed flames to achieve MILD combustion. The QRPD of MILD methane flame with Y_{egr}=0.50 (*Case C*) is also presented in Figure 3.17 (c). As it can be noticed above, Y_{egr} is set to 0.50, so that, in addition to the analysis performed for understanding the effects of the addition of exhaust gas on the reaction pathways of fuel decomposition and product formation of CH_4/CO/H_2 flames, the QRPD generated for CH_4/CO/H_2 flames can be compared with the QRPD of MILD methane flames to understand the effect of syngas addition on the fuel decomposition and product formation pathways of MILD methane flames. *GRI 3.0* is a reduced mechanism developed for the investigation of combustion characteristics and NO_x emission levels. However, it is not suitable for the reaction pathways analysis. On the other hand, reaction pathways analysis requires a detailed chemical mechanism that is suitable for MILD CH_4/CO/H_2 flames. Therefore, the reaction pathway analyses in this section are performed using Curran mechanism which is a detailed mechanism with 113 species and 710 reactions.

The procedure followed for the generation of QRPDs in the present work is explained as follows. First, frozen results of counterflow diffusion of oxidiser and fuel are calculated. Since, the fuel contains a significant quantity of hydrogen, complex transport model is employed to accurately predict the preferential diffusion effects. The stoichiometric mixture fraction is determined from the frozen mixing solutions. Then the evolution of temperature as a function of time is calculated for the stoichiometric composition using homogeneous reactor models in CHEMKIN. Finally, the QRPDs that show the fuel decomposition and product formation paths are generated using reaction path analyser package in CHEMKIN from the homogeneous reactor results at the timestep where the temperature rise (ΔT) is 50 K. Since the homogeneous reactor results are used to generate the QRPDs, the initial temperature of the reactants must be greater than the self-ignition temperature. Therefore, in

the present case, 1000 K, which is above the self-ignition temperature of all the fuel species considered, is chosen as the inlet temperature of the reactants for frozen calculations.

The QRPDs of CH_4 to CO_2 and H_2O oxidation pathways of pure and EGR cases are shown in Figure 3.17 (a) and 3.17 (b). In the present work, the fuel considered is CH_4/CO/H_2. Therefore, choosing CH_4 to CO_2 and H_2O would capture the CH_4, H_2, and CO oxidation pathways with important intermediate species. The numbers indicated in the arrows correspond to the flux rate between two species. The thickness of the arrows of all the three diagrams are scaled using the following relation in Equation 3.12 to make a visual qualitative comparison, and the flux rate of a thicker arrow is greater than that of a thinner arrow.

$$Thickness\ of\ arrow\ ar\ = \left(\frac{SFR_{ar} - SFR_{min}}{SFR_{max} - SFR_{min}}\right)\left(* \ T_{ul} \ + \ T_{ll}, \right. \tag{3.12}$$

where, SFR stands for net species flux rate, SFR_{ar} is the net species flux rate of arrow ar, SFR_{min} is the lowest net species flux rate observed among the three QRPDs, SFR_{max} is the highest net species flux rate observed among the three QRPDs, and Th_{ul} and Th_{ll} are arbitrary constants utilised to scale the arrows between an upper limit and a lower limit. The Th_{ul} and Th_{ll} in this study is set to 8 and 0.5, respectively. Therefore, the thickness of the arrow that correspond to SFR_{max} is 8.5 (upper limit) and SFR_{min} is 0.5 (lower limit). Please note that, the arrow heads in the figures are not scaled. In the QRPDs presented in this section, only the major intermediate species and major reaction pathways are shown. In this context, major intermediate species means the top intermediate species (in terms of concentration) that are formed during the combustion process. In this study, the top twelve intermediate species (including the reactants and products) in terms of concentration are used to generate the QRPDs. Furthermore, the major reaction pathways indicate the reaction pathways with flux rate greater than the relative cut-off fraction 0.05. The value for relative

cut-off fraction is chosen as 0.05, because, below that value, many low flux rate reaction pathways appear in the QRPDs which make the diagrams too congested and unreadable.

Figure 3.17 (a) and 3.17 (b) show that, for both *Case A* and *Case B*, the important pathways involved in the decomposition of CH_4 are CH_3O - CH_2O - HCO - CO and C_2H_6 - C_2H_5 - C_2H_4 - HCO - CO. The oxidation pathways of CO and H_2 are not shown separately. The reason is obvious: the CO to CO_2 and H_2 to H_2O oxidation paths are the integral part of methane oxidation pathways. Furthermore, the QRPDs show that exhaust gas addition does not affect the intermediate species involved, however, it decreases the flux rate between the species. This means, for the fuel mixture considered in the present work, for the same initial temperature, diluting oxidiser stream with exhaust gas species reduces the concentration of the oxygen content and therefore, increases the time taken for the evolution of temperature. However, it does not have a significant impact on the major intermediate species.

Figure 3.17 (b) and Figure 3.17 (c) compare the fuel decomposition and product formation pathways of *case B* and *case C*. In both cases, all the parameters are same except the fuel composition. It is apparent in the figures that the addition of syngas in MILD methane flames significantly increases the flux rate between the species and changes the reaction pathways between the species. However, the major intermediate species formed during the combustion reactions are identical. In *case C*, the maximum flux rate observed between the species is 1.06e$-$7 (between CH_4 to CH_3). This is lower by an order of 10^{-1} compared to the maximum species flux rate observed in *case B* which is about 1.48e$-$6 (between CH_4 to CH_3). Moreover, in *case B*, the flux rates between the species are generally in the order of 10e$-$7 while in *case C*, it is in the order of 10e$-$8. Furthermore, it has also affected the major reaction pathways between the intermediate species. This means, the addition of syngas or H_2/CO in the MILD methane flames leads to a reduction in time taken for the evolution of temperature or increases the reaction rate and changes the reaction pathways. However, it does not affects the major intermediate species formed during the combustion process.

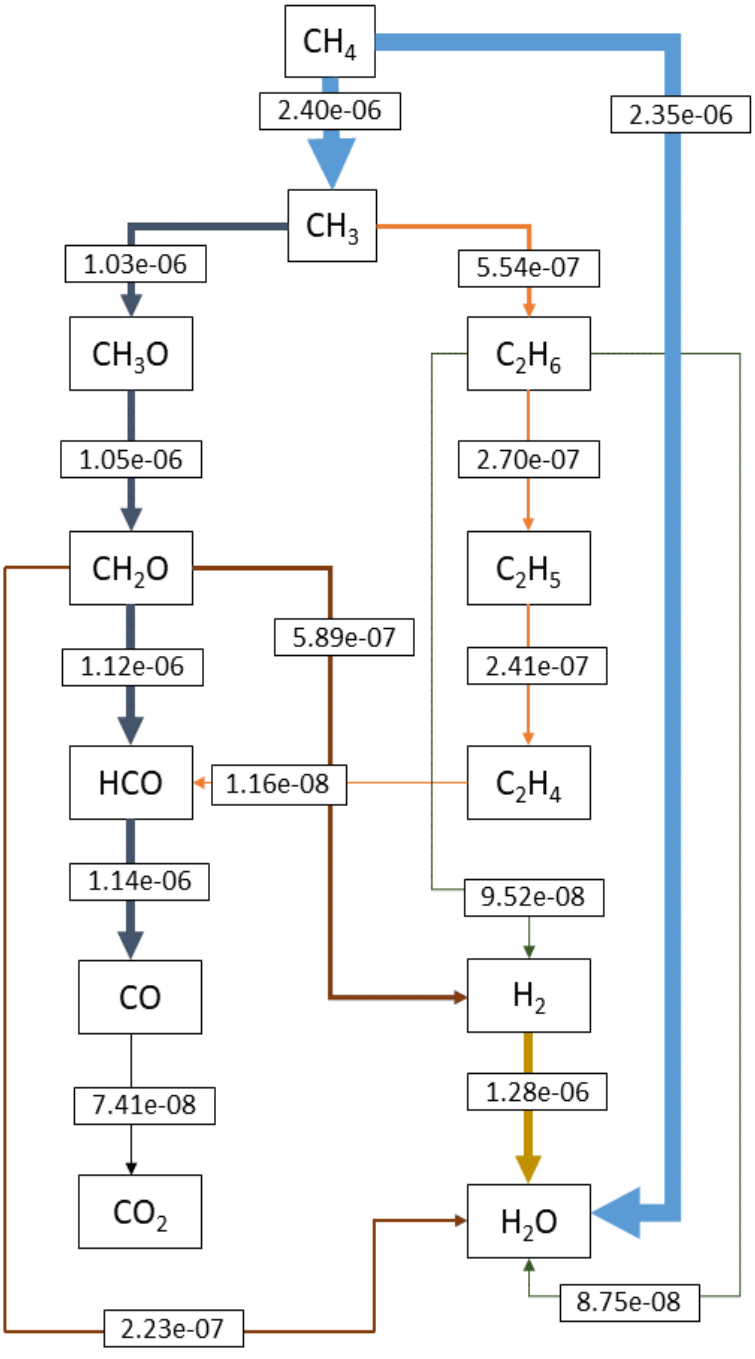

(a)

Fig. 3.17 Quantitative Reaction Path Diagrams (QRPDs) of CH_4 to H_2O and CO_2 of (a) syngas enriched methane flames without EGR, i.e. $Y_{egr} = 0$ (*Pure case*) at ΔT=50 K.

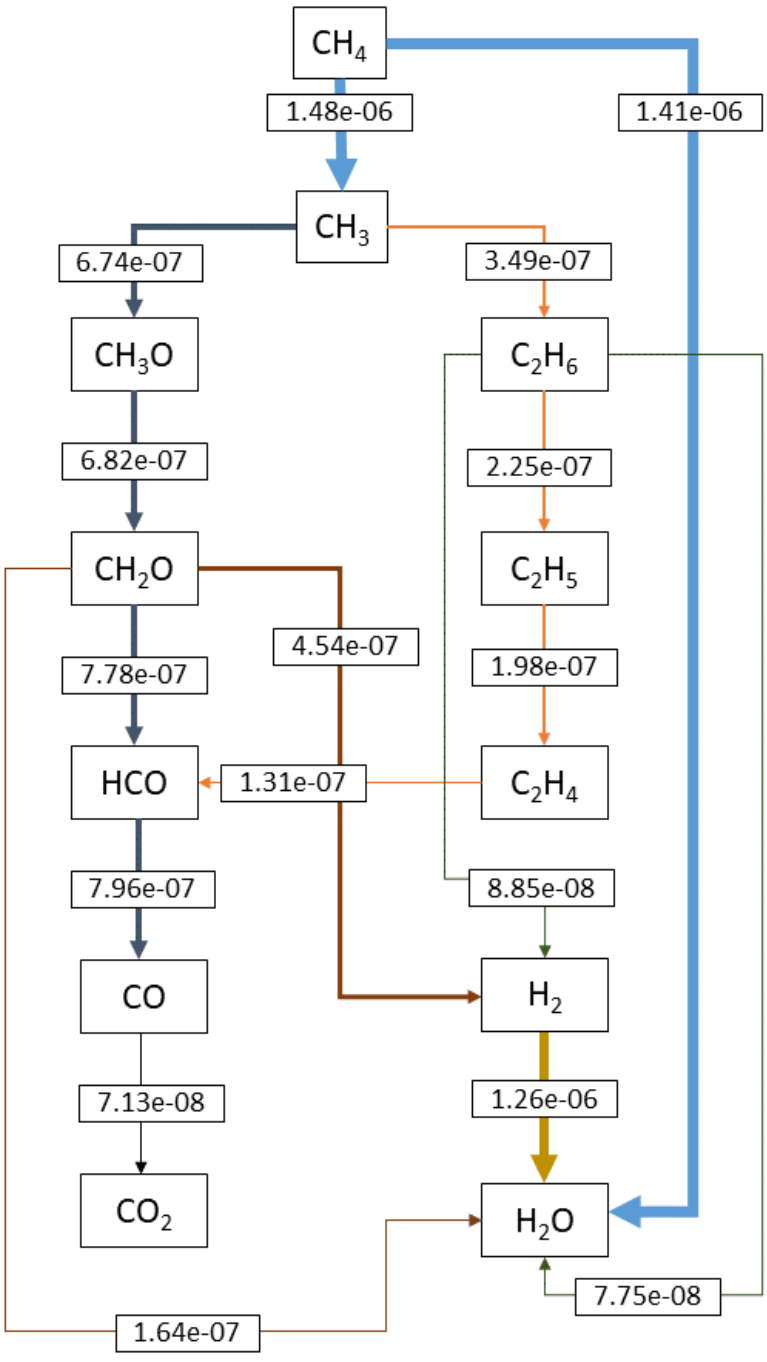

(b)

Fig. 3.17 Quantitative Reaction Path Diagrams (QRPDs) of CH_4 to H_2O and CO_2 of (b) syngas enriched MILD methane flames or CH_4/CO/H_2 with $Y_{egr} = 0.50$ at ΔT=50 K.

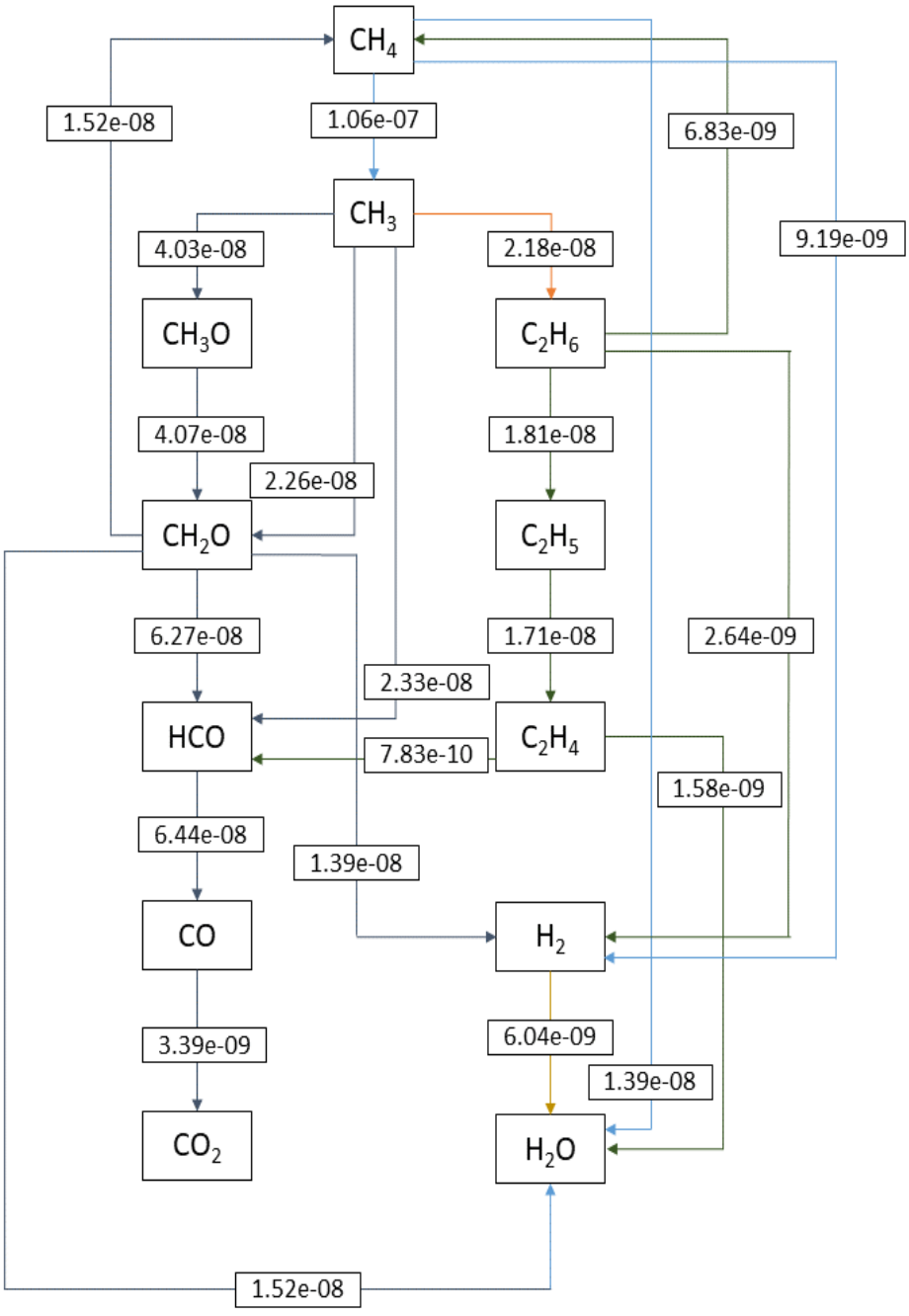

(c)

Fig. 3.17 Quantitative Reaction Path Diagrams (QRPDs) of CH_4 to H_2O and CO_2 of (c) MILD methane flames with Y_{egr}=0.50 at ΔT=50 K.

3.4 Effects of syngas addition on MILD methane flames

As mentioned in the beginning of the chapter, the effects of syngas addition on the combustion characteristics and reaction pathways of MILD methane flames are analysed in this section. The investigation of syngas addition on MILD methane flames would help us to develop fuel flexible combustors which encourages the utilisation of renewable fuels in combustion systems. As discussed earlier, the chapter investigates the effects of exhaust gas or burnt gas addition on combustion characteristics and reaction pathways of syngas enriched methane flames. For this purpose, simulations were performed by increasing exhaust gas mass fraction of Y_{egr} in the oxidiser stream from 0 to 1. Since MILD combustion is achieved by highly preheating and highly diluting the oxidiser stream using exhaust gas, simulation of syngas enriched methane flames or CH_4/CO/H_2 flames by the variation of Y_{egr} values from 0 to 1, by default, include MILD combustion regime. Moreover, in case of unsteady simulations and reactions pathways analysis, the oxygen molar fractions in the oxidiser stream of all the simulations is less than or equal to 9%. As mentioned in subsection 3.3.3, such molar fractions of oxygen is used in previous researchers to achieve MILD combustion. Furthermore, the initial temperatures of the reactants of all the cases of unsteady simulations and QRPD analyses is higher than that of autoignition temperature and the overall temperature rise due to combustion is less than that of autoignition temperature which satisfy with the criteria defined by the most widely accepted definition of MILD combustion presented in Chatper 1.

The comparison of the results of the present work that correspond to the syngas enriched MILD methane flames with the MILD methane flames results would help us to understand the difficulties that arise when natural gas/syngas are co-fired under MILD operating conditions. The comparison of the steady state results of MILD methane flames from (Abtahizadeh, van Oijen & de Goey 2012) and the syngas enriched MILD flames results of the present work shows that, in general, in both studies, T_{max} decreases with increasing exhaust gas

content in the reactants and the prompt route is a major contributor to the total NO formation, and thermal NO seems to be negligible. However, the results reveal that the addition of syngas in MILD methane flames reduces the NO formation levels. For instance, at Y_{egr} =0.5, the maximum NO mass fraction in MILD methane flames is in the order of 10^{-4} while in syngas added MILD methane flames, for the same Y_{egr} value (=0.50) the maximum NO mass fraction is in the orfer of 10^{-5}. The reason is, as seen in Section 3.3.1, CH_4 concentration plays an important role in prompt NO formation. Hence, cofiring or simply the addition of syngas with natural gas reduces the CH_4 concentration in the reacting mixture which leads to a lower prompt NO emission levels compared to that of pure natural gas combustion.

On the other hand, the major differences are observed in the unsteady results. In (Abtahizadeh, van Oijen & de Goey 2012), for all the cases, τ_{ign} calculated is in the magnitude of 10^{-1} s to 10^{-3} s and τ_{ign} values do not drop below 10^{-3} s. Moreover, increasing the amount of exhaust gas in the reactants decreases the order of magnitude of τ_{ign}. In the present work, as mentioned in Section 3.3.2, τ_{ign} was in the order of magnitude of 10^{-3} s to 10^{-5} s. Similar to MILD methane flames, the increasing Y_{egr} reduces the order of τ_{ign}. However, as it can be seen, order of magnitude of τ_{ign} of MILD CH_4/CO/H_2 flames is lower than that of MILD CH_4 flames by an order of 10^{-2} at all the values of Y_{egr}. The reason is, the presence of a highly reactive gas hydrogen in the fuel mixture.

In non-premixed coflow burners, ignition delay can be related to flame lift-off heights. A short ignition delay means the flame is attached to the burner giving no or very little time for the mixing of fuel and oxidiser. On the other hand, a long ignition delay means the flame would occur far away from the burner giving sufficient time for the mixing of fuel and oxidiser. The evolution of temperature can be related to flame length. For example, slow evolution of temperature means the flame is long while if it is fast means the flame is short. Both lift-off height and flame length plays a significant role in the design of the burner. Optimum values of τ_{ign} and reasonable time for the evolution of temperature are preferred to

give a sufficient lift-off height and flame length, respectively. This is necessary to achieve desirable mixing and complete combustion while keeping the combustor size small.

As mentioned above, τ_{ign} of CH_4/CO/H_2 flames is very low due to the presence of H_2, and it is very sensitive to the amount of H_2 present in the mixture. Furthermore, the results of the experiments performed by Arteaga Mendez et al. (2015) reveal that increasing hydrogen concentration in the natural gas jet-in-hot-coflow flames decreases the flame lift-off height. Therefore, when co-firing of syngas/natural gas is considered, both hydrogen and exhaust gas content in the fuel plays a major role in deciding the lift-off height while Y_{egr} plays a major factor in deciding the flame length. On the other hand, it is worth mentioning that, in case of CH_4 flames, the amount of exhaust gas in the reactants is the only factor that plays a major role in deciding both lift-off height and flame length.

The present work clearly shows that the addition of syngas in methane flames reduces the NO formation levels and EGR further reduces the NO formation levels in syngas/natural gas mixtures, and when the flame enters the MILD regimes, NO formation is almost negligible. The observations of this study clearly shows that the cofiring of syngas and the addition of exhaust gas in the oxidiser stream has significant environmental advantages. Moreover, as this study was conducted by considering EGR in oxidiser stream with exhaust gas mass fraction in the reactants streams ranging from 0 to 1, the quantitative output of this study could be used as a reference in the design process of experimental set-ups and industrial burners that consider cofiring of syngas with natural gas and EGR.

3.5 Conclusions

The numerical codes, geometry, chemical mechanisms, and simulation parameters suitable for the investigation of the effects of syngas addition to MILD methane flames were identified in this chapter. Then, 1D steady and unsteady simulations of methane flames enriched with syngas and exhaust gas were performed. The results of the simulations were analysed to

understand the effects of syngas addition to the MILD methane flames. Additionally, the effects of the exhaust gas or burnt gas addition to CH_4/CO/H_2 counterflow diffusion flames were analysed. Finally, the effects of syngas addition on the reaction pathways of MILD methane flames and the effects of EGR addition on the reaction pathways of methane flames were analysed using QRPDs. With these, in this chapter, objectives 1, 2, 3, 4, and 6 relevant to syngas addition are achieved. By achieving these objectives, the effects of syngas addition on the combustion, ignition, flame structure, and emission characteristics of MILD methane flames are understood. The important conclusions that are drawn from the results of the present chapter are discussed as follow.

Firstly, the conclusions derived based on the observations made on the investigations performed to analyse the effects of exhaust gas addition on CH_4/CO/H_2 flames are discussed. In exhaust gas added CH_4/CO/H_2 flames, the chemical species present in the reactants and the stream in which exhaust gas is entrained have a larger influence on the flame structure and location of stoichiometric mixture fraction compared to that of strain rate and the inlet temperature of the reactants. The prompt route remains the major contributor to the total NO formation for the CH_4/CO/H_2 and air counterflow diffusion flame. The effect of strain rate on NO formation via the prompt route is significant. For the fuel considered in the present study, increasing the amount of exhaust gas reduces lift-off height and the flame length. In addition, the hydrogen percentage in the fuel has a significant influence on lift-off height. Complex, mixture-averaged and constant Lewis number transport models predict a similar autoignition behaviour. On the other hand, discrepancies were observed between unity Lewis number assumption and other transport models. Additionally, the discrepancies observed in the results of unity Lewis number assumption are not only because of the presence of hydrogen in the fuel, but, also due to the presence of exhaust gas in the reactants in which the discrepancies increase with increasing Y_{egr}. Quantitative reaction path diagrams show that, for the fuel considered in the present work, the addition of exhaust gas to reactants does not

cause significant changes in the important intermediate species formation. On the other hand, for the same initial temperature, the dilution of oxidiser stream with exhaust gas species reduces the flux rate between the intermediate species.

Now, the conclusions derived based on the comparison of the results of syngas enriched MILD methane flames and MILD methane flames are listed. The effects of the addition of syngas on the flame temperature, and NO formation pathways in MILD methane flames are negligible while it reduces the NO emission levels in the MILD methane flames by an order of at least 10^{-1}. Also, syngas addition reduces the ignition delay of MILD methane flames by an order of 10^{-2}. Furthermore, syngas addtion make preferntial diffusion effects realisable in MILD methane flames. Apart from these, in case of MILD methane flames, only the exhaust gas content in the reactants governs the lift-off height and flame length. In syngas enriched MILD methane flames, both hydrogen content and exhaust gas content of the reactants mixture governs the lift-off height, and the flame length is mainly governed by the exhaust gas content. The reaction pathways analyses show that the addition of syngas in MILD methane flames increases the flux rate between the major intermediate species of these flames.

To conclude, this study clearly shows that the addition of syngas and exhaust gas in the oxidiser stream enhances the flame characteristics and favours the environment by reducing emission levels. Moreover, this study was conducted by considering the exhaust gas recirculation in fuel and/or oxidizer stream(s) with exhaust gas mass fraction in the reactants streams ranging from 0 to 1. Hence, the quantitative output of this study could be used as a reference in the design process of experimental set-ups and industrial burners that consider cofiring of syngas with natural gas and EGR. Nevertheless, it should be noted that the conclusions of this chapter are drawn by analysing the 1D laminar flame and 0D flame results. However, the practical applications are usually 3D flow and operate in turbulent flow regime. Hence, one should carefully apply these findings to practical applications.

Chapter 4. DNS of CO enriched adiabatic MILD CH_4 flames

4.1 Overview

In this chapter, the effects of carbon monoxide addition on non-premixed MILD methane flames are investigated using 1D and 2D direct numerical simulations. The investigations of this chapter are performed in both laminar and turbulent flame regimes. First, the numerical methods and simulation set-up are explained. Then, the results are presented to discuss the effects of the addition of carbon monoxide on the ignition characteristics and flame characteristics of MILD methane flames. Additionally, the possibility for the development of Igniting Mixing Layer (IML) based Flamelet Generated Manifold (FGM) model for the prediction of adiabatic MILD flames for the flame configuration considered in this chapter is analysed. Next, the effect of unity Lewis number assumption of MILD CH_4 and MILD CH_4/CO flames are analysed to understand the significance of preferential diffusion in these flames. It should be noted that the investigation performed in this chapter are limited to adiabatic MILD flames. Finally, the main findings and conclusions of this chapter are summarised.

4.2 Numerical methods and simulation setup

The effects of carbon monoxide addition to non-premixed MILD methane flames are studied using both 1D and 2D direct numerical simulations. Similar to Chapter 3, CHEM1D is utilized for performing the one-dimensional direct numerical simulations. The reason for choosing CHEM1D is, the other one-dimensional reaction flow solvers like CHEMKIN, CANTERA, and Star-CCM+ do not have the feature to simulate the one-dimensional Igniting

Mixing Layers (IML) flames investigated in this chapter. The DNS codes considered for performing the 2D DNS cases are S3D (Chen et al. 2009), DNS code (Jin et al. 2013), DiSco (Bastiaans et al. 2001, Groot 2003, Van Oijen et al. 2007), and PENCIL (Brandenburg et al. 2020). The codes S3D and DNS code (Jin et al. 2013) were used by Chen et al. (2009) and Jin et al. (2013), respectively, for simulating a similar flame configuration. However, the license to DNS code is not available to the author of this thesis. It is accessible only for the researchers belonging to the group in which it has been built and maintained. In the case of S3D, although its license is available upon request, it is developed for the simulation of hydrogen combustion. The fuels considered in the present investigation are methane and methane-carbon monoxide mixtures. So, it is necessary to implement a new chemical mechanism in S3D for simulating these fuel mixtures. In addition, the implemented chemical mechanism should not cause solution divergence. Although the licence for S3D is available upon request, the technical support available for this code is limited. Solving these issues without on-demand technical support could be a humongous task and a very time-consuming process. The PENCIL DNS code is an open-source code, and the instructions are well documented. However, the PENCIL DNS code is developed for studying Magnetohydrodynamic turbulence, and it is not particularly developed for combustion applications. Major modifications are required to use PENCIL for simulating the cases considered in this chapter. Since it is an open-source code, on-demand technical support is unavailable, and help is only available in the form of community support which is not very efficient to attempt major modifications on such a complex numerical code. DiSco is exclusively developed for methane-based fuel mixtures, and the chemical mechanisms for calculating methane chemistry has already been implemented on the code. It has been shown that these chemical mechanisms do not cause solution divergence. The other advantages are on-demand technical support and unrestricted access to the license are available for DiSco. Moreover, even though codes like S3D and PENCIL need significant modification and enormous effort to make them suitable for the

fuels and flame configurations considered in this chapter, the resulting accuracy achieved through these codes is the same as the accuracy achieved using the DiSco. Because all these codes are DNS codes built using high-resolution discretisation schemes. Hence, DiSco is chosen for performing the two-dimensional direct numerical simulations of this chapter and the direct numerical simulations of Chapter 5. The MILD flames results calculated using this code were accepted in peer-reviewed journals (Van Oijen 2013, Abtahizadeh et al. 2015, Göktolga et al. 2015). Moreover, in Subsection 4.2.1, the code is verified against the 1D direct numerical simulation results calculated using CHEM1D and the preprocessing steps are checked. The governing equations in their fully compressible forms are solved by the DNS code to resolve the reacting flow problem. The governing equations are:

$$\frac{\partial \rho}{\partial t} + \nabla \cdot (\rho \boldsymbol{u}) = 0, \tag{4.1}$$

$$\frac{\partial (\rho \boldsymbol{u})}{\partial t} + \rho \boldsymbol{u} \nabla \boldsymbol{u} = -\nabla p + \nabla \sigma, \tag{4.2}$$

$$\rho \frac{\partial Y_\alpha}{\partial t} + \rho \boldsymbol{u} \nabla Y_\alpha = -\nabla \cdot \left(\frac{\lambda}{Le_\alpha c_p} \nabla Y_\alpha \right) + \omega_\alpha, (\alpha = 1, ..., N-1), \tag{4.3}$$

$$\rho c_v \frac{\partial T}{\partial t} + \rho c_v \boldsymbol{u} \nabla T = -\nabla \cdot (\lambda \nabla T) - p \nabla \boldsymbol{u} + \sigma \nabla \boldsymbol{u} + \nabla \cdot \quad \sum_{\alpha=1}^{N-1} h_\alpha^{'} \frac{\lambda}{Le_{\alpha c_p}} \nabla Y_\alpha \Bigg) \Bigg($$

$$- \sum_{\alpha=1}^{N-1} (h_\alpha^{'} - R_\alpha^{'} T) \Big[\omega_\alpha + \nabla \cdot \left(\left(\frac{\lambda}{Le_\alpha c_p} \nabla Y_\alpha \right) \right) \Big], \tag{4.4}$$

where, σ is the stress tensor, λ and c_v are thermal conductivity and specific heat capacity at constant volume of the mixture, respectively. The variables $\dot{\omega}_\alpha$ and Le_α correspond to source term and Lewis number of the species α, respectively. In Equation 4.3, equations are solved for only N-1 species excluding N_2. The diffusion correction is imposed by $\sum Y_\alpha = 1$.

In Equation 4.4, for each species, enthalpy and gas constant are defined as $h'_\alpha = h_\alpha - h_{N_2}$ and $R'_\alpha = R_\alpha - R_{N_2}$, respectively, to take into account the diffusion correction. As seen in Equation 4.4, the dufour effect, the Soret effect and species diffusion due to pressure gradients are neglected. However, the transport equation for temperature (Equation 4.4) takes into account the viscous dissipation. In the above set of equations, Equation 4.1 to Equation 4.4, the number of unknown variables are greater than the number of equations solved. Hence, Ideal gas law is used to close the set of equations,

$$p = \rho RT \sum_{\alpha=1}^{N} Y_\alpha / M_\alpha, \tag{4.5}$$

where, R is the universal gas constant. In this study, for both the fuels, viscosity coefficient (μ) and thermal conductivity (λ) of the mixtures are computed using polynomial expressions. They are,

CH_4 case,

$$\lambda = c_p * 1.52 * 10^{-5} * \left(\frac{T}{298}\right)^{0.992} \tag{4.6}$$

$$\mu = Pr * \left(\frac{\lambda}{c_p}\right) \left(where\ Pr = 0.7577 - 9.65 * 10^{-4} T + 2.82 * 10^{-8} T^2 \right. \tag{4.7}$$

CH_4/CO case,

$$\lambda = c_p * 2.0 * 10^{-5} * \left(\frac{T}{298}\right)^{0.839} \tag{4.8}$$

$$\mu = Pr * (\frac{\lambda}{c_p}),\ where\ Pr = 0.7318 - 6.34 * 10^{-4} T + 1.83 * 10^{-8} T^2 \tag{4.9}$$

The coefficients in Equation 4.6 - Equation 4.9 and Lewis number of species are calculated by fitting the solutions obtained from the 1D simulations performed with complex transport models. Boundary conditions and reactants composition used for the calculation of these fitting expression coefficients are adapted from Table 4.1. In DiSco, the diffusion terms

of the governing equations are discretised by using the sixth-order accurate compact finite difference method (Lele 1992) and the convective terms are discretised using the fifth-order method (de Lange 2007). An explicit compact-storage third order Runge-Kutta scheme is used to carry out the time integration.

In this present work, DRM19 reaction mechanism Kazakov & Frenklach (1994) is employed for resolving the chemistry. DRM19 chemical mechanism is a reduced mechanism of GRI 1.2 mechanism (Frenklach et al. 1995, 1994). DRM19 mechanism consists of 21 species and 84 reactions. The species enthalpies h_α, species source terms $\dot{\omega}_\alpha$ and specific heat capacities c_p and c_v are calculated using the data provided by DRM19 mechanism. In Figure 4.1, the evolution of maximum H mass fraction calculated using USC Mech II, GRI 3.0 and DRM19 for CH_4 case and CH_4/CO case are shown. The boundary conditions considered for this calculation are adapted from Table 4.1. The results presented here correspond to the unsteady Igniting Mixing Layers (IML) flamelet solutions. The figure shows that, for both cases, the deviation between the results of USC Mech II and GRI 3.0 and the results of DRM19 is about 17%. For this study, this agreement is considered as satisfactory. Moreover, performing DNS with GRI 3.0 or USC Mech II is computationally very expensive compared to that of DRM19 as the number of species and reactions in them is much higher than that of DRM19. The USC Mech II consists of 111 species and 784 reactions, and GRI 3.0 consists of 53 species and 325 reactions. As a result, compared to DRM19, the expected increase in simulation time in the case of USC Mech II is at least 800% and in case of GRI 3.0, it is at least 400%. Therefore, DRM19 is chosen for the present study as it provides a good trade-off between computational cost and accuracy. Moreover, it is proven in Section 4.3 that the trends predicted by DRM19 are reliable.

Highly preheated and highly diluted oxidiser is considered to achieve MILD flames. The composition of the oxidiser stream is adapted from (Abtahizadeh et al. 2017). A very high temperature of 1700 K is assumed for the oxidiser stream. Such a high temperature is chosen

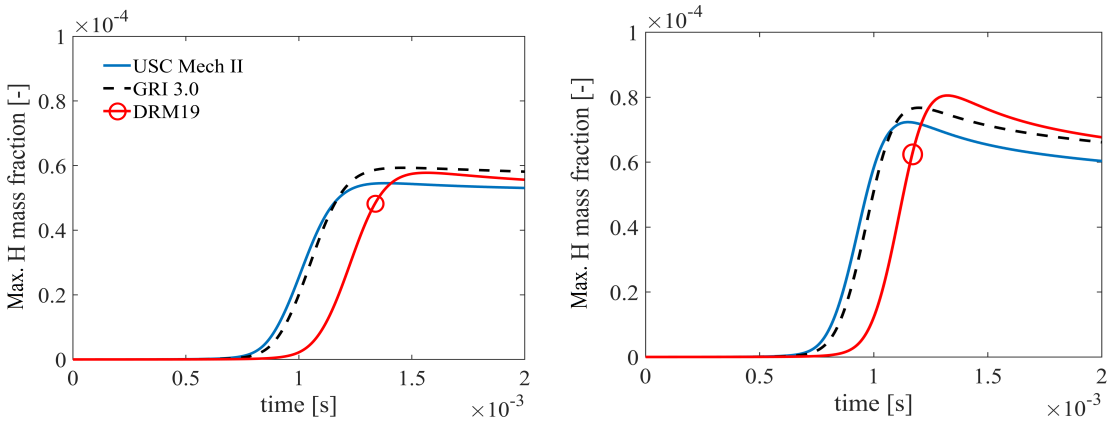

Fig. 4.1 Evolutions of maximum H mass fraction calculated using USC Mech II, GRI 3.0 and DRM19 for (a) CH_4 case, and (b) CH_4/CO case. The results presented here is calculated with IML flame configuration. The results show that the agreement between the DRM19 results and USC Mech II is about 17%.

for the oxidiser stream to achieve an ignition delay of less than 1 ms. Such a low ignition delay is necessary for this study. Because, for an adiabatic case with approximately 1 ms ignition delay, a simulation time of at least 1.5 ms is required to capture the ignition and flame characteristics. Even for the 2D DNS cases considered in this study, based on the available resources, the expected wall clock time required to simulate 1.5 ms is about 5 days per case. Moreover, in the next chapter, non-adiabatic cases are simulated in the 3D environment. The consideration of heat loss is excepted to significantly lengthen the ignition delay, and therefore, the simulation time is expected to be between 2 ms and 3 ms to capture the ignition and flame characteristics. Based on the available resources, the estimated wall clock time for the expected simulation time of 2.5 ms for a 3D case is about 35-40 days. Even a 100 K reduction in oxidiser temperature is expected to increase the ignition delay by at least 50% and also slows down the flame development time which consequently would increase the wall clock time by at least 50% to capture the ignition and flame characteristics. That means, for 3D simulations, the expected wall clock time would be at least 60 days to 65 days per case which is practically not feasible considering the available resources and timelines of

this thesis. Therefore, it is decided to use an oxidiser temperature of 1700 K. Furthermore, the objective of this study is to understand the effects of carbon monoxide addition on MILD methane flames which is entirely possible at the considered temperature. Moreover, oxidiser temperature as high as 1810 K was used to study the effects of temperature on lift-off height of CH_4 JHC flames by Arndt et al. (2013). Therefore, the choice of such a high oxidiser temperature is justified.

The flame geometry considered for 2D DNS cases in this study replicates the Jet-in-Hot-Coflow (JHC) flame configuration. Further details about the flame geometry are discussed in the latter part of this section. As mentioned in Chapter 1, the JHC flame configuration is chosen, because, this flame configuration decouples the combustion process of reacting flows found in practical combustion systems from the associated recirculation fluid mechanics (Cabra 2003). This provides a well-defined flow-field and mixture-field for the investigation of combustion chemistry, diffusion behaviour and interactions of reactants, and the interaction between turbulence and chemistry. Additionally, the IML flame configuration is considered for the 1D unsteady simulations performed in this study which is the best representation of JHC flame configuration (Abtahizadeh et al. 2015, Knikkerr et al. 2003).

As discussed above, the objective of this study is to understand the effects of carbon monoxide addition on MILD methane flames in JHC flame configuration. Since the simulation of real JHC burner geometry is not feasible in DNS, a small model geometry is required. The main criteria of the small model geometry are, its design should replicate the JHC burner geometry and it should be able to capture the reacting flow physics behind the JHC flame configurations. The geometry used in this study is shown in Figure 4.2. Göktolga et al. (2015), Lu et al. (2010), Wang et al. (2007), Luo et al. (2012), and Van Oijen (2013) used a similar or identical geometry for the direct numerical simulation of JHC flames. According to their assessments, this flame geometry is the best representation of JHC burner configuration and its physics. As seen in the figure, the flame geometry consists of a central

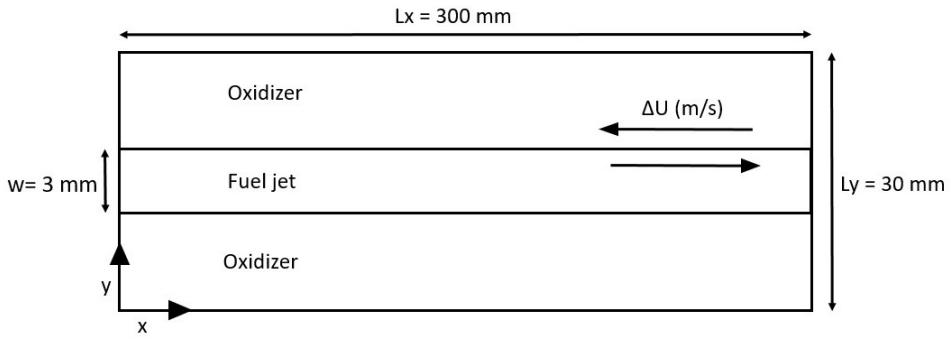

Fig. 4.2 The geometry of the 2D DNS case utilised for the simulations of CH_4 and CH_4/CO cases. Please note that the dimensions of the geomtery are not in scale.

fuel jet sandwiched between oxidiser streams. The central fuel width is set to 3 mm. The streamwise (x-direction) and the transverse (y-direction) dimensions are 300 mm and 30 mm, respectively. The flow direction of fuel and oxidiser streams are opposite to each other. The number of grid points in streamwise and transverse directions is 7689 and 777, respectively. This results in a grid resolution of 39 µm. The boundary conditions and operating conditions of the non-premixed flame cases simulated in this chapter are summarized in Table 4.1.

In this study, two different initial jet Reynolds numbers (1500 and 3870) are used in the DNS of JHC flames. Since the objective of the study is to understand the effects of carbon monoxide addition on turbulent MILD methane flames using DNS, any choice of jet Reynolds number that could help us to achieve this objective is acceptable. Yet, these jet Reynolds numbers are in the range of two of the jet Reynolds numbers used in the JHC experiments by Medwell & Dally (2012*b*). In Section 4.3.1, the results simulated using both the jet Reynolds number are presented and compared to understand the effects of turbulence in ignition delay. However, for the further discussions of results, only the results generated using the jet Reynolds number 1500 are presented and discussed. The reason is, the effects of carbon monoxide on MILD methane flames are more lucid and comprehensible compared to that of the results of jet Reynolds number 3870.

It should be noted that, even though the initial jet Reynolds number of CH_4 and CH_4/CO cases is identical, the main source of the turbulence in this flow configuration is the develop-

ment of shear instabilities and the turbulence levels of the flow field depend on the density difference between fuel and oxidiser stream. To achieve the jet Reynolds number 3870, the relative velocity (ΔU) between fuel and oxidiser is set to 49.77 $\mathrm{m\,s^{-1}}$ (for CH_4 case) and 43.748 $\mathrm{m\,s^{-1}}$ (for CH_4/CO case), while the jet Reynolds number 1500 is achieved by setting the relative velocity between fuel and oxidiser to 19.3 $\mathrm{m\,s^{-1}}$ (for CH_4 case) and 16.3 $\mathrm{m\,s^{-1}}$ (for CH_4/CO case). The fuel jet is perturbed with homogenous isotropic turbulence to trigger instabilities in the shear layers. The turbulence intensity ($u'/\Delta U$) at the fuel jet is set to 0.05 (5%), where, u' corresponds to the root-mean-square (rms) velocity in the fuel jet region ($|y| < 1.5$ mm). The Kolmogorov length scales ($(\nu^3/\varepsilon)^{1/4}$) computed for CH_4 and CH_4/CO cases under the above-mentioned conditions are less than 66 µm for the jet Reynolds number 3870 and 76 µm for the jet Reynolds number 1500 throughout the simulation time, where, ε corresponds to the mean turbulence dissipation rate in the fuel jet region. The grid resolution is approximately 39 µm which is smaller than the Kolmogorov scales. (Moin & Mahesh 1998) stated that the Kolmogorov scale can be resolved if the order of grid resolution is in the same order of Kolmogorov scales. Therefore, in the current study, the grid spacing is fine enough to resolve the Kolmogorov scale. Based on the simulation parameters used in the study, a time step of 10*e*-8 s is chosen to meet the stability criteria. The validity of this choice of timestep is confirmed by the calculation of the CFL number for acoustic waves which is less 1 for all the cases considered in this study.

The initial profiles of temperature and reactants mass fractions of CH_4 and CH_4/CO cases are illustrated in Figure 4.3, respectively, using 1D plots. As mentioned above, laminar 1D IML results are presented and compared with 2D turbulent DNS results. To make this comparison meaningful and quantitative, the initial profiles of 2D DNS cases are created from the initial profiles of 1D IML cases. Moreover, the same grid resolution is considered for 1D IML and 2D DNS cases. However, the number of grid points and domain length considered in 1D IML cases are only half of the respective values considered in the y-direction of 2D

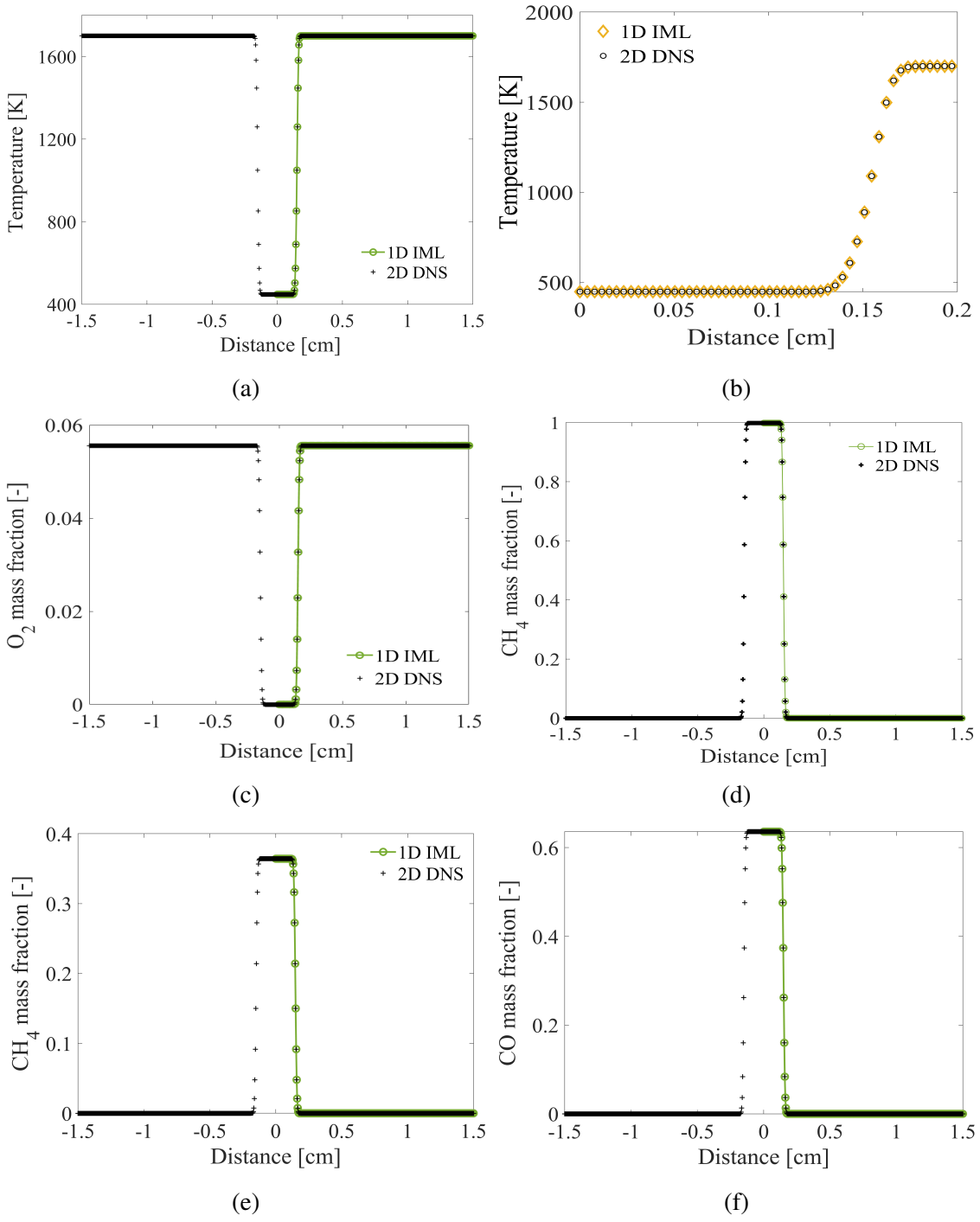

Fig. 4.3 (a) Initial temperature profiles of 1D IML and 2D DNS (both CH_4 and CH_4/CO) plotted across domain width. (b) Initial temperature profiles clipped between 0 cm and 0.2 cm to show that the initial profiles of 2D DNS are created by one-to-one interpolation from the initial profiles of 1D IML cases. (c) Initial profile of O_2 mass fraction of 1D IML and 2D DNS cases of both CH_4 and CH_4/CO cases. Initial profile of (d) CH_4 mass fraction (CH_4 case), (e) CH_4 mass fraction (CH_4/CO case), and (f) CO mass fraction (CH_4/CO case) of 1D IML and 2D DNS cases.

Table 4.1 Boundary conditions and operating conditions of the non-premixed flames.

Fuel composition (molar fraction)	i) CH_4 case: CH_4 - 1.00 ii) CH_4/CO case: CH_4-0.50 CO-0.50
Oxidiser composition (molar fraction)	O_2-0.04847 CO_2-0.072735 H_2O-0.14523 N_2-0.733561
Fuel temperature	448 K
Oxidiser temperature	1700 K
Pressure	1 atm
Domain size ($L_x x L_y$)	300 mm x 30 mm
Number of grid points ($N_x x N_y$)	7689 * 777
Jet Reynolds number	3870 and 1500
Relative velocity between fuel and oxidiser (ΔU) for jet Reynolds number 3870	i) CH_4 case: 49.77 $m\,s^{-1}$ ii) CH_4/CO case: 43.748 $m\,s^{-1}$
Relative velocity between fuel and oxidiser (ΔU) for jet Reynolds number 1500	i) CH_4 case: 19.3 $m\,s^{-1}$ ii) CH_4/CO case: 16.3 $m\,s^{-1}$
Heat loss	None (adiabatic flame)

DNS cases. The reason is, as the 1D IML cases are laminar, symmetry is assumed for 1D IML calculations. Because of turbulence, this symmetry assumption is not appropriate for 2D DNS case, and therefore full flame is simulated. In Figure 4.3 (b), the initial temperature profile clipped between 0 cm and 0.2 cm to show that the initial profiles of 2D DNS cases are indeed created through one-to-one interpolation from the initial profiles of 1D IML cases.

4.2.1 Verification of DNS code and the pre-processing procedures

In this section, the DNS code is verified by plotting the calculated DNS results against the results of the 1D IML calculations. It should be noted that the 1D IML calculations are performed using CHEM1D solver and this solver is validated in Chapter 3 using experimental

Table 4.2 Boundary conditions and operating conditions of the reference DNS case.

Fuel composition	CH_4-100%
Oxidiser composition (molar fraction percentage)	O_2-3% CO_2-5.5% H_2O-6.5% N_2-8.5%
Fuel temperature	298 K
Oxidiser temperature	1700 K
Pressure	1 atm
Heat loss	None (adiabatic flame)
Domain size ($L_x x L_y$)	10 mm x 20 mm
Number of grid points ($N_x x N_y$)	257*521
Fuel jet width	2 mm
Velocity	0 $\mathrm{m\,s^{-1}}$

measurements of flame speeds. For this verification study, a simplified 2D DNS case is considered. The velocity field of the simplified case is set to zero. Therefore, similar to the 1D IML case, the considered 2D DNS problem reduces to a 1D reaction-diffusion problem. Moreover, the operating conditions and simulation parameters are similar for both 1D IML case and 2D DNS case. Hence, the results of the 1D IML simulations can be used to verify the 2D DNS results. The boundary oxidiser composition for these cases is adapted from the experimental work performed by Abtahizadeh et al. (2015). The boundary conditions and simulation parameters are tabulated in Table 4.2.

The contour plots of temperature at time $t = 0$ s and at time $t = 1.5$ ms are shown in Figure 4.4. The figure clearly shows that, at $t = 1.5$ ms, the gradients of temperature are non-zero along the y-axis and zero along the x-axis. That is, during the progress of the reaction, the diffusion of temperature and species took place only in the cross-stream direction and not in the stream-wise direction. Therefore, this proves that the 2D DNS flow problem behaves like a 1D reaction-diffusion problem. In Figure 4.5, the evolution of maximum H mass

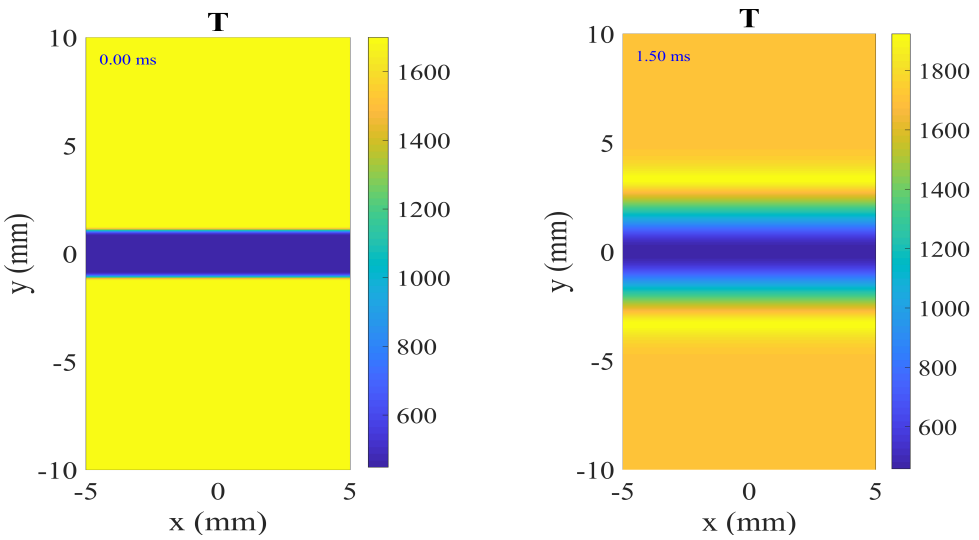

Fig. 4.4 Contour plots of temperature at (a) $t = 0$ s and (b) $t = 1.5$ ms. The plots correspond to 2D DNS reference case to verify the DNS code. The contour plots shows that the gradients along y-direction or the cross-stream direction are non-zero and the gradients along the streamwise direction are zero. This shows that the 2D case behaves like a 1D reaction-diffusion case.

fraction and maximum temperature in the domain of the 2D DNS calculations are plotted against the results calculated using 1D IML simulations. The figure shows an excellent agreement between the 2D DNS results and 1D IML results. Thus, the outcome of the DNS code is as intended. Therefore, the DNS code can be employed for further calculations.

4.3 Results and discussion

4.3.1 Effects of CO addition on ignition characteristics of MILD methane flames

In Figure 4.6, the evolution of maximum H mass fraction in the domain is plotted as a function of time for CH_4 and CH_4/CO flames. For both the cases, the 2D DNS results are plotted against the 1D IML results.

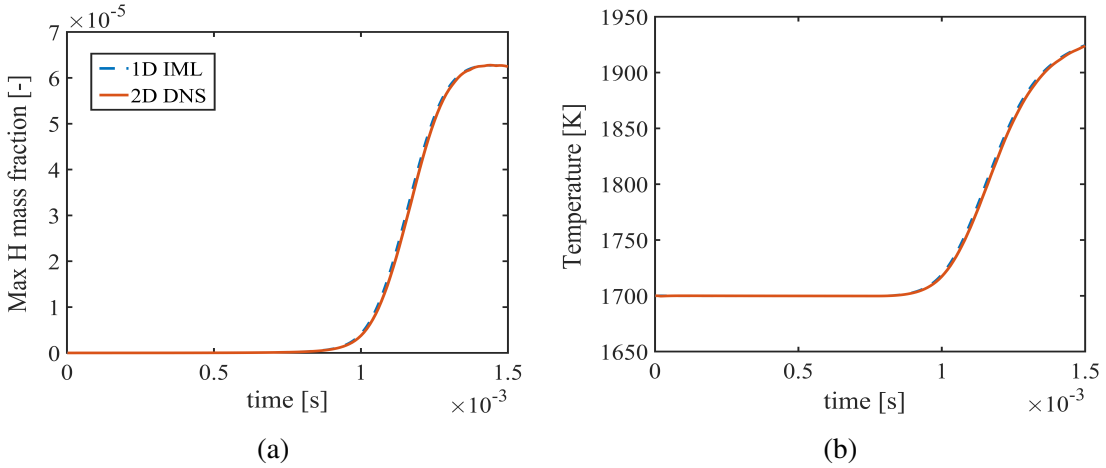

Fig. 4.5 Evolution of (a) maximum H mass fraction and (b) maximum temperature in the domain of the simplified 2D DNS case are plotted against the 1D IML results. It can be seen that the results of 1D IML and 2D DNS are identical.

To calculate the ignition delays (τ_{ign}), as proposed by Echekki & Chen (2003), the maximum H mass fraction is used as the ignition delay marker for both 1D IML and 2D DNS cases. The maximum H mass fraction at the ignition delay is determined using the following procedure. First, a steady frozen mixing solution of fuel and oxidiser is calculated using counterflow diffusion flame configuration. The temperature and species data at various mixture fractions (Z) obtained from the steady frozen mixing solution are used as inputs for the 0D reactor simulations. Using the solutions obtained through 0D reactors calculations at various Z, the most reactive mixture fraction (Z_{mr}) is determined. Z_{mr} is the mixture fraction at which the shortest ignition delay occurs. The ignition delay for the 0D reactor solutions is defined as the time at which the maximum temperature gradient is realised. The corresponding H mass fraction at the time at which the maximum temperature gradient occurs is determined as the H mass fraction at the ignition delay. This H mass fraction value is used as the ignition delay indicator for the 1D IML and 2D DNS cases. The H mass fraction calculated at ignition delay of Z_{mr} of CH_4 and CH_4/CO flames obtained from the 0D reactor solutions is $4.21e-06$ and $2.86e-06$, respectively. The ignition delays determined for CH_4 and CH_4/CO 1D IML flames using the H mass fraction are 1.01 ms and 0.91 ms,

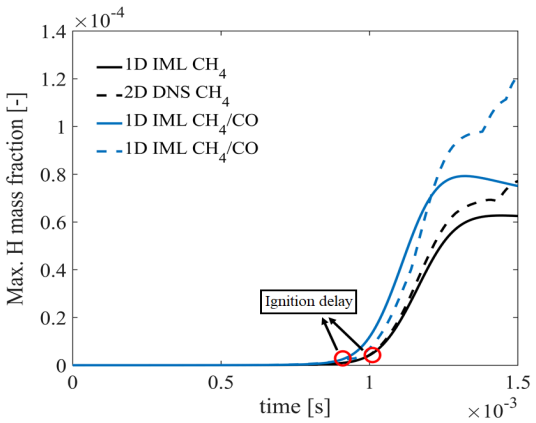

Fig. 4.6 Evolution of maximum H mass fraction in the domain plotted as a function of time for CH_4 and CH_4/CO flames. The continuous line and the dotted line correspond to the 1D IML and 2D DNS results, respectively. The 2D DNS results are calculated using a jet Reynolds number 3870. The ignition delays of the flames are marked with circle marker. The ignition delays calculated for CH_4 and CH_4/CO cases are 1.01 ms and 0.91 ms, respectively.

respectively. This clearly shows that the ignition delay of CH_4/CO flames is about 10 % shorter than that of CH_4 flames. However, it should be noticed that this difference observed here is at a very high oxidiser temperature of 1700 K.

In Table 4.3, the ignition delays of CH_4 and CH_4/CO flames for oxidiser temperatures from 1400 K to 1700 K are listed. The tabulated results correspond to 1D IML flames and they are determined using GRI mechanism. Even though the ignition delay calculated using GRI 3.0 mechanism is different from that of DRM19, alike DRM19, the ignition delay calculated for CH_4/CO flames are shorter than that of CH_4 flames. This shows that the trends predicted by both GRI 3.0 and DRM19 mechanisms agree with each other. Also, the difference in ignition delays increases with decreasing the oxidiser temperature. As is evident above, the addition of carbon monoxide in methane flames shortens the ignition delay. This is clearly due to the increase in the production of H radical in MILD methane flames as a result of the addition of carbon monoxide. This is apparent in Figure 4.6, as H radical starts to build up in CH_4/CO flames earlier than that of CH_4 flames. Moreover, at all the times, the magnitude of H radical formed in CH_4/CO flames is higher than that of CH_4 flames.

Table 4.3 Ignition delays of CH_4 and CH_4/CO flames for oxidiser temperatures from 1400 K to 1700 K. The results correspond to 1D IML flames and are determined using GRI 3.0 mechanism. The results show that the addition of carbon monoxide shortens the ignition delay of MILD methane flames.

T_{ox}	CH_4	CH_4/CO
1400	7.69 ms	6.41 ms
1500	3.48 ms	3.03 ms
1600	1.67 ms	1.54 ms
1700	0.83 ms	0.76 ms

The increase in H radical production due to carbon monoxide addition in MILD methane flames is the result of the increase in the reaction rate of the reaction CO+OH<=>CO_2+H which is due to an increase in carbon monoxide concentration. As mentioned in Chapter 1, one of the main findings of the previous studies is that carbon monoxide addition to premixed methane flames increases its burning velocity (Konnov et al. 2008, Wu et al. 2012, 2009). Furthermore, Wu et al. (2009) concluded that the reaction rate of the reaction CO+OH<=>CO_2+H and the flame temperature increase with an increase in carbon monoxide concentration in the fuel stream of methane flames. Additionally, they revealed that this reaction dominates the overall reaction rate and also most of the positive heat release in the preheated and oxidiser zone is contributed by this reaction. It should be noted that H radical is one of the products of the forward reaction CO+OH<=>CO_2+H and an increase in the reaction rate of this reaction increases H radical production. The discussion shows that the addition of CO increases flame temperature, heat release, and H radical production due to an increase in the reaction rate of the reaction CO+OH<=>CO_2+H. Consequently, the ignition delay of methane flames shortens due to carbon monoxide addition. Moreover, the reaction rate of the reaction CO+OH<=>CO_2+H for the 1D IML CH_4 and CH_4/CO is shown in Figure 4.7. The figure shows that the addition of carbon monoxide increases the reaction rate of the reaction CO+OH<=>CO_2+H. Moreover, the maximum value of the reaction rate

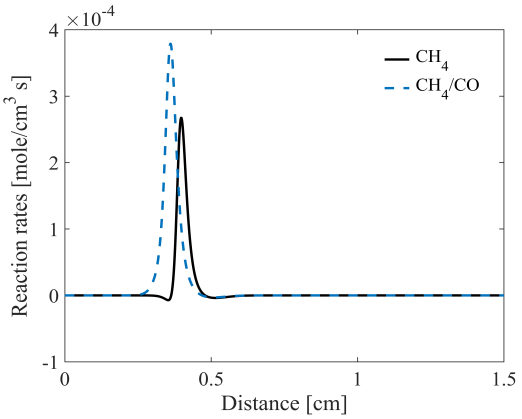

Fig. 4.7 The reaction rates of the reaction CO+OH<=>CO_2+H of 1D IML of CH_4 and CH_4/CO flames plotted as a function of distance. The figure shows that the addition of carbon monoxide increases the reaction rate of the reaction CO+OH<=>CO_2+H. Moreover, the maximum value of the reaction rate of CH_4/CO case is 30% higher than that of CH_4 case.

of CH_4/CO case is 30% higher than that of CH_4 case. Additionally, the small consumption region with negative reaction rate observed in CH_4 case does not exist in CH_4/CO case.

It can be seen in Figure 4.6 that, for both CH_4 and CH_4/CO flames, the ignition delays determined using 1D IML and 2D DNS cases show a good agreement. Moreover, in CH_4 case, the ignition delay determined by 1D IML and 2D DNS are identical, while, in CH_4/CO case, only a 4% difference is observed between the 1D IML and 2D DNS ignition delay results. Also, in Figure 4.6, it can be seen that the evolution of H mass fraction calculated using 2D DNS shows an excellent agreement with the 1D IML result for both cases approximately until 1.2 ms. However, the agreement between 1D IML and 2D DNS results of CH_4 case is better than that of CH_4/CO case. Then, in both cases, the H mass fractions of 2D DNS results are higher than that of 1D IML results after 1.2 ms. The reason is, in the beginning, turbulence is not strong enough to influence the mixing process. Hence, it is mainly controlled by molecular diffusion. Therefore, up to 1.2 ms, the H mass fraction formed in 2D DNS case is similar to that of the 1D IML case. However, beyond 1.2 ms, due to the development of shear instabilities triggered by the velocity differences between the fuel and oxidiser streams, turbulence has grown strong enough to dominate the mixing process of fuel and oxidiser.

Consequently, a higher degree of mixing is realised in 2D DNS case compared to that of the 1D IML case. Subsequently, this speeds up the combustion process of 2D DNS case. As a result, higher levels of intermediate species formation is realised in 2D DNS case. This is reflected in the evolution of maximum H mass fraction. Furthermore, during the investigation of CH_4/H_2 flames under similar conditions considered in this study, a similar trend was observed by Göktolga et al. (2015). Besides, it can be seen that the deviation observed in the ignition delay and evolution of H mass fraction of 1D IML and 2D DNS cases is higher in CH_4/CO flames compared to that of CH_4 flames. The reason is, the replacement of 50% (molar volume) of CH_4 with CO in methane flames increases its fuel jet density by 37%. As a consequence, stronger shear instabilities are realised in CH_4/CO case compared to that of CH_4 case. As already discussed in Section 4.2, the shear instabilities are the source of turbulence in these flame configurations. Thus, the turbulence intensity in the CH_4/CO case would be higher than that of CH_4 case. Due to quicker development of turbulence in CH_4/CO case, discrepancies between 1D IML and 2D DNS results are realised much earlier in CH_4/CO case compared to that of CH_4 case. Also, at 1.5 ms, due to higher levels of turbulence in CH_4/CO, the deviation between H mass fraction calculated by 1D IML and 2D DNS of CH_4/CO case is 38% higher compared to that of CH_4 case.

In Figure 4.8, the evolution of maximum H mass fraction in the domain calculated using 1D IML and 2D DNS cases plotted as a function of time for CH_4 and CH_4/CO flames using a jet Reynolds number (*Re*) of 1500. It can be seen that, when the jet Reynolds number is reduced, the deviations between the ignition delay and the evolution of H mass fraction determined using 1D IML and 2D DNS cases are minimised as a result of lower level of turbulence compared to that of 3870 *jet Re* case. Moreover, unlike the 3870 *jet Re* case, in the 1500 *jet Re* case, the ignition delay predicted by 1D IML and 2D DNS is identical even for the CH_4/CO case. This corroborates the above discussion that the higher deviation observed in CH_4/CO case is due to the higher level of turbulence realised in CH_4/CO case

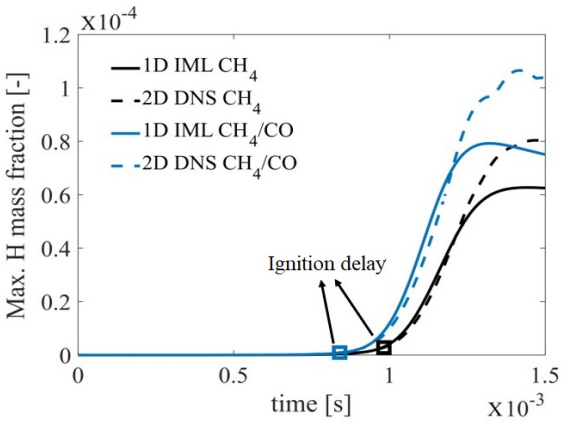

Fig. 4.8 Evolution of maximum H mass fraction in the domain calculated using 1D IML and 2D DNS cases plotted as a function of time for CH_4 and CH_4/CO flames. The 2D DNS results are calculated using a jet Reynolds number 1500. The ignition delay is marked using square marker. The results show that, when the jet Reynolds number is reduced (compared to Figure 4.6), the deviations between the results of 1D IML and 2D DNS cases are minimised.

compared to that of CH_4 case. Moreover, in 1500 *jet Re* case, the deviation between H mass fraction calculated by 1D IML and 2D DNS of CH_4/CO case is only 9% higher compared to that of CH_4 case.

As discussed above, the ignition delay and evolution of maximum H mass fraction predicted by 2D DNS case shows a good agreement with 1D IML case. This shows that with a careful choice of simulation parameters, Flamelet Generated Manifold (FGM) model developed using IML flamelet solutions can be used to predict the ignition delay stage or stages where the mixing process is governed by molecular diffusion of the MILD CH_4 and CH_4/CO flames for the flame configuration considered in this study. However, the consideration of IML based FGM model for the prediction of flame stages where turbulence governs the mixing process (e.g. post flame development stage) might impose several modelling challenges.

In Figure 4.9, the conditional means and scatter plots of H mass fraction and scalar dissipation rate (χ), calculated using the relation $(\chi =)2D\left(\frac{\partial Z}{\partial x_i}\frac{\partial Z}{\partial x_i}\right)$, are plotted for both CH_4 and CH_4/CO cases during the induction phase (t=0.85 ms). The variable D corresponds to the diffusivity coefficient of the scalar. For clarity, the plots are shown close to stoichiometric

mixture fraction. The mixture fraction range shown in the figure corresponds to the shear layers region where mixing and reaction between fuel and oxidiser take place. Z_{mr} calculated for CH_4 and CH_4/CO cases are 0.0021 and 0.0035, respectively. For both cases, Z_{mr} is less than Z_{st} and lies close to the oxidiser stream. It can be seen in Figure 4.9 (a) and Figure 4.9 (b) that during the induction phase, the peak of the mean H mass fraction occurs at mixture fraction close to Z_{mr}. This explains the reason behind the induction of reaction at Z_{mr}. Apart from this, from Figures 4.9 (c) and (d), it can be seen that Z_{mr} is located in a region with very low scalar dissipation rate which is favourable for the induction of the ignition process. Moreover, this agrees with the findings of Göktolga et al. (2015) in which they observed that induction of reaction started at Z_{mr} located at low scalar dissipation regions.

As expected, the conditional mean plots of H mass fraction clearly shows that the mean H mass fraction of CH_4/CO case is higher than that of CH_4 case (refer to Figures 4.9 (a) and (b)). Also, the scattering of H radical is stronger in CH_4/CO case compared to that of CH_4 case. However, close to Z_{mr}, the lower limit of H radical in the scatter plots are almost same in both cases, and the upper limit is higher in CH_4/CO compared to that of CH_4 case. The reason for the stronger scattering of H radical observed in CH_4/CO case is due to the higher density of the fuel stream. Addition of CO in CH_4 increases the density of the fuel mixture. Since density difference between fuel and oxidiser streams in CH_4/CO case is higher than that of CH_4 case, the instabilities triggered at the jet shear layers are stronger in CH_4/CO case compared to that of CH_4 case. Therefore, the turbulence level at the shear layers of CH_4/CO case is higher than that of CH_4 case. As a consequence, stronger scattering of H radical is observed in CH_4/CO case compared to that of CH_4 case.

Apart from the above-mentioned consequence, the higher density of fuel stream of CH_4/CO case results in higher scalar dissipation rate compared to that of CH_4 case. This is apparent in Figure 4.9 (c) and Figure 4.9 (d). The mean scalar dissipation rate of CH_4/CO case is almost five times greater than that of CH_4 case at all values of (Z/Z_{st}) greater than

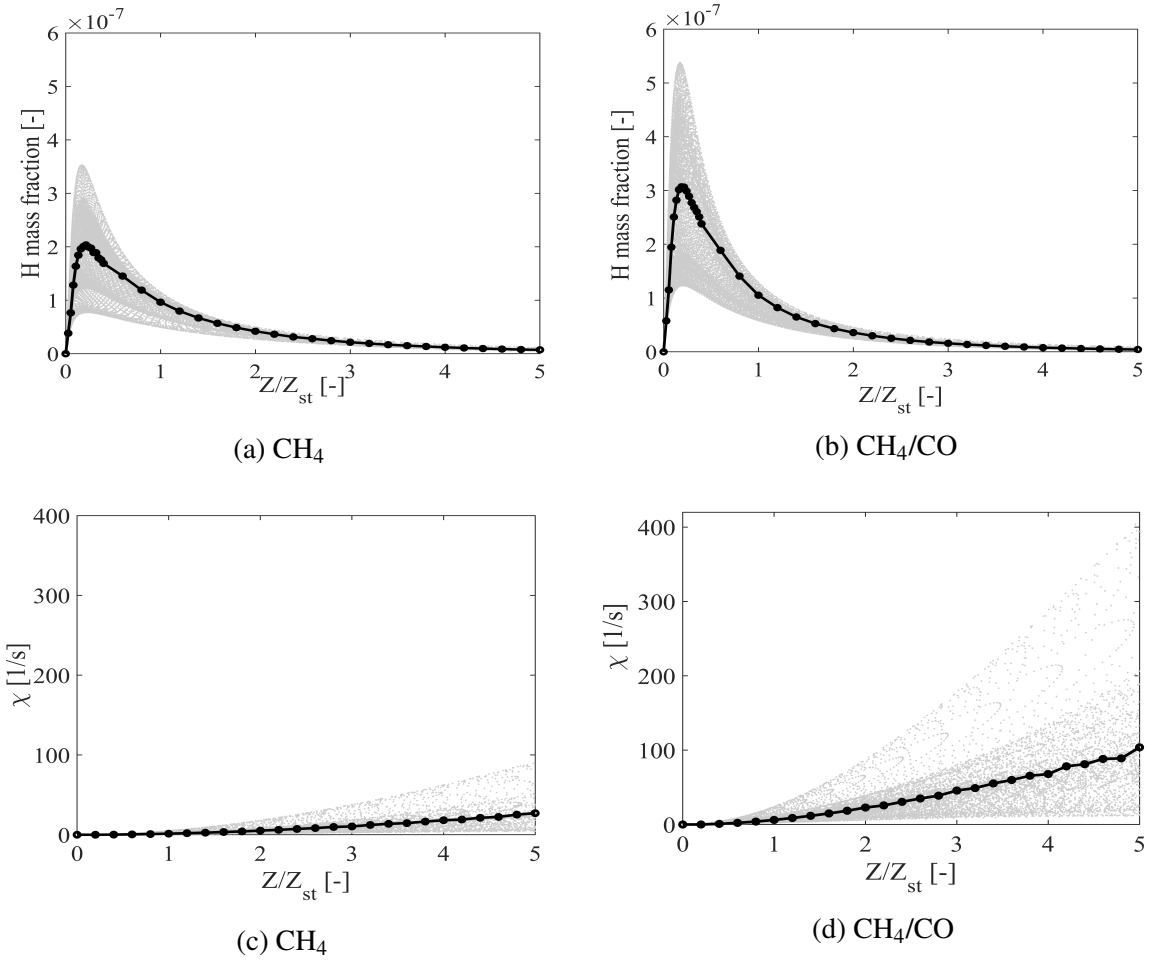

(a) CH_4 (b) CH_4/CO

(c) CH_4 (d) CH_4/CO

Fig. 4.9 Conditional means (•) and scatter plots (light dots) of Y_H (top) and log χ (bottom) plotted as a function of mixture fraction for CH_4 and CH_4/CO cases plotted at t=0.85 ms (close to ignition time). For clarity, the plots are shown only close to the stoichiometric mixture fraction. The plots show that the addition of carbon monoxide increases the mean scalar dissipation rate of CH_4 flames by approximately five times.

0.5. The scalar dissipation rate plays an important role in the non-premixed combustion process. The scalar dissipation rate indicates the rate at which molecular diffusion processes lead to micro-scale mixing of fuel and oxidiser molecules. Higher scalar dissipation rate means stronger mixing of fuel and oxidiser molecules which leads to accelerated combustion reactions. Even though the scalar dissipation rate of CH_4/CO case is higher than that of CH_4 case, it can be seen that the effect of higher scalar dissipation rate on the ignition delay and combustion process of the CH_4/CO flames is not realisable during the induction phase. Moreover, the shorter ignition delay observed in CH_4/CO case compared to that of CH_4 case is mainly influenced by chemistry (the higher H mass fraction) and the initial profiles of species and temperature, and not because of higher scalar dissipation rate resulted due to high density of the fuel stream. The reason is, in the current study, as seen in Section 4.2, nominal profile (step function) is used to create the initial species and temperature profiles. That means, at the intersection of fuel and oxidiser streams, the temperature abruptly changes from 448 K to 1700 K. This is the case for species distribution and other thermochemical properties distribution as well. As a result of using the nominal profile, the scalar dissipation rate is very large ($>> 10^3$) at time $t = 0$ s. Therefore, once the simulation begins, due to this large scalar dissipation rate, the fuel molecules come in contact with the high-temperature oxidiser molecules in a fraction of a millisecond. Thus, in both CH_4 and CH_4/CO cases, the ignition delay is strongly influenced by the chemistry and scalar dissipation rate resulted due to the nominal profile. Then, as the mixing of fuel and oxidiser progresses with time, the nominal profiles of temperature and species diminish. As a consequence, the high scalar dissipation decays with the progress of the mixing process. The decay of scalar dissipation continues and approaches the scalar dissipation values resulted due to the density difference between fuel and oxidiser stream, and turbulence. In addition, as already discussed above, it can be seen in Figure 4.6, the H mass fractions calculated from 1D IML case and 2D DNS case show an excellent agreement until 1.2 ms. And the effect of turbulence is realised after

1.2 ms. Therefore, the influence of the scalar dissipation rate on the combustion reactions due to the density difference between fuel stream and oxidiser stream might be realisable at times greater than 1.2 ms. In addition, the significance of higher scalar dissipation rate on the combustion process of CH_4/CO flames compared to that of CH_4 case could be realised if heat-loss effects of hot oxidiser to cold fuel are considered in the initial temperature profiles.

4.3.2 Effects of CO addition on flame structure of MILD methane flames

The contour plots of important intermediate species of CH_4 and CH_4/CO flames are shown in Figure 4.10 to provide a visual comparison. The contour plots are plotted at 0.4 ms post ignition delay; $\tau_{ign} + 0.4$ ms of CH_4 and CH_4/CO flames are 1.4 ms and 1.31 ms, respectively. $\tau_{ign} + 0.4$ ms is chosen, because, as observed in the figure, a continuous layer of intermediates species are formed in the reaction zone that are suitable for the comparison analysis. The contour plots of CH_4/CO flames at 1.4 ms are presented as a compliment. As seen in Figure 4.10, the contour plots of three intermediate species such as H, OH, and CH_2O are plotted. For clarity, the contour plots are clipped between negative and positive fifteen millimetres in the stream-wise direction (x-axis).

The plot shows that, in general, based on the intermediate species distribution, no significant difference is observed between the flame shapes. However, intermediate species profiles are different in those flames. The H contour profiles of CH_4/CO flames are brighter than that of CH_4 flames. On the other hand, the CH_2O contours at the shear layers of CH_4 flames are much brighter and thicker than that of CH_4/CO flames. The CH_2O contours of CH_4 flames are also brighter and thicker than that of CH_4/CO flames plotted at 1.4 ms. The distribution of CH_2O inside the fuel stream is also higher in CH_4 flames compared to that of CH_4/CO flames. The contours of OH at the shear layers of both flames are almost similar. In

both the flames, the formation of H and OH is only observed in the jet shear layers; unlike CH_2O, they are not diffused or formed inside the fuel stream.

The contour plots only provide a qualitative comparison between CH_4 and CH_4/CO flames. For a quantitative comparison, the spatial averages of intermediate species of CH_4 and CH_4/CO flames are plotted at $\tau_{ign} + 0.4$ ms and they are shown in Figure 4.11. The trends observed in the spatial averages agree with the trends observed in the contour plots. As observed in the contour plots, the H mass fractions of CH_4/CO flames are 25% higher than that of CH_4 flames. On the other hand, the CH_2O mass fraction of CH_4 flames is higher than that of CH_4/CO flames. In spatial averages plots, it is clear that CH_2O molecules are observed inside the fuel stream. Especially, a significant amount of CH_2O is formed or diffused inside the fuel stream. Apart from that, the spatial average plots show that the peaks of the CH_2O profiles are slightly inward and closer compared to the peaks of other intermediates species. This agrees with the findings in Göktolga et al. (2015) for CH_4/H_2.

In Medwell et al. (2007), they observed a reduction in reaction rates at the regions of low O_2 levels which subsequently weakened the reaction zones. These weak reaction zones lead to the formation of partially premixed zones, which was evident through the presence of CH_2O molecules. The mass fraction plots of CH_2O and O_2 conditioned on mixture fraction are plotted at $\tau_{ign} + 0.4$ ms for CH_4 and CH_4/CO flames, please refer to Figure 4.12. The figure clearly shows that, in both CH_4 and CH_4/CO flames, a significant amount of O_2 is diffused into the fuel stream. Moreover, the presence of CH_2O in the fuel stream is due to the diffusion of O_2 into the fuel stream and indicates partial premixing zones. This behaviour of CH_4 and CH_4/CO flames agrees with the observation made in Medwell et al. (2007). Also, similar to the observations made in Figure 4.10 and Figure 4.11, Figure 4.12 shows that, the formation of CH_2O inside the fuel stream is higher in CH_4 flames compared to that of CO added CH_4 flames. The reasons is, as discussed in Subsection 3.3.3, the reaction pathway for the formation of CH_2O radical is CH_4-CH_3-CH_3O-CH_2O. It can be seen that the formation

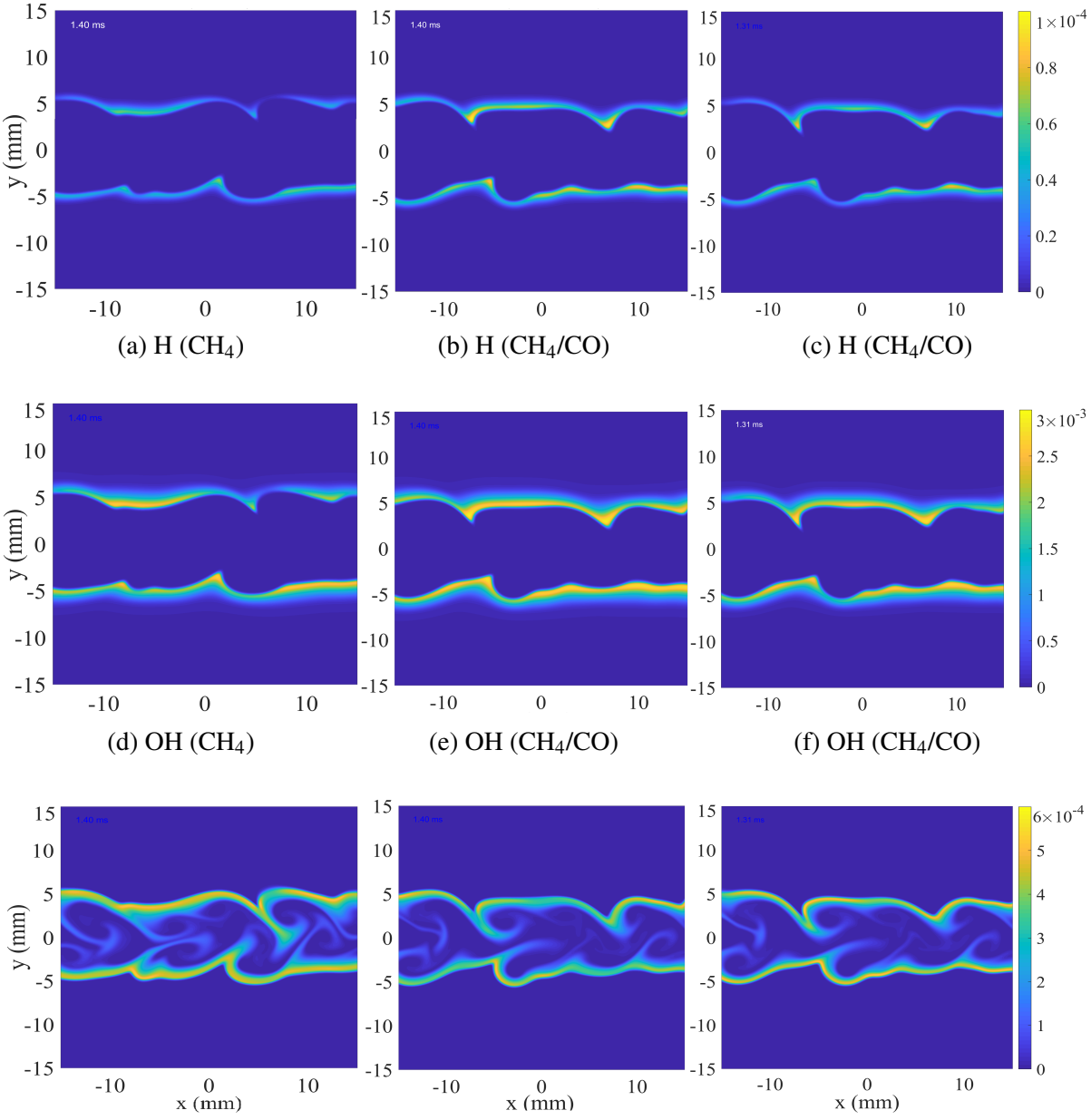

(a) H (CH_4) (b) H (CH_4/CO) (c) H (CH_4/CO)

(d) OH (CH_4) (e) OH (CH_4/CO) (f) OH (CH_4/CO)

(g) CH_2O (CH_4) (h) CH_2O (CH_4/CO) (i) CH_2O (CH_4/CO)

$\tau_{ign}+0.4$ ms (1.4 ms) 1.4 ms $\tau_{ign}+0.4$ ms (1.31 ms)

Fig. 4.10 Contour plots of important intermediate species of CH_4 (right) and CH_4/CO (left) flames plotted at $\tau_{ign}+0.4$ ms. The contour plots of CH_4/CO (middle) flames at 1.4 ms are presented as a compliment. A visual comparison of the contour plots show that the flame structure of CH_4 and CH_4/CO flames look very similar to each other.

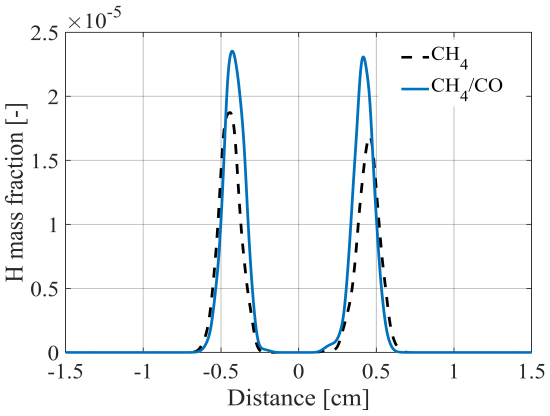

(a) H

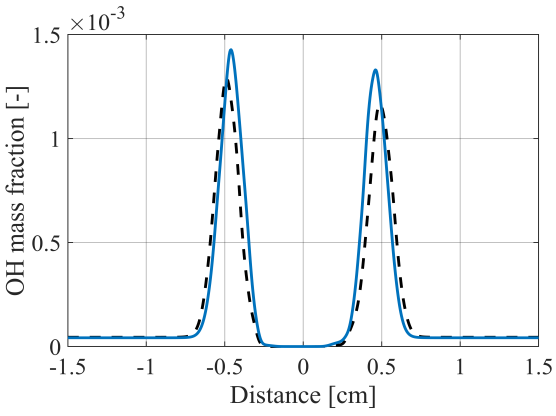

(b) OH

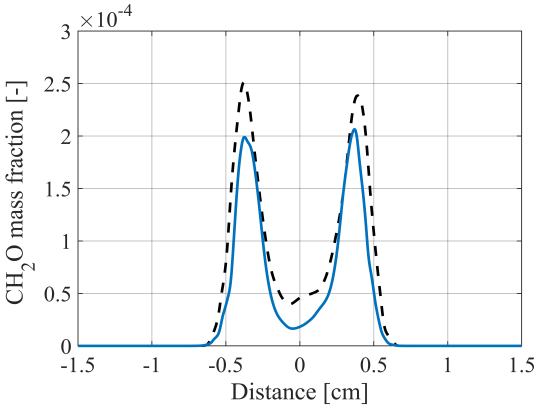

(c) CH_2O

Fig. 4.11 Spatial averages of intermediate species such as (a) H, (b) OH, and (c) CH_2O of CH_4 and CH_4/CO flames plotted at $\tau_{ign} + 0.4$ ms. Figure (a) clearly shows that the addition of carbon monoxide in MILD methane flames results in a higher H mass fraction. The OH mass fraction of CH_4/CO flames are also slightly higher than that of CH_4 flames. However, the CH_2O mass fraction of CH_4/CO case is slightly smaller than CH_4 case.

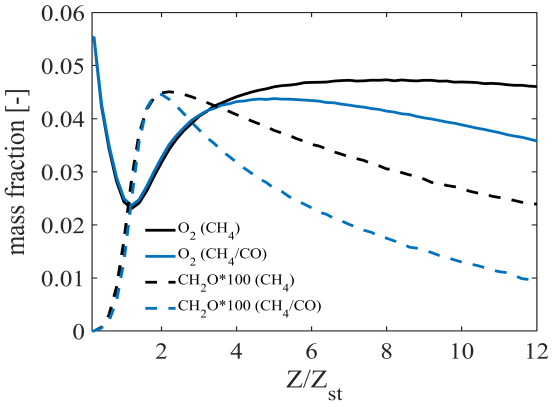

Fig. 4.12 Mass fractions of O_2 and CH_2O conditionally averaged on mixture fraction plotted at regions closer to stoichiometric mixture fraction Z_{st}. The figure shows that O_2 and CH_2O mass fractions in the fuel jet region is higher in CH_4 flames compared to that of CH_4/CO flames. Also, it can be seen that the formation of CH_2O is due to the penetration of O_2 inside the fuel stream.

of CH_2O is from the CH_4 molecules. Therefore, the addition of CO in CH_4 flames reduces the CH_4 concentration, and as a result, the CH_2O concentration inside the fuel stream in CH_4/CO flames is lower than that of CH_4 flames. In adddition, the diffusion of O_2 molecules into the fuel streams is lower in case of CH_4/CO case compared to that of CH_4 case which further reduces the formation of CH_2O.

4.3.3 Effects of transport models on MILD CH_4 and CH_4/CO flames

The significance of preferential diffusion effects on ignition characteristics of CH_4 and CH_4/CO flames are evaluated in this section. For this purpose, 2D direct numerical simulations are performed using unity Lewis number and constant Lewis number assumptions.

In Figure 4.13, the unity Lewis number results are plotted against the constant Lewis number results. The 2D direct numerical simulation results are supplemented with 1D IML results. Figure 4.13 (a) shows that, for CH_4 flames, the ignition delay and the evolution of maximum H mass fractions calculated using unity Lewis number and constant lewis number assumptions show an excellent agreement. However, Figure 4.13 (b) shows that, in case of

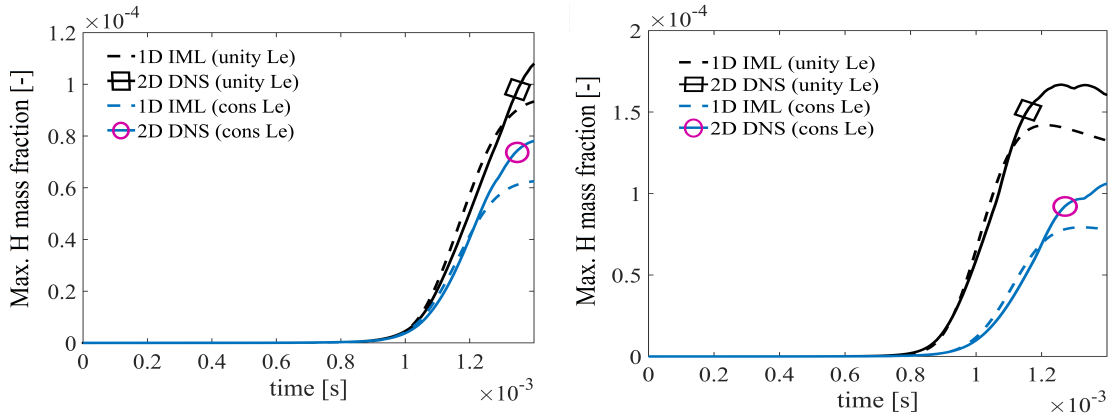

Fig. 4.13 Evolution of maximum H mass fraction of (a) CH_4 and (b) CH_4/CO flames calculated using unity Lewis number and Constant Lewis number assumptions. The dashed line and the solid line correspond to the 1D IML and 2D DNS cases, respectively. The figure shows that the unity Lewis number assumption results differs significantly from that of constant Lewis number results of CH_4/CO flames. This shows preferential diffusion effects become significant when carbon monoxide is added in CH_4 flames.

CH_4/CO flames, the ignition delay and the evolution of maximum H mass fractions calculated using unity Lewis number differ significantly from the results of constant Lewis number assumption. Also, unity Lewis number assumption results in earlier ignition. The difference between maximum H fractions calculated using unity Lewis number assumption and constant Lewis number assumption increases with time which is 45% at 1.5 ms. The evolution of maximum H mass fractions of CH_4/CO flames is calculated using GRI 3.0 with complex, constant Lewis number assumption and unity Lewis number assumption transport models, and the results are plotted in Figure 4.14. The figure shows that, even though the maximum H mass fraction values differ from that of the values calculated using DRM19 mechanism, alike DRM19 results, the unity Lewis number assumption results in earlier ignition and higher H mass fraction values compared to that of other transport models. The reason for earlier ignition is explained as follow. The addition of CO in CH_4 flames increases the forward reaction rate of CO+OH<=>CO_2+H thereby increasing the H radical production. Because of the unity Lewis number assumption, the produced H radical accumulates in the reaction

zone. The accumulation of H radical accelerates the ignition process. In contrast, in constant Lewis number case, because of the high diffusivity of H radical, the produced H radical

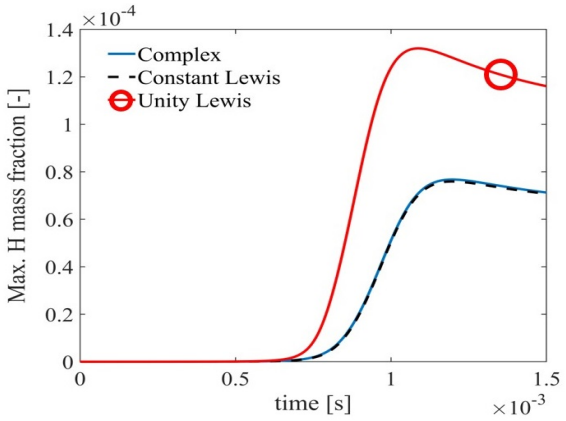

Fig. 4.14 Evolution of H mass fraction of CH_4/CO case calculated using GRI 3.0 mechanism with three different transport models such as complex, constant Lewis, and unity Lewis number assumptions.

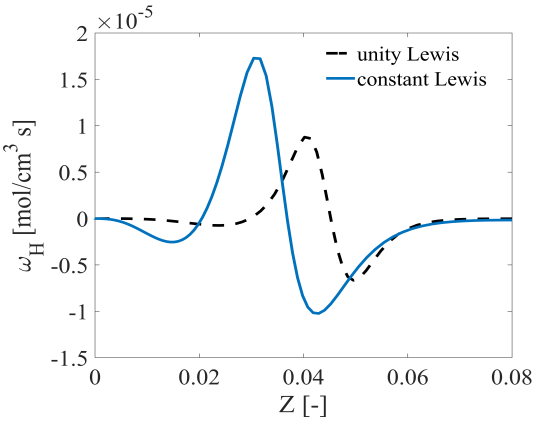

Fig. 4.15 Source term of H radical plotted as a function of mixture fraction for steady counterflow diffusion flames with unity and constant Lewis number transport model. The figure shows that the consumption zone of H radical in constant Lewis number case is much broader than that of unity Lewis number case.

quickly diffuses away from the reaction zone. As a consequence, the ignition delay and maximum H mass fraction observed in the constant Lewis number case is significantly smaller than that of unity Lewis number case. The source terms of H radical calculated using steady counterflow diffusion flames with unity and constant Lewis number assumptions

are plotted to show the higher diffusivity of H radical in the constant Lewis number case, please refer to Figure 4.15. The figure clearly shows that, in constant Lewis number case, the consumption zone of H radical is much broader than that of unity Lewis number case. This shows that the diffusion of H radical in constant Lewis number case is higher than that of unity Lewis number case.

4.4 Conclusions

The effects of carbon monoxide addition on (1D and 2D) MILD methane flames were investigated using direct numerical simulations results. The direct numerical simulations were performed using IML (1D cases) and JHC (2D cases) flame configurations. The DNS codes CHEM1D and DiSco were chosen to perform the 1D- and 2D- direct numerical simulations, respectively. A 2D geometry that represents the JHC flame configuration was chosen for the simulations of 2D cases. The chemical mechanism, oxidiser composition, and other simulation parameters were adapted from Abtahizadeh et al. (2017). For the DNS cases, a temperature as high as 1700 K was considered for oxidiser stream. To investigate the effects of carbon monoxide addition to adiabatic MILD methane flames, simulations were performed with fuel stream consists of pure methane and methane/carbon monoxide mixtures, and the results were compared. Finally, the possibilities of the development of IML based FGM model for modelling adiabatic MILD methane flames enriched with carbon monoxide was also evaluated and discussed. Heat loss effects were not considered. With these, the objectives 1, 2, 3 and 7 relevant to carbon monoxide addition to adiabatic MILD methane flames are addressed. By addressing these objectives, the combustion characteristics of non-premixed MILD methane flames enriched with carbon monoxide are analysed.

The main conclusions derived from this chapter are explained as follows; the addition of carbon monoxide in methane flames shortens the ignition delay of the methane flames. Also, the difference in ignition delay between CH_4 and CH_4/CO flames increases with decreasing

oxidiser temperature, and the difference is as high as 1.28 ms at oxidiser temperature 1400 K. The addition of carbon monoxide on methane flames increases the H radical concentration by almost 25% at the flame development stage and slightly decreases the CH_2O in the reacting mixture. However, the effects on other intermediate species formation is insignificant. The addition of carbon monoxide on methane flames increases its scalar dissipation rate by approximately five times. In case of methane flames, the results calculated with unity Lewis number assumption agrees with complex transport models and constant Lewis number assumption. However, the addition of carbon monoxide in methane flames makes preferential diffusion important, and the agreement between the unity Lewis number results and constant Lewis number results is poor. Moreover, at 1.5 ms, the difference between the maximum H mass fraction determined using unity Lewis and constant Lewis number assumption is as much as 45%. For both CH_4 and CH_4/CO cases, the IML based FGM can be used for the prediction of ignition stages or the stages where the mixing process is governed by molecular diffusion. However, the consideration of IML based FGM model for the prediction of flame stages where turbulence governs the mixing process (e.g. post flame development stage) might impose several modelling challenges. It should be noted that, in case of CH_4/CO flames, preferential diffusional effects cannot be neglected during the model development process.

It should be noted that, most of the unsteady simulations were performed with DRM19 mechanism whose accuracy is lower than that of GRI Mech 3.0 and USC Mech II at these high oxidizer temperature. However, the findings of DRM19 are supported with GRI 3.0 wherever it is necessary. Also, the trends predicted by DRM19 agrees with the trends predicted by GRI Mech 3.0. Apart from this, some conclusions mentioned above are derived from the 2D DNS results. As 2D turbulence energy cascade and turbulence decay mechanism are different from that of 3D turbulence. As a result, scalar dissipation rate in 3D turbulent flow might be different than that of 2D turbulence which could increase ignition delay and

effect post-flame behaviour. However, the trends predicted using 2D turbulence results are expected to be the same as of that 3D turbulence cases (for example, carbon monoxide addition reduces ignition delay). Moreover, this is validated in the next chapter where the results of 2D and 3D DNS are compared. Also, the conclusions derived in this chapter is based on analysing the effects of CO addition to CH_4 flames, however, the findings can be related to all hydrocarbon flames and can be used to get a glimpse on what would happen to these flames upon carbon monoxide addition.

Chapter 5. DNS of CO enriched non-adiabatic MILD CH_4 flames

5.1 Overview

The investigations of this chapter are performed using MILD flames with the inclusion of heat loss effects. In this chapter, firstly, the numerical methods and simulations set-up that are employed for performing the direct numerical simulations of non-adiabatic MILD flames are explained. Secondly, the effects of heat loss on the ignition delay of MILD flames are discussed. The effects of turbulence on the ignition delay of non-adiabatic MILD flames are also discussed. Thirdly, the effects of carbon monoxide addition on the ignition delay, mixing and flame characteristics of non-adiabatic MILD methane flames are discussed. Additionally, the possibility for the development of IML based FGM model for the prediction of non-adiabatic MILD CH_4 and CH_4/CO flames are discussed. Then, importance of preferential diffusion in non-adiabatic MILD flames are investigated by the comparison of the results of unity Lewis number and constant Lewis number assumption transport models. Next, the effects of carbon monoxide addition on the oxidation pathways of MILD methane flames are analysed using quantitative reaction path diagrams. Finally, the important findings and conclusions drawn are summarised.

5.2 Numerical methods and simulation setup

The effects of CO addition on MILD CH_4 JHC flames with the inclusion of heat loss effects are analysed using direct numerical simulations. Since the primary goal of the study conducted in this chapter is to understand the effects of the inclusion of heat loss on MILD

flames, only the temperature profile is altered to include the heat loss effects. The initial species profile, boundary conditions and operating conditions are kept identical to the DNS cases considered in Chapter 4. However, the thermodynamic properties such as density and enthalpy are calculated to match the temperature profile. The boundary conditions and operating conditions used for the DNS calculations of this chapter are listed in Table 5.1. The geometry and its dimensions considered in the 2D DNS calculations of Chapter 4 are retained for the 2D DNS calculations performed in this chapter, please refer to Figure 4.2. For 3D DNS calculations, the width of the fuel jet and the oxidiser channel (or the width (y-direction) of the geometry) are kept similar to that of 2D DNS case considered in Chapter 4. On the other hand, the length of the geometry or the length in the x-direction is decreased to 10 mm and the depth of the geometry (z-direction) is set to 5 mm. The dimensions of the geometry considered for 3D DNS calculations of this chapter are listed in Table 5.2. The reasons for choosing 10 mm as the length of the geometry for 3D DNS calculations are explained as follow. The total number of grid points of the 3D DNS geometry for the dimensions mentioned in Table 5.2 is about 26.5 million (N_xxN_yxN_z = 265x777x129), and the computational time is about 35 days with the available resources for the estimated simulation time (=2.5 ms). For a 300 mm domain length in the x-axis, the required number of grid points would be around 800 million, and with the available resource, the expected computation time would be approximately 3 years for the estimated simulation time (= 2.5 ms) which is not practically possible for the current thesis. The effects of domain size are plotted on the ignition delay of adiabatic 2D DNS CH_4 case dealt in Chapter 4 is shown in Figure 5.1. The figure shows the effect of domain length on ignition delay is insignificant. The ignition delay predicted in 2D DNS calculations with the domain length 300 mm and 50 mm is 1.01 ms and 1.03 ms, respectively. As is evident above, the difference in ignition delay predicted by the 2D DNS cases (300 mm and 50 mm) is less than 2 %. Hence, a domain length of 10

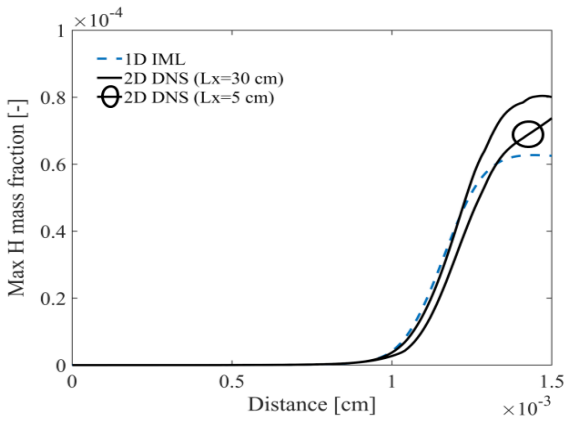

Fig. 5.1 Evolution of maximum H mass fraction in the domain plotted as a function of time for CH_4 flames. The effect of the choice of domain size (Lx = 5 cm and 30 cm) has been analysed using the 2D DNS case with jet Reynolds number 1500. The results of the 2D DNS cases are plotted against the 1D IML result. As is evident in the figure, the difference in ignition delay predicted by the 2D DNS cases (300 mm and 50 mm) is less than 2 %.

mm is chosen for all the 3D DNS calculations performed in this chapter which is expected to provide reliable accuracy.

The geometry and its dimensions considered for the 3D DNS calculations performed in this chapter is illustrated in Figure 5.2. On the other hand, the computation time of 2D DNS case even with a 300 mm domain length is expected to be approximately eight days for the estimated simulation time (= 2.5 ms) which is very much feasible with the available computational resources. Therefore, for all the 2D DNS calculations, similar to the calculations of the previous chapter, the domain length is set to 300 mm.

The varying temperature profile considered in the present investigation is shown in Figure 5.3 (1D plot) and Figure 5.4 (2D plot). In addition to the varying temperature profile, the nominal temperature profile (without the inclusion of heat loss) which is used in Chapter 4 is presented for a visual qualitative comparison. Alike Chapter 4, direct numerical simulations are performed using the same DNS code (Bastiaans, Somers & de Lange 2001, Groot 2003, Van Oijen, Bastiaans & De Goey 2007) and 1D simulations are performed using CHEM1D (Somers 1994). The reaction pathway analysis is performed using CHEMKIN Reaction Path Analyser (*ANSYS Chemkin Theory Manual 17.0 (15151)* 2015). Again, DRM19 chemical

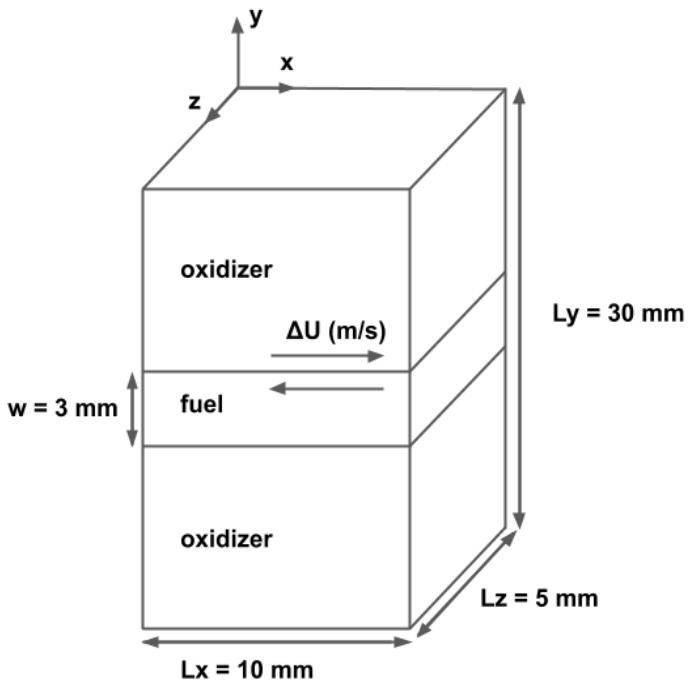

Fig. 5.2 Illustration of the geometry of the 3D DNS case considered for the calculations of CH_4 and CH_4/CO cases with the inclusion of heat loss. Please note that the geometry is not scaled.

Table 5.1 Boundary conditions and operating conditions of the non-premixed flames.

Fuel composition (molar fraction)	i) CH_4 case: CH_4 - 1.00 ii) CH_4/CO case: CH_4 - 0.50 CO - 0.50
Oxidiser composition (molar fraction)	O_2 - 0.04847 CO_2 - 0.072735 H_2O - 0.14523 N_2 - 0.733561
Fuel temperature	448 K
Oxidiser temperature	1700 K
Pressure	1 atm
Jet Reynolds number	3870
Relative velocity between fuel and oxidiser (ΔU)	i) CH_4 case: 49.77 $m\,s^{-1}$ ii) CH_4/CO case: 43.748 $m\,s^{-1}$
Heat loss	Variable temperature profile

Table 5.2 Dimensions of the geometry considered for the 2D DNS and 3D DNS calculations.

	2D DNS	3D DNS
Domain size	300 mm *x* 30 mm (L_x *x* L_y)	10 mm *x* 30 mm *x* 5 mm (L_x *x* L_y *x* L_z)
Number of grid points	7689*x*777 ($N_x x N_y$)	265*x*777*x*129 ($N_x x N_y x N_z$)

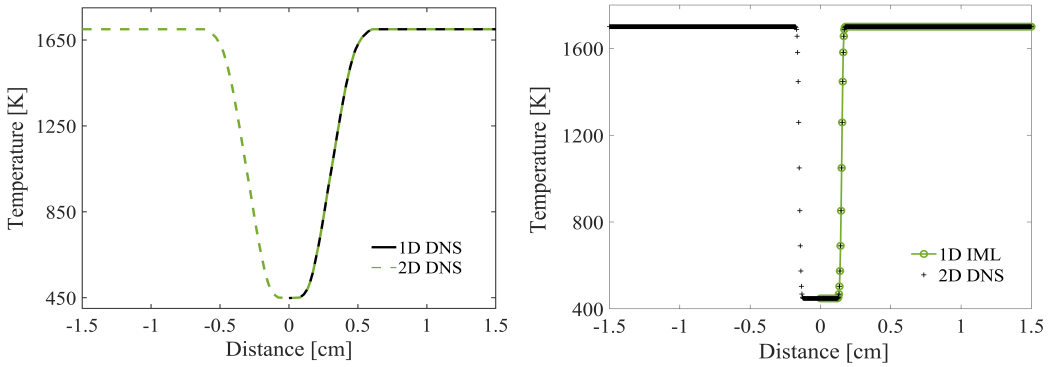

(a) (b)

Fig. 5.3 (a) One dimensional plot of the initial temperature profile (t = 0 ms) considered in the present study to model heat loss (on the left). As is seen in the figure, a varying temperature profile is used to model heat loss effects. (b) One dimensional plot of the nominal temperature profile without heat loss which is used in Chapter 4 (on the right) is presented for a visual qualitative comparison.

mechanism (Kazakov & Frenklach 1994) is used for the simulation of DNS cases. Since DRM19 chemical mechanism is a reduced mechanism, it is not appropriate for reaction pathway analysis. Therefore, the reaction pathway analysis is performed using Curran mechanism (Burke et al. 2015).

5.3 Results

5.3.1 Ignition characteristics of non-adiabatic MILD flames

In this section, the effects of heat loss and turbulence on ignition delay of MILD flames are investigated. The effects of CO addition on the ignition delay of MILD methane flames with

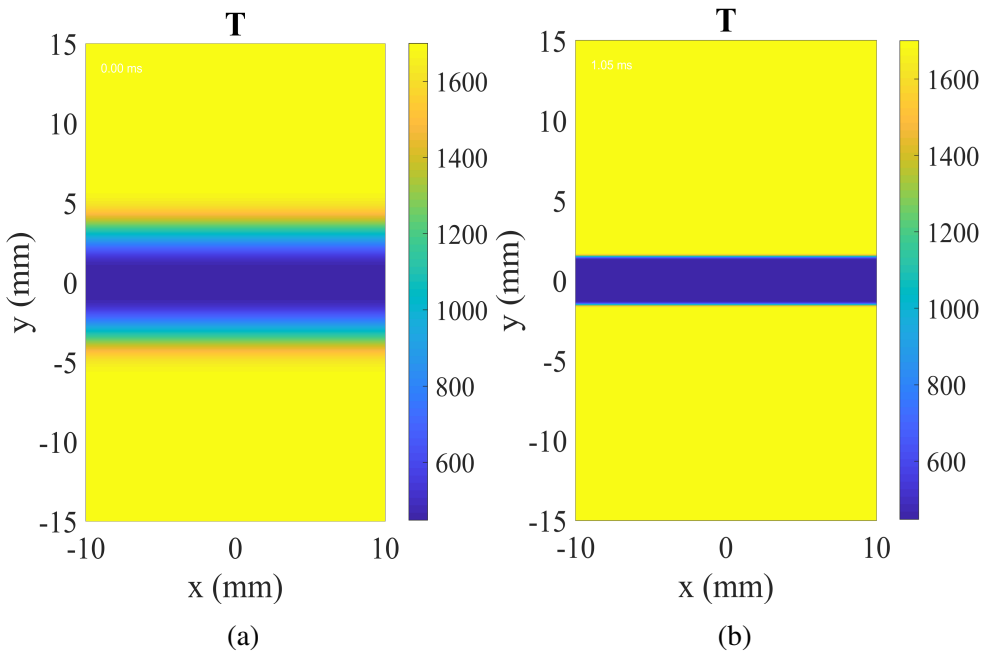

Fig. 5.4 Contour plot of the initial the initial temperature profile (t = 0 ms) considered in the present study to model heat loss (on the left). As is seen in the figure, a varying temperature profile is used to model heat loss effects. (b) Contour plot of the nominal temperature profile without heat loss which is used in Chapter 4 (on the right) is presented for a visual qualitative comparison.

the inclusion of heat loss are also investigated. The ignition delay results of 2D DNS results versus 3D DNS results and 1D DNS results versus 3D DNS results are plotted in Figure 5.5.

Alike Section 4.3, the maximum H mass fraction is used as the ignition delay marker for the MILD flames with the inclusion of heat loss. In general, the most reactive mixture fraction Z_{mr} lies close to the maximum domain temperature. Hence, a 10 K to 50 K rise in maximum domain temperature can be used as an ignition marker. However, such a definition for ignition marker is not suitable for the cases considered in this study. The reason is, due to the varying temperature profile considered in the generation of initial profile and the occurrence of extensive mixing before ignition, Z_{mr} lies far away from the maximum temperature. Since the temperature of Z_{mr} is much less than 1700 K, even if the ignition events begin at Z_{mr} and increases its temperature, the maximum temperature of the domain would remain the same even after a 10 K or 50 K temperature rise at Z_{mr}. Hence, a definition

Table 5.3 Ignition delays predicted using the maximum H mass fraction values for 2D DNS and 3D DNS cases of CH_4 and CH_4/CO MILD flames with the inclusion of heat loss.

	1D IML/2D DNS (adiabatic)	2D DNS (heat loss)	3D DNS (heat loss)
CH_4	1.01 ms	1.58 ms	2.12 ms
CH_4/CO	0.91 ms	1.5 ms	1.92 ms

based on temperature rise would result in an inaccurate ignition delay value. As proposed by Echekki & Chen (2003), the maximum H mass fraction is used as an ignition marker. The procedure followed to calculate the ignition delay is same as the procedure followed in Chapter 4. However, for the convenience of the readers, the explanation of the procedure is provided again.

First, using counterflow diffusion flame configuration, a steady frozen mixing solution of fuel and oxidiser is obtained. The temperature and species data of all the grid points in mixture fraction space are used as input for the 0D reaction simulations. In the solutions of the 0D reactor simulations, the mixture fraction with the shortest ignition delay is identified as Z_{mr}. The ignition delay for the 0D reactor solutions is defined as the time at which the maximum temperature gradient is realised. The corresponding H mass fraction at the time of maximum temperature gradient is determined as the H mass fraction at the ignition delay. This H mass fraction value obtained from 0D calculations is used as an ignition delay indicator for the MILD flames with the inclusion of heat loss. The H mass fraction calculated at ignition delay of Z_{mr} of CH_4 and CH_4/CO flames obtained from the 0D reactor solutions are $4.21e-6$ and $2.86e-06$, respectively.

Based on the evolution of maximum H mass fraction plots in Figure 5.5, the ignition delay values calculated for 2D DNS and 3D DNS cases of CH_4 and CH_4/CO are listed in Table 5.3. The ignition delay values predicted for adiabatic cases of CH_4 and CH_4/CO are also listed for comparison purpose. As is seen in Chapter 4, in adiabatic flames, ignition delay predicted for 1D IML and 2D DNS with turbulent flow resulted in same values.

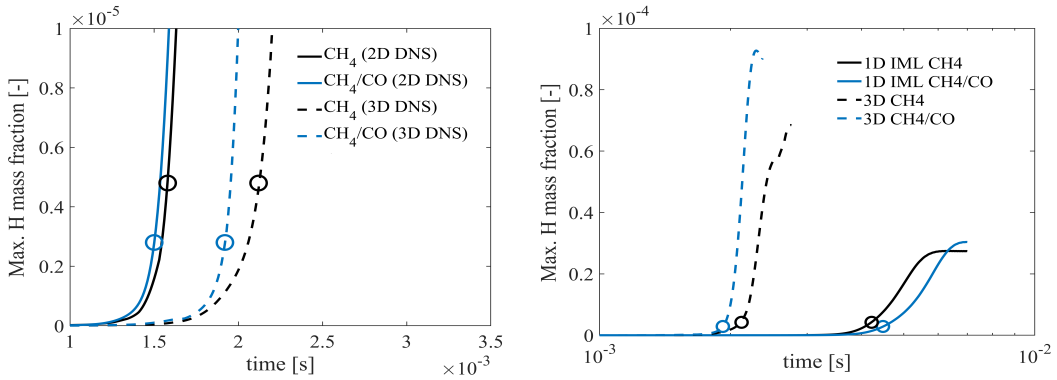

(a) (b)

Fig. 5.5 Evolutions of maximum H mass fraction in the domain plotted as a function of time for CH_4 and CH_4/CO flames, where (a) 2D DNS cases versus the 3D DNS cases (left),and (b) 1D DNS cases versus 3D DNS cases (right). The black and blue lines correspond to the results of CH_4 and CH_4/CO cases, respectively. The circle markers indicate the ignition delay of the respective cases of the data line on which it is marked. The results show that, for both CH_4 and CH_4/CO cases, the increase in turbulence levels shortens the ignition delay.

I. Effects of heat loss on ignition delay

Ignition delay values in Table 5.3 clearly show that the inclusion of heat loss significantly lengthened the ignition events to occur. In 2D DNS cases, due to the effects of heat loss, in both CH_4 and CH_4/CO cases, ignition delay increases by approximately 60%. On the other hand, in the case of 3D DNS cases, the ignition delay of CH_4 and CH_4/CO cases increases by approximately 100%.

The reason is, for the ignition events to occur or begin, firstly, the completely separated low-temperature fuel and the high-temperature oxidiser should come in contact at a molecular level which takes place as a result of the mixing process. Due to the mixing process, pockets of mixtures of fuel and oxidiser with various mixture fraction values occur at the intersection (the shear layers) of fuel and oxidiser stream. As previously discussed, the ignition starts at the pockets of mixtures with mixture fraction Z_{mr}. In MILD flames with the inclusion of heat loss, the heat loss is modelled using a varying temperature profile, and the temperature increases from the fuel stream to the oxidiser stream in a gradual manner. As a result, even

though the pockets with mixture fraction Z_{mr} are formed after the beginning of the mixing process, the temperatures of those pockets formed in the MILD flames with the inclusion of heat loss is lesser than the temperatures of such pockets formed in MILD flames without heat loss (adiabatic). Because, in MILD flames without heat loss, the temperature profile is a step function (as discussed in Chapter 4), and as a result, the temperature of the mixture pockets formed at the intersection would be closer to the maximum domain temperature. According to the Arrhenius equation, with mixtures with the same composition, the reaction rate of the high-temperature mixture would be higher than that of the low-temperature mixture. Therefore, the reaction rate of the mixture pockets with mixture fraction Z_{mr} formed in MILD flames with the inclusion of heat loss is lesser than that of the mixture pockets with mixture fraction Z_{mr} formed in adiabatic MILD flames. Because of the slower reaction rate at Z_{mr}, longer ignition delays are realised in MILD flames with the inclusion of heat loss compared to that of adiabatic MILD flames.

II. Effects of turbulence on ignition delay

It can be noticed in Table 5.3 that even though both 2D DNS and 3D DNS calculations are performed with the same turbulence intensity levels, and same initial jet Reynolds number, in both CH_4 and CH_4/CO cases, the ignition delay predicted using 2D DNS calculations are about 30% shorter than the ignition delay predicted using 3D DNS calculations. The reason behind these discrepancies that arise from the characteristics of 2D turbulence. In actuality, the interaction among turbulent eddies of various scales passes the kinetic energy of the turbulent flow sequentially from the larger eddies gradually to the smaller ones, and finally, the kinetic energy dissipates in the form of heat due to viscous forces at Kolmogorov scales. This process is known as turbulent energy cascade (Mathieu & Scott 2000). In 3D DNS, the energy cascade process and the dissipation of turbulent kinetic energy take place in the same mode as described above or as the same mode as the actuality. As a result, in

3D turbulence, the turbulence intensity level or simply the flow turbulence decreases with time. To sustain turbulence in the 3D flow, kinetic energy must be supplied to the large-scale eddies continuously through external means. However, on the other hand, in 2D DNS, the energy transfer takes place to the large-scale eddies from the small-scale eddies which means the turbulent kinetic energy sequentially passes from the small scale eddies to the large scale eddies during their interactions with each other, and the process is called as inverse energy cascade (Alexakis & Biferale 2018). As a result, in 2D turbulence, the flow turbulence increases with time. Therefore, even though the 2D and 3D DNS are initiated with same turbulence intensity level and jet Reynolds number, at a given point in time, the turbulence level in 2D DNS cases is higher than that of 3D DNS case. Consequently, the degree of mixing in 2D DNS cases is higher than that of 3D DNS cases. As a result of accelerated mixing in 2D DNS cases, the ignition events beginning to occur earlier in 2D DNS cases compared to that of 3D DNS cases. The contours plots of mixture fraction of 2D DNS and 3D DNS (CH_4/CO) cases at 1.5 ms are plotted in Figure 5.6. The contour plots clearly show that the width of the mixing layers in 2D DNS case is about 35% larger than that of 3D DNS cases which is the result of accelerated mixing due to higher flow turbulence levels in 2D DNS case compared to that of 3D DNS case, and this refers to a deeper penetration of fuel molecules into the oxidiser stream which favours the ignition process.

The above discussion clearly shows that, for MILD flames with the inclusion of heat loss, the increase in flow turbulence shortens the ignition delay. Moreover, this is very apparent in Figure 5.5 (b), where, in 3D DNS case, in case of both CH_4 and CH_4/CO flames, the ignition delay is shortened by 50% compared to that of 1D IML case due to the accelerated mixing process as a result of turbulence, while the mixing process in 1D IML flames is governed by the molecular diffusion process. Hence, the FGM model developed using 1D IML flame solution is not suitable for the prediction of the ignition delay of non-adiabatic MILD flames. It should be noted that, in case of adiabatic flames, as discussed in Chapter 4, the ignition

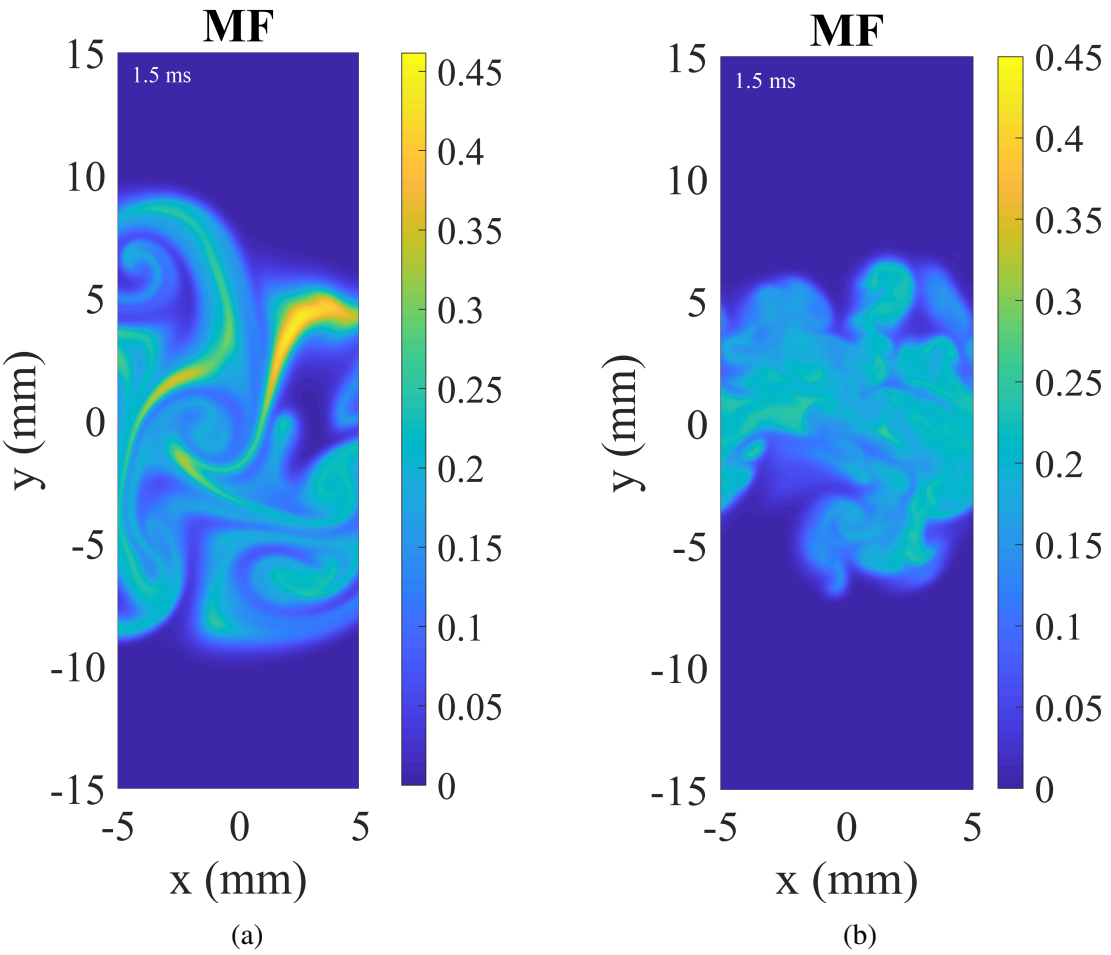

Fig. 5.6 Contour plots of mixture fraction of (a) 2D DNS case (left) and (b) 3D DNS case (right) of CH_4/CO MILD flames plotted at 1.5 ms. The figures show that, even though the 2D DNS and 3D DNS calculations are initiated with same turbulence intensity and jet Reynolds number, the width of mixing layers of 2D DNS case is about 35% larger than that of 3D DNS case as a result of higher flow turbulence in 2D DNS case.

delay predicted using 1D IML and 2D DNS (with turbulence) calculations are the same. This shows that in the absence of heat loss, the ignition delay is government by molecular diffusion and chemical kinetics.

III. Effects of carbon monoxide addition on ignition delay

Figure 5.5 (a) shows that the addition of carbon monoxide in MILD methane flames reduces its ignition delay by about 0.09 ms in 2D DNS calculations and 0.2 ms in 3D DNS calculations. It should be noted that these differences are for oxidiser temperature 1700 K, and as seen in Chapter 4, decreasing the oxidiser temperature under the circumstances of heat loss would increase the differences between the ignition delay of CH_4 and CH_4/CO flames. This clearly shows that the addition of carbon monoxide in turbulent MILD methane flames shortens the ignition delay, and this behaviour agrees with the observations made in the 2D DNS results of Chapter 4. Again, as seen in Chapter 4, the reason for the shorter ignition delay observed in the carbon monoxide enriched methane flames is, the CO addition increases the reaction rate of CO+OH<=>H+CO_2, consequently, the H radical production is accelerated. This leads to a shorter ignition delay.

Apart from this, it should be noted in Figure 5.5 that the difference in ignition delay predicted between CH_4 and CH_4/CO flames using 2D DNS calculations is shorter than that of the difference in ignition delay predicted in 3D DNS calculations. The reason is, in addition to turbulence, molecular diffusion also influences the mixing process. Since the flow turbulence levels are lower in 3D DNS than that of 2D DNS, the molecular diffusion effects on the mixing process are more pronounced in 3D DNS cases compared to that of 2D DNS cases. Further discussion on the effects of molecular diffusion is investigated in Section 5.3.2.

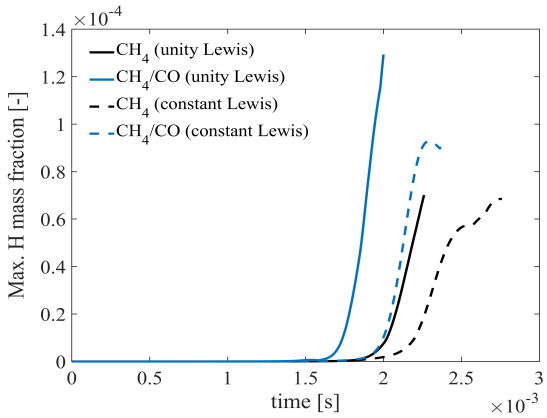

Fig. 5.7 Evolutions of H mass fraction of CH_4 and CH_4/CO cases calculated using two different transport models such as unity Lewis number assumption and constant Lewis number assumption.

5.3.2 Effects of preferential diffusion

The importance of preferential diffusional effects on the ignition behaviour of MILD CH_4 and CH_4/CO flames are analysed in this section. As mentioned earlier, 2D DNS results are presented only for comparison purposes. Because of the inverse energy cascade of 2D turbulence, such a scenario is usually not possible in actuality. In MILD flames with the inclusion of heat loss, turbulence is one of the major parameters that governs the ignition characteristics. Therefore, for preferential diffusion analysis, 2D DNS results are not appropriate. Hence, 3D DNS results are considered for preferential diffusion analysis. For that purpose, 3D direct numerical simulations are performed for CH_4 and CH_4/CO cases, with unity Lewis number assumption and constant Lewis assumption, and the results are compared.

The evolution of H mass fraction calculated using unity Lewis and constant Lewis number assumptions for the flames considered in this study are plotted in Figure 5.7. The results clearly show that in both CH_4 and CH_4/CO flames, the unity lewis number assumption results in an earlier ignition (or shortens the ignition delay τ_{ign}). The unity Lewis number assumption shortens the ignition delay by 7.5% and 13% in CH_4 and CH_4/CO flames, respectively. Post

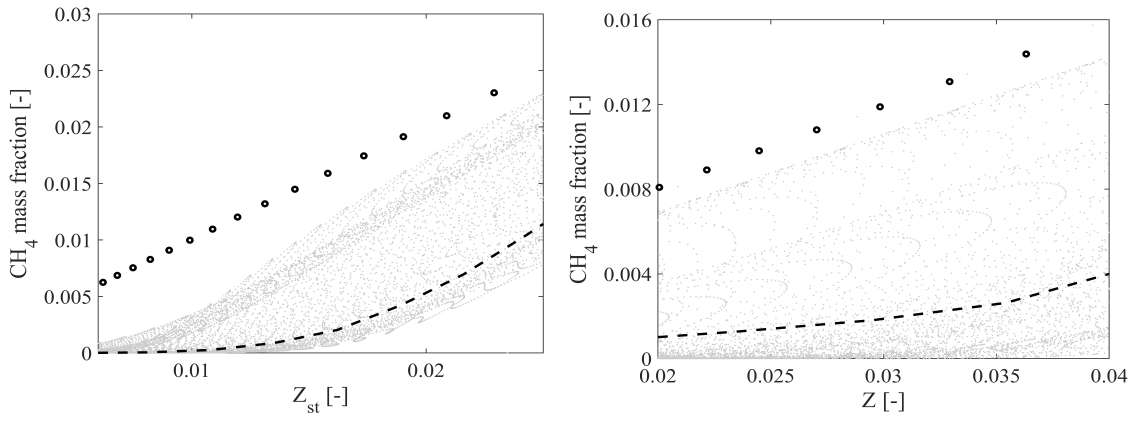

Fig. 5.8 Scatter plots (light dots) and conditional plots (dashed lines) of CH_4 mass fractions of (a) CH_4 (left) and (b) CH_4/CO (right) flames plotted around stoichiometric mixture fractions at $\tau_{ign} + 0.4$ ms. The line (circle dot) corresponds to the 1D laminar mixing solutions obtained using constant Lewis number assumption. The plots show that the scattering of CH_4 in CH_4/CO flames are higher than that of CH_4 flames. Additionally, even though mixing behaviour of both the flames are different from 1D mixing behaviour, the mixing characteristics of CH_4/CO flames are closer to 1D mixing characteristics compared to that of CH_4 flames.

the ignition stage, the discrepancies between the H mass fractions predicted between the unity Lewis number results and constant Lewis number results increases with time and with the flame development process. The trends observed in the CH_4/CO flames and the discrepancies observed in the H mass fractions during the post ignition stage between unity Lewis number and constant Lewis number assumptions are consistent with the observations made in Chapter 4. However, the trends observed in the CH_4 flames with the inclusion of heat loss are conflicting with the trends observed in the adiabatic CH_4 flames in Chapter 4. In case of adiabatic CH_4 flames, the preferential diffusion effects seem to be negligible, and the results of unity Lewis number assumption and constant Lewis number assumption agreed well with each other until 1.2 ms, and discrepancies started to occur beyond 1.2 ms when turbulence started to govern the mixing process. With the inclusion of heat loss, since the turbulence starts to dominate the mixing process even at the ignition stage, the preferential diffusion effects become realisable in CH_4 flames during the ignition phase itself.

Additionally, the discrepancies increase with time during the flame development post the ignition stage. Again, the discrepancies between unity Lewis number and constant Lewis number assumptions arise due to the hydrogen radical that are formed during the combustion process. In case of constant Lewis number cases, H radicals that are formed diffuses away from the reaction zone. However, in case of unity Lewis number cases, H radical that are formed build up in the reaction zone which accelerates the reaction rate. Hence, the ignition delay of unity Lewis number case is shorter than that of constant Lewis number case. When turbulent dominate the mixing process, a higher degree of mixing is realised compared to that of molecular diffusion dominated mixing. As a result, the H radical production is higher than that of the H radical produced as a result of molecular diffusion dominated mixing process. Hence, the discrepancies realised between the unity Lewis and constant Lewis number assumptions of non-adiabatic cases (where turbulence governs mixing) are higher than that of the discrepancies realised in adiabatic cases (where molecular diffusion governs mixing) at ignition stage.

In Figure 5.7, the discrepancies observed between the unity Lewis number assumption and constant Lewis number assumption in the CH_4/CO case is higher than that of CH_4 case. That means, the preferential diffusion effects are higher in CH_4/CO case is higher than that of CH_4 case. In Figure 5.8, scatter plots (dots) and conditional plots (dotted line) of CH_4 mass fractions of (a) CH_4 (left) and CH_4/CO (right) flames plotted around stoichiometric mixture fractions at $\tau_{ign} + 0.4$ ms. The line (dotted circle) corresponds to the 1D laminar mixing solutions obtained using constant Lewis number assumption. The plots show that the scattering of CH_4 in CH_4/CO flames is higher than that of CH_4 flames. Additionally, even though mixing behaviour of both the flames is different from 1D mixing behaviour, the mixing characteristics of CH_4/CO flames are closer to 1D mixing characteristics compared to that of CH_4 flames. This show that the preferential diffusional effects are more pronounced in CH_4/CO flames compared to that of CH_4 flames.

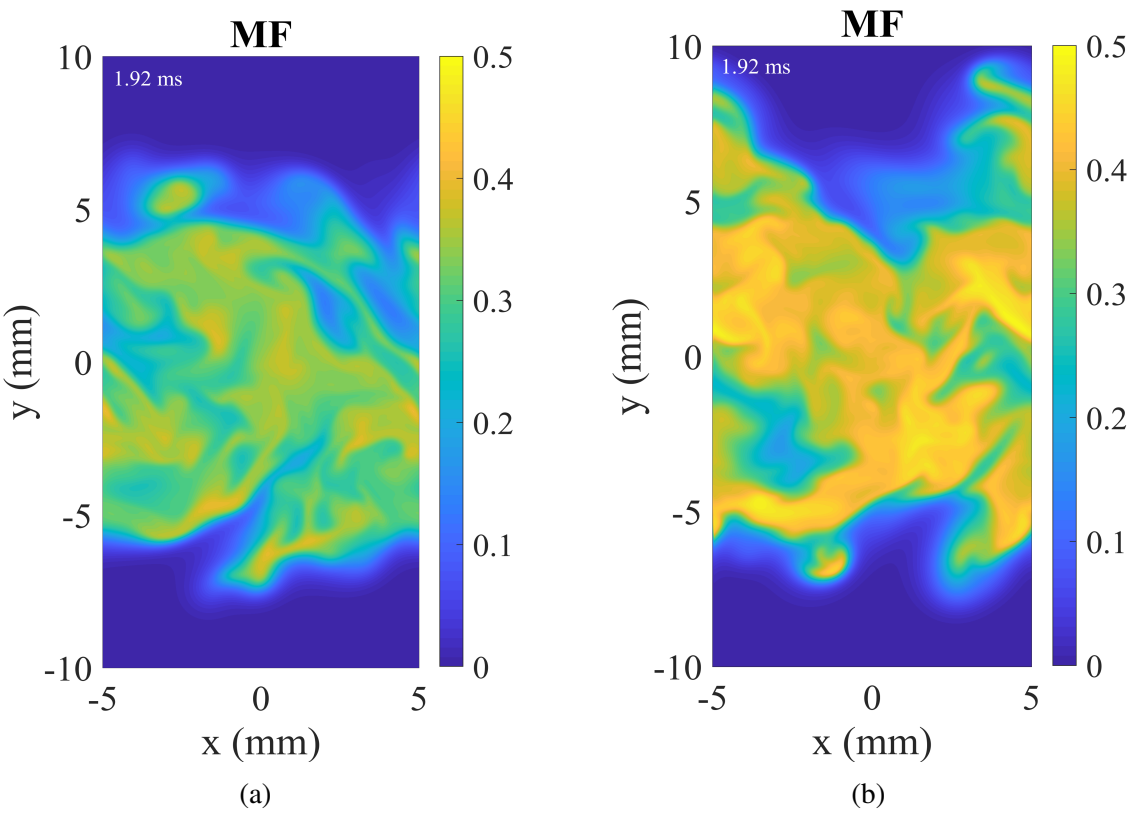

Fig. 5.9 Contour plots of mixture fraction of 3D DNS case of (a) CH_4 (left) and (b) CH_4/CO (right) flames plotted at 1.92 ms. The figure shows that the addition of carbon monoxide in MILD methane flames increases its jet mixing area (by 10%).

5.3.3 Effects of CO addition on mixing

In Figure 5.9, the mixture fraction snapshots of CH_4 and CH_4/CO cases are plotted to show the effects of carbon monoxide addition on the mixing of MILD CH_4 flames. The snapshots are taken at $z = 0$ mm, and at time 1.92 ms. It is apparent from the figure that the mixing zone of CH_4/CO flames is larger than that of CH_4 flames. At the location $z = 0$ mm, the carbon monoxide addition increases the mixing zone area by 13%. When considering the entire domain, the carbon monoxide addition increases the mixing zone area by an average value of 10%.

In Figure 5.10, the distribution of the scalar dissipation rate (χ) of CH_4 and CH_4/CO flames around the stoichiometric mixture fraction (Z_{st}) are shown at time 1.92 ms. The scalar

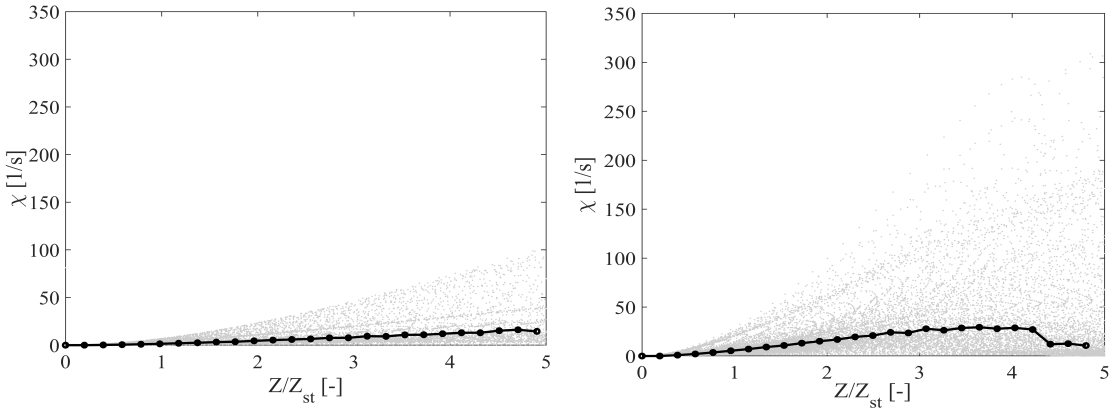

Fig. 5.10 The scatter (light dots) and conditional plots (•) of scalar dissipation rate (χ) plotted at 1.92 ms for (a) CH_4 (left) and (b) CH_4/CO (right) flames. The plot shows that the mean χ of CH_4/CO flames is almost double the mean χ of CH_4 flames. Additionally, the maximum values of χ of CH_4/CO flames is almost three times higher than that of CH_4 flames.

dissipation rate is calculated using the relation $(\chi =)2D\left(\frac{\partial Z}{\partial x_i}\frac{\partial Z}{\partial x_i}\right)$ for the mixture fraction data shown in Figure 5.9, where D corresponds to the diffusion coefficient of the scalar. The dots correspond to the scatter plot and the dotted line corresponds to the conditional mean of scalar dissipation rate conditioned on mixture fraction. The plots clearly show that the addition of carbon monoxide increases the scalar dissipation rate. Moreover, the conditional mean plots show that the carbon monoxide addition on CH_4 flames doubles the average scalar dissipation rate close to Z_{st}. Additionally, the scatter plot shows that the maximum values of the scalar dissipation rate of carbon monoxide enriched CH_4 flames are almost three times greater than that of the CH_4 flames. The increase in the scalar dissipation rate is due to the higher fuel jet density of CH_4/CO flames. Furthermore, the higher scalar dissipation rate observed in CH_4/CO flames is the reason for the higher jet mixing width observed in them.

5.3.4 Flame characteristics

In Figure 5.11, the contour plots of intermediate species H, OH, O, and CH_2O are plotted for both CH_4 and CH_4/CO cases. The plots are plotted at location $z = 0$ mm and at time

$\tau_{ign} + 0.4$ ms. Time $\tau_{ign} + 0.4$ ms is chosen, because, 0.4 ms after τ_{ign}, a continuous layer of intermediate species are formed which is the indication of flame development, please refer to Figure 5.11. The plots show that alike the adiabatic MILD flames, in MILD flames with the inclusion of heat loss, the flames are developed at the shear layers. Even though a high degree of mixing takes place before the beginning of ignition events, Z_{st} and Z_{mr} occur at the shear layers, and the ignition events begin at the shear layers followed by the flame development at the shear layers.

The contour plots show that both CH_4 and CH_4/CO flames look alike, and no significant difference is observed between them. However, the CH_2O levels are slightly higher in the fuel jet stream of CH_4 flames compared to that of CH_4/CO flames. This observation is similar to that of adiabatic flames.

The contour plots only provide a qualitative comparison. Therefore, in Figure 5.12, the conditional mean plots of intermediate species such as H, OH, O and CH_2O are plotted to provide a quantitative comparison of CH_4 and CH_4/CO flames. The plots show the average values of intermediate species conditioned on mixture fraction at $z = 0$ mm and at time $\tau_{ign} + 0.4$ ms. Since the flame is realised at shear layers or the regions close to Z_{st}, the conditional plots are shown only at mixture fractions close to the stoichiometric mixture fraction. Moreover, even in Figure 5.12, it can be seen that the intermediate species takes the maximum values at the Z/Z_{st} close to 1 and reduces beyond $Z/Z_{st} = 1$. The conditional plots show that the addition of carbon monoxide on CH_4 flames increases the mass fractions of H, OH, and O, while it slightly decreases the mass fractions of CH_2O. Especially, the peak of the mean H mass fraction of CH_4/CO flames is twice that of CH_4 flames. This shows that, even though the addition of carbon monoxide in CH_4 flames does not affect the flame structure, the levels of intermediate species formed in CH_4 flames are significantly affected.

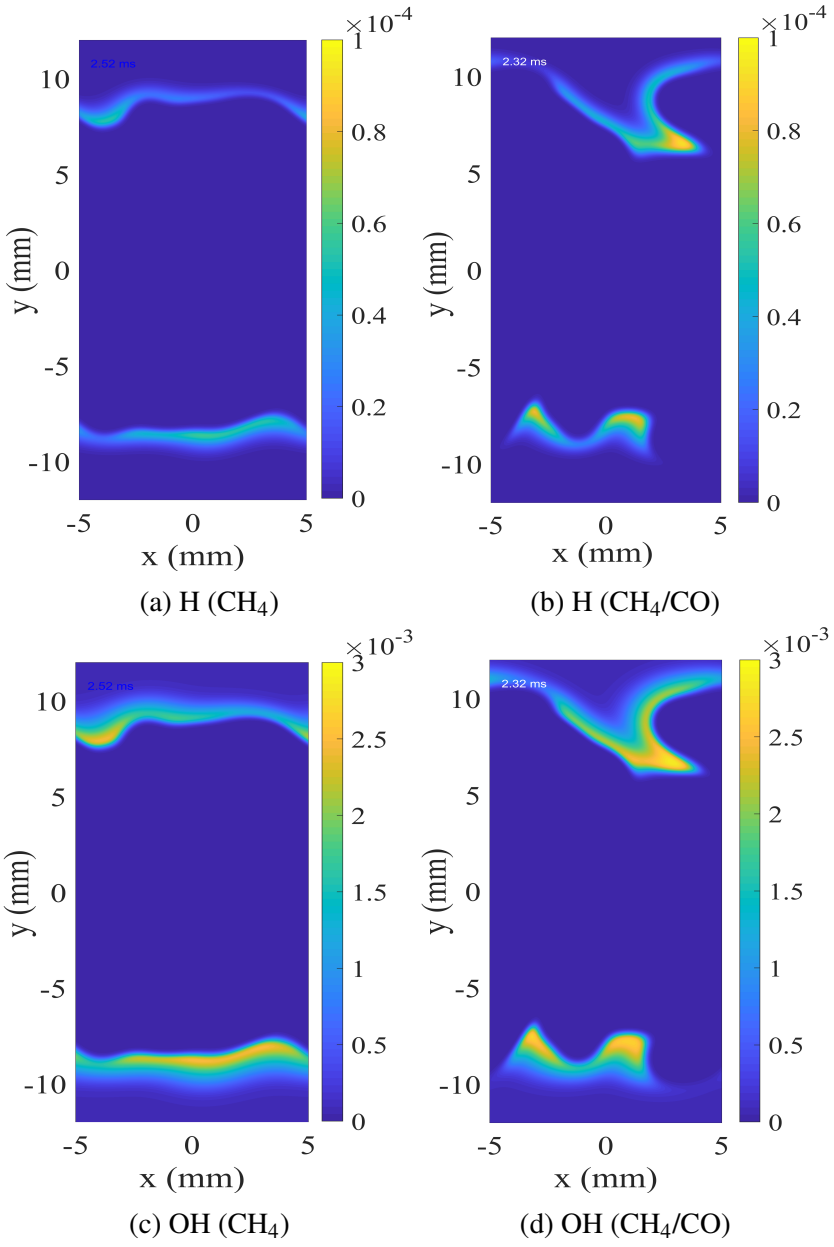

(a) H (CH_4) (b) H (CH_4/CO)

(c) OH (CH_4) (d) OH (CH_4/CO)

Fig. 5.11 The contours of H and OH mass fractions plotted at τ_{ign}+0.4ms of CH_4 and CH_4/CO cases. As is seen, H concentrations are slightly higher in CH_4/CO compared to that of CH_4 case.

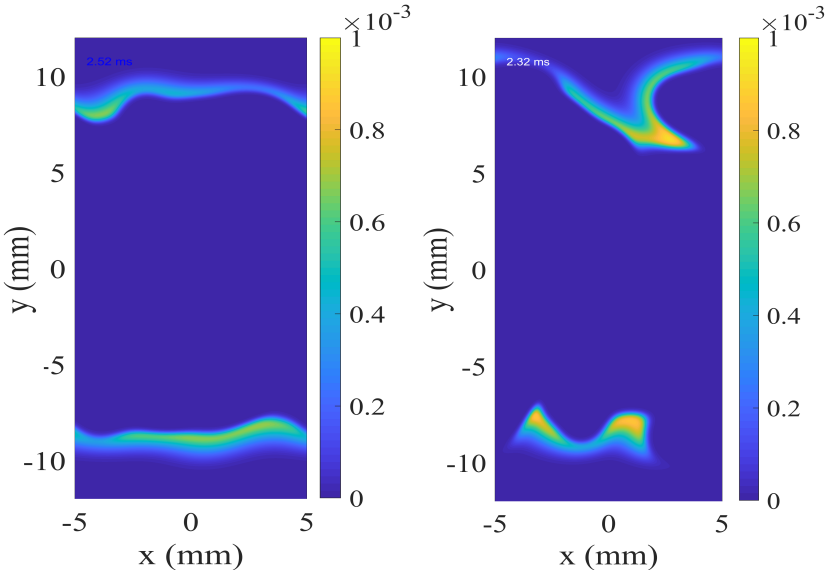

Fig. 5.11 The contours of O and CH_2O mass fractions plotted at τ_{ign}+0.4ms of CH_4 and CH_4/CO cases. As is seen, O and CH_2O concentrations are almost similar in both the flames.

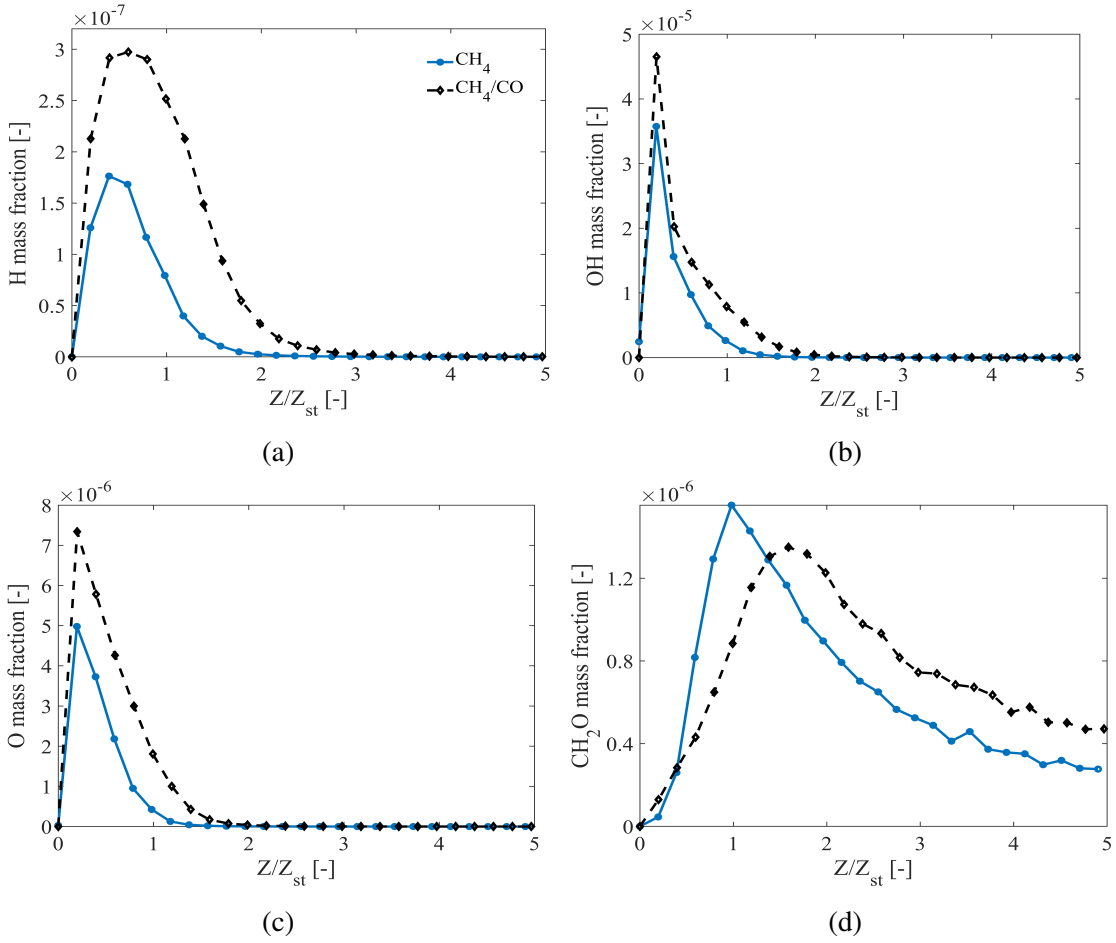

Fig. 5.12 Conditional plots of (a) H, (b) OH, (c) O, and (d) CH_2O mass fractions plotted as a function of Z/Z_{st}, where Z and Z_{st} correspond to the mixture fraction and stoichiometric mixture fraction, respectively. The plots show that the addition of CO in methane flames increases the intermediate species formation and the mass fractions of H, OH and O radicals, however, the CH_2O mass fractions is slightly higher in CH_4 case compared to that of CH_4/CO case.

5.3.5 Reaction pathway analysis

The results presented in Chapter 4 and the current chapter clearly shows that the addition of CO in MILD methane flames affects the ignition behaviour and flame characteristics. In this section, the Quantitative Reaction Path Diagrams (QRPDs) are generated to analyse the effects of CO addition on the reaction pathways of CH_4 to CO_2 and H_2O. The intermediate species that are formed during the oxidation of CH_4 to CO_2 and H_2O are also reported. The QRPDS of CO_2 and H_2O formation pathways are plotted separately to make the comparison study unambiguous. As already mentioned, since DRM19 is a reduced mechanism developed for the investigation of ignition behaviour and flame characteristics, and it is not appropriate for reaction pathway analysis. Therefore, a detailed mechanism is chosen to perform the reaction pathways analysis. Alike in Chapter 3, Curran mechanism (Burke et al. 2015) which is a detailed mechanism with 113 species and 710 reactions is chosen to generate the QRPDs and to perform the reaction pathway analysis.

The homogeneous reactor model available in CHEMKIN is utilised for the generation of the QRPDs. For fuel composition, the molar fraction of CH_4 is set to 1 for CH_4 case, and for CH_4/CO case, the molar fractions of CH_4 and CO are set to 0.5 and 0.5, respectively. The oxidiser composition is similar to the composition mentioned in Table 5.1. The calculations are performed for the stoichiometric composition. Therefore, the equivalence ratio of the mixture is set to 1. In non-adiabatic cases, the average temperature at the locations of stoichiometric metric composition at the time of ignition for CH_4 and CH_4/CO cases are close to 1600 K. Therefore, the initial temperature of the reactants for all the homogeneous reactor calculations are set to 1600 K. The QRPDs are generated from the homogeneous reactor results at $\Delta T = 50$ K which is close to ignition delay and thermal runaway.

The QRPDs of CH_4 to CO_2 oxidation pathways of CH_4 flames and CH_4/CO flames are shown in Figure 5.13 (a) and Figure 5.13 (b), respectively. The numbers indicated in the arrows correspond to the flux rate between two species. The thickness of the arrows of both

diagrams are scaled using a common reference value to make a visual qualitative comparison, and the flux rate of a thicker arrow is greater than that of a thinner arrow. The thickness of the arrows are calculated using the relation given in Equation 3.12. Please note that the arrowheads in the figures are not scaled.

The figures clearly show that the addition of CO in MILD CH_4 flames has a significant effect on the CH_4 to CO_2 oxidation pathways, intermediate species formation and the flux rate between the intermediate species. The important pathway involved in the decomposition of CH_4 and formation of CO_2 in case of CH_4 flames is CH_3-C_2H_6-C_2H_5-C_2H_4-C_2H_3-C_2H_2-HCCO-CO_2. On the other hand, in the case of CH_4/CO flames, the important pathways involved in the decomposition of CH_4 and formation of CO_2 are CH_3-C_2H_6-C_2H_5-C_2H_4-C_2H_3 and CH_3-CH_2O-HCO-CO-CO_2. As is evident above, in MILD CH_4 flames, only the ethane to the vinyl pathway is dominant in the CH_4 to CO_2 oxidation pathway, and the major intermediate species formed are associated with this pathway. On the other hand, in MILD CH_4/CO flames, the two pathways, ethane to vinyl and aldehyde pathways become dominant in CH_4 to CO_2 oxidation pathways. In addition, the concentration of the intermediate species HCO and CO increases, and become a major participator when CO is added in MILD CH_4 flames. Apart from these, the figures show that the CO addition also increases the flux rate between all the intermediate species. Especially, the CO addition even increases the flux rate of CH_4 to CH_3 by 30%. The rate of production of CH_3 of the reaction CH_4+OH<=>CH_3+H_2O, which is the major contributor of CH_3, increases by 33% due to the CO addition.

The QRPDs of CH_4 to H_2O oxidation pathways are presented in Figure 5.14. The figures show that, unlike CH_4 to CO_2 oxidation pathways, the CO addition does not affect either the oxidation pathways of CH_4 to H_2O or the major intermediate species formed during the oxidation process of CH_4 to H_2O. However, as seen above, the flux rate between the intermediate species are increased when CO is added in MILD CH_4 flames.

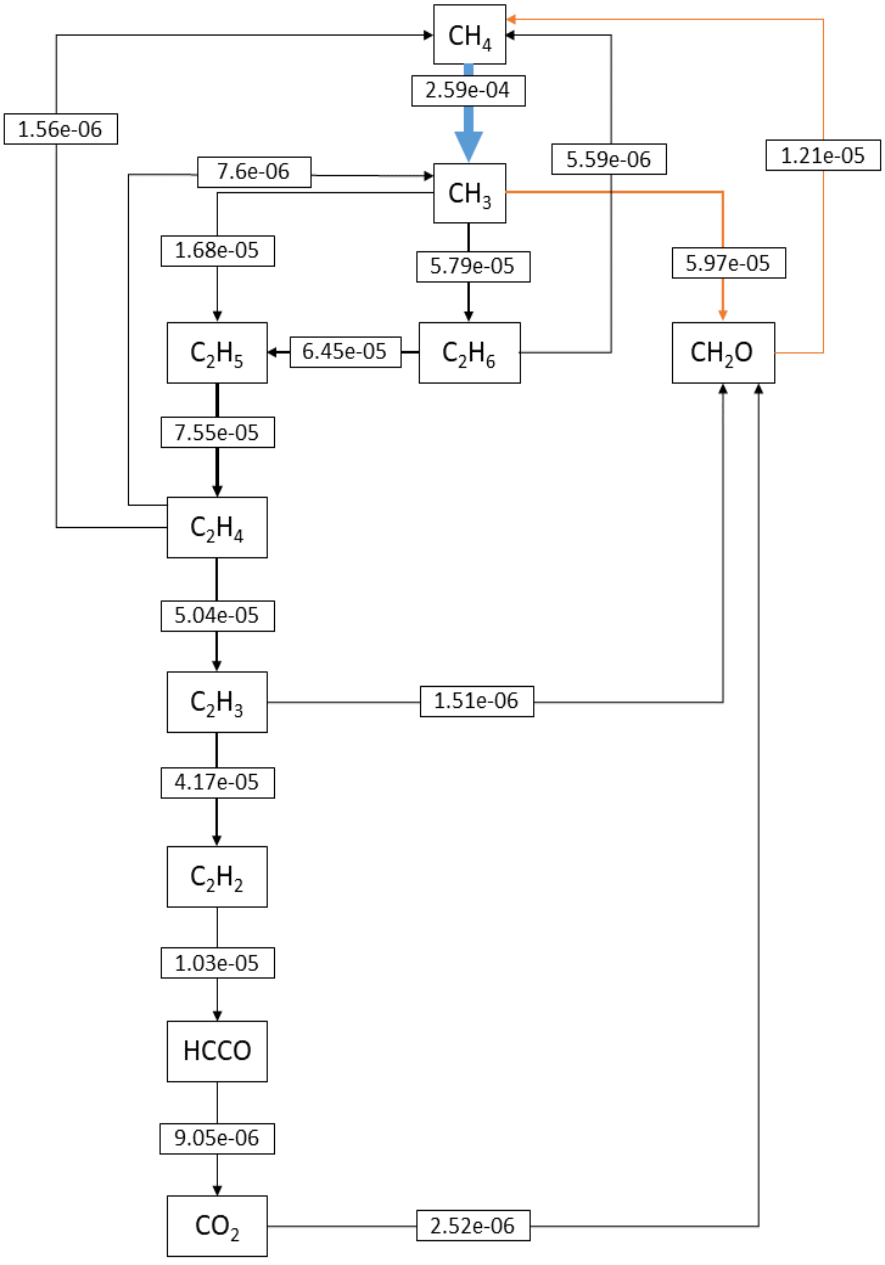

(a)

Fig. 5.13 (a) Quantitative Reaction Path Diagram (QRPD) of CH_4 to CO_2 of MILD CH_4 flames.

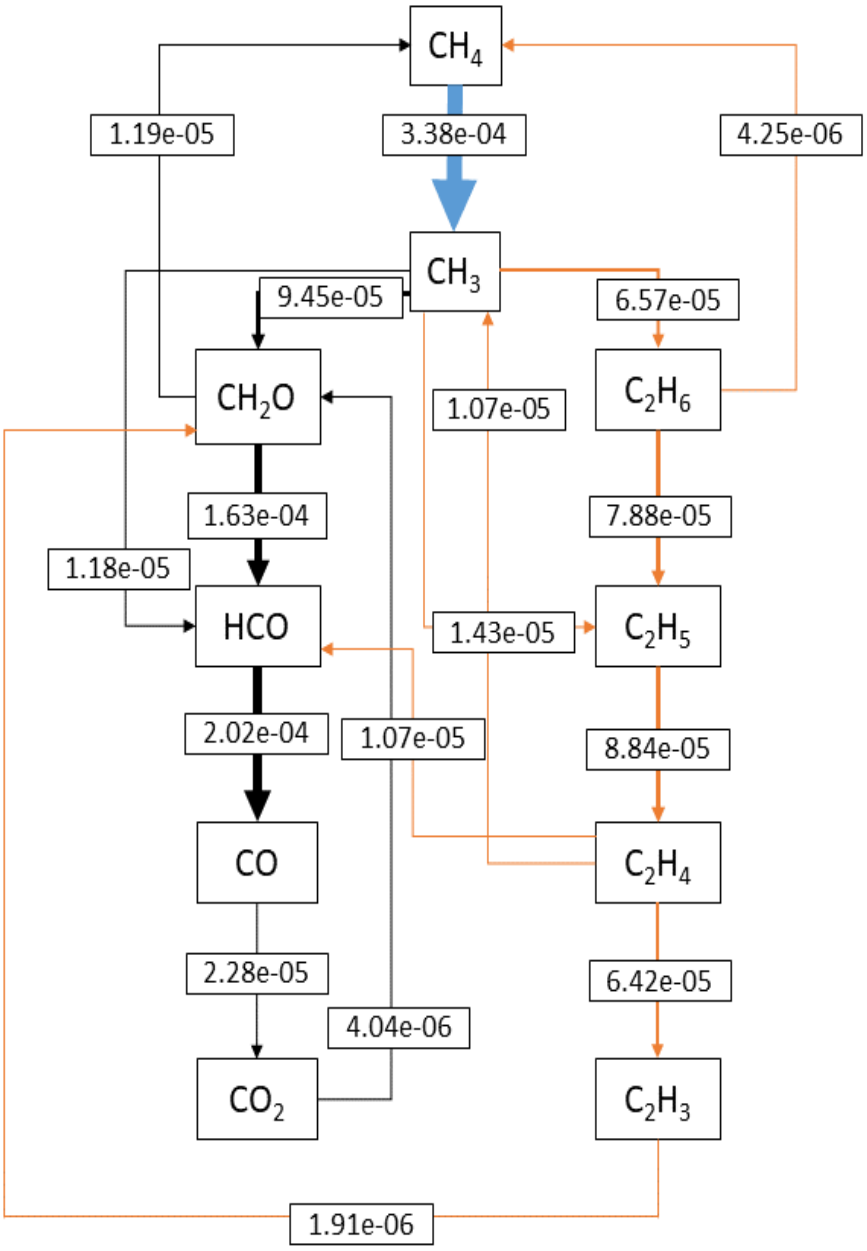

(b)

Fig. 5.13 (b) Quantitative Reaction Path Diagram (QRPD) of CH_4 to CO_2 of MILD CH_4/CO flames.

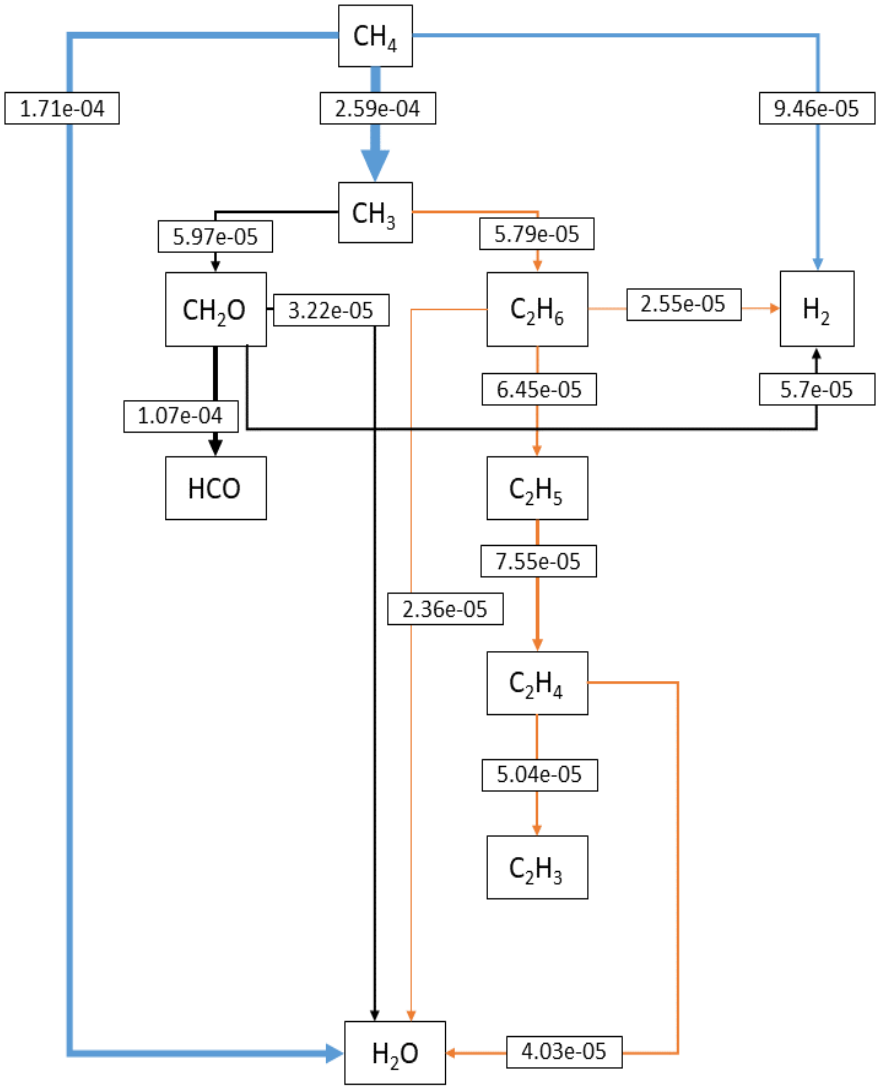

Fig. 5.14 (a) Quantitative Reaction Path Diagram (QRPD) of CH_4 to H_2O of MILD CH_4 flames.

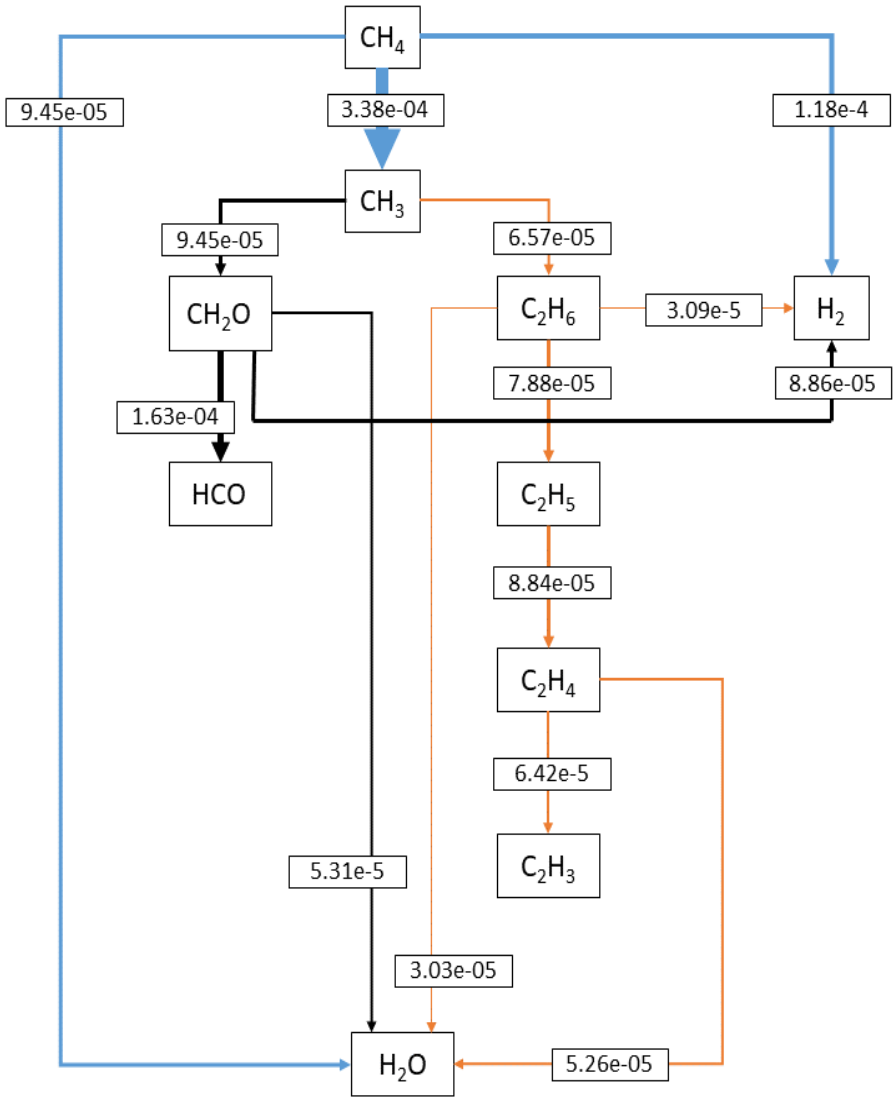

Fig. 5.14 (b) Quantitative Reaction Path Diagram (QRPD) of CH_4 to H_2O of MILD CH_4 flames.

5.4 Conclusions

In this chapter, the effects of heat loss on the ignition and combustion of MILD flames were investigated. Additionally, the effects of carbon monoxide addition on non-adiabatic MILD methane flames were investigated. For this purpose, 1D, 2D, and 3D direct numerical simulations of MILD methane flames and MILD methane flames enriched with carbon monoxide were performed with the inclusion of heat loss effects. The chemical mechanism, inlet compositions, 2D geometry (for the simulation of 2D cases) and other simulation parameters were kept similar to that of Chapter 4. The initial temperature profile was modified to include the heat loss effects and it was adapted from the work done by Göktolga et al. (2015). A 3D geometry that represents the JHC flame configuration was chosen for the simulations of 3D cases. The possibilities of the development of IML based FGM model for modelling adiabatic MILD methane flames enriched with carbon monoxide was also evaluated and discussed. Finally, the QRPDs were generated to analyse the effects of carbon monoxide addition on the reaction pathways of MILD methane flames. With these, the objectives 1, 4, 5, 6, and 7 relevant to carbon monoxide addition to non-adiabatic MILD methane flames are addressed. By addressing these objectives, the combustion characteristics of non-adiabatic non-premixed MILD methane flames enriched with carbon monoxide are analysed.

The results of this chapter show that, at oxidiser temperature 1700 K, the heat loss effects lengthened the ignition delay of MILD methane flames and carbon monoxide enriched MILD methane flames by 1.11 ms and 1.01 ms, respectively. In case of non-adiabatic MILD CH_4 and CH_4/CO flames, turbulence plays a major role in mixing and governs the ignition delay, however, molecular diffusion effects on the ignition delay and mixing are also realizable. Since turbulence plays a major role in mixing and ignition delay in the presence of heat loss, the FGM model derived from 1D IML flames are not suitable for the prediction of ignition

delay. Because, in 1D IML flames, ignition delay is governed by molecular diffusion. The investigation of carbon monoxide addition in MILD methane flames with the inclusion of heat loss reveals that such trends agree well with those trends observed in the adiabatic MILD methane flames. Similar to adiabatic flames, carbon monoxide addition to non-adiabatic MILD methane flames increases the H mass fractions, OH mass fractions, shortens the ignition delay, increases scalar dissipation rate and accelerates the mixing process.

The reaction pathway analysis shows that the carbon monoxide addition to MILD methane flames increases the flux rate between the intermediate species. In addition, in MILD methane flames, only the ethane to vinyl pathway seems to be important in the methane to carbon dioxide oxidation pathway. In carbon monoxide enriched MILD methane flames both ethane to vinyl and aldehyde pathways become important in the methane to carbon dioxide oxidation pathway. However, in both flames, the top intermediate species involved in methane to water vapour oxidation pathways are identical, and their oxidation pathways are similar.

The simulations of this chapter were performed using CH_4 and CH_4/CO as base fuel. However, it is reasonable to assume that the findings and the conclusions derived using the results of this chapter can be extended to any similar JHC flames with any hydrocarbon fuels. Particularly, the findings relevant to the effects of CO addition, 3D turbulence and heat loss on MILD combustion. As mentioned in chapter 4, the main limitation of the results calculated and the conclusions derived in this chapter arises from the DRM19 mechanism. The DRM19 mechanism is less accurate than GRI 3.0 at higher oxidiser temperatures. Yet, the DRM19 mechanism is used instead of GRI 3.0 because of the lack of computational power that is required to run DNS with GRI 3.0 mechanism. However, it has been already shown in chapter 4 that the trends predicted using DRM19 mechanism is similar to that of the trends predicted using GRI 3.0.

Chapter 6. Conclusions and recommendations for future work

6.1 Conclusions

Moderate or Intense Low-oxygen Dilution (MILD) combustion is an emerging combustion technology which can simultaneously improve the efficiency and reduce the emission levels of the combustion systems. It can also help us to make a smooth transition towards the renewable energy. Even though MILD combustion has several advantages, many fundamental issues associated with the ignition characteristics, reaction kinetics, and flame characteristics of MILD combustion are yet to be resolved or require further understanding which limits the range of its application. The consideration of renewable fuels further increases the complexity of the MILD combustion process.

This thesis primarily reports Direct Numerical Simulations (DNS) of non-premixed Moderate Intense Low-oxygen Dilution (MILD) flames. Investigations were performed to understand the combustion characteristics and reaction pathways of MILD methane flames enriched with gaseous additives. For this purpose, DNS of syngas enriched and carbon monoxide enriched MILD methane flames were performed and the results were compared with the results of MILD methane flames. The effects of heat loss on the ignition behaviour of MILD flames and the effects of exhaust gas addition on the combustion characteristics of CH_4/CO/H_2 flames were also investigated. Investigations were performed in both laminar and turbulent flame regimes. GRI 3.0 mechanism was used to resolve the chemistry in 1D flame model. DRM19 mechanism was used for resolving the chemistry in 2D and 3D direct numerical simulations. The reaction pathway analyses were conducted using a detailed

kinetic mechanism called Curran. The reaction flow solver CHEM1D was used for solving the 1D reacting flow problems while the 2D and 3D DNS were performed using DiSCo. The reaction pathway analyses were performed using Quantitative Reaction Path Diagrams (QRPD) which were generated using CHEMKIN reaction pathway analyser. In what follows, the important findings of previous chapters and the conclusions derived using these findings are summarised.

It is observed that the addition of exhaust gas to CH_4/CO/H_2 and air 1D laminar counterflow diffusion flames reduces its flame temperature, NO emission levels, ignition delay, flame length and affects the species flux rate during the combustion process. The changes observed in these parameters and properties depend on the amount of exhaust gas added to these flames. For instance, when the exhaust gas content is increased to 50% of the mass fraction of the oxidizer stream, the flame enters MILD regime. At these operating ranges, the total NO and thermal NO levels are negligible, and for exhaust gas mass fractions greater than 80%, the total NO formation is very low. Hence, as discussed in Chapter 1, exhaust gas addition and MILD combustion are very interesting for combustion applications that are developed to achieve low NO formation levels.

The addition of syngas in MILD methane flames reduces the ignition delay by an order of 10^{-2}. It also increases the flux rate between the species during the combustion process, which are due to the presence of highly reactive hydrogen gas in syngas. This clearly shows that the addition of syngas in MILD methane flames increases the reactivity of the combusting mixture. Hence, the advantages of hydrogen addition to MILD flames such as flame stability can be achieved by the addition of syngas to MILD flames. Apart from these, the addition of syngas in MILD methane flames also reduces the NO emission levels. The reason is that the addition of syngas in MILD methane flames reduces the CH_4 concentration in these flames, which is the primary contributor to prompt NO. As discussed above, the addition of exhaust gas already alleviates the NO formation levels significantly, and the addition of syngas further

reduces the NO formation levels. Hence the combination of MILD combustion technology and the syngas addition could be very interesting for the development of combustion systems (especially charged using natural gas) to achieve ultra-low NO emission levels.

One of the major findings of this study is the addition of carbon monoxide to MILD methane flames can significantly affect their combustion characteristics. The addition of carbon monoxide to MILD methane flames shortens their ignition delay, increases the mixture reactivity and the scalar dissipation rate. It also increases the production of major intermediate species such as H and OH in MILD methane flames. Flame stabilization is an important criteria, but it is very challenging to achieve in MILD regime because of its slow reaction rate. The increase in mixture reactivity, scalar dissipation rate and shortened ignition delay can increase the flame stability. Hence, the addition of carbon monoxide in MILD methane flames can increase flame stability which is useful for applications. Furthermore, this also shows that, in addition to hydrogen, carbon monoxide also plays a significant role in syngas enriched methane flames.

The inclusion of heat loss effects significantly lengthens the ignition delay of MILD flames. In case of non-adiabatic MILD flames, which replicates Jet-in-hot-coflow (JHC) configurations, both turbulence and molecular diffusion influence the mixing process at the ignition stage; however, the mixing process is dominated by turbulence. In contrast, in adiabatic MILD JHC flames, the mixing process during the ignition stage is solely governed by molecular diffusion. As a consequence, the Igniting Mixing Layers (IML) based Flamelet Generated Manifold (FGM) model can be used for the prediction of the ignition of adiabatic MILD JHC flames. However, such a model is not suitable for the prediction of the ignition of non-adiabatic MILD JHC flames. Apart from these, the investigation into carbon monoxide addition to turbulent MILD methane flames with the inclusion of heat loss reveals that such trends agree well with those observed in the adiabatic turbulent MILD methane flames.

Direct numerical simulations of non-premixed MILD flames were performed, and the results reveal that the addition of syngas and carbon monoxide to MILD methane flames significantly alters their combustion characteristics which cannot be neglected while modelling these flames. The data generated in this thesis using DNS can be used in combustion model development specific to MILD combustion of CH_4 flames and also MILD CH_4 flames enriched with CO. It is evident that both MILD combustion technology and syngas addition to hydrocarbon flames can reduce the formation of pollutants (NO and CO) and greenhouse gases (CO_2). The addition of syngas to MILD combustion reduces the ignition delay and increases the reactivity of the MILD flames. This shows that syngas can replace hydrogen for improving the flammability of MILD combustion. The findings of this study have also shown that carbon monoxide addition to hydrocarbon flames can alter their combustion characteristics. Thus, the findings of this thesis challenge the conclusions of previous studies by providing novel insight into the effects of CO addition to hydrocarbon flames. This shows that this thesis work has generated new data about MILD combustion, pollution formation and addition of gaseous additives to MILD flames, and it has provided novel insights in these areas. The above discussions show that the findings and the data provided by this thesis are a valuable addition to the existing literature. It can accelerate the diffusion of this technology in industrial applications and can encourage us to consider the enrichment of MILD flames with gaseous additives. These can help us reduce emission levels and accelerate our shift towards renewable energy.

To summarise, the findings of this study are relevant and can provide directions for other combustion researchers, particularly those conducting the investigations to understand the effects of renewable gaseous additives in MILD combustion, developing numerical models for the prediction of MILD combustion, and developing ultra-low emission combustion systems.

6.2 Strength and weakness of this thesis

The main strength of this thesis is, the results are generated using direct numerical simulations. The results of direct numerical simulations have given deeper insights into the physics and chemistry of the combustion process compared to the experimental results. As mentioned in Chapter 1, MILD combustion is featured by low or no emission of visible radiation. Hence, the investigation of MILD combustion using experimental methods can not give the level of information regarding the intermediate species formation and pollution formation in the reaction zone compared to that of numerical investigation. Also, the thesis investigates the effects of syngas and carbon monoxide addition to MILD combustion. This makes this research stand out and makes it becomes more original compared to other topics. For instance, the direct simulation results of CH_4 flames and CH_4/CO flames presented in this thesis are the first of their kind.

The main weakness also arises due to the consideration of direct numerical simulations for the investigations conducted in this thesis. Direct numerical simulations are computationally intensive. So, with the resources available for this thesis, the author was able to perform only two 3D cases. As a result of this, 2D DNS results were used for the investigation of CH_4/CO flames without heat loss and only one composition was considered for the investigation of the effects of CO addition to MILD CH_4 flames. If the author of this thesis had the resources to generate 3D DNS results for more fuel compositions and flames without heat loss, it would have further strengthened our understanding of CH_4 and CH_4/CO flames.

6.3 Achievement of specific objectives

The aim of this thesis is to perform start-of-the-art numerical simulations to understand the underlying physics of ignition and combustion of non-premixed MILD methane flames enriched with renewable gases. This is achieved in this thesis by performing start-of-the-

art direct numerical simulations to understand the effects of syngas and carbon monoxide addition on the combustion of MILD methane flames. The objectives, presented in Section 1.2, are addressed in this thesis as described as follow,

- **Identify the numerical modelling techniques that are suitable for the examination of combustion characteristics and reaction pathways of non-premixed MILD flames. Next, choose numerical codes that are developed suitable for the identified numerical modelling techniques, chemical mechanisms, geometry, and simulation parameters that are appropriate for the investigation of the combustion characteristics of non-premixed MILD flames.**

  The numerical modelling techniques that are suitable for the examination of combustion characteristics and reaction pathways of non-premixed MILD flames were identified in Chapter 2. For syngas enriched MILD methane flames, the numerical codes, chemical mechanisms, and simulation parameters were identified in Chapter 3. Also, the justifications for these choices were addressed in Chapter 3. For carbon monoxide enriched flames, the numerical methods, numerical codes, chemical mechanisms, and simulation parameters were identified and justifications for those choices were presented in Chapter 4 (adiabatic) and Chapter 5 (non-adiabatic).

- **Perform numerical simulations of adiabatic MILD methane flames and adiabatic MILD methane flames enriched with syngas and carbon monoxide.**

  To achieve this objective, time-independent and transient 1D direct numerical simulations of non-premixed adiabatic MILD methane flames with and without syngas enrichment were performed in Chapter 3. Then, transient 2D direct simulations of non-premixed adiabatic MILD methane flames with and without carbon monoxide enrichment were performed in Chapter 4.

- **Compare and analyse the adiabatic numerical simulation results to understand the effects of syngas and carbon monoxide addition on the combustion characteristics of adiabatic MILD methane flames. Additionally, analyse the effects of exhaust gas addition to syngas enriched methane flames.**

  The results of the numerical simulations that were performed to understand the effects of syngas and exhaust gas addition to methane flames were presented and discussed in Chapter 3. Steady state results were presented and discussed to understand the effects of syngas and exhaust gas addition to the combustion temperature, heat release, flame structure, and pollution formation of methane flames. Transient results were used to understand the ignition delay. The results of the simulations that were performed to understand the effects of carbon monoxide addition to MILD methane flames were presented and discussed in Chapter 4. One-dimensional and two-dimensional direct numerical simulations results were analysed to understand the effects of carbon monoxide addition on the ignition and combustion of adiabatic MILD methane flames.

- **Perform numerical simulations of non-adiabatic MILD methane flames and non-adiabatic MILD methane flames enriched with carbon monoxide.**

  To achieve this objective, transient 3D direct numerical simulations of non-adiabatic MILD methane flames with and without the enrichment of carbon monoxide were performed in Chapter 5.

- **Investigate the effects of carbon monoxide addition on the combustion characteristics of non-adiabatic MILD methane flames. Additionally, analyse the non-adiabatic results to understand the effects of heat loss on the ignition characteristics of MILD flames.**

  The results of the direct numerical simulations of non-adiabatic MILD methane flames enriched with and without carbon monoxide were presented and discussed in Chapter

5. The results were analysed to understand the effects of carbon monoxide addition on the mixing, ignition, and the combustion of non-adiabatic MILD methane flames. Also, the effect of heat loss on ignition delay of MILD methane flames was analysed.

- **Generate Quantitative Reaction Path Diagrams (QRPDs) of MILD flames, and investigate the effects of syngas addition and carbon monoxide addition on the reaction pathways of MILD methane flames.**

  The quantitative reaction pathway diagrams for MILD methane and MILD methane flames enriched with syngas were generated in Chapter 3. The results of the simulations were presented and analysed to understand the effects of syngas addition on the chemical reaction pathways of MILD methane flames. Similarly, the quantitative reaction pathway diagrams for MILD methane and MILD methane flames enriched with carbon monoxide were generated in Chapter 5. The results of the simulations were presented and analysed to understand the effects of carbon monoxide addition on the chemical reaction pathways of MILD methane flames.

- **Evaluate the possibility of the development of Igniting Mixing Layers (IML) based Flamelet Generated Manifold (FGM) model for the prediction of ignition behaviour and flame characteristics of adiabatic and non-adiabatic MILD flames.**

  To achieve this objective, the 2D and 3D results of direct numerical simulations were compared with 1D results, and discussions were presented that explains the suitability of IML based FGM model for the prediction of ignition behaviour and flame characteristics of adiabatic and non-adiabatic MILD flames. The results and discussions for adiabatic flames were presented in Chapter 4, while for non-adiabatic flames, they were presented in Chapter 5.

6.4 Recommendations for the future works

The thesis findings have provided insights into syngas and carbon monoxide enriched MILD methane flames and non-adiabatic MILD flames. It has helped to reach the objectives framed in Chapter 1. Nevertheless, it has also presented opportunities for further research, experiments and numerical modelling, as follows.

- The investigations in this thesis are performed with methane as base fuel. It is worthwhile to investigate the effects of syngas addition on the ignition and combustion characteristics of MILD flames of complex hydrocarbon fuels such as ethane, ethylene, Dimethyl Ether (DME) and heptane. Moreover, previous studies showed that the addition of hydrogen to MILD flames of these fuels increased their flame stability. Conducting such studies would encourage the use of these fuels along with syngas instead of hydrogen and MILD combustion in commercial combustion systems which have several environmental benefits.

- The investigations of the effects of syngas addition on MILD methane flames are performed in 1D laminar flames. Since many practical combustion systems operate under turbulent regime, the experimental and numerical investigations must be performed to understand the effects of syngas addition in turbulent MILD methane flames. Such investigations are necessary to further our understanding on the role of syngas on MILD methane flames and on the possibility of replacing hydrogen with syngas as an additive for MILD flames in turbulent combustion applications.

- The results of this study reveal that the carbon monoxide addition to MILD methane flame increases the scalar dissipation rate, enhances mixing and affect the major intermediate species formed during the combustion process. Further investigations are required to understand the role of carbon monoxide in syngas added turbulent

MILD methane flames and how these effects are reflected in those flames. Especially, investigations are required to understand the effects of carbon monoxide molar fraction on the flame stability, mixing, and scalar dissipation rate on the syngas enriched MILD methane flames.

- DNS of carbon monoxide enriched methane flames are performed using DRM19 mechanism which does not include NO formation mechanism. Hence, investigations are required to be done to see the effects of carbon monoxide addition on the NO formation of laminar and turbulent MILD methane flames.

- The comparison of 1D IML and DNS results reveal that the IML based FGM model can be used for the prediction of adiabatic MILD JHC flames. Hence, it is worthwhile to develop and assess the IML based FGM model for prediction of ignition and combustion of adiabatic MILD CH_4 and CH_4/CO JHC flames. It should be noted that, in case of CH_4/CO flames, preferential diffusional effects must be taken into account in the model development.

- Chapter 5 results show that the IML-based FGM model is not appropriate for the prediction of non-adiabatic MILD JHC flames. Therefore, it is necessary to identify and develop an appropriate numerical model for the prediction of non-adiabatic MILD JHC flames. Göktolga (2019) developed a novel FGM model called MuSt-FGM model to predict ignition and combustion of non-adiabatic MILD JHC flames. His model predicted the ignition delay accurately. However, the number of control variables required by the model is four to model a turbulent flames using large eddy simulation method which complicates the model development process. The inclusion of preferential diffusion effects and the selection of progress variables for various the stages of combustion in MuSt-FGM model further complicates the model development process. Moreover, he observed that the mean heat release trends were not accurately

captured by MuSt-FGM model. Therefore, it would be worthwhile to investigate the possibility to develop a numerical model that could be applied for both adiabatic and non-adiabatic MILD JHC flames. Such a model should be easy to develop, able to accurately model all the stages of combustion of the above-mentioned flames, and modelling pollution formation and preferential diffusion effects must be easier.

References

Abbasi, T. & Abbasi, S. (2011), "renewable'hydrogen: prospects and challenges', *Renewable and Sustainable Energy Reviews* **15**(6), 3034–3040.

Abelsohn, A., Sanborn, M. D., Jessiman, B. J. & Weir, E. (2002), 'Identifying and managing adverse environmental health effects: 6. carbon monoxide poisoning', *Cmaj* **166**(13), 1685–1690.

Abtahizadeh, E., de Goey, P. & van Oijen, J. (2015), 'Development of a novel flamelet-based model to include preferential diffusion effects in autoignition of ch4/h2 flames', *Combustion and Flame* **162**(11), 4358–4369.

Abtahizadeh, E., de Goey, P. & van Oijen, J. (2017), 'Les of delft jet-in-hot coflow burner to investigate the effect of preferential diffusion on autoignition of ch4/h2 flames', *Fuel* **191**, 36–45.

Abtahizadeh, E., van Oijen, J. & de Goey, L. P. H. (2012), 'Numerical study of mild combustion with entrainment of burned gas into oxidizer and/or fuel streams', *Combustion and Flame* **159**(6), 2155–2165.

Al-Noman, S. M., Choi, B. C. & Chung, S. H. (2018), 'Autoignited lifted flames of dimethyl ether in heated coflow air', *Combustion and Flame* **195**, 75–83.

Al Qubeissi, M. (2019), *Introductory Chapter: Biofuels-Challenges and Opportunities*, IntechOpen.

Al Qubeissi, M. & El-Kharouf, A. (2020), *Renewable Energy: Resources, Challenges and Applications*, IntechOpen. DOI: 10.5772/intechopen.81765. ISBN: 978-1-78984-284-5.

Alavandi, S. K. & Agrawal, A. K. (2008), 'Experimental study of combustion of hydrogen-syngas/methane fuel mixtures in a porous burner', *International Journal of Hydrogen Energy* **33**(4), 1407–1415.

Alexakis, A. & Biferale, L. (2018), 'Cascades and transitions in turbulent flows', *Physics Reports* **767**, 1–101.

Amin, V., Katzlinger, G., Saxena, P., Pucher, E. & Seshadri, K. (2015), 'The influence of carbon monoxide and hydrogen on the structure and extinction of nonpremixed and premixed methane flames', *Proceedings of the Combustion Institute* **35**(1), 955–963.

ANSYS Chemkin Theory Manual 17.0 (15151) (2015).

Archer, D., Eby, M., Brovkin, V., Ridgwell, A., Cao, L., Mikolajewicz, U., Caldeira, K., Matsumoto, K., Munhoven, G., Montenegro, A. et al. (2009), 'Atmospheric lifetime of fossil fuel carbon dioxide', *Annual review of earth and planetary sciences* **37**.

Arndt, C. M., Schießl, R., Gounder, J. D., Meier, W. & Aigner, M. (2013), 'Flame stabilization and auto-ignition of pulsed methane jets in a hot coflow: influence of temperature', *Proceedings of the Combustion Institute* **34**(1), 1483–1490.

Arteaga Mendez, L., Tummers, M., van Veen, E. & Roekaerts, D. (2015), 'Effect of hydrogen addition on the structure of natural-gas jet-in-hot-coflow flames', *Proceedings of the Combustion Institute* **35**(3), 3557–3564.

Bakali, A. E., Pillier, L., Desgroux, P., Lefort, B., Gasnot, L., Pauwels, J. & Da Costa, I. (2006), 'No prediction in natural gas flames using gdf-kin® 3.0 mechanism ncn and hcn contribution to prompt-no formation', *Fuel* **85**(7-8), 896–909.

Barbato, P. S., Landi, G. & Russo, G. (2013), 'Catalytic combustion of $CH_4 - H_2 - CO$ mixtures at pressure up to 10 bar', *Fuel Processing Technology* **107**, 147–154.

Bastiaans, R., Somers, L. & de Lange, H. (2001), 'Modern simulation strategies for turbulent flow bj geurts editor (edwards, philadelphia, usa, 2001)', pp. 247–261.

Beck, J., Krzyzanowski, M. & Koffi, B. (1998), Tropospheric ozone in eu-the consolidated report, Technical Report 8, European Environmental Agency.

Benim, A. C. & Syed, K. J. (2014), *Flashback mechanisms in lean premixed gas turbine combustion*, Academic press.

Bilger, R. W., Stårner, S. H. & Kee, R. J. (1990), 'On reduced mechanisms for methane-air combustion in nonpremixed flames', *Combustion and Flame* **80**(2), 135–149.

Boden, T., Andres, R. & Marland, G. (2017), Global, regional, and national fossil-fuel co_2 emissions $(1751 - 2014)(v.2017)$, Technical report, Environmental System Science Data Infrastructure for a Virtual Ecosystem ....

Botkin, D. (2013), 'Saving a million species: Extinction risk from climate change ed. by lee hannah', Ecological Restoration 31(1), 99–100.

Brandenburg, A., Johansen, A., Bourdin, P. A., Dobler, W., Lyra, W., Rheinhardt, M., Bingert, S., Haugen, N. E. L., Mee, A., Gent, F. et al. (2020), 'The pencil code, a modular mpi code for partial differential equations and particles: multipurpose and multiuser-maintained', *arXiv preprint arXiv:2009.08231* .

Burke, U., Somers, K. P., O'Toole, P., Zinner, C. M., Marquet, N., Bourque, G., Petersen, E. L., Metcalfe, W. K., Serinyel, Z. & Curran, H. J. (2015), 'An ignition delay and kinetic modeling study of methane, dimethyl ether, and their mixtures at high pressures', *Combustion and flame* **162**(2), 315–330.

Cabra, R. (2003), 'Turbulent jet flames into a vitiated coflow', *NASA Cr-2003212887* .

Cabra, R., Chen, J.-Y., Dibble, R., Karpetis, A. & Barlow, R. (2005), 'Lifted methane–air jet flames in a vitiated coflow', *Combustion and Flame* **143**(4), 491–506.

Cabra, R., Myhrvold, T., Chen, J., Dibble, R., Karpetis, A. & Barlow, R. (2002), 'Simultaneous laser raman-rayleigh-lif measurements and numerical modeling results of a lifted turbulent h2/n2 jet flame in a vitiated coflow', *Proceedings of the Combustion Institute* **29**(2), 1881–1888.

Cavaliere, A. & de Joannon, M. (2004), 'Mild combustion', *Progress in Energy and Combustion science* **30**(4), 329–366.

Centre for Environmental Assessment RTP division (National). (2016), I*ntegrated science assessment for oxides of nitrogen – health criteria,* Technical report, Environmental Protection agency - United States .

Chen, J. H., Choudhary, A., De Supinski, B., DeVries, M., Hawkes, E. R., Klasky, S., Liao, W.-K., Ma, K.-L., Mellor-Crummey, J., Podhorszki, N. et al. (2009), 'Terascale direct numerical simulations of turbulent combustion using s3d', *Computational Science and Discovery* **2**(1), 015001.

Chigier, N. A. (1981), *Energy, combustion, and environment*, McGraw-Hill New York.

Choi, B. & Chung, S.-H. (2010), 'Autoignited laminar lifted flames of methane, ethylene, ethane, and n-butane jets in coflow air with elevated temperature', *Combustion and flame* **157**(12), 2348–2356.

Christo, F. C. & Dally, B. B. (2005), 'Modeling turbulent reacting jets issuing into a hot and diluted coflow', *Combustion and flame* **142**(1-2), 117–129.

Combustion (1999).
URL: *https://www.grc.nasa.gov/www/k-12/airplane/combst1.html*

Cook, P. J. (2012), 'Clean energy, climate and carbon', *Carbon Management* **3**(3), 259–263.

Dai, X., Ji, C., Wang, S., Liang, C., Liu, X. & Ju, B. (2012), 'Effect of syngas addition on performance of a spark-ignited gasoline engine at lean conditions', *International journal of hydrogen energy* **37**(19), 14624–14631.

Dally, B. B., Karpetis, A. & Barlow, R. (2002), 'Structure of turbulent non-premixed jet flames in a diluted hot coflow', *Proceedings of the combustion institute* **29**(1), 1147–1154.

Dally, B., Masri, A., Barlow, R. & Fiechtner, G. (1998), 'Instantaneous and mean compositional structure of bluff-body stabilized nonpremixed flames', *Combustion and Flame* **114**(1-2), 119–148.

De Joannon, M., Matarazzo, A., Sabia, P. & Cavaliere, A. (2007), 'Mild combustion in homogeneous charge diffusion ignition (HCDI) regime', *Proceedings of the Combustion Institute* **31**(2), 3409–3416.

De Joannon, M., Sabia, P., Sorrentino, G. & Cavaliere, A. (2009), 'Numerical study of mild combustion in hot diluted diffusion ignition (HDDI) regime', *Proceedings of the Combustion Institute* **32**(2), 3147–3154.

de Lange, H. (2007), 'Acoustic upwinding for sub-and super-sonic turbulent channel flow at low reynolds number', *International journal for numerical methods in fluids* **55**(3), 205–223.

Dixon-Lewis, G.-N. (1968), 'Flame structure and flame reaction kinetics ii. transport phenomena in multicomponent systems', *Proceedings of the Royal Society of London. Series A. Mathematical and Physical Sciences* **307**(1488), 111–135.

Doan, N. A. K. & Swaminathan, N. (2019), 'Autoignition and flame propagation in non-premixed mild combustion', *Combustion and Flame* **201**, 234–243.

Echekki, T. & Chen, J. H. (2003), 'Direct numerical simulation of autoignition in non-homogeneous hydrogen-air mixtures', *Combustion and Flame* **134**(3), 169–191.

EIA (2019), International energy outlook 2019, Technical report, US Energy Information Administration.

Field, C. B. (2014), *Climate change 2014–Impacts, adaptation and vulnerability: Regional aspects*, Cambridge University Press.

for Environmental Information, N. N. C. (2020), State of the climate: Global climate report for annual 2019, Technical report, National Oceanic and Atmospheric Administration. **URL:** *https://www.ncdc.noaa.gov/sotc/global/201913*

Frenklach, M., Wang, H., Goldenberg, M., Smith, G. & Golden, D. (1995), Gri-mech: An optimized detailed chemical reaction mechanism for methane combustion. topical report, september 1992-august 1995, Technical report, SRI International, Menlo Park, CA (United States).

Frenklach, M., Wang, H., Yu, C., Goldenberg, M., Bowman, C., Hanson, R., Davidson, D., Chang, E., Smith, G., Golden, D., Gardiner, W. & Lissianski, V. (1994), 'Gri1.2 reaction mechanism'.

Glassman, I., Yetter, R. A. & Glumac, N. G. (2014), *Combustion*, Academic press.

Gökalp, I. & Lebas, E. (2004), 'Alternative fuels for industrial gas turbines (aftur)', *Applied Thermal Engineering* **24**(11-12), 1655–1663.

Göktolga, M. (2019), MuSt-FGM: development of a novel chemistry tabulation method for MILD combustion, PhD thesis, Department of Mechanical Engineering. Proefschrift.

Göktolga, M. U., van Oijen, J. A. & de Goey, L. P. H. (2015), '3d dns of mild combustion: a detailed analysis of heat loss effects, preferential diffusion, and flame formation mechanisms', *Fuel* **159**, 784–795.

Goodwin, D. (2019), Cantera: An object-oriented software toolkit for chemical kinetics, thermodynamics, and transport processes, Technical report, California Institute of Technology, Pasadena.

Grcar, J. F., Day, M. S. & Bell, J. B. (2006), 'A taxonomy of integral reaction path analysis', *Combustion Theory and Modelling* **10**(4), 559–579.

Groot, G. R. A. (2003), *Modelling of propagating spherical and cylindrical premixed flames*, Technische Universiteit Eindhoven.

Guo, H. & Neill, W. S. (2009), 'A numerical study on the effect of hydrogen/reformate gas addition on flame temperature and NO formation in strained methane/air diffusion flames', *Combustion and Flame* **156**(2), 477–483.

Guo, H., Smallwood, G. J., Liu, F., Ju, Y. & Gülder, Ö. L. (2005), 'The effect of hydrogen addition on flammability limit and NO_x emission in ultra-lean counterflow CH_4/air premixed flames', *Proceedings of the combustion institute* **30**(1), 303–311.

Jansohn, P. (2013), *Modern gas turbine systems: High efficiency, low emission, fuel flexible power generation*, Elsevier.

Jin, T., Luo, K., Lu, S. & Fan, J. (2013), 'Dns investigation on flame structure and scalar dissipation of a supersonic lifted hydrogen jet flame in heated coflow', *International journal of hydrogen energy* **38**(23), 9886–9896.

Jung, K. S., Kim, S. O., Lu, T., Chung, S. H., Lee, B. J. & Yoo, C. S. (2018), 'Differential diffusion effect on the stabilization characteristics of autoignited laminar lifted methane/hydrogen jet flames in heated coflow air', *Combustion and Flame* **198**, 305–319.

Katsuki, M. & Hasegawa, T. (1998), The science and technology of combustion in highly preheated air, *in* 'International symposium on combustion', Vol. 27 (2), Elsevier, pp. 3135–3146.

Kazakov, A. & Frenklach, M. (1994), 'Drm19 reaction mechanism'.

Knikkerr, R., Dauptain, A., Cuenot, B. & Poinsot, T. (2003), 'Comparison of computational methodologies for ignition of diffusion layers', *Combustion Science and Technology* **175**(10), 1783–1806.

Konnov, A. A., Alvarez, G. P., Rybitskaya, I. & Ruyck, J. D. (2008), 'The effects of enrichment by carbon monoxide on adiabatic burning velocity and nitric oxide formation in methane flames', *Combustion science and technology* **181**(1), 117–135.

Kurtz, J., Sprik, S. & Bradley, T. H. (2019), 'Review of transportation hydrogen infrastructure performance and reliability', *International Journal of Hydrogen Energy* **44**(23), 12010–12023.

Lammel, O., Stöhr, M., Kutne, P., Dem, C., Meier, W. & Aigner, M. (2012), 'Experimental analysis of confined jet flames by laser measurement techniques', *Journal of Engineering for Gas Turbines and Power* **134**(4).

Lele, S. K. (1992), 'Compact finite difference schemes with spectral-like resolution', *Journal of computational physics* **103**(1), 16–42.

Li, P., Mi, J., Dally, B., Wang, F., Wang, L., Liu, Z., Chen, S. & Zheng, C. (2011), 'Progress and recent trend in mild combustion', *Science China Technological Sciences* **54**(2), 255–269.

Lieuwen, T. C. (2012), *Unsteady combustor physics*, Cambridge University Press.

Lu, T., Yoo, C. S., Chen, J. & Law, C. K. (2010), 'Three-dimensional direct numerical simulation of a turbulent lifted hydrogen jet flame in heated coflow: a chemical explosive mode analysis', *Journal of Fluid Mechanics* **652**, 45.

Luo, K., Wang, H., Fan, J. & Yi, F. (2012), 'Direct numerical simulation of pulverized coal combustion in a hot vitiated co-flow', *Energy & fuels* **26**(10), 6128–6136.

Mardani, A. & Tabejamaat, S. (2010), 'Effect of hydrogen on hydrogen–methane turbulent non-premixed flame under mild condition', *International Journal of Hydrogen Energy* **35**(20), 11324–11331.

Mardani, A., Tabejamaat, S. & Ghamari, M. (2010), 'Numerical study of influence of molecular diffusion in the mild combustion regime', *Combustion Theory and Modelling* **14**(5), 747–774.

Mastorakos, E. (2009), 'Ignition of turbulent non-premixed flames', *Progress in Energy and Combustion Science* **35**(1), 57–97.

Mathieu, J. & Scott, J. (2000), *An introduction to turbulent flow*, Cambridge University Press.

Medwell, P. R. (2007), Laser diagnostics in MILD combustion., PhD thesis, Department of Mechanical Engineering.

Medwell, P. R., Blunck, D. L. & Dally, B. B. (2014), 'The role of precursors on the stabilisation of jet flames issuing into a hot environment', *Combustion and flame* **161**(2), 465–474.

Medwell, P. R. & Dally, B. B. (2012*a*), 'Effect of fuel composition on jet flames in a heated and diluted oxidant stream', *Combustion and flame* **159**(10), 3138–3145.

Medwell, P. R. & Dally, B. B. (2012*b*), 'Experimental observation of lifted flames in a heated and diluted coflow', *Energy & fuels* **26**(9), 5519–5527.

Medwell, P. R., Kalt, P. A. & Dally, B. B. (2007), 'Simultaneous imaging of oh, formaldehyde, and temperature of turbulent nonpremixed jet flames in a heated and diluted coflow', *Combustion and Flame* **148**(1-2), 48–61.

Medwell, P. R., Kalt, P. A. & Dally, B. B. (2008), 'Imaging of diluted turbulent ethylene flames stabilized on a jet in hot coflow (jhc) burner', *Combustion and Flame* **152**(1-2), 100–113.

Milani, A. & Saponaro, A. (2001), 'Diluted combustion technologies', *IFRF Combustion Journal* **1**, 1–32.

Miller, J. A. & Bowman, C. T. (1989), 'Mechanism and modeling of nitrogen chemistry in combustion', *Progress in energy and combustion science* **15**(4), 287–338.

Moin, P. & Mahesh, K. (1998), 'Direct numerical simulation: a tool in turbulence research', *Annual review of fluid mechanics* **30**(1), 539–578.

Moore, N., McCraw, J. & Lyons, K. (2008), 'Observations on jet-flame blowout', *International Journal of Reacting Systems* **2008**.

Moskaleva, L. & Lin, M. (2000), 'The spin-conserved reaction ch+n2h+ncn: A major pathway to prompt no studied by quantum/statistical theory calculations and kinetic modeling of rate constant', *Proceedings of the Combustion Institute* **28**(2), 2393–2401.

Oh, J., Noh, D. & Lee, E. (2013), 'The effect of co addition on the flame behavior of a non-premixed oxy-methane jet in a lab-scale furnace', *Applied energy* **112**, 350–357.

Oijen, van, J. (2002), Flamelet-generated manifolds: development and application to premixed laminar flames, PhD thesis, Department of Mechanical Engineering.

Oldenhof, E., Tummers, M., Van Veen, E. & Roekaerts, D. (2010), 'Ignition kernel formation and lift-off behaviour of jet-in-hot-coflow flames', *Combustion and Flame* **157**(6), 1167–1178.

Oldenhof, E., Tummers, M., Van Veen, E. & Roekaerts, D. (2011), 'Role of entrainment in the stabilisation of jet-in-hot-coflow flames', *Combustion and Flame* **158**(8), 1553–1563.

Park, O., Veloo, P., Liu, N. & Egolfopoulos, F. N. (2009), 'Propagation, Extinction, and Ignition of $CH_4/H_2/CO$/Air mixtures', *Fall Technical Meeting WSS-CI* pp. 09F–015.

Park, S. & Kim, Y. (2017), 'Effects of nitrogen dilution on the no_x formation characteristics of CH_4/CO/H_2 syngas counterflow non-premixed flames', *International Journal of Hydrogen Energy* **42**(16), 11945–11961.

Perpignan, A. A., Rao, A. G. & Roekaerts, D. J. (2018), 'Flameless combustion and its potential towards gas turbines', *Progress in Energy and Combustion Science* **69**, 28–62.

Peters, N. (1992), 'Fifteen lectures on laminar and turbulent combustion', *Ercoftac Summer School* **1428**, 245.

Peters, N. (2000), *Turbulent combustion*, Cambridge University.

Poinsot, T. & Veynante, D. (2005), *Theoretical and numerical combustion*, RT Edwards, Inc.

Pope, S. B. (2000), *Turbulent flows*, Cambridge University Press.

Popovich, N. (2016), 'The synergy of rocks, rafts and rivers: a brief primer on hydrodynamics'. *https://watershed.ucdavis.edu/education/classes/ecogeomorphology-grand-canyon-2016/flogs/synergy*-rocks-rafts-and-rivers-brief-primer- hydrodynamics. Accesed-2020-12-03.

Rossini, F. D., Stull, D. & Prophet, M. (1971), 'Janaf thermochemical tables'.

Sabia, P., De Joannon, M., Fierro, S., Tregrossi, A. & Cavaliere, A. (2007), 'Hydrogen-enriched methane mild combustion in a well stirred reactor', *Experimental Thermal and Fluid Science* **31**(5), 469–475.

Sabia, P., de Joannon, M., Picarelli, A. & Ragucci, R. (2013), 'Methane auto-ignition delay times and oxidation regimes in mild combustion at atmospheric pressure', *Combustion and Flame* **160**(1), 47–55.

Sahu, A. B. & Ravikrishna, R. V. (2016), 'Quantitative LIF measurements and kinetics assessment of NO formation in H_2/CO syngas–air counterflow diffusion flames', *Combustion and Flame* **173**, 208–228.

Sepman, A., Abtahizadeh, S., Mokhov, A., van Oijen, J., Levinsky, H. & de Goey, L. (2013), 'Numerical and experimental studies of the no formation in laminar coflow diffusion flames on their transition to mild combustion regime', *Combustion and Flame* **160**(8), 1364–1372.

Sequera, D. & Agrawal, A. K. (2007), Effect of fuel composition on emissions from a low-swirl burner, *in* 'ASME Turbo Expo 2007: Power for Land, Sea, and Air', American Society of Mechanical Engineers, pp. 789–799.

Shih, H.-Y. (2009), 'Computed extinction limits and flame structures of h2/o2 counterflow diffusion flames with co2 dilution', *International Journal of Hydrogen Energy* **34**(9), 4005–4013.

Siemens Digital Industries Software (2016), 'Simcenter STAR-CCM+ User Guide v. 2016'.

Singh, A. & Agrawal, M. (2007), 'Acid rain and its ecological consequences', *Journal of Environmental Biology* **29**(1), 15.

Smith, G. P., Golden, D. M., Frenklach, M., Moriarty, N. W., Eiteneer, B., Goldenberg, M., Bowman, C. T., Hanson, R. K., Song, S., Gardiner Jr, W. C. et al. (1999), 'Gri 3.0 mechanism', *Gas Research Institute, Des Plaines, IL, accessed Aug* **21**, 2017.

Som, S., Ramirez, A. I., Hagerdorn, J., Saveliev, A. & Aggarwal, S. K. (2008), 'A numerical and experimental study of counterflow syngas flames at different pressures', *Fuel* **87**(3), 319–334.

Somers, L. M. T. (1994), 'The simulation of flat flames with detailed and reduced chemical models', *Eindhoven University of Technology, Eindhoven* .

Staffelbach, G., Senoner, J. M., Gicquel, L. & Poinsot, T. (2008), Large eddy simulation of combustion on massively parallel machines, *in* 'International Conference on High Performance Computing for Computational Science', Springer, pp. 444–464.

Tang, Z., Ma, P., Li, Y.-L., Tang, C., Xing, X. & Lin, Q. (2010), 'Design and experiment research of a novel pulverized coal gasifier based on flameless oxidation technology', *Proc CSEE* **30**(8), 50–55.

Turns, S. (2000), *An Introduction to Combustion: Concepts and Application*, Mc Graw Hill.

Typical setup of flue gas recirculation system with WM burner (n.d.). Accessed: 2020-09-25. **URL:** *https://www.weishaupt-corp.com/presse/fachpresse/2017/gasbrenner-in-lownox-ausfuehrung-4ln-mit-abgasrueckfuehrung-bis-23-000-kw*

UNEP & Partnership, U. D. (2020), Emissions gap report 2020, Technical report, United Nations, Nairobi.

Van Oijen, J. (2013), 'Direct numerical simulation of autoigniting mixing layers in mild combustion', *Proceedings of the Combustion Institute* **34**(1), 1163–1171.

Van Oijen, J., Bastiaans, R. & De Goey, L. (2007), 'Low-dimensional manifolds in direct numerical simulations of premixed turbulent flames', *Proceedings of the Combustion Institute* **31**(1), 1377–1384.

Wang, Z., Fan, J., Zhou, J. & Cen, K. (2007), 'Direct numerical simulation of hydrogen turbulent lifted jet flame in a vitiated coflow', *Chinese Science Bulletin* **52**(15), 2147–2156.

Wang, Z., Fan, J., Zhou, J. & Cen, K. Wang . (2007), 'Usc mech version ii, high-temperature combustion reaction model of h2/co/c1-c4 compounds'. URL: http://ignis.usc.edu/USCMechII.htm

Warnatz, J., Maas, U. & Dibble, R. (1996), 'Combustion springer-verlag'.

Williams, F. A. (1985), *Combustion Theory*, Benjamin and Cummings, Menlo park, California, The US.

Wu, C.-Y., Chao, Y.-C., Cheng, T., Chen, C.-P. & Ho, C.-T. (2009), 'Effects of co addition on the characteristics of laminar premixed ch4/air opposed-jet flames', *Combustion and Flame* **156**(2), 362–373.

Wu, C.-Y., Li, Y.-H. & Chang, T.-W. (2012), 'Effects of co addition on the propagation characteristics of laminar ch4 triple flame', *Combustion and flame* **159**(9), 2806–2816.

Wünning, J. A. & Wünning, J. G. (1997), 'Flameless oxidation to reduce thermal NO-formation', *Progress in energy and combustion science* **23**(1), 81–94.

Ye, J., Medwell, P. R., Kleinheinz, K., Evans, M. J., Dally, B. B. & Pitsch, H. G. (2018), 'Structural differences of ethanol and dme jet flames in a hot diluted coflow', *Combustion and Flame* **192**, 473–494.

Yoo, C. S., Sankaran, R. & Chen, J. (2009), 'Three-dimensional direct numerical simulation of a turbulent lifted hydrogen jet flame in heated coflow: flame stabilization and structure', *Journal of Fluid Mechanics* **640**(1), 453–481.

Zhou, H., Yang, T., Dally, B. & Ren, Z. (2020), 'Les/tpdf investigation of the role of reaction and diffusion timescales in the stabilization of a jet-in-hot-coflow ch4/h2 flame', *Combustion and Flame* **211**, 477–492.

Zhu, R. & Lin, M.-C. (2005), 'Ab initio study of the oxidation of ncn by o2', *International journal of chemical kinetics* **37**(10), 593–598.

Zhu, R. & Lin, M.-C. (2007), 'Ab initio study on the oxidation of ncn by o (3p): Prediction of the total rate constant and product branching ratios', *The Journal of Physical Chemistry A* **111**(29), 6766–6771.

Zhu, R., Nguyen, H. M. & Lin, M.-C. (2009), 'Ab initio study on the oxidation of ncn by oh: prediction of the individual and total rate constants', *The Journal of Physical Chemistry A* **113**(1), 298–304.

Appendix A. MATLAB program for the addition of exhaust gas to oxidiser

MATLAB program used for the addition of exhaust gas to fresh oxidiser is given in Listing A.1. The program also includes script to write the inlet composition (exhaust gas and oxidiser mixture) to a file that can be used as the oxidiser stream input to run counterflow diffusion flame using CHEM1D.

Listing A.1 MATLAB program for the addition of exhaust gas to oxidiser

```
clear all; close all; clc;

global Runiv El Sp1 Re PHI P
load species_36.mat;
load element.mat;
Runiv = 8.314;                  % Universal gas constant
P = 1.01325e5;                  % Atmospheric pressure
PHI = 1.0;                      % Constant

Tf = 300;                       % Fuel temperature
T_egr = 1400;                   % Exhaust gas temperature

target.dir = '';
results.dir = '';

egr = 0.00;                     % EGR mass fraction Y_egr

for n1 = 1:53

X(n1) = 0;

end

%%% oxidizer composition without exhaust gas
```

```
X(4) = 0.21;
X(48) = 0.79;

for n2 = 1:53

Y1(n2) = 0;

end

Y1(4) = 0.2329175 ;
Y1(48) = 0.767082 ;

Loop = 21;
EgrStep = 0.05;

% Addition of exhaust gas in oxidiser based on the exhaust gas mass fra
% Exhaust gas mass fraction (Y_egr) in the oxidiser stream can be incre
% 1.EgrStep can be used to specify the step size in which the exhaust m
% fraction is increased in the oxidiser stream. For EgrStep=0.05, the
% number of steps required to reach Y_egr=1 is 21 (=Loop).

for n = 1:Loop


MeanMolarMass = 0;

for n3 = 1:36

X_in(n3) = 0;

end

% Stoichiometric composition of fuel and oxidiser to calculate burnt ga

X_in(1) = 0.017897727272 ;
X_in(4) = 0.184943181818 ;
X_in(14) = 0.0835227272727 ;
X_in(15) = 0.017897727272 ;
X_in(31) = 0.69573863 ;

% Calculation of equilibrium mixture or the burnt gas mixture

[X_eqi,T_eq] = ChemEquil(X_in,300,101325);
```

```
% addition of exhaust gas in oxidiser stream

for vb = 1:30

X_eq(vb) = X_eqi(vb);

end

for vb = 1:17

X_eq(30+vb) = 0;

end

for vb = 1:6

X_eq(47+vb) = X_eqi(30+vb);

end

for n4 = 1:53

MeanMolarMass = (MeanMolarMass + X_eq(n4)*[Sp1(1,n4).Mass * 1000]) ;
end

for n5 = 1:53

Y_eq(n5) = [(Sp1(1,n5).Mass * 1000) / MeanMolarMass] * X_eq(n5);

end

Y_egr = Y_eq;
Y = egr * Y_egr;
Y(4) = Y(4) + (1-egr) * Y1(4);
Y(48) = Y(48) + (1-egr) * Y1(48);

ONEbyWmean = 0;

for n6 = 1:53

ONEbyWmean = ONEbyWmean + [Y(n6)/(Sp1(1,n6).Mass*1000)];
```

```
end

Wmean = 1 / ONEbyWmean;

for n7 = 1:53

X(n7) =     (Wmean / [Sp1(1,n7).Mass*1000]) * Y(n7);

end

total_X = sum(X);
total_Y = sum(Y);

for h_c = 1:53

h_f(h_c) = ThermProp(Tf,Sp1(h_c),'Enthalpy','Mass');

end

for h_c = 1:53

h_egr(h_c) = ThermProp(T_egr,Sp1(h_c),'Enthalpy','Mass');

end

h_f_tot = dot(Y1,h_f);
h_egr_tot = dot(Y_egr,h_egr);
h_mix = egr*h_egr_tot + (1-egr)*h_f_tot;
Tin_egr = 300;
DeltaT_egr = 10;

while abs(DeltaT_egr)>1.0e-10

for i=1:53

hi(i) = ThermProp(Tin_egr,Sp1(i),'Enthalpy','Mass');

end

h_mixn_egr = dot(Y,hi);

for i=1:53
```

```
cpi(i) = ThermProp(Tin_egr,Sp1(i),'Cp','Mass');

end

cp_mixn_egr = dot(Y,cpi);
DeltaT_egr = (h_mix-h_mixn_egr)/cp_mixn_egr;
Tin_egr=Tin_egr+DeltaT_egr;

end

Tin = Tin_egr;

% Writing the oxidiser composition and temperature in a
% file for simulations input

fid = fopen('settings.csf','a');

fprintf(fid,'[GASMIXTURE_OXIDIZERCOMPOSITION]\n');
fprintf(fid,'H2      %4.4E\n',X(1));
fprintf(fid,'H       %4.4E\n',X(2));
fprintf(fid,'O       %4.4E\n',X(3));
fprintf(fid,'O2      %4.4E\n',X(4));
fprintf(fid,'OH      %4.4E\n',X(5));
fprintf(fid,'H2O     %4.4E\n',X(6));
fprintf(fid,'HO2     %4.4E\n',X(7));
fprintf(fid,'H2O2    %4.4E\n',X(8));
fprintf(fid,'C       %4.4E\n',X(9));
fprintf(fid,'CH      %4.4E\n',X(10));
fprintf(fid,'CH2     %4.4E\n',X(11));
fprintf(fid,'CH2(S)  %4.4E\n',X(12));
fprintf(fid,'CH3     %4.4E\n',X(13));
fprintf(fid,'CH4     %4.4E\n',X(14));
fprintf(fid,'CO      %4.4E\n',X(15));
fprintf(fid,'CO2     %4.4E\n',X(16));
fprintf(fid,'HCO     %4.4E\n',X(17));
fprintf(fid,'CH2O    %4.4E\n',X(18));
fprintf(fid,'CH2OH   %4.4E\n',X(19));
fprintf(fid,'CH3O    %4.4E\n',X(20));
fprintf(fid,'CH3OH   %4.4E\n',X(21));
fprintf(fid,'C2H     %4.4E\n',X(22));
fprintf(fid,'C2H2    %4.4E\n',X(23));
fprintf(fid,'C2H3    %4.4E\n',X(24));
fprintf(fid,'C2H4    %4.4E\n',X(25));
```

```
fprintf(fid,'C2H5      %4.4E\n',X(26));
fprintf(fid,'C2H6      %4.4E\n',X(27));
fprintf(fid,'HCCO      %4.4E\n',X(28));
fprintf(fid,'CH2CO     %4.4E\n',X(29));
fprintf(fid,'HCCOH     %4.4E\n',X(30));
fprintf(fid,'N         %4.4E\n',X(31));
fprintf(fid,'NH        %4.4E\n',X(32));
fprintf(fid,'NH2       %4.4E\n',X(33));
fprintf(fid,'NH3       %4.4E\n',X(34));
fprintf(fid,'NNH       %4.4E\n',X(35));
fprintf(fid,'NO        %4.4E\n',X(36));
fprintf(fid,'NO2       %4.4E\n',X(37));
fprintf(fid,'N2O       %4.4E\n',X(38));
fprintf(fid,'HNO       %4.4E\n',X(39));
fprintf(fid,'CN        %4.4E\n',X(40));
fprintf(fid,'HCN       %4.4E\n',X(41));
fprintf(fid,'H2CN      %4.4E\n',X(42));
fprintf(fid,'HCNN      %4.4E\n',X(43));
fprintf(fid,'HCNO      %4.4E\n',X(44));
fprintf(fid,'HOCN      %4.4E\n',X(45));
fprintf(fid,'HNCO      %4.4E\n',X(46));
fprintf(fid,'NCO       %4.4E\n',X(47));
fprintf(fid,'N2        %4.4E\n',X(48));
fprintf(fid,'AR        %4.4E\n',X(49));
fprintf(fid,'C3H7      %4.4E\n',X(50));
fprintf(fid,'C3H8      %4.4E\n',X(51));
fprintf(fid,'CH2CHO    %4.4E\n',X(52));
fprintf(fid,'CH3CHO    %4.4E\n',X(53));
fprintf(fid,'NCN       0.000\n');
fprintf(fid,'[ENDOF_OXIDIZERCOMPOSITION]\n');

fprintf(fid,'[BOUNDARY_INLETTEMPERATURE]\n');
fprintf(fid,'300.00    %4.4f\n',Tin);

if egr>0
fprintf(fid,'[PREPROCESSING_STARTSOLUTIONFILE]\n');
fprintf(fid,'yiend-%0.2f.dat',(egr-0.05));
end

fclose(fid);

% Running 1D simulations using chem1d
```

```
system('chem1d');

egr = egr + EgrStep;

end
```

Appendix B. Modified GRI 3.0 mechanism with NCN pathway

As mentioned in Chapter 3, the NCN pathway is implemented in the NO sub-mechanism of the GRI 3.0 mechanism, and the reaction relevant to HCN pathway is removed. The number of species and reactions in the modified GRI 3.0 mechanism are 54 and 329, respectively. Modified GRI 3.0 with NCN pathway is given in CHEMKIN format in Listing B .1. The coefficients of thermodynamic and transport properties (the NASA polynomials) of all the species of GRI 3.0 mechanism are also given in Listing B.2 and Listing B.3, respectively. It should be noted that these data are given in the standard CHEMKIN input format.

Listing B.1 Modified GRI 3.0 mechanism with NCN pathway for prompt NO calculations is given in CHEMKIN input format.

```
! GRI-Mech Version 3.0 7/30/99 CHEMKIN-II format
! See README30 file at anonymous FTP site unix.sri.com, directory gri;
! WorldWideWeb home page http://www.me.berkeley.edu/gri_mech/ or
! through http://www.gri.org , under 'Basic  Research',
! for additional information, contacts, and disclaimer
ELEMENTS
O H C N AR
END
SPECIES
H2          H           O           O2          OH          H2O         HO2         H2O2
C           CH          CH2         CH2(S)      CH3         CH4         CO          CO2
HCO         CH2O        CH2OH       CH3O        CH3OH       C2H         C2H2        C2H3
C2H4        C2H5        C2H6        HCCO        CH2CO       HCCOH       N           NH
NH2         NH3         NNH         NO          NO2         N2O         HNO         CN
HCN         H2CN        HCNN        HCNO        HOCN        HNCO        NCO         N2
AR          C3H7        C3H8        CH2CHO      CH3CHO      NCN
END
!THERMO
! Insert GRI-Mech thermodynamics here or use in default file
!END
REACTIONS
```

```
2O+M<=>O2+M                                1.200E+17   -1.000
.00
H2/ 2.40/ H2O/15.40/ CH4/ 2.00/ CO/ 1.75/ CO2/ 3.60/ C2H6/ 3.00/ AR/
.83/
O+H+M<=>OH+M                               5.000E+17   -1.000
.00
H2/2.00/ H2O/6.00/ CH4/2.00/ CO/1.50/ CO2/2.00/ C2H6/3.00/ AR/ .70/
O+H2<=>H+OH                                3.870E+04    2.700    6260.00
O+HO2<=>OH+O2                              2.000E+13     .000
.00
O+H2O2<=>OH+HO2                            9.630E+06    2.000    4000.00
O+CH<=>H+CO                                5.700E+13     .000
.00
O+CH2<=>H+HCO                              8.000E+13     .000
.00
O+CH2(S)<=>H2+CO                           1.500E+13     .000
.00
O+CH2(S)<=>H+HCO                           1.500E+13     .000
.00
O+CH3<=>H+CH2O                             5.060E+13     .000
.00
O+CH4<=>OH+CH3                             1.020E+09    1.500    8600.00
O+CO(+M)<=>CO2(+M)                         1.800E+10     .000    2385.00
LOW/ 6.020E+14     .000     3000.00/
H2/2.00/ O2/6.00/ H2O/6.00/ CH4/2.00/ CO/1.50/ CO2/3.50/ C2H6/3.00/ AR/ .50/
O+HCO<=>OH+CO                              3.000E+13     .000
.00
O+HCO<=>H+CO2                              3.000E+13     .000
.00
O+CH2O<=>OH+HCO                            3.900E+13     .000    3540.00
O+CH2OH<=>OH+CH2O                          1.000E+13     .000
.00
O+CH3O<=>OH+CH2O                           1.000E+13     .000
.00
O+CH3OH<=>OH+CH2OH                         3.880E+05    2.500    3100.00
O+CH3OH<=>OH+CH3O                          1.300E+05    2.500    5000.00
O+C2H<=>CH+CO                              5.000E+13     .000
.00
O+C2H2<=>H+HCCO                            1.350E+07    2.000    1900.00
O+C2H2<=>OH+C2H                            4.600E+19   -1.410   28950.00
O+C2H2<=>CO+CH2                            6.940E+06    2.000    1900.00
O+C2H3<=>H+CH2CO                           3.000E+13     .000
.00
O+C2H4<=>CH3+HCO                           1.250E+07    1.830     220.00
O+C2H5<=>CH3+CH2O                          2.240E+13     .000
.00
```

```
O+C2H6<=>OH+C2H5                                  8.980E+07    1.920    5690.00
O+HCCO<=>H+2CO                                    1.000E+14     .000
.00
O+CH2CO<=>OH+HCCO                                 1.000E+13     .000    8000.00
O+CH2CO<=>CH2+CO2                                 1.750E+12     .000    1350.00
O2+CO<=>O+CO2                                     2.500E+12     .000   47800.00
O2+CH2O<=>HO2+HCO                                 1.000E+14     .000   40000.00
H+O2+M<=>HO2+M                                    2.800E+18    -.860
.00
O2/  .00/ H2O/  .00/ CO/  .75/ CO2/1.50/ C2H6/1.50/ N2/  .00/ AR/  .00/
H+2O2<=>HO2+O2                                    2.080E+19   -1.240
.00
H+O2+H2O<=>HO2+H2O                                11.26E+18    -.760
.00
H+O2+N2<=>HO2+N2                                  2.600E+19   -1.240
.00
H+O2+AR<=>HO2+AR                                  7.000E+17    -.800
.00
H+O2<=>O+OH                                       2.650E+16    -.6707  17041.00
2H+M<=>H2+M                                       1.000E+18   -1.000
.00
H2/  .00/ H2O/  .00/ CH4/2.00/ CO2/  .00/ C2H6/3.00/ AR/  .63/
2H+H2<=>2H2                                       9.000E+16    -.600
.00
2H+H2O<=>H2+H2O                                   6.000E+19   -1.250
.00
2H+CO2<=>H2+CO2                                   5.500E+20   -2.000
.00
H+OH+M<=>H2O+M                                    2.200E+22   -2.000
.00
H2/  .73/ H2O/3.65/ CH4/2.00/ C2H6/3.00/ AR/  .38/
H+HO2<=>O+H2O                                     3.970E+12     .000     671.00
H+HO2<=>O2+H2                                     4.480E+13     .000    1068.00
H+HO2<=>2OH                                       0.840E+14     .000     635.00
H+H2O2<=>HO2+H2                                   1.210E+07    2.000    5200.00
H+H2O2<=>OH+H2O                                   1.000E+13     .000    3600.00
H+CH<=>C+H2                                       1.650E+14     .000
.00
H+CH2(+M)<=>CH3(+M)                               6.000E+14     .000
.00
LOW   /   1.040E+26    -2.760    1600.00/
TROE/    .5620   91.00   5836.00   8552.00/
H2/2.00/ H2O/6.00/ CH4/2.00/ CO/1.50/ CO2/2.00/ C2H6/3.00/ AR/  .70/
H+CH2(S)<=>CH+H2                                  3.000E+13     .000
.00
H+CH3(+M)<=>CH4(+M)                               13.90E+15    -.534     536.00
```

```
LOW   /   2.620E+33    -4.760    2440.00/
TROE/     .7830    74.00   2941.00   6964.00 /
H2/2.00/ H2O/6.00/ CH4/3.00/ CO/1.50/ CO2/2.00/ C2H6/3.00/ AR/ .70/
H+CH4<=>CH3+H2                                6.600E+08    1.620   10840.00
H+HCO(+M)<=>CH2O(+M)                          1.090E+12     .480    -260.00
LOW   /   2.470E+24    -2.570     425.00/
TROE/     .7824   271.00   2755.00   6570.00 /
H2/2.00/ H2O/6.00/ CH4/2.00/ CO/1.50/ CO2/2.00/ C2H6/3.00/ AR/ .70/
H+HCO<=>H2+CO                                 7.340E+13     .000
.00
H+CH2O(+M)<=>CH2OH(+M)                        5.400E+11     .454    3600.00
LOW   /   1.270E+32    -4.820    6530.00/
TROE/     .7187   103.00   1291.00   4160.00 /
H2/2.00/ H2O/6.00/ CH4/2.00/ CO/1.50/ CO2/2.00/ C2H6/3.00/
H+CH2O(+M)<=>CH3O(+M)                         5.400E+11     .454    2600.00
LOW   /   2.200E+30    -4.800    5560.00/
TROE/     .7580    94.00   1555.00   4200.00 /
H2/2.00/ H2O/6.00/ CH4/2.00/ CO/1.50/ CO2/2.00/ C2H6/3.00/
H+CH2O<=>HCO+H2                               5.740E+07    1.900    2742.00
H+CH2OH(+M)<=>CH3OH(+M)                       1.055E+12     .500      86.00
LOW   /   4.360E+31    -4.650    5080.00/
TROE/     .600   100.00   90000.0   10000.0 /
H2/2.00/ H2O/6.00/ CH4/2.00/ CO/1.50/ CO2/2.00/ C2H6/3.00/
H+CH2OH<=>H2+CH2O                             2.000E+13     .000
.00
H+CH2OH<=>OH+CH3                              1.650E+11     .650    -284.00
H+CH2OH<=>CH2(S)+H2O                          3.280E+13    -.090     610.00
H+CH3O(+M)<=>CH3OH(+M)                        2.430E+12     .515      50.00
LOW   /   4.660E+41    -7.440    14080.0/
TROE/     .700   100.00   90000.0 10000.00 /
H2/2.00/ H2O/6.00/ CH4/2.00/ CO/1.50/ CO2/2.00/ C2H6/3.00/
H+CH3O<=>H+CH2OH                              4.150E+07    1.630    1924.00
H+CH3O<=>H2+CH2O                              2.000E+13     .000
.00
H+CH3O<=>OH+CH3                               1.500E+12     .500    -110.00
H+CH3O<=>CH2(S)+H2O                           2.620E+14    -.230    1070.00
H+CH3OH<=>CH2OH+H2                            1.700E+07    2.100    4870.00
H+CH3OH<=>CH3O+H2                             4.200E+06    2.100    4870.00
H+C2H(+M)<=>C2H2(+M)                          1.000E+17   -1.000
.00
LOW   /   3.750E+33    -4.800    1900.00/
TROE/     .6464   132.00   1315.00   5566.00 /
H2/2.00/ H2O/6.00/ CH4/2.00/ CO/1.50/ CO2/2.00/ C2H6/3.00/ AR/ .70/
H+C2H2(+M)<=>C2H3(+M)                         5.600E+12     .000    2400.00
LOW   /   3.800E+40    -7.270    7220.00/
TROE/     .7507    98.50   1302.00   4167.00 /
```

```
H2/2.00/ H2O/6.00/ CH4/2.00/ CO/1.50/ CO2/2.00/ C2H6/3.00/ AR/ .70/
H+C2H3(+M)<=>C2H4(+M)                    6.080E+12     .270     280.00
LOW   /  1.400E+30   -3.860   3320.00/
TROE/    .7820  207.50  2663.00  6095.00 /
H2/2.00/ H2O/6.00/ CH4/2.00/ CO/1.50/ CO2/2.00/ C2H6/3.00/ AR/ .70/
H+C2H3<=>H2+C2H2                         3.000E+13     .000
.00
H+C2H4(+M)<=>C2H5(+M)                    0.540E+12     .454    1820.00
LOW   /  0.600E+42   -7.620   6970.00/
TROE/    .9753  210.00   984.00  4374.00 /
H2/2.00/ H2O/6.00/ CH4/2.00/ CO/1.50/ CO2/2.00/ C2H6/3.00/ AR/ .70/
H+C2H4<=>C2H3+H2                         1.325E+06    2.530   12240.00
H+C2H5(+M)<=>C2H6(+M)                    5.210E+17    -.990    1580.00
LOW   /  1.990E+41   -7.080   6685.00/
TROE/    .8422  125.00  2219.00  6882.00 /
H2/2.00/ H2O/6.00/ CH4/2.00/ CO/1.50/ CO2/2.00/ C2H6/3.00/ AR/ .70/
H+C2H5<=>H2+C2H4                         2.000E+12     .000
.00
H+C2H6<=>C2H5+H2                         1.150E+08    1.900    7530.00
H+HCCO<=>CH2(S)+CO                       1.000E+14     .000
.00
H+CH2CO<=>HCCO+H2                        5.000E+13     .000    8000.00
H+CH2CO<=>CH3+CO                         1.130E+13     .000    3428.00
H+HCCOH<=>H+CH2CO                        1.000E+13     .000
.00
H2+CO(+M)<=>CH2O(+M)                     4.300E+07    1.500   79600.00
LOW   /  5.070E+27   -3.420  84350.00/
TROE/    .9320  197.00  1540.00 10300.00 /
H2/2.00/ H2O/6.00/ CH4/2.00/ CO/1.50/ CO2/2.00/ C2H6/3.00/ AR/ .70/
OH+H2<=>H+H2O                            2.160E+08    1.510    3430.00
2OH(+M)<=>H2O2(+M)                       7.400E+13    -.370
.00
LOW   /  2.300E+18    -.900  -1700.00/
TROE/    .7346   94.00  1756.00  5182.00 /
H2/2.00/ H2O/6.00/ CH4/2.00/ CO/1.50/ CO2/2.00/ C2H6/3.00/ AR/ .70/
2OH<=>O+H2O                              3.570E+04    2.400   -2110.00
OH+HO2<=>O2+H2O                          1.450E+13     .000    -500.00
DUPLICATE
OH+H2O2<=>HO2+H2O                        2.000E+12     .000     427.00
DUPLICATE
OH+H2O2<=>HO2+H2O                        1.700E+18     .000   29410.00
DUPLICATE
OH+C<=>H+CO                              5.000E+13     .000
.00
OH+CH<=>H+HCO                            3.000E+13     .000
.00
```

```
OH+CH2<=>H+CH2O                                  2.000E+13      .000
.00
OH+CH2<=>CH+H2O                                  1.130E+07     2.000     3000.00
OH+CH2(S)<=>H+CH2O                               3.000E+13      .000
.00
OH+CH3(+M)<=>CH3OH(+M)                           2.790E+18    -1.430     1330.00
LOW   /   4.000E+36    -5.920    3140.00/
TROE/    .4120   195.0   5900.00   6394.00/
H2/2.00/ H2O/6.00/ CH4/2.00/ CO/1.50/ CO2/2.00/ C2H6/3.00/
OH+CH3<=>CH2+H2O                                 5.600E+07     1.600     5420.00
OH+CH3<=>CH2(S)+H2O                              6.440E+17    -1.340     1417.00
OH+CH4<=>CH3+H2O                                 1.000E+08     1.600     3120.00
OH+CO<=>H+CO2                                    4.760E+07     1.228       70.00
OH+HCO<=>H2O+CO                                  5.000E+13      .000
.00
OH+CH2O<=>HCO+H2O                                3.430E+09     1.180     -447.00
OH+CH2OH<=>H2O+CH2O                              5.000E+12      .000
.00
OH+CH3O<=>H2O+CH2O                               5.000E+12      .000
.00
OH+CH3OH<=>CH2OH+H2O                             1.440E+06     2.000     -840.00
OH+CH3OH<=>CH3O+H2O                              6.300E+06     2.000     1500.00
OH+C2H<=>H+HCCO                                  2.000E+13      .000
.00
OH+C2H2<=>H+CH2CO                                2.180E-04     4.500    -1000.00
OH+C2H2<=>H+HCCOH                                5.040E+05     2.300    13500.00
OH+C2H2<=>C2H+H2O                                3.370E+07     2.000    14000.00
OH+C2H2<=>CH3+CO                                 4.830E-04     4.000    -2000.00
OH+C2H3<=>H2O+C2H2                               5.000E+12      .000
.00
OH+C2H4<=>C2H3+H2O                               3.600E+06     2.000     2500.00
OH+C2H6<=>C2H5+H2O                               3.540E+06     2.120      870.00
OH+CH2CO<=>HCCO+H2O                              7.500E+12      .000     2000.00
2HO2<=>O2+H2O2                                   1.300E+11      .000    -1630.00
DUPLICATE
2HO2<=>O2+H2O2                                   4.200E+14      .000    12000.00
DUPLICATE
HO2+CH2<=>OH+CH2O                                2.000E+13      .000
.00
HO2+CH3<=>O2+CH4                                 1.000E+12      .000
.00
HO2+CH3<=>OH+CH3O                                3.780E+13      .000
.00
HO2+CO<=>OH+CO2                                  1.500E+14      .000    23600.00
HO2+CH2O<=>HCO+H2O2                              5.600E+06     2.000    12000.00
C+O2<=>O+CO                                      5.800E+13      .000      576.00
```

```
C+CH2<=>H+C2H                                   5.000E+13      .000
.00
C+CH3<=>H+C2H2                                  5.000E+13      .000
.00
CH+O2<=>O+HCO                                   6.710E+13      .000
.00
CH+H2<=>H+CH2                                   1.080E+14      .000     3110.00
CH+H2O<=>H+CH2O                                 5.710E+12      .000     -755.00
CH+CH2<=>H+C2H2                                 4.000E+13      .000
.00
CH+CH3<=>H+C2H3                                 3.000E+13      .000
.00
CH+CH4<=>H+C2H4                                 6.000E+13      .000
.00
CH+CO(+M)<=>HCCO(+M)                            5.000E+13      .000
.00
LOW   /   2.690E+28    -3.740    1936.00/
TROE/    .5757   237.00   1652.00   5069.00  /
H2/2.00/ H2O/6.00/ CH4/2.00/ CO/1.50/ CO2/2.00/ C2H6/3.00/ AR/ .70/
CH+CO2<=>HCO+CO                                 1.900E+14      .000    15792.00
CH+CH2O<=>H+CH2CO                               9.460E+13      .000     -515.00
CH+HCCO<=>CO+C2H2                               5.000E+13      .000
.00
CH2+O2=>OH+H+CO                                 5.000E+12      .000     1500.00
CH2+H2<=>H+CH3                                  5.000E+05     2.000     7230.00
2CH2<=>H2+C2H2                                  1.600E+15      .000    11944.00
CH2+CH3<=>H+C2H4                                4.000E+13      .000
.00
CH2+CH4<=>2CH3                                  2.460E+06     2.000     8270.00
CH2+CO(+M)<=>CH2CO(+M)                          8.100E+11      .500     4510.00
LOW   /   2.690E+33    -5.110    7095.00/
TROE/    .5907   275.00   1226.00   5185.00  /
H2/2.00/ H2O/6.00/ CH4/2.00/ CO/1.50/ CO2/2.00/ C2H6/3.00/ AR/ .70/
CH2+HCCO<=>C2H3+CO                              3.000E+13      .000
.00
CH2(S)+N2<=>CH2+N2                              1.500E+13      .000      600.00
CH2(S)+AR<=>CH2+AR                              9.000E+12      .000      600.00
CH2(S)+O2<=>H+OH+CO                             2.800E+13      .000
.00
CH2(S)+O2<=>CO+H2O                              1.200E+13      .000
.00
CH2(S)+H2<=>CH3+H                               7.000E+13      .000
.00
CH2(S)+H2O(+M)<=>CH3OH(+M)                      4.820E+17    -1.160     1145.00
LOW   /   1.880E+38    -6.360    5040.00/
TROE/    .6027   208.00   3922.00   10180.0  /
```

```
H2/2.00/ H2O/6.00/ CH4/2.00/ CO/1.50/ CO2/2.00/ C2H6/3.00/
CH2(S)+H2O<=>CH2+H2O                          3.000E+13     .000
.00
CH2(S)+CH3<=>H+C2H4                           1.200E+13     .000    -570.00
CH2(S)+CH4<=>2CH3                             1.600E+13     .000    -570.00
CH2(S)+CO<=>CH2+CO                            9.000E+12     .000
.00
CH2(S)+CO2<=>CH2+CO2                          7.000E+12     .000
.00
CH2(S)+CO2<=>CO+CH2O                          1.400E+13     .000
.00
CH2(S)+C2H6<=>CH3+C2H5                        4.000E+13     .000    -550.00
CH3+O2<=>O+CH3O                               3.560E+13     .000   30480.00
CH3+O2<=>OH+CH2O                              2.310E+12     .000   20315.00
CH3+H2O2<=>HO2+CH4                            2.450E+04    2.470    5180.00
2CH3(+M)<=>C2H6(+M)                           6.770E+16   -1.180     654.00
LOW   /   3.400E+41    -7.030    2762.00/
TROE/    .6190   73.20   1180.00   9999.00 /
H2/2.00/ H2O/6.00/ CH4/2.00/ CO/1.50/ CO2/2.00/ C2H6/3.00/ AR/ .70/
2CH3<=>H+C2H5                                 6.840E+12     .100   10600.00
CH3+HCO<=>CH4+CO                              2.648E+13     .000
.00
CH3+CH2O<=>HCO+CH4                            3.320E+03    2.810    5860.00
CH3+CH3OH<=>CH2OH+CH4                         3.000E+07    1.500    9940.00
CH3+CH3OH<=>CH3O+CH4                          1.000E+07    1.500    9940.00
CH3+C2H4<=>C2H3+CH4                           2.270E+05    2.000    9200.00
CH3+C2H6<=>C2H5+CH4                           6.140E+06    1.740   10450.00
HCO+H2O<=>H+CO+H2O                            1.500E+18   -1.000   17000.00
HCO+M<=>H+CO+M                                1.870E+17   -1.000   17000.00
H2/2.00/ H2O/ .00/ CH4/2.00/ CO/1.50/ CO2/2.00/ C2H6/3.00/
HCO+O2<=>HO2+CO                               13.45E+12     .000     400.00
CH2OH+O2<=>HO2+CH2O                           1.800E+13     .000     900.00
CH3O+O2<=>HO2+CH2O                            4.280E-13    7.600   -3530.00
C2H+O2<=>HCO+CO                               1.000E+13     .000    -755.00
C2H+H2<=>H+C2H2                               5.680E+10    0.900    1993.00
C2H3+O2<=>HCO+CH2O                            4.580E+16   -1.390    1015.00
C2H4(+M)<=>H2+C2H2(+M)                        8.000E+12     .440   86770.00
LOW   /   1.580E+51    -9.300    97800.00/
TROE/    .7345   180.00   1035.00   5417.00 /
H2/2.00/ H2O/6.00/ CH4/2.00/ CO/1.50/ CO2/2.00/ C2H6/3.00/ AR/ .70/
C2H5+O2<=>HO2+C2H4                            8.400E+11     .000    3875.00
HCCO+O2<=>OH+2CO                              3.200E+12     .000     854.00
2HCCO<=>2CO+C2H2                              1.000E+13     .000
.00
N+NO<=>N2+O                                   2.700E+13     .000     355.00
N+O2<=>NO+O                                   9.000E+09    1.000    6500.00
```

```
N+OH<=>NO+H                                          3.360E+13      .000      385.00
N2O+O<=>N2+O2                                        1.400E+12      .000    10810.00
N2O+O<=>2NO                                          2.900E+13      .000    23150.00
N2O+H<=>N2+OH                                        3.870E+14      .000    18880.00
N2O+OH<=>N2+HO2                                      2.000E+12      .000    21060.00
N2O(+M)<=>N2+O(+M)                                   7.910E+10      .000    56020.00
LOW   /   6.370E+14      .000   56640.00/
H2/2.00/ H2O/6.00/ CH4/2.00/ CO/1.50/ CO2/2.00/ C2H6/3.00/ AR/ .625/
HO2+NO<=>NO2+OH                                      2.110E+12      .000     -480.00
NO+O+M<=>NO2+M                                       1.060E+20    -1.410
.00
H2/2.00/ H2O/6.00/ CH4/2.00/ CO/1.50/ CO2/2.00/ C2H6/3.00/ AR/ .70/
NO2+O<=>NO+O2                                        3.900E+12      .000     -240.00
NO2+H<=>NO+OH                                        1.320E+14      .000      360.00
NH+O<=>NO+H                                          4.000E+13      .000
.00
NH+H<=>N+H2                                          3.200E+13      .000      330.00
NH+OH<=>HNO+H                                        2.000E+13      .000
.00
NH+OH<=>N+H2O                                        2.000E+09     1.200
.00
NH+O2<=>HNO+O                                        4.610E+05     2.000     6500.00
NH+O2<=>NO+OH                                        1.280E+06     1.500      100.00
NH+N<=>N2+H                                          1.500E+13      .000
.00
NH+H2O<=>HNO+H2                                      2.000E+13      .000    13850.00
NH+NO<=>N2+OH                                        2.160E+13     -.230
.00
NH+NO<=>N2O+H                                        3.650E+14     -.450
.00
NH2+O<=>OH+NH                                        3.000E+12      .000
.00
NH2+O<=>H+HNO                                        3.900E+13      .000
.00
NH2+H<=>NH+H2                                        4.000E+13      .000     3650.00
NH2+OH<=>NH+H2O                                      9.000E+07     1.500     -460.00
NNH<=>N2+H                                           3.300E+08      .000
.00
NNH+M<=>N2+H+M                                       1.300E+14     -.110     4980.00
H2/2.00/ H2O/6.00/ CH4/2.00/ CO/1.50/ CO2/2.00/ C2H6/3.00/ AR/ .70/
NNH+O2<=>HO2+N2                                      5.000E+12      .000
.00
NNH+O<=>OH+N2                                        2.500E+13      .000
.00
NNH+O<=>NH+NO                                        7.000E+13      .000
.00
```

```
NNH+H<=>H2+N2                                 5.000E+13      .000
.00
NNH+OH<=>H2O+N2                               2.000E+13      .000
.00
NNH+CH3<=>CH4+N2                              2.500E+13      .000
.00
H+NO+M<=>HNO+M                                4.480E+19    -1.320      740.00
H2/2.00/ H2O/6.00/ CH4/2.00/ CO/1.50/ CO2/2.00/ C2H6/3.00/ AR/ .70/
HNO+O<=>NO+OH                                 2.500E+13      .000
.00
HNO+H<=>H2+NO                                 9.000E+11      .720      660.00
HNO+OH<=>NO+H2O                               1.300E+07     1.900     -950.00
HNO+O2<=>HO2+NO                               1.000E+13      .000    13000.00
CN+O<=>CO+N                                   7.700E+13      .000
.00
CN+OH<=>NCO+H                                 4.000E+13      .000
.00
CN+H2O<=>HCN+OH                               8.000E+12      .000     7460.00
CN+O2<=>NCO+O                                 6.140E+12      .000     -440.00
CN+H2<=>HCN+H                                 2.950E+05     2.450     2240.00
NCO+O<=>NO+CO                                 2.350E+13      .000
.00
NCO+H<=>NH+CO                                 5.400E+13      .000
.00
NCO+OH<=>NO+H+CO                              0.250E+13      .000
.00
NCO+N<=>N2+CO                                 2.000E+13      .000
.00
NCO+O2<=>NO+CO2                               2.000E+12      .000    20000.00
NCO+M<=>N+CO+M                                3.100E+14      .000    54050.00
H2/2.00/ H2O/6.00/ CH4/2.00/ CO/1.50/ CO2/2.00/ C2H6/3.00/ AR/ .70/
NCO+NO<=>N2O+CO                               1.900E+17    -1.520      740.00
NCO+NO<=>N2+CO2                               3.800E+18    -2.000      800.00
HCN+M<=>H+CN+M                                1.040E+29    -3.300   126600.00
H2/2.00/ H2O/6.00/ CH4/2.00/ CO/1.50/ CO2/2.00/ C2H6/3.00/ AR/ .70/
HCN+O<=>NCO+H                                 2.030E+04     2.640     4980.00
HCN+O<=>NH+CO                                 5.070E+03     2.640     4980.00
HCN+O<=>CN+OH                                 3.910E+09     1.580    26600.00
HCN+OH<=>HOCN+H                               1.100E+06     2.030    13370.00
HCN+OH<=>HNCO+H                               4.400E+03     2.260     6400.00
HCN+OH<=>NH2+CO                               1.600E+02     2.560     9000.00
H+HCN(+M)<=>H2CN(+M)                          3.300E+13      .000
.00
LOW /   1.400E+26    -3.400      1900.00/
H2/2.00/ H2O/6.00/ CH4/2.00/ CO/1.50/ CO2/2.00/ C2H6/3.00/ AR/ .70/
H2CN+N<=>N2+CH2                               6.000E+13      .000      400.00
```

```
C+N2<=>CN+N                                6.300E+13    .000   46020.00
CH+N2<=>NCN+H                              3.120E+09   0.880   20130.00
! Changed reaction products to NCN
CH+N2(+M)<=>HCNN(+M)                       3.100E+12    .150
.00
LOW   /   1.300E+25   -3.160    740.00/
TROE/    .6670   235.00   2117.00   4536.00 /
H2/2.00/ H2O/6.00/ CH4/2.00/ CO/1.50/ CO2/2.00/ C2H6/3.00/ AR/ 1.0/
CH2+N2<=>HCN+NH                            1.000E+13    .000   74000.00
CH2(S)+N2<=>NH+HCN                         1.000E+11    .000   65000.00
C+NO<=>CN+O                                1.900E+13    .000
.00
C+NO<=>CO+N                                2.900E+13    .000
.00
CH+NO<=>HCN+O                              4.100E+13    .000
.00
CH+NO<=>H+NCO                              1.620E+13    .000
.00
CH+NO<=>N+HCO                              2.460E+13    .000
.00
CH2+NO<=>H+HNCO                            3.100E+17  -1.380    1270.00
CH2+NO<=>OH+HCN                            2.900E+14   -.690     760.00
CH2+NO<=>H+HCNO                            3.800E+13   -.360     580.00
CH2(S)+NO<=>H+HNCO                         3.100E+17  -1.380    1270.00
CH2(S)+NO<=>OH+HCN                         2.900E+14   -.690     760.00
CH2(S)+NO<=>H+HCNO                         3.800E+13   -.360     580.00
CH3+NO<=>HCN+H2O                           9.600E+13    .000   28800.00
CH3+NO<=>H2CN+OH                           1.000E+12    .000   21750.00
HCNN+O<=>CO+H+N2                           2.200E+13    .000
.00
HCNN+O<=>HCN+NO                            2.000E+12    .000
.00
HCNN+O2<=>O+HCO+N2                         1.200E+13    .000
.00
HCNN+OH<=>H+HCO+N2                         1.200E+13    .000
.00
HCNN+H<=>CH2+N2                            1.000E+14    .000
.00
HNCO+O<=>NH+CO2                            9.800E+07   1.410    8500.00
HNCO+O<=>HNO+CO                            1.500E+08   1.570   44000.00
HNCO+O<=>NCO+OH                            2.200E+06   2.110   11400.00
HNCO+H<=>NH2+CO                            2.250E+07   1.700    3800.00
HNCO+H<=>H2+NCO                            1.050E+05   2.500   13300.00
HNCO+OH<=>NCO+H2O                          3.300E+07   1.500    3600.00
HNCO+OH<=>NH2+CO2                          3.300E+06   1.500    3600.00
HNCO+M<=>NH+CO+M                           1.180E+16    .000   84720.00
```

```
H2/2.00/ H2O/6.00/ CH4/2.00/ CO/1.50/ CO2/2.00/ C2H6/3.00/ AR/ .70/
HCNO+H<=>H+HNCO                                  2.100E+15   -.690    2850.00
HCNO+H<=>OH+HCN                                  2.700E+11    .180    2120.00
HCNO+H<=>NH2+CO                                  1.700E+14   -.750    2890.00
HOCN+H<=>H+HNCO                                  2.000E+07   2.000    2000.00
HCCO+NO<=>HCNO+CO                                0.900E+13    .000
.00
CH3+N<=>H2CN+H                                   6.100E+14   -.310     290.00
CH3+N<=>HCN+H2                                   3.700E+12    .150     -90.00
NH3+H<=>NH2+H2                                   5.400E+05   2.400    9915.00
NH3+OH<=>NH2+H2O                                 5.000E+07   1.600     955.00
NH3+O<=>NH2+OH                                   9.400E+06   1.940    6460.00
NH+CO2<=>HNO+CO                                  1.000E+13    .000   14350.00
CN+NO2<=>NCO+NO                                  6.160E+15  -0.752     345.00
NCO+NO2<=>N2O+CO2                                3.250E+12    .000    -705.00
N+CO2<=>NO+CO                                    3.000E+12    .000   11300.00
O+CH3=>H+H2+CO                                   3.370E+13    .000
.00
O+C2H4<=>H+CH2CHO                                6.700E+06   1.830     220.00
O+C2H5<=>H+CH3CHO                                1.096E+14    .000
.00
OH+HO2<=>O2+H2O                                  0.500E+16    .000   17330.00
DUPLICATE
OH+CH3=>H2+CH2O                                  8.000E+09    .500   -1755.00
CH+H2(+M)<=>CH3(+M)                              1.970E+12    .430    -370.00
LOW/ 4.820E+25  -2.80  590.0 /
TROE/ .578  122.0  2535.0  9365.0 /
H2/2.00/ H2O/6.00/ CH4/2.00/ CO/1.50/ CO2/2.00/ C2H6/3.00/ AR/ .70/
CH2+O2=>2H+CO2                                   5.800E+12    .000    1500.00
CH2+O2<=>O+CH2O                                  2.400E+12    .000    1500.00
CH2+CH2=>2H+C2H2                                 2.000E+14    .000   10989.00
CH2(S)+H2O=>H2+CH2O                              6.820E+10    .250    -935.00
C2H3+O2<=>O+CH2CHO                               3.030E+11    .290      11.00
C2H3+O2<=>HO2+C2H2                               1.337E+06   1.610    -384.00
O+CH3CHO<=>OH+CH2CHO                             2.920E+12    .000    1808.00
O+CH3CHO=>OH+CH3+CO                              2.920E+12    .000    1808.00
O2+CH3CHO=>HO2+CH3+CO                            3.010E+13    .000   39150.00
H+CH3CHO<=>CH2CHO+H2                             2.050E+09   1.160    2405.00
H+CH3CHO=>CH3+H2+CO                              2.050E+09   1.160    2405.00
OH+CH3CHO=>CH3+H2O+CO                            2.343E+10   0.730   -1113.00
HO2+CH3CHO=>CH3+H2O2+CO                          3.010E+12    .000   11923.00
CH3+CH3CHO=>CH3+CH4+CO                           2.720E+06   1.770    5920.00
H+CH2CO(+M)<=>CH2CHO(+M)                         4.865E+11   0.422   -1755.00
LOW/ 1.012E+42  -7.63  3854.0/
TROE/ 0.465  201.0  1773.0  5333.0 /
H2/2.00/ H2O/6.00/ CH4/2.00/ CO/1.50/ CO2/2.00/ C2H6/3.00/ AR/ .70/
```

```
O+CH2CHO=>H+CH2+CO2                                1.500E+14     .000        .00
O2+CH2CHO=>OH+CO+CH2O                              1.810E+10     .000        .00
O2+CH2CHO=>OH+2HCO                                 2.350E+10     .000        .00
H+CH2CHO<=>CH3+HCO                                 2.200E+13     .000        .00
H+CH2CHO<=>CH2CO+H2                                1.100E+13     .000        .00
OH+CH2CHO<=>H2O+CH2CO                              1.200E+13     .000        .00
OH+CH2CHO<=>HCO+CH2OH                              3.010E+13     .000        .00
CH3+C2H5(+M)<=>C3H8(+M)                            .9430E+13     .000        .00
LOW/ 2.710E+74  -16.82  13065.0 /
TROE/ .1527  291.0  2742.0  7748.0 /
H2/2.00/ H2O/6.00/ CH4/2.00/ CO/1.50/ CO2/2.00/ C2H6/3.00/ AR/ .70/
O+C3H8<=>OH+C3H7                                   1.930E+05     2.680    3716.00
H+C3H8<=>C3H7+H2                                   1.320E+06     2.540    6756.00
OH+C3H8<=>C3H7+H2O                                 3.160E+07     1.800     934.00
C3H7+H2O2<=>HO2+C3H8                               3.780E+02     2.720    1500.00
CH3+C3H8<=>C3H7+CH4                                0.903E+00     3.650    7154.00
CH3+C2H4(+M)<=>C3H7(+M)                            2.550E+06     1.600    5700.00
LOW/ 3.00E+63  -14.6  18170./
TROE/ .1894  277.0  8748.0  7891.0 /
H2/2.00/ H2O/6.00/ CH4/2.00/ CO/1.50/ CO2/2.00/ C2H6/3.00/ AR/ .70/
O+C3H7<=>C2H5+CH2O                                 9.640E+13     .000        .00
H+C3H7(+M)<=>C3H8(+M)                              3.613E+13     .000        .00
LOW/ 4.420E+61  -13.545  11357.0/
TROE/ .315  369.0  3285.0  6667.0 /
H2/2.00/ H2O/6.00/ CH4/2.00/ CO/1.50/ CO2/2.00/ C2H6/3.00/ AR/ .70/
H+C3H7<=>CH3+C2H5                                  4.060E+06     2.190     890.00
OH+C3H7<=>C2H5+CH2OH                               2.410E+13     .000        .00
HO2+C3H7<=>O2+C3H8                                 2.550E+10     0.255    -943.00
HO2+C3H7=>OH+C2H5+CH2O                             2.410E+13     .000        .00
CH3+C3H7<=>2C2H5                                   1.927E+13    -0.320       .00
NCN+H<=>HCN+N                                      1.890E+14     0.0      8425.0
! Adapated from Lin 2000
NCN+O<=>CN+NO                                      2.550E+13     0.15      -34.0
! Adapated from Lin 2005 and increased 2 times
NCN+OH<=>HCN+NO                                    4.690E+10     0.44     4000.0
! Adapated from Lin 2005
NCN+O2<=>NO+NCO                                    3.800E+09     0.51    24590.0
! Adapated from Lin 2005
END
```

Listing B.2 The coefficients of thermodynamic properties of various species of the GRI 3.0 mechanism in CHEMKIN input format.

```
THERMO
! GRI-Mech Version 3.0 Thermodynamics released 7/30/99
! NASA Polynomial format for CHEMKIN-II
```

```
! see README file for disclaimer
O                 L 1/90O   1                 G   200.000  3500.000
1000.000    1
2.56942078E+00-8.59741137E-05 4.19484589E-08-1.00177799E-11 1.22833691E-15
2
2.92175791E+04 4.78433864E+00 3.16826710E+00-3.27931884E-03 6.64306396E-06
3
-6.12806624E-09 2.11265971E-12 2.91222592E+04 2.05193346E+00
4
O2                TPIS89O   2                 G   200.000  3500.000
1000.000    1
3.28253784E+00 1.48308754E-03-7.57966669E-07 2.09470555E-10-2.16717794E-14
2
-1.08845772E+03 5.45323129E+00 3.78245636E+00-2.99673416E-03 9.84730201E-06
3
-9.68129509E-09 3.24372837E-12-1.06394356E+03 3.65767573E+00
4
H                 L 7/88H   1                 G   200.000  3500.000
1000.000    1
2.50000001E+00-2.30842973E-11 1.61561948E-14-4.73515235E-18 4.98197357E-22
2
2.54736599E+04-4.46682914E-01 2.50000000E+00 7.05332819E-13-1.99591964E-15
3
2.30081632E-18-9.27732332E-22 2.54736599E+04-4.46682853E-01
4
H2                TPIS78H   2                 G   200.000  3500.000
1000.000    1
3.33727920E+00-4.94024731E-05 4.99456778E-07-1.79566394E-10 2.00255376E-14
2
-9.50158922E+02-3.20502331E+00 2.34433112E+00 7.98052075E-03-1.94781510E-05
3
2.01572094E-08-7.37611761E-12-9.17935173E+02 6.83010238E-01
4
OH                RUS 78O   1H  1             G   200.000  3500.000
1000.000    1
3.09288767E+00 5.48429716E-04 1.26505228E-07-8.79461556E-11 1.17412376E-14
2
3.85865700E+03 4.47669610E+00 3.99201543E+00-2.40131752E-03 4.61793841E-06
3
-3.88113333E-09 1.36411470E-12 3.61508056E+03-1.03925458E-01
4
H2O               L 8/89H   2O  1             G   200.000  3500.000
1000.000    1
3.03399249E+00 2.17691804E-03-1.64072518E-07-9.70419870E-11 1.68200992E-14
2
```

```
-3.00042971E+04  4.96677010E+00  4.19864056E+00-2.03643410E-03  6.52040211E-06
3
-5.48797062E-09  1.77197817E-12-3.02937267E+04-8.49032208E-01
4
HO2                 L 5/89H   1O   2            G    200.000   3500.000
1000.000      1
4.01721090E+00  2.23982013E-03-6.33658150E-07  1.14246370E-10-1.07908535E-14
2
1.11856713E+02  3.78510215E+00  4.30179801E+00-4.74912051E-03  2.11582891E-05
3
-2.42763894E-08  9.29225124E-12  2.94808040E+02  3.71666245E+00
4
H2O2                L 7/88H   2O   2            G    200.000   3500.000
1000.000      1
4.16500285E+00  4.90831694E-03-1.90139225E-06  3.71185986E-10-2.87908305E-14
2
-1.78617877E+04  2.91615662E+00  4.27611269E+00-5.42822417E-04  1.67335701E-05
3
-2.15770813E-08  8.62454363E-12-1.77025821E+04  3.43505074E+00
4
C                   L11/88C   1               G    200.000   3500.000
1000.000      1
2.49266888E+00  4.79889284E-05-7.24335020E-08  3.74291029E-11-4.87277893E-15
2
8.54512953E+04  4.80150373E+00  2.55423955E+00-3.21537724E-04  7.33792245E-07
3
-7.32234889E-10  2.66521446E-13  8.54438832E+04  4.53130848E+00
4
CH                  TPIS79C   1H   1            G    200.000   3500.000
1000.000      1
2.87846473E+00  9.70913681E-04  1.44445655E-07-1.30687849E-10  1.76079383E-14
2
7.10124364E+04  5.48497999E+00  3.48981665E+00  3.23835541E-04-1.68899065E-06
3
3.16217327E-09-1.40609067E-12  7.07972934E+04  2.08401108E+00
4
CH2                 L S/93C   1H   2            G    200.000   3500.000
1000.000      1
2.87410113E+00  3.65639292E-03-1.40894597E-06  2.60179549E-10-1.87727567E-14
2
4.62636040E+04  6.17119324E+00  3.76267867E+00  9.68872143E-04  2.79489841E-06
3
-3.85091153E-09  1.68741719E-12  4.60040401E+04  1.56253185E+00
4
CH2(S)              L S/93C   1H   2            G    200.000   3500.000
1000.000      1
```

```
2.29203842E+00  4.65588637E-03 -2.01191947E-06  4.17906000E-10 -3.39716365E-14
2
5.09259997E+04  8.62650169E+00  4.19860411E+00 -2.36661419E-03  8.23296220E-06
3
-6.68815981E-09  1.94314737E-12  5.04968163E+04 -7.69118967E-01
4
CH3                 L11/89C   1H   3            G   200.000  3500.000
1000.000      1
2.28571772E+00  7.23990037E-03 -2.98714348E-06  5.95684644E-10 -4.67154394E-14
2
1.67755843E+04  8.48007179E+00  3.67359040E+00  2.01095175E-03  5.73021856E-06
3
-6.87117425E-09  2.54385734E-12  1.64449988E+04  1.60456433E+00
4
CH4                 L 8/88C   1H   4            G   200.000  3500.000
1000.000      1
7.48514950E-02  1.33909467E-02 -5.73285809E-06  1.22292535E-09 -1.01815230E-13
2
-9.46834459E+03  1.84373180E+01  5.14987613E+00 -1.36709788E-02  4.91800599E-05
3
-4.84743026E-08  1.66693956E-11 -1.02466476E+04 -4.64130376E+00
4
CO                  TPIS79C   1O   1            G   200.000  3500.000
1000.000      1
2.71518561E+00  2.06252743E-03 -9.98825771E-07  2.30053008E-10 -2.03647716E-14
2
-1.41518724E+04  7.81868772E+00  3.57953347E+00 -6.10353680E-04  1.01681433E-06
3
9.07005884E-10 -9.04424499E-13 -1.43440860E+04  3.50840928E+00
4
CO2                 L 7/88C   1O   2            G   200.000  3500.000
1000.000      1
3.85746029E+00  4.41437026E-03 -2.21481404E-06  5.23490188E-10 -4.72084164E-14
2
-4.87591660E+04  2.27163806E+00  2.35677352E+00  8.98459677E-03 -7.12356269E-06
3
2.45919022E-09 -1.43699548E-13 -4.83719697E+04  9.90105222E+00
4
HCO                 L12/89H   1C   1O   1       G   200.000  3500.000
1000.000      1
2.77217438E+00  4.95695526E-03 -2.48445613E-06  5.89161778E-10 -5.33508711E-14
2
4.01191815E+03  9.79834492E+00  4.22118584E+00 -3.24392532E-03  1.37799446E-05
3
-1.33144093E-08  4.33768865E-12  3.83956496E+03  3.39437243E+00
4
```

```
CH2O                L  8/88H   2C   1O   1       G   200.000  3500.000
1000.000       1
1.76069008E+00 9.20000082E-03-4.42258813E-06 1.00641212E-09-8.83855640E-14
2
-1.39958323E+04 1.36563230E+01 4.79372315E+00-9.90833369E-03 3.73220008E-05
3
-3.79285261E-08 1.31772652E-11-1.43089567E+04 6.02812900E-01
4
CH2OH               GUNL93C   1H   3O   1       G   200.000  3500.000
1000.000       1
3.69266569E+00 8.64576797E-03-3.75101120E-06 7.87234636E-10-6.48554201E-14
2
-3.24250627E+03 5.81043215E+00 3.86388918E+00 5.59672304E-03 5.93271791E-06
3
-1.04532012E-08 4.36967278E-12-3.19391367E+03 5.47302243E+00
4
CH3O                121686C   1H   3O   1       G   300.00   3000.00
1000.000       1
0.03770799E+02 0.07871497E-01-0.02656384E-04 0.03944431E-08-0.02112616E-12
2
0.12783252E+03 0.02929575E+02 0.02106204E+02 0.07216595E-01 0.05338472E-04
3
-0.07377636E-07 0.02075610E-10 0.09786011E+04 0.13152177E+02
4
CH3OH               L  8/88C   1H   4O   1       G   200.000  3500.000
1000.000       1
1.78970791E+00 1.40938292E-02-6.36500835E-06 1.38171085E-09-1.17060220E-13
2
-2.53748747E+04 1.45023623E+01 5.71539582E+00-1.52309129E-02 6.52441155E-05
3
-7.10806889E-08 2.61352698E-11-2.56427656E+04-1.50409823E+00
4
C2H                 L  1/91C   2H   1       G   200.000  3500.000
1000.000       1
3.16780652E+00 4.75221902E-03-1.83787077E-06 3.04190252E-10-1.77232770E-14
2
6.71210650E+04 6.63589475E+00 2.88965733E+00 1.34099611E-02-2.84769501E-05
3
2.94791045E-08-1.09331511E-11 6.68393932E+04 6.22296438E+00
4
C2H2                L  1/91C   2H   2       G   200.000  3500.000
1000.000       1
4.14756964E+00 5.96166664E-03-2.37294852E-06 4.67412171E-10-3.61235213E-14
2
2.59359992E+04-1.23028121E+00 8.08681094E-01 2.33615629E-02-3.55171815E-05
3
```

```
 2.80152437E-08-8.50072974E-12  2.64289807E+04  1.39397051E+01
4
C2H3                L  2/92C    2H    3           G    200.000   3500.000
 1000.000      1
 3.01672400E+00  1.03302292E-02-4.68082349E-06  1.01763288E-09-8.62607041E-14
2
 3.46128739E+04  7.78732378E+00  3.21246645E+00  1.51479162E-03  2.59209412E-05
3
-3.57657847E-08  1.47150873E-11  3.48598468E+04  8.51054025E+00
4
C2H4                L  1/91C    2H    4           G    200.000   3500.000
 1000.000      1
 2.03611116E+00  1.46454151E-02-6.71077915E-06  1.47222923E-09-1.25706061E-13
2
 4.93988614E+03  1.03053693E+01  3.95920148E+00-7.57052247E-03  5.70990292E-05
3
-6.91588753E-08  2.69884373E-11  5.08977593E+03  4.09733096E+00
4
C2H5                L12/92C    2H    5           G    200.000   3500.000
 1000.000      1
 1.95465642E+00  1.73972722E-02-7.98206668E-06  1.75217689E-09-1.49641576E-13
2
 1.28575200E+04  1.34624343E+01  4.30646568E+00-4.18658892E-03  4.97142807E-05
3
-5.99126606E-08  2.30509004E-11  1.28416265E+04  4.70720924E+00
4
C2H6                L  8/88C    2H    6           G    200.000   3500.000
 1000.000      1
 1.07188150E+00  2.16852677E-02-1.00256067E-05  2.21412001E-09-1.90002890E-13
2
-1.14263932E+04  1.51156107E+01  4.29142492E+00-5.50154270E-03  5.99438288E-05
3
-7.08466285E-08  2.68685771E-11-1.15222055E+04  2.66682316E+00
4
CH2CO               L  5/90C    2H    2O    1     G    200.000   3500.000
 1000.000      1
 4.51129732E+00  9.00359745E-03-4.16939635E-06  9.23345882E-10-7.94838201E-14
2
-7.55105311E+03  6.32247205E-01  2.13583630E+00  1.81188721E-02-1.73947474E-05
3
 9.34397568E-09-2.01457615E-12-7.04291804E+03  1.22156480E+01
4
HCCO                SRIC91H    1C    2O    1     G    300.00    4000.00
 1000.000      1
 0.56282058E+01  0.40853401E-02-0.15934547E-05  0.28626052E-09-0.19407832E-13
2
```

```
0.19327215E+05-0.39302595E+01 0.22517214E+01 0.17655021E-01-0.23729101E-04
3
0.17275759E-07-0.50664811E-11 0.20059449E+05 0.12490417E+02
4
HCCOH                SRI91C    2O    1H    2       G    300.000   5000.000
1000.000       1
0.59238291E+01 0.67923600E-02-0.25658564E-05 0.44987841E-09-0.29940101E-13
2
0.72646260E+04-0.76017742E+01 0.12423733E+01 0.31072201E-01-0.50866864E-04
3
0.43137131E-07-0.14014594E-10 0.80316143E+04 0.13874319E+02
4
H2CN                 41687H    2C    1N    1       G    300.00    4000.000
1000.000       1
0.52097030E+01 0.29692911E-02-0.28555891E-06-0.16355500E-09 0.30432589E-13
2
0.27677109E+05-0.44444780E+01 0.28516610E+01 0.56952331E-02 0.10711400E-05
3
-0.16226120E-08-0.23511081E-12 0.28637820E+05 0.89927511E+01
4
HCN                  GRI/98H   1C    1N    1       G    200.000   6000.000
1000.000       1
0.38022392E+01 0.31464228E-02-0.10632185E-05 0.16619757E-09-0.97997570E-14
2
0.14407292E+05 0.15754601E+01 0.22589886E+01 0.10051170E-01-0.13351763E-04
3
0.10092349E-07-0.30089028E-11 0.14712633E+05 0.89164419E+01
4
HNO                  And93 H   1N    1O    1       G    200.000   6000.000
1000.000       1
0.29792509E+01 0.34944059E-02-0.78549778E-06 0.57479594E-10-0.19335916E-15
2
0.11750582E+05 0.86063728E+01 0.45334916E+01-0.56696171E-02 0.18473207E-04
3
-0.17137094E-07 0.55454573E-11 0.11548297E+05 0.17498417E+01
4
N                    L 6/88N   1                G    200.000   6000.000
1000.000       1
0.24159429E+01 0.17489065E-03-0.11902369E-06 0.30226245E-10-0.20360982E-14
2
0.56133773E+05 0.46496096E+01 0.25000000E+01 0.00000000E+00 0.00000000E+00
3
0.00000000E+00 0.00000000E+00 0.56104637E+05 0.41939087E+01
4
NNH                  T07/93N   2H    1       G    200.000   6000.000
1000.000       1
```

```
0.37667544E+01  0.28915082E-02-0.10416620E-05  0.16842594E-09-0.10091896E-13
2
0.28650697E+05  0.44705067E+01  0.43446927E+01-0.48497072E-02  0.20059459E-04
3
-0.21726464E-07  0.79469539E-11  0.28791973E+05  0.29779410E+01
4
N2O                 L 7/88N   2O   1            G   200.000  6000.000
1000.000      1
0.48230729E+01  0.26270251E-02-0.95850874E-06  0.16000712E-09-0.97752303E-14
2
0.80734048E+04-0.22017207E+01  0.22571502E+01  0.11304728E-01-0.13671319E-04
3
0.96819806E-08-0.29307182E-11  0.87417744E+04  0.10757992E+02
4
NH                  And94 N   1H   1            G   200.000  6000.000
1000.000      1
0.27836928E+01  0.13298430E-02-0.42478047E-06  0.78348501E-10-0.55044470E-14
2
0.42120848E+05  0.57407799E+01  0.34929085E+01  0.31179198E-03-0.14890484E-05
3
0.24816442E-08-0.10356967E-11  0.41880629E+05  0.18483278E+01
4
NH2                 And89 N   1H   2            G   200.000  6000.000
1000.000      1
0.28347421E+01  0.32073082E-02-0.93390804E-06  0.13702953E-09-0.79206144E-14
2
0.22171957E+05  0.65204163E+01  0.42040029E+01-0.21061385E-02  0.71068348E-05
3
-0.56115197E-08  0.16440717E-11  0.21885910E+05-0.14184248E+00
4
NH3                 J 6/77N   1H   3            G   200.000  6000.000
1000.000      1
0.26344521E+01  0.56662560E-02-0.17278676E-05  0.23867161E-09-0.12578786E-13
2
-0.65446958E+04  0.65662928E+01  0.42860274E+01-0.46605230E-02  0.21718513E-04
3
-0.22808887E-07  0.82638046E-11-0.67417285E+04-0.62537277E+00
4
NO                  RUS 78N   1O   1            G   200.000  6000.000
1000.000      1
0.32606056E+01  0.11911043E-02-0.42917048E-06  0.69457669E-10-0.40336099E-14
2
0.99209746E+04  0.63693027E+01  0.42184763E+01-0.46389760E-02  0.11041022E-04
3
-0.93361354E-08  0.28035770E-11  0.98446230E+04  0.22808464E+01
4
```

```
NO2                 L 7/88N   1O   2            G   200.000  6000.000
1000.000      1
0.48847542E+01 0.21723956E-02-0.82806906E-06 0.15747510E-09-0.10510895E-13
2
0.23164983E+04-0.11741695E+00 0.39440312E+01-0.15854290E-02 0.16657812E-04
3
-0.20475426E-07 0.78350564E-11 0.28966179E+04 0.63119917E+01
4
HCNO                BDEA94H   1N   1C   1O   1G   300.000  5000.000
1382.000      1
6.59860456E+00 3.02778626E-03-1.07704346E-06 1.71666528E-10-1.01439391E-14
2
1.79661339E+04-1.03306599E+01 2.64727989E+00 1.27505342E-02-1.04794236E-05
3
4.41432836E-09-7.57521466E-13 1.92990252E+04 1.07332972E+01
4
HOCN                BDEA94H   1N   1C   1O   1G   300.000  5000.000
1368.000      1
5.89784885E+00 3.16789393E-03-1.11801064E-06 1.77243144E-10-1.04339177E-14
2
-3.70653331E+03-6.18167825E+00 3.78604952E+00 6.88667922E-03-3.21487864E-06
3
5.17195767E-10 1.19360788E-14-2.82698400E+03 5.63292162E+00
4
HNCO                BDEA94H   1N   1C   1O   1G   300.000  5000.000
1478.000      1
6.22395134E+00 3.17864004E-03-1.09378755E-06 1.70735163E-10-9.95021955E-15
2
-1.66599344E+04-8.38224741E+00 3.63096317E+00 7.30282357E-03-2.28050003E-06
3
-6.61271298E-10 3.62235752E-13-1.55873636E+04 6.19457727E+00
4
NCO                 EA 93 N   1C   1O   1      G   200.000  6000.000
1000.000      1
0.51521845E+01 0.23051761E-02-0.88033153E-06 0.14789098E-09-0.90977996E-14
2
0.14004123E+05-0.25442660E+01 0.28269308E+01 0.88051688E-02-0.83866134E-05
3
0.48016964E-08-0.13313595E-11 0.14682477E+05 0.95504646E+01
4
CN                  HBH92 C   1N   1            G   200.000  6000.000
1000.000      1
0.37459805E+01 0.43450775E-04 0.29705984E-06-0.68651806E-10 0.44134173E-14
2
0.51536188E+05 0.27867601E+01 0.36129351E+01-0.95551327E-03 0.21442977E-05
3
```

```
-0.31516323E-09-0.46430356E-12  0.51708340E+05  0.39804995E+01
4
HCNN                SRI/94C   1N   2H   1        G    300.000   5000.000
1000.000       1
0.58946362E+01  0.39895959E-02-0.15982380E-05  0.29249395E-09-0.20094686E-13
2
0.53452941E+05-0.51030502E+01  0.25243194E+01  0.15960619E-01-0.18816354E-04
3
0.12125540E-07-0.32357378E-11  0.54261984E+05  0.11675870E+02
4
N2                  121286N   2                 G    300.000   5000.000
1000.000       1
0.02926640E+02  0.14879768E-02-0.05684760E-05  0.10097038E-09-0.06753351E-13
2
-0.09227977E+04  0.05980528E+02  0.03298677E+02  0.14082404E-02-0.03963222E-04
3
0.05641515E-07-0.02444854E-10-0.10208999E+04  0.03950372E+02
4
AR                  120186AR  1                 G    300.000   5000.000
1000.000       1
0.02500000E+02  0.00000000E+00  0.00000000E+00  0.00000000E+00  0.00000000E+00
2
-0.07453750E+04  0.04366000E+02  0.02500000E+02  0.00000000E+00  0.00000000E+00
3
0.00000000E+00  0.00000000E+00-0.07453750E+04  0.04366000E+02
4
C3H8                L 4/85C   3H   8            G    300.000   5000.000
1000.000       1
0.75341368E+01  0.18872239E-01-0.62718491E-05  0.91475649E-09-0.47838069E-13
2
-0.16467516E+05-0.17892349E+02  0.93355381E+00  0.26424579E-01  0.61059727E-05
3
-0.21977499E-07  0.95149253E-11-0.13958520E+05  0.19201691E+02
4
C3H7                L 9/84C   3H   7            G    300.000   5000.000
1000.000       1
0.77026987E+01  0.16044203E-01-0.52833220E-05  0.76298590E-09-0.39392284E-13
2
0.82984336E+04-0.15480180E+02  0.10515518E+01  0.25991980E-01  0.23800540E-05
3
-0.19609569E-07  0.93732470E-11  0.10631863E+05  0.21122559E+02
4
CH3CHO              L 8/88C   2H   4O   1        G    200.000   6000.000
1000.000       1
0.54041108E+01  0.11723059E-01-0.42263137E-05  0.68372451E-09-0.40984863E-13
2
```

```
-0.22593122E+05-0.34807917E+01 0.47294595E+01-0.31932858E-02 0.47534921E-04
3
-0.57458611E-07 0.21931112E-10-0.21572878E+05 0.41030159E+01
4
CH2CHO               SAND86O   1H   3C   2      G   300.000   5000.000
1000.000      1
0.05975670E+02 0.08130591E-01-0.02743624E-04 0.04070304E-08-0.02176017E-12
2
0.04903218E+04-0.05045251E+02 0.03409062E+02 0.10738574E-01 0.01891492E-04
3
-0.07158583E-07 0.02867385E-10 0.15214766E+04 0.09558290E+02
4
!
! Thermodynamic data added by M.C. Lin
!
C2                   121286C   2                G   300.000   5000.000
1000.000      1
0.04135978E+02 0.06531618E-03 0.01837099E-05-0.05295085E-09 0.04712137E-13
2
0.09967272E+06 0.07472923E+01 0.06996045E+02-0.07400601E-01 0.03234703E-04
3
0.04802535E-07-0.03295917E-10 0.09897487E+06-0.13862268E+02
4
NCN                  32800C   1N   2    0      G   300.000   3000.000
1000.000      1     ! swapped upper -lower
0.46154976E+01 0.39674551E-02-0.22572669E-05 0.59242161E-09-0.59008401E-13
2
0.52131730E+05-0.58241642E+00 0.32398157E+01 0.60062278E-02-0.76348655E-07
3
-0.44237436E-08 0.21131475E-11 0.52580660E+05 0.69202528E+01
4
CH2N                 DUMMY C   1H   2N   1      G   300.000   5000.000
1000.000      1
0.54956026E+01 0.89018531E-02-0.29834273E-05 0.43930859E-09-0.23263757E-13
2
0.81332734E+04-0.55127306E+01 0.28112087E+01 0.11668280E-01 0.18374703E-05
3
-0.75577553E-08 0.30708968E-11 0.92079258E+04 0.97456837E+01
4
C2N2                 121286C   2N   2              G   300.000   5000.000
1000.000      1
0.06548002E+02 0.03984707E-01-0.16342164E-05 0.03038596E-08-0.02111069E-12
2
0.03490716E+06-0.09735790E+02 0.04265459E+02 0.11922569E-01-0.13420142E-04
3
```

```
0.09192297E-07-0.02778941E-10  0.03547887E+06  0.01713212E+02
4
CH3CN                9289 C    2H    3N    1       G    300.000   5000.000
1000.000       1
0.54956026E+01  0.89018531E-02-0.29834273E-05  0.43930859E-09-0.23263757E-13
2
0.81332734E+04-0.55127306E+01  0.28112087E+01  0.11668280E-01  0.18374703E-05
3
-0.75577553E-08  0.30708968E-11  0.92079258E+04  0.97456837E+01
4
H2CNH                41687C    1H    3N    1       G    300.000   4000.000
1000.000       1
0.05221589E+02  0.04748525E-01-0.04179158E-05-0.02606612E-08  0.04703140E-12
2
0.08657219E+05-0.04500776E+02  0.02365878E+02  0.06780570E-01  0.02422999E-04
3
-0.06157824E-08-0.16150971E-11  0.09971141E+05  0.12307176E+02
4
C2N                 121286C    2N    1            G    300.000   5000.000
1000.000       1
0.06151561E+02  0.15116498E-02-0.06629362E-05  0.12861485E-09-0.09160830E-13
2
0.06484318E+06-0.08177850E+02  0.03498544E+02  0.08554433E-01-0.06288697E-04
3
0.08638478E-08  0.04915996E-11  0.06556611E+06  0.05548374E+02
4
CH2CN               DUMMY C    2H    2N    1       G    300.000   5000.000
1000.000       1
0.54956026E+01  0.89018531E-02-0.29834273E-05  0.43930859E-09-0.23263757E-13
2
0.81332734E+04-0.55127306E+01  0.28112087E+01  0.11668280E-01  0.18374703E-05
3
-0.75577553E-08  0.30708968E-11  0.92079258E+04  0.97456837E+01
4
CH2NC               DUMMY C    2H    2N    1       G    300.000   5000.000
1000.000       1
0.54956026E+01  0.89018531E-02-0.29834273E-05  0.43930859E-09-0.23263757E-13
2
0.81332734E+04-0.55127306E+01  0.28112087E+01  0.11668280E-01  0.18374703E-05
3
-0.75577553E-08  0.30708968E-11  0.92079258E+04  0.97456837E+01
4
HCCN                DUMMY C    2H    1N    1       G    300.000   4000.000
1000.000       1
0.04923292E+02  0.03332897E-01-0.03370896E-05-0.01901619E-08  0.03531825E-12
2
```

```
0.03132669E+06-0.16325088E+01 0.02759456E+02 0.06103386E-01 0.07713149E-05
3
-0.02063093E-07 0.01931919E-11 0.03217247E+06 0.10574895E+02
4
NHC                 DUMMY C    1H    2N    1       G    300.000   5000.000
1000.000      1
0.54956026E+01 0.89018531E-02-0.29834273E-05 0.43930859E-09-0.23263757E-13
2
0.81332734E+04-0.55127306E+01 0.28112087E+01 0.11668280E-01 0.18374703E-05
3
-0.75577553E-08 0.30708968E-11 0.92079258E+04 0.97456837E+01
4
HNC                 112694H    1C    1N    1       G    300.000   5000.000
1000.000      1
0.40661430E+01 0.28766873E-02-0.10374717E-05 0.17645919E-09-0.11517431E-13
2
0.21937809E+05 0.66837311E+00 0.30930109E+01 0.89668389E-02-0.14020659E-04
3
0.11771928E-07-0.37408189E-11 0.22040590E+05 0.48591442E+01
4
HNCN                 32700C    1H    1N    2      0G    300.000   3000.000
1000.000      1    ! swap lower - upper
0.26862885E+02-0.39011814E-01 0.25372739E-04-0.69038868E-08 0.68006679E-12
2
0.27624725E+05-0.12037196E+03 0.30267920E+01 0.50517850E-01-0.15374081E-03
3
0.17043989E-06-0.63243702E-10 0.34849332E+05 0.11754123E+01
4
END
```

Listing B.3 The coefficients of transport properties of various species of the GRI 3.0 mechanism in CHEMKIN input format.

```
AR                  0      136.500      3.330      0.000      0.000      0.000
C                   0       71.400      3.298      0.000      0.000      0.000
C2                  1       97.530      3.621      0.000      1.760      4.000
C2O                 1      232.400      3.828      0.000      0.000      1.000
CN2                 1      232.400      3.828      0.000      0.000      1.000
C2H                 1      209.000      4.100      0.000      0.000      2.500
C2H2                1      209.000      4.100      0.000      0.000      2.500
C2H2OH              2      224.700      4.162      0.000      0.000      1.000
C2H3                2      209.000      4.100      0.000      0.000      1.000
C2H4                2      280.800      3.971      0.000      0.000      1.500
C2H5                2      252.300      4.302      0.000      0.000      1.500
C2H6                2      252.300      4.302      0.000      0.000      1.500
C2N                 1      232.400      3.828      0.000      0.000      1.000
```

C2N2	1	349.000	4.361	0.000	0.000	1.000
C3H2	2	209.000	4.100	0.000	0.000	1.000
C3H4	1	252.000	4.760	0.000	0.000	1.000
C3H6	2	266.800	4.982	0.000	0.000	1.000
C3H7	2	266.800	4.982	0.000	0.000	1.000
C4H6	2	357.000	5.180	0.000	0.000	1.000
I*C3H7	2	266.800	4.982	0.000	0.000	1.000
N*C3H7	2	266.800	4.982	0.000	0.000	1.000
C3H8	2	266.800	4.982	0.000	0.000	1.000
C4H	1	357.000	5.180	0.000	0.000	1.000
C4H2	1	357.000	5.180	0.000	0.000	1.000
C4H2OH	2	224.700	4.162	0.000	0.000	1.000
C4H8	2	357.000	5.176	0.000	0.000	1.000
C4H9	2	357.000	5.176	0.000	0.000	1.000
I*C4H9	2	357.000	5.176	0.000	0.000	1.000
C5H2	1	357.000	5.180	0.000	0.000	1.000
C5H3	1	357.000	5.180	0.000	0.000	1.000
C6H2	1	357.000	5.180	0.000	0.000	1.000
C6H5	2	412.300	5.349	0.000	0.000	1.000
C6H5O	2	450.000	5.500	0.000	0.000	1.000
C5H5OH	2	450.000	5.500	0.000	0.000	1.000
C6H6	2	412.300	5.349	0.000	0.000	1.000
C6H7	2	412.300	5.349	0.000	0.000	1.000
CH	1	80.000	2.750	0.000	0.000	0.000
CH2	1	144.000	3.800	0.000	0.000	0.000
CH2(S)	1	144.000	3.800	0.000	0.000	0.000
CH2*	1	144.000	3.800	0.000	0.000	0.000
CH2CHCCH	2	357.000	5.180	0.000	0.000	1.000
CH2CHCCH2	2	357.000	5.180	0.000	0.000	1.000
CH2CHCH2	2	260.000	4.850	0.000	0.000	1.000
CH2CHCHCH	2	357.000	5.180	0.000	0.000	1.000
CH2CHCHCH2	2	357.000	5.180	0.000	0.000	1.000
CH2CO	2	436.000	3.970	0.000	0.000	2.000
CH2O	2	498.000	3.590	0.000	0.000	2.000
CH2OH	2	417.000	3.690	1.700	0.000	2.000
CH3	1	144.000	3.800	0.000	0.000	0.000
CH3CC	2	252.000	4.760	0.000	0.000	1.000
CH3CCCH2	2	357.000	5.180	0.000	0.000	1.000
CH3CCCH3	2	357.000	5.180	0.000	0.000	1.000
CH3CCH2	2	260.000	4.850	0.000	0.000	1.000
CH3CHCH	2	260.000	4.850	0.000	0.000	1.000
CH3CH2CCH	2	357.000	5.180	0.000	0.000	1.000
CH3CHO	2	436.000	3.970	0.000	0.000	2.000
CH2CHO	2	436.000	3.970	0.000	0.000	2.000
CH3CO	2	436.000	3.970	0.000	0.000	2.000
CH3O	2	417.000	3.690	1.700	0.000	2.000

CH3OH	2	481.800	3.626	0.000	0.000	1.000
CH4	2	141.400	3.746	0.000	2.600	13.000
CH4O	2	417.000	3.690	1.700	0.000	2.000
CN	1	75.000	3.856	0.000	0.000	1.000
CNC	1	232.400	3.828	0.000	0.000	1.000
CNN	1	232.400	3.828	0.000	0.000	1.000
CO	1	98.100	3.650	0.000	1.950	1.800
CO2	1	244.000	3.763	0.000	2.650	2.100
H	0	145.000	2.050	0.000	0.000	0.000
H2C4O	2	357.000	5.180	0.000	0.000	1.000
H2	1	38.000	2.920	0.000	0.790	280.000
H2CCCCH	2	357.000	5.180	0.000	0.000	1.000
H2CCCCH2	2	357.000	5.180	0.000	0.000	1.000
H2CCCH	2	252.000	4.760	0.000	0.000	1.000
H2CN	1	569.000	3.630	0.000	0.000	1.000
H2NO	2	116.700	3.492	0.000	0.000	1.000
H2O	2	572.400	2.605	1.844	0.000	4.000
H2O2	2	107.400	3.458	0.000	0.000	3.800
HC2N2	1	349.000	4.361	0.000	0.000	1.000
HCCHCCH	2	357.000	5.180	0.000	0.000	1.000
HCCO	2	150.000	2.500	0.000	0.000	1.000
HCNN	2	150.000	2.500	0.000	0.000	1.000
HCCOH	2	436.000	3.970	0.000	0.000	2.000
HCN	1	569.000	3.630	0.000	0.000	1.000
HCO	2	498.000	3.590	0.000	0.000	0.000
HE	0	10.200	2.576	0.000	0.000	0.000
HCNO	2	232.400	3.828	0.000	0.000	1.000
HOCN	2	232.400	3.828	0.000	0.000	1.000
HNCO	2	232.400	3.828	0.000	0.000	1.000
HNNO	2	232.400	3.828	0.000	0.000	1.000
HNO	2	116.700	3.492	0.000	0.000	1.000
HNOH	2	116.700	3.492	0.000	0.000	1.000
HO2	2	107.400	3.458	0.000	0.000	1.000
N	0	71.400	3.298	0.000	0.000	0.000
N2	1	97.530	3.621	0.000	1.760	4.000
N2H2	2	71.400	3.798	0.000	0.000	1.000
N2H3	2	200.000	3.900	0.000	0.000	1.000
N2H4	2	205.000	4.230	0.000	4.260	1.500
N2O	1	232.400	3.828	0.000	0.000	1.000
NCN	1	232.400	3.828	0.000	0.000	1.000
NCO	1	232.400	3.828	0.000	0.000	1.000
NH	1	80.000	2.650	0.000	0.000	4.000
NH2	2	80.000	2.650	0.000	2.260	4.000
NH3	2	481.000	2.920	1.470	0.000	10.000
NNH	2	71.400	3.798	0.000	0.000	1.000
NO	1	97.530	3.621	0.000	1.760	4.000

NCNO	2	232.400	3.828	0.000	0.000	1.000
NO2	2	200.000	3.500	0.000	0.000	1.000
O	0	80.000	2.750	0.000	0.000	0.000
O2	1	107.400	3.458	0.000	1.600	3.800
OH	1	80.000	2.750	0.000	0.000	0.000
HNCN	2	150.000	2.500	0.000	0.000	1.000
CH2CN	2	417.000	3.690	1.700	0.000	2.000
CH2NC	2	417.000	3.690	1.700	0.000	2.000
CH2N	2	498.000	3.590	0.000	0.000	2.000
HNC	1	569.000	3.630	0.000	0.000	1.000
NHC	1	569.000	3.630	0.000	0.000	1.000
HCCN	2	150.000	2.500	0.000	0.000	1.000
CH3CN	2	481.800	3.626	0.000	0.000	1.000
H2CNH	2	252.000	4.760	0.000	0.000	1.000
CH2N	2	498.000	3.590	0.000	0.000	2.000